Colección de Estudios de Física 92

Low temperature calorimetry applications: radiation detectors and material characterisation

María Parra Borderías

Low Temperature Calorimetry Applications: Radiation Detectors and Material Characterisation

Colección de Estudios de Física
Vol. 92

Esta colección recoge las tesis presentadas en el Departamento de Física de la Materia Condensada de la Universidad de Zaragoza desde su constitución en 1987.

Colección de Estudios de Física Vol. 92

Low Temperature Calorimetry Applications: Radiation Detectors and Material Characterisation

María Parra Borderías

Prensas Universitarias
Universidad Zaragoza

PARRA BORDERÍAS, María

Low temperature calorimetry applications : radiation detectors and material characterisation / María Parra Borderías. — Zaragoza : Prensas Universitarias de Zaragoza, 2011

XVI, 255 p. : il. ; 25 cm. — (Colección de Estudios de Física ; 92)

Bibliografía: p. 227-245. — ISBN 978-84-15274-87-2

Calor–Medición–Tesis doctorales

536.6(043.2)

1.ª edición, 2011

Prensas Universitarias de Zaragoza. Edificio de Ciencias Geológicas, c/ Pedro Cerbuna, 12, 50009 Zaragoza, España. Tel.: 976 761 330. Fax: 976 761 063
puz@unizar.es http://puz.unizar.es

Impreso en España
Imprime: Servicio de Publicaciones. Universidad de Zaragoza
D.L.: Z-2749/2011

A mis padres
y a mi hermano Andrés...

Contents

Introduction **xiii**

I Calorimetry as an analysis tool. Study of the competing interactions in $NdFe_xGa_{(1-x)}O_3$ compounds and its effects on magnetic ordering **1**

1 Heat capacity in magnetic systems **3**
1.1 Introduction . . . 3
1.2 Lattice contribution . . . 4
1.3 Electronic contribution . . . 6
1.4 Magnetic contribution . . . 6
1.5 Conclusions . . . 8

2 $NdFe_xGa_{(1-x)}O_3$ compounds: a case study **9**
2.1 Introduction: Nd orthorhombic perovskites . . . 9
2.2 Synthesis . . . 11
2.3 Crystalline structure . . . 11
2.3.1 Spatial group . . . 11
2.3.2 Structural characterisation . . . 13
2.4 Magnetic structure . . . 15

3 Calorimetric study of the inhibition of Nd magnetic order in $NdFe_xGa_{(1-x)}O_3$ **19**
3.1 Introduction . . . 19
3.2 Experimental details . . . 20
3.3 Experimental results: specific heat measurements . . . 22
3.4 Analysis of the experimental specific-heat data . . . 25
3.4.1 Study of the different specific-heat contributions . . . 25
3.4.2 Specific-heat response of the $NdFe_{0.2}Ga_{0.8}O_3$ sample as a function of an applied field . . . 30
3.4.3 Estimation of the total magnetic entropy . . . 32

3.5 Conclusions 34

4 Complementary experimental techniques 37
4.1 Introduction 37
4.2 Magnetic analysis: magnetisation and susceptibility 38
4.3 Magnetic structure: neutron diffraction 39
4.3.1 Why to use neutrons? 39
4.3.2 Description of neutron powder diffractometers 41
4.4 X-ray magnetic circular dichroism 44
4.4.1 Why to use XMCD? 44
4.4.2 Brief theoretical basis of XMCD 45
4.4.3 Description of the Circular Polarisation Beamline 47

5 Fe magnetic ordering in $NdFe_xGa_{(1-x)}O_3$ 49
5.1 Introduction 49
5.2 Magnetisation measurements 51
5.3 Susceptibility measurements 52
5.4 Neutron measurements 56
5.5 Conclusions 64

6 Nd magnetic ordering in $NdFe_xGa_{(1-x)}O_3$ 67
6.1 Introduction 67
6.2 Neutron diffraction measurements 68
6.3 Susceptibility measurements 73
6.4 Conclusions 77

7 Negative magnetisation on the $NdFe_xGa_{(1-x)}O_3$ series 81
7.1 Introduction 81
7.2 Magnetisation measurements 82
7.3 Susceptibility measurements 86
7.3.1 Description of $NdFe_xGa_{(1-x)}O_3$ χ_{AC} measurements . . . 86
7.3.2 Detailed study of $NdFe_{0.8}Ga_{0.2}O_3$ *ac* susceptibility measurements: Experimental results 88
7.3.3 Magnetic relaxation models 91
7.3.4 Detailed study of $NdFe_{0.8}Ga_{0.2}O_3$ susceptibility measurements: Analysis of χ_{AC} measurements 92
7.4 Possible origins of negative magnetisation in $NdFe_xGa_{(1-x)}O_3$ series 94
7.5 Selective magnetometry by X-ray Magnetic Circular Dichroism (XMCD) in $NdFe_{0.8}Ga_{0.2}O_3$ 96
7.6 Conclusions 100

8 Part I Final Conclusions 103

II Calorimetry as a detection tool. TES based bolometers and calorimeters for radiation detection 107

9 Calorimeters and bolometers based in superconducting materials 109
9.1 Superconducting cryogenic detectors for astronomical applications 109
9.2 Transition edge sensors . . . 111
9.2.1 Superconductivity . . . 111
9.2.2 Proximity effect . . . 113
9.2.3 Voltage bias and negative electro-thermal feedback . . . 114
9.2.4 Different parts and requirements of TES . . . 116

10 Materials for TES: structural and functional characterisation 119
10.1 Introduction . . . 119
10.2 Experimental techniques . . . 121
10.3 Superconducting material: Molibdenum . . . 123
10.3.1 Properties dependence on deposition conditions . . . 123
10.3.2 Size effects in Molybdenum layers. . . . 131
10.4 Normal metal materials: Copper and Gold . . . 141
10.4.1 Metal layer morphology . . . 142
10.4.2 Metal layer normal resistance by sputtering and electron beam deposition . . . 143
10.5 Conclusions. . . . 144

11 Bilayers: design and characterisation 147
11.1 Introduction . . . 147
11.2 Experimental details . . . 148
11.3 Sputtering samples: Mo/Au and Mo/Cu . . . 150
11.4 The trilayer solution . . . 152
11.5 Critical temperature as a function of Mo thickness . . . 154
11.6 DC sputtered Mo in Mo/Au bilayers . . . 159
11.7 Annealing effects on bilayer functional properties. . . . 161
11.8 Conclusions . . . 164

12 Towards a Mo/Au TES 167
12.1 Introduction . . . 167
12.2 Measurement system . . . 167
12.3 Lithographic processes . . . 169
12.4 Mo/Au TES thermometers: superconducting functional properties 170
12.5 Conclusions . . . 172

13 AC bias characterisation of a TES microcalorimeter 175
13.1 Introduction . . . 175

13.1.1 Frequency domain multiplexing versus time domain multiplexing . . . 175
13.1.2 Other multiplexing methods. . . . 177
13.2 Measurement system . . . 177
13.3 AC bias measurement analysis . . . 179
13.3.1 Recovery of sensor response information. . . . 179
13.3.2 Feedback loop gain estimation. . . . 181
13.3.3 Extra negative resistance in the TES bias circuit . . . 183
13.3.4 TES loading curve. . . . 185
13.4 I-V measurements . . . 187
13.4.1 Measurement conditions optimisation. . . . 187
13.4.2 I-V measurements for different bath temperatures: estimation of the thermal conductivity of the sensor. . . . 192
13.5 Complex impedance and noise measurements . . . 195
13.5.1 Complex impedance under AC bias . . . 195
13.5.2 Noise measurements under AC bias . . . 199
13.6 Conclusions. . . . 201

14 AC-DC bias characterisation of a TES bolometer 203
14.1 Introduction . . . 203
14.2 Sensors and measurement system . . . 204
14.3 IV measurements under DC bias . . . 206
14.4 Noise measurements under DC bias . . . 208
14.5 IV measurements under AC bias . . . 210
14.5.1 Calibration of IV measurements under AC bias . . . 210
14.5.2 I-V curves analysis under AC bias . . . 214
14.6 Noise measurements under AC bias . . . 215
14.7 Complex impedance measurements under DC . . . 217
14.8 Conclusions . . . 219

15 Part II Final Conclusions 223

Bibliography 227

Publications 247

Acknowledgements 253

Introduction

The temperature response of a body to applied heat, measured by the heat capacity, is one of the most important basic parameters of solid stated physics research, since, as any other thermodynamic property, it has the power of generality. Not only any temperature-dependent phenomena taking place in a system will contribute to the heat capacity, but also, every theoretical description proposed for that system has to satisfy the thermodynamic relations and thus, be able to account for the obtained calorimetric results. Heat capacity measurements provide a general knowledge of the different energetic contributions playing a role in the studied system, from phonons and spins to crystallographic transitions, what makes heat capacity experiments a powerful tool in a large variety of areas of physics and chemistry, i.e. thermodynamic studies, electronic or magnetic research, crystallography or cooperative phenomena.

The question of specific heat has been closely related to low-temperature physics, not only because of its connection with the development of cryogenic refrigerators. The proposition of the third law of thermodynamics by Nernst at the beginning of the 20th century established that the entropy, and thus, the heat capacity of a perfect crystal should tend to zero when the absolute zero temperature is approached. Eintein and Debye models for the specific heat of solids established the existence of quantum effects in specific heat measurements at low temperature, paving the way to relate the energy states of a system with its specific heat measurements. Any microscopic model of a system is aimed to obtain the set of energy levels that characterise it, independently of whether the system is a solid, a liquid or a gas. Statistical mechanics allows to derive thermodynamic parameters such as heat capacity or entropy from these models, being the inverse process impossible. Thus, although specific heat measurements alone do not determine the finer details of the structure of a physical system, the complete overview of the integrated energy process taking place in the sample that these experiments provide, permits to directly test any theoretical model of the system.

Different experimental methods have been developed to determine the heat capacity of the different physical systems, but all of them have one thing in common: the use of a heating source that applies a known amount of heat, and the monitoring of the associated temperature changes. It is evident that a system of known heat capacity can be used to extract information about the received heat by measuring its temperature change. This is the base of radiation thermal detectors: bolometers and calorimeters.

When in 1800 Herschel discovered infrared radiation by measuring the temperature of the different colours of the visible spectrum separated by a prism, the existence of non-visible forms of light was clearly established. This discovery led to the development of new radiation detection techniques, such as the bolometer, invented in 1878 by Langley. In this device, an element of known heat capacity is used as radiation absorber connected through a weak link to a heat sink, and its temperature variations with respect to it are determined with a thermometer well coupled to the absorber. The same operational principle is used in calorimeters, being the only difference with bolometers the system characteristic relaxation time that, in the calorimeter case, allows to measure individual photons or particles, instead of radiation flux.

Before the 1960's, bolometers and calorimeters were hardly used for radiation detection since other room temperature detectors such as the Golay cell or the thermopile were simpler and more sensitive. Although in 1935 Simon observed that calorimetric detectors would have enhanced sensitivity when operated at low temperatures, it was not until the introduction of carbon radio resistors as thermometers that calorimetric detectors became a competitive radiation detection tool. Thermal detectors are, in general, more attractive than ionisation detectors for many applications, since they do not require efficient charge transport, are sensitive to non ionising radiation and operate in equilibrium. Due to these advantages and their low temperature operation, cryogenic bolometers and calorimeters are among the most sensitive and versatile radiation detectors available nowadays.

In this thesis we deal with the two branches of calorimetry above described: the use of calorimetry in the study of the physical properties of a system and its use for particle and radiation thermal detection.

Regarding the former objective, it has been already mentioned that specific heat measurements provide information on the energy levels of a system, which are given by different modes of energy such as vibrations of atoms about their equilibrium lattice positions, the movement of electrons inside metals or changes in the crystallographical structure of the system. Therefore, the issue of the specific heat of physical systems is extraordinary wide. In this thesis we focus on the magnetic contribution to specific heat. The interaction of

magnetic moments with external fields or with other moments in the system, leads to a modification of the energy levels of the system, that will depend on temperature and will change abruptly with cooperative transitions, thus providing a remarkable contribution to the specific heat measurement of the system. In **Chapter 1** a brief description of how to isolate and analyse this magnetic contribution is offered.

For the purpose of this thesis the $NdFe_xGa_{(1-x)}O_3$ series has been selected as a case study. In these compounds three competing magnetic interactions arise: Nd–Nd, Fe–Fe and Fe–Nd, their influence in the ordering processes taking place in the samples being dependent on the concentration of magnetic vacancies. The scenario set by the interplay of these interactions in the different compounds allows to test the strengths and weakness of calorimetry when applied to describe the behaviour of magnetic systems with variable complexity. In **Chapter 2** the basic properties of the $NdFe_xGa_{(1-x)}O_3$ compounds are presented, while in **Chapter 3** results from the calorimetric analysis of these samples are discussed.

The following chapters deal with the results obtained by the complementary techniques –described in **Chapter 4**– selected to achieve a full understanding of the different magnetic processes displayed by the $NdFe_xGa_{(1-x)}O_3$ samples. By means of susceptibility, magnetisation and neutron diffraction measurements conclusions extracted from specific heat measurements are corroborated or complemented, which allow us to draw a complete phase diagram of the studied compounds. In **Chapter 5** we focus on the magnetic ordering effects on the Fe sublattice, while in **Chapter 6** the Nd sublattice is analysed. Finally, in **Chapter 7** interesting results on magnetisation measurements, showing negative magnetisation in some of the $NdFe_xGa_{(1-x)}O_3$ compounds, are discussed by means of ac susceptibility and X-ray magnetic circular dichroism. This first part is closed with **Chapter 8** where the main conclusions of the study of the $NdFe_xGa_{(1-x)}O_3$ series are discussed.

With respect to the second objective of this thesis, we concentrate on a particular type of bolometers and calorimeters, the ones based on Transition Edge Sensors, since due to their extreme sensitivity, they are the base for the new generation of instruments being developed for astrophysics, astronomy or nuclear physics. This type of sensors uses the steep temperature dependence of the resistance in a superconducting-to-normal transition to translate temperature into an electrical signal. **Chapter 9** provides a more detailed description of what a TES is and how it is operated, and a brief summary of the physics involved in the detector response is also offered. In the following chapters we deal with the development and fabrication of Molybdenum based TES aimed for X-ray detection as part of the European 7th–Framework Eureca project. In

Chapter 10 optimal deposition conditions of the different materials involved are determined by analysing the dependance of the functional properties with the deposition parameters. To do so, resistivity measurements are combined with structural characterisation. This study allows to deposit TES bilayers with excellent performance to be used as radiation sensors. **Chapter 11** provides a description of the development and characterisation of these samples and an analysis of their properties. **Chapter 12** shows the transformation of the deposited materials into sensors by lithographic processes and a preliminary characterisation of the resulting TES thermometers.

In **Chapter 13** and **14** TES based on a different superconducting material –Titanium– and fabricated at SRON-Utrecht are fully characterised. These sensors have already proven excellent sensitivity both as calorimeters and bolometers. Thus, the objective in this case is to compare their behaviour under DC and AC bias, so as to show the viability of the frequency domain multiplexed technique to read TES arrays. This is a crucial point for TES development since high-performance multiplexing schemes are essential to guarantee a large enough active area with low enough heat load, as required for the missions under study at ESA, such as the International X-ray Observatory (IXO) and the Japanese infrared telescope SPICA. Finally, the main conclusions of this second part are summarised in **Chapter 15**. All the references cited in this thesis are collected in the section **bibliography**, followed by a list of the publications resulting from the work of the thesis defendant at the Departamento de Física de la Materia Condensada de la Universidad de Zaragoza and at the Instituto de Ciencia de Materiales de Aragón (CSIC-Universidad de Zaragoza).

Part I

Calorimetry as an analysis tool. Study of the competing interactions in $NdFe_xGa_{(1-x)}O_3$ compounds and its effects on magnetic ordering

Chapter 1

Heat capacity in magnetic systems

1.1 Introduction

The total heat capacity of a system is defined as the heat amount, ΔQ one has to provide to the system in order to make the temperature raise a quantity ΔT and is expressed as:

$$C_{x,y,...} = \lim_{T \to 0} \frac{dQ}{dT}_{x,y,...} \tag{1.1}$$

Dividing by the mass of the sample, the specific heat with the parameters $x, y, ...$ kept constant is obtained. Usually in solids, as it will be our case, the quantity kept constant is the pressure, thus the corresponding specific heat expression reduces to:

$$C_p = \frac{dQ}{dT}_p = T\frac{\delta S}{\delta T}_p \tag{1.2}$$

where δS is the associated change in the sample entropy.

From the statistical mechanics point of view, the specific heat of a system can be obtained by differentiating with respect to the temperature the system partition function, that is obtained from the system energy level distribution. Thus, the experimental specific heat of a sample is given by the global contribution of all the energy levels of the system. In a magnetic system, the interaction of magnetic moments between themselves and with external magnetic fields modifies the energy levels of the system, thus significantly contributing

to the total system specific heat. To extract the magnetic component of the specific heat, a good knowledge of the rest of C_p contributions is required.

Most of the developments and results in calorimetry of magnetic systems occur at low temperatures, since, due to the drastic reduction of C_p by a factor of $10^4 - 10^7$ with respect to room temperature [1], the lattice contribution becomes small enough to allow to determine the magnetic contribution more precisely. In this chapter, the main contributions to the specific heat in this temperature range are summarised and the temperature dependence of the different models applied for every case is described.

1.2 Lattice contribution

In the classical theory, a solid with N atoms can be considered as formed by 3N independent harmonic oscillators –one per each direction– with associated kinetic and potential energies. According to the energy equipartition theorem, in a system in thermal equilibrium, each atom has the same average energy –$k_BT/2$– associated with each independent degree of freedom of their motion, being the total energy per atom in this case $3k_BT$. Assuming a system with n atoms per molecule, the molar internal energy will be given by:

$$U = 3nN_Ak_BT = 3nRT \tag{1.3}$$

where R is the universal constant of ideal gases. The molar specific heat can then be obtained differentiating Eq. 1.3 as a function of temperature, getting the classical Dulong-Petit law for the specific heat:

$$C_M = \left(\frac{\delta U}{\delta T}\right)_M = 3nR \tag{1.4}$$

that only reproduces experimental data at high temperatures. At lower temperatures, a more complex approximation is required. Two are the main models describing the lattice specific heat in the basis of the harmonic approximation: the Einstein and the Debye model. In both cases, thermal vibration of the atoms about their equilibrium positions are treated as a superposition of motions of harmonic oscillators, according to the laws of quantum statistics.

The first theory that successfully explained the behaviour of a solid specific heat at low temperatures was formulated by Einstein in 1907 [2]. In this model the solid is also formed by 3N unidimensional independent harmonic oscillators, but in this case, all of them display the same characteristic frequency, ω_E.

According to the quantum theory, the energy of a linear harmonic oscillator of frequency ω_E is quantised as:

$$\varepsilon = (n + 1/2)\hbar\omega_E \tag{1.5}$$

Taking into account these assumptions the heat capacity can be derived by means of statistical methods [3]:

$$C = \frac{3R(\theta_E/T)^2 e^{\theta_E/T}}{(e^{\theta_E/T} - 1)^2} \tag{1.6}$$

where $\theta_E = \hbar\omega_E/k_B$ is the Einstein temperature. Despite its simplicity, this model was able to predict that the heat capacity of a solid, and in particular of diamond, tends to zero as temperature decreases, maintaining the classical Dulong-Petit law for high temperatures. The Einstein model explains qualitatively the heat capacity of most of the compounds at low temperature, but it does not properly adjust these results, that show a T^3 dependency, instead of the exponential temperature dependency predicted by the model.

A more realistic model is the one due to Debye. On the basis of quantum statistics, the internal energy of a solid at low temperatures is basically determined by the low frequency modes of vibration [4]. These acoustic branches can be assumed to propagate through the solid as if it was a continuum, since their wavelengths are much larger than the interatomic distances. In this model, the solid is still assimilated to a system of 3N quantum harmonic oscillators, however, the oscillation frequency is not a common value for all of them, but a discrete distribution of values with a given density of states. In the Debye model, the discreteness of the solid limits the range of frequencies to some maximum or cut-off frequency known as the Debye frequency, ω_D. The lattice heat capacity –phonon contribution– in this model is given by the following expression [3]:

$$C = 9R\Big(\frac{T}{\theta_D}\Big)^3 \int_0^{\theta_D/T} \frac{x^4 e^x dx}{(e^x - 1)^2} \tag{1.7}$$

where $\theta_D = \hbar\omega_D/k_B$ is the Debye temperature. In this case both high an low temperature limits are properly predicted by the lattice heat capacity model:

$$C = 3R\Big(1 - \frac{1}{20}\frac{\theta_D^2}{T} + ...\Big) \text{at high temperatures, T} \gg \theta_D$$
$$C = \frac{12}{5}\pi^4 R\Big(\frac{T}{\theta_D}\Big)^3 \text{at low temperatures, T} \ll \theta_D \tag{1.8}$$

The practical problem of estimating the lattice heat capacity can be approached by different methods: estimation of phonon spectra from lattice dynamics calculation or measurement of an isostructural non-magnetic compound, among others. However, as mentioned above, in most of the cases of specific heat measurements in magnetic system, only the low temperature region is analysed. Thus, the lattice specific heat can be estimated as $C \propto T^3$.

1.3 Electronic contribution

In metallic materials the additional contribution of the free electrons to the heat capacity has to be considered. Since conduction electrons can be considered a Fermi gas, they obey the Fermi-Dirac statistics, from which the specific heat can be estimated as:

$$C_e = \frac{\pi^2}{3} n(\varepsilon_F) k_B^2 T = \gamma T \tag{1.9}$$

where the electronic coefficient, γ, is proportional to the density of states at the Fermi level, $n(\varepsilon_F)$ [3].

1.4 Magnetic contribution

The magnetic part of the specific heat is divided between the isolated and the interacting magnetic moments contributions.

In the general case of magnetic moments interacting with an external magnetic field, a set of different magnetic moments with different energy levels and degeneracies will be found. The population of each level, p_i will be given by the Boltzmann statistics:

$$p_i = \frac{g_i e^{-E_i/(k_B T)}}{\sum_i g_i e^{-E_i/(k_B T)}} \tag{1.10}$$

The magnetic energy can then be calculated as:

$$U_m = \frac{\sum_i E_i g_i e^{-E_i/(k_B T)}}{\sum_i g_i e^{-E_i/(k_B T)}} \tag{1.11}$$

and, from U_m, the heat capacity is obtained by derivation with respect to temperature. The result is the so called Schottky contribution, that, for the particular case of a two-level system reduces to [5]:

$$C = N \frac{E_1^2}{k_B T^2} \frac{g_0}{g_1} \frac{e^{E_1/(k_B T)}}{\left[1 + \frac{g_0}{g_1} e^{E_1/(k_B T)}\right]} \tag{1.12}$$

where g_0 and g_1 are the degeneracies of the ground and first excited level lying at energy E_1. The low-temperature part is exponential with the same temperature dependence as the Einstein model given in Eq. 1.6 at low temperatures, while the high-temperature part follows a T^{-2} dependency. Low temperature energy levels, like the ones often displayed in rare-earth compounds, are shown in specific heat measurements as Schottky anomalies and, if they are sufficiently separated, the splitting and degeneracy can be determined from calorimetric measurements.

When magnetic moments interact, the structure of the energy levels is modified. However, when cooperative phenomena produces long range correlation, the interaction cannot be solved in a limited number of energy states, as in the previous case. Only in the absence of thermal vibrations, the ideal magnetic order state can be found, otherwise spin-waves, similar to lattice vibrations, perturb the fundamental state. Thus, the magnetic contribution to the specific heat can be associated to magnons that, as phonons for lattice vibrations, are the quanta of the spin-waves [1]. This spin dependent contribution to the specific heat can be expressed by the Heisenberg-Dirac hamiltonian, that provides a general anisotropic hamiltonian for spin interactions.

$$\mathbf{H} = -2 \sum_{i<j}^{nn} J_{i,j} [a S_{iz} S_{jz} + b(S_{ix} S_{jx} + S_{iy} S_{jy})] - g \mu_B \overrightarrow{H} \sum_i \overrightarrow{S}_i \tag{1.13}$$

where the spin dimensionality is given by the coefficients a and b [5]. The model that should be applied to the specific heat measurements of a magnetic system depends on the combination of spin and lattice dimensionalities of the system. Among the different models only a few have an exact solution. For the rest, measurements are divided into three different regions: low temperature $T < T_C$ –the spin-wave region–, the critical region $T \approx T_C$ and the high temperature region $T > T_C$.

At low temperatures, the dispersion relations of the spin waves can be found, being dependent on the type of interaction and the lattice dimensionality. For a 3d lattice, the heat capacity contribution of an antiferromagnet is proportional to T^3, while the contribution of a ferromagnet is proportional to $T^{3/2}$ [4].

In the critical region, the heat capacity is divided into two different expressions:

$$\begin{aligned} C &= A\Big(\frac{T_C - T}{T_C}\Big)^{-\alpha'} \text{ for } T < T_C \\ C &= A\Big(\frac{T - T_C}{T_C}\Big)^{-\alpha} \text{for } T > T_C \end{aligned} \tag{1.14}$$

where α' and α are the critical exponent that can be obtained from different techniques, such as renormalization group techniques, Monte Carlo simulations or high temperature series expansion [5]. Again, the obtained value depends on the dimensionality of the spin and magnetic lattice.

Magnetic order transitions produce singularities denoted as λ-anomalies in the specific heat. This type of features is not only limited to magnetic transitions, but are characteristics of cooperative phenomena, turning specific heat measurements into one of the most suitable tools to identify phase transitions. Several examples are electronic transitions such as superconductivity or ferroelectricity, crystallographic transitions, order-disorder transitions, superfluity or molecular rotational vibrations.

1.5 Conclusions

The enormous variety of phenomena whose nature can be evidenced through specific heat measurements turns calorimetry data into a powerful tool in many areas of physics and chemistry. When applied to magnetism, this macroscopic technique describes the behaviour of the complete magnetic system. Once the magnetic contribution is isolated by subtracting the lattice and electronic contributions, valuable information on the magnetic energy levels can be extracted, since the specific heat shape will be a footprint of the different magnetic interactions taking place in the system.

Chapter 2

$NdFe_xGa_{(1-x)}O_3$ compounds: a case study

2.1 Introduction: Nd orthorhombic perovskites

Rare-earth oxide compounds with perovskite structure (RMO_3) have been widely studied in solid-state physics due to its rather simple structure and the rich variety of electronic and magnetic phenomena observed, such as magnetoresistance [6] and superconductivity [7, 8]. In rare earth (R) and transition metal (M) perovskites both components order in two interspersed simple cubic sublattices that determine the magnetic properties of the sample through the three present magnetic interactions [9]. In general, these interactions follow the hierarchy of M-M, M-R and R-R in descending strength.

Nd orthorhombic perovskites RMO_3 are particularly attractive because of the great number of magnetic and non-magnetic metal ions (M) that can be substituted while maintaining the same structure; an orthorhombically distorted perovskite with four formula units per elementary cell and space group $D_{2h}^{16} - Pbnm$ [9].

For non-magnetic M ions as Ga, only the collective antiferromagnetic ordering of Nd at $T = 0.97$ K is present [10] due to Nd-Nd exchange interaction. When M is a $3d$ magnetic ion as Fe, Ni or Cr, the M sublattice orders antiferromagnetically with a small canting angle at high temperature T_{N1} due to M-M interaction. T_{N1} ranges from ∼700 K for $NdFeO_3$ [11] to ∼200 K for $NdCrO_3$ [12] and $NdNiO_3$ [13]. Below T_{N1} the anisotropic M-Nd exchange induces spin reorientation transitions of the M sublattice. In many cases, the antiferromagnetic ordering of M sublattice does not imply a full compensation of the M magnetic moments due to a weak ferromagnetic component. A com-

bination of isotropic and anisotropic M-Nd exchange interactions originated by the weak ferromagnetic and the antiferromagnetic M order, respectively, creates an effective field on the Nd site, H_{M-Nd}. This effective field polarises the Nd^{3+} spins by splitting the Nd ground state, thus reducing the magnetic entropy available for cooperative Nd-Nd ordering at low temperatures. This Nd polarisation has been observed in powder neutron diffraction experiments at low temperatures [14, 15]. Depending on the strength of this H_{M-Nd}, cooperative order of Nd sublattice appears, f.e. in $NdFeO_3$ [16] or $NdNiO_3$ [17], at a similar temperature to that of the case where M is a non magnetic metal, whereas it is fully inhibited in others such as in $NdCrO_3$ [18] or $NdMnO_3$ [19]. It is interesting to note that $NdCrO_3$, the only member of the family in which the low-temperature M magnetic structure is purely antiferromagnetic, is the one with the largest energy splitting of the Nd ground doublet: $\Delta/k_B = 27$ K [12, 18].

Another source of rich phenomenology in magnetic orthorhombic perovskites is the introduction of magnetic vacancies in the M sublattice by substitution with a non-magnetic M' ion. The effects of the dilution are not negligible even for a small concentration of vacancies and its relevance depends on the nature of the rare-earth ion. In $DyFe_xAl_{(1-x)}O_3$, the Morin phase transition temperature increases [20], in $TbFe_xAl_{(1-x)}O_3$ the reorientation transition temperature decreases [21] while the Tb long-range is inhibited. The same last effect is observed in $NdFe_xCo_{(1-x)}O_3$ [22], where Co is in a low-spin state. Even in $HoFe_xAl_{(1-x)}O_3$ a new transition to a Γ_1 magnetic structure is induced by vacancies [23].

In this work we consider the case M = Fe, with the substitution of Fe ions by non-magnetic Ga ions to form the $NdFe_xGa_{(1-x)}O_3$ series. Each Ga atom is equivalent to the introduction of a magnetic vacancy in the Fe sublattice. In this case, the nearly complete antiferromagnetic compensation is destroyed around the neighbouring Nd^{3+} ions and a large, extra isotropic exchange field acting on both R and Fe sublattices arises.

This chapter is organised as follows: In Section 2.2 the sample synthesis process is described. In Section 2.3 both the crystalline structure of $NdFeO_3$ and $NdGaO_3$ pure compounds –Section 2.3.1– and the structural characterisation of $NdFe_xGa_{(1-x)}O_3$ series –Section 2.3.2– are discussed. Finally, in Section 2.4, the magnetic structure of the pure compounds is detailed. The relevant changes generated by substituting Fe ions by Ga non-magnetic ions that are likely to affect both Fe and Nd ordering processes are also presented.

2.2 Synthesis

$NdFe_xGa_{(1-x)}O_3$ powder samples were obtained by a standard ceramic route at the Instituto de Ciencia de Materiales de Aragón. In this type of process, where elements are placed in tight contact, the reaction is produced by diffusion or atomic mobility, since temperature throughout the procedure is lower than the melting point of each component. The main advantage of this solid-state method, besides its simplicity, is that, since temperatures are relatively low, pure metals segregation is avoided, making it easier to achieve single-phase oxides.

All samples studied in this part are prepared from binary oxide powders: Ga_2O_3 of 99.99% purity, Fe_2O_3 of 99.8% purity and Nd_2O_3 of 99.9% purity. A stoichiometric mixture of these binary oxides was calcined in air in three consecutive steps. The first step is carried out in a muffle furnace where samples are placed at 1000°C for 20 hours with a 5°C/min rate. The next two steps are carried out in a tubular furnace at air atmospheric pressure, being the first one of 60h. at 1200°C and the second one of 80 hours at 1400°C. Between every process the resulting material is grinded and pressed into pellets at $\sim$ 7 tons/cm^2. Samples x=0.4 and x=0.5 were subjected to an extra step of 48 hours at 1400°C, to ensure proper homogeneity throughout the samples close to percolation ($x_c \approx 0.31$) (See Chapter 5).

2.3 Crystalline structure

2.3.1 Spatial group

The studied compounds crystallise in a perovskite structure. Ideal perovskite unit cell, ABO_3 (see Fig.2.1) is cubic, belonging the the spacial group *Pm-3m*, with only one formula unit per unit cell. Atoms are located in special positions: atom A is placed in the cell centre in the Wyckoff 1b position (1/2, 1/2, 1/2), atom B is placed in the unit cell origin (0, 0, 0), while O atoms are located in the middle of the edges of the cube faces, in position 3d (0, 0, 1/2).

In perovskites, cation A is bigger than B, and it is coordinated with twelve O anions, while cation B is coordinated with 6 O anions. Using a ionic model of solid spheres, the maximum stability situation, provided by the maximum contact between ions, is represented by Eq. 2.1

$$R_a + \frac{R_b}{\sqrt{2}R_b + R_o} = 1 \tag{2.1}$$

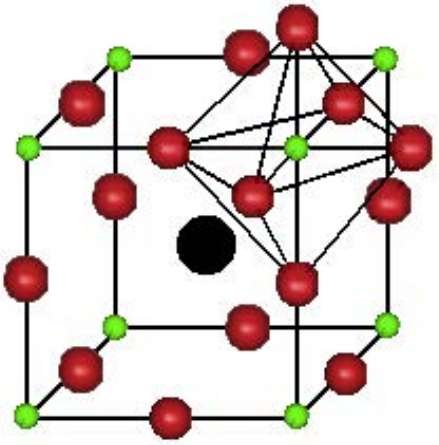

Figure 2.1: Crystallographic structure of a cubic perovskite $-Pm-3m-$, with the cation B in the cube vertex. This position is the centre of the oxygen octahedron.

Assuming anion O to be oxygen, A a rare earth element (R) and B a transition metal cation in a proper oxidation state (M), ionic radius R_a, R_b and R_o fulfilled approximately Eq. 2.1. That is the reason why, when proportion is 1:1, most rare-earth transition metal oxides crystallised in this solid structure.

This structure can be considered to be a cubic close packed (ccp) of oxygen and R atoms, being the RO_3 layer parallel to the (111) plane of the cubic structure. M atoms are placed in a quarter of the structure octahedral sites, the ones corresponding to the cubic vertex shown in Fig. 2.1. The octahedral sites in the cubic faces and the tetrahedral ones are empty.

Usually the ideal cubic symmetry is not found, because ion size, together with electrostatic interactions, tend to distort the cubic symmetry of perovskites. Most common structures are rhombohedrically distorted perovskites (*R-3c*) and orthorhombically distorted perovskites (*Pbnm*). Both $NdFeO_3$ and $NdGaO_3$ belong to this group being their crystal structure an orthorhombically slightly distorted perovskite described in the space group *Pbnm* [24–26], (Z=4). In this structure c axis is duplicated, what translates into four formula units per unit cell. Plus, compared to the ideal perovskite parameter a_0, unit cell parameters are $a = \sqrt{2}a_0$, $b = \sqrt{2}a_0$ and $c = 2a_0$.

In $NdFeO_3$ and $NdGaO_3$, atoms are located on the following crystallographic sites: Nd^{3+} ions in (4c), Fe^{3+} or Ga^{3+} in (4b) and O^{2-} in (4c) and (8d). Fe^{3+} ions are coordinated by six O^{2-} ions forming FeO_6 octahedral. Therefore the diluted compounds $NdFe_xGa_{(1-x)}O_3$ are expected to have the same structure. 4b are special positions and therefore the Fe and/or Ga atoms

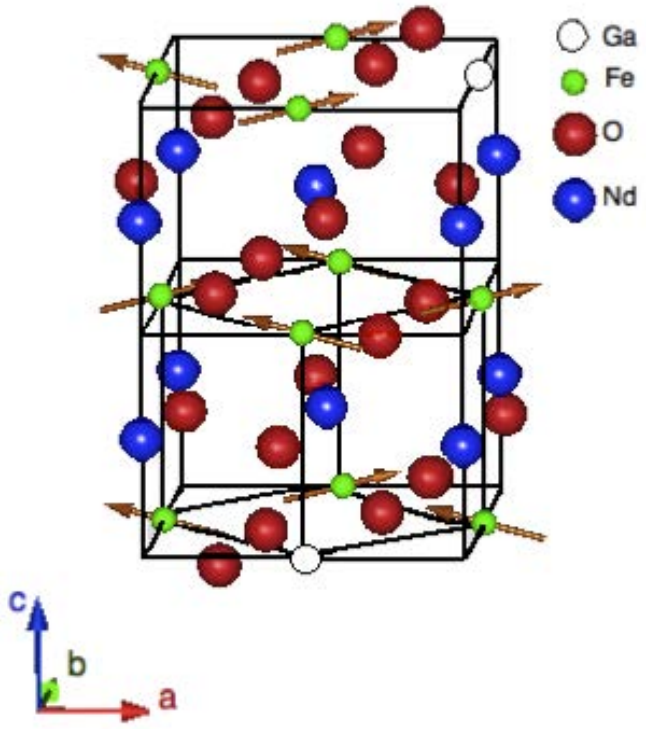

Figure 2.2: Crystallographic and magnetic structure of $NdFe_{0.8}Ga_{0.2}O_3$ at T=94 K. The positions of the depicted Ga ions have been chosen randomly.

form a perfect simple cubic (sc) lattice, while the Nd ions are slightly displaced from the ideal sc positions at the middle of the Fe/Ga cubes. A schematic representation of $NdFe_{0.8}Ga_{0.2}O_3$ crystallographic structure is illustrated in figure 2.2 together with its magnetic structure.

2.3.2 Structural characterisation

As described in Section 2.2 $NdFe_xGa_{(1-x)}O_3$ is easily synthesised since, as explained in Section 2.3, perovskite structure in oxides of rare earth and transition metal in proportion 1:1 is stable. However, intermediate phases such as gallium garnet, Nd_2O_3 or Ga_2O_3 are also stable and can be found in our samples. To study the possible presence of these intermediate phases, to confirm the *Pbnm* structure of $NdFe_xGa_{(1-x)}O_3$ and to analyse how the parameters describing the crystal ordering change along the series, X-ray diffraction studies were performed.

These studies were carried out in the Rigaku D/MAX 2500 X-ray diffractometer of the Servicio de Difracción de Polvo at the Servicios de Apoyo a la

Investigación of the University of Zaragoza. Measurements were taken in the region $20° \leqslant 2\theta \leqslant 80°$ with a 0.03° step at room temperature. The diffractometer works at 40 kV and 80 mA, with a rotating Cu anode and high linearity scintillation counter. A graphite diffracted-beam monochromator was used to select the $K\alpha_1$($\lambda = 1.5406$ $\mathring{A}$) and $K\alpha_2$($\lambda = 1.5444$ $\mathring{A}$) lines.

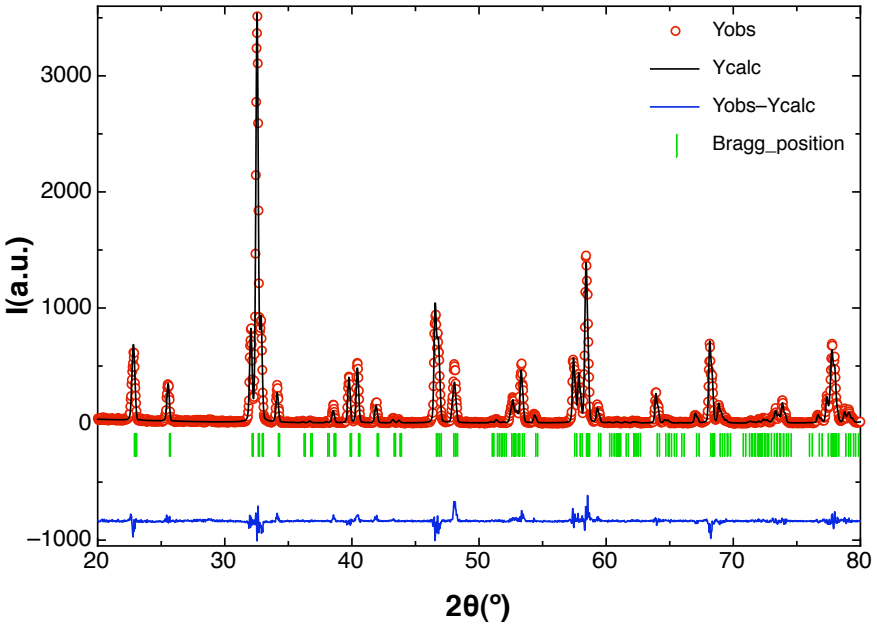

Figure 2.3: X ray diffraction diagram at room temperature of sample $x = 0.95$. ○ represents the observed intensity, − is the calculated intensity, | are the Bragg reflections and − is the difference between the observed intensity and the calculated one.

X-ray diffraction patterns of the studied compounds revealed no traces of any impurity phase at the technique sensitivity limit of $\sim 1\%$ in volume. In Fig. 2.3, a diffractogram of one of the samples, $x = 0.95$, is shown, together with the expected Bragg reflections of the main phase, the refined intensity and the difference between the observed intensity and the calculated one. X-ray data were analysed using the FULLPROF program [27, 28]. The parameters describing the crystal ordering, refined by the Rietveld method, are displayed on figure 2.4. Structural parameters of $NdFeO_3$ and $NdGaO_3$ from [25] and [29] were taken as starting parameters in our analysis. Since gallium ion is slightly smaller ($r = 76$ pm) than the high-spin iron one ($r = 78.5$ pm), the lattice parameter values and the unit cell volume increased with the iron content. No discontinuities were observed in lattice parameters in the whole range of iron concentration and, as expected, all the studied compounds comply with the *Pbnm* space group. As can be seen in figure 2.4, our results are in

good agreement with previous ones on the non-diluted perovskites and follow Vegard's law. The obtained values of the lattice parameters are displayed in Table 5.1 in Chapter 5.

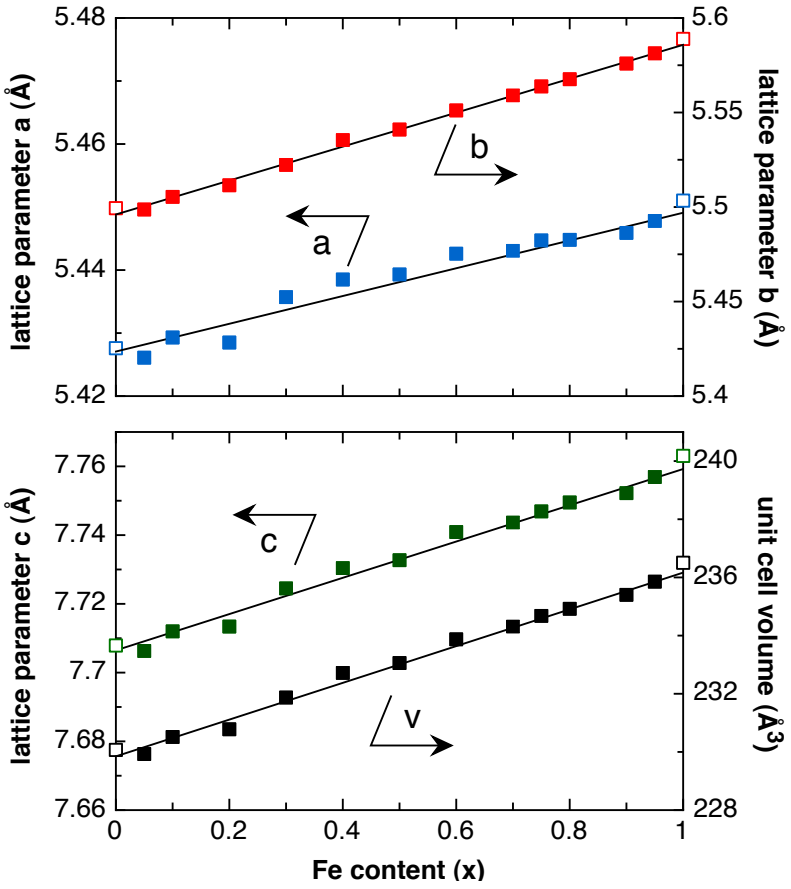

Figure 2.4: Upper panel: a (■) and b (■) lattice parameters obtained from the Rietveld refinement as a function of iron content. Lower panel: refined c lattice parameter (■) and unit cell volume (■) as a function of iron content. In both panels, lattice parameters of non-diluted compounds from [25] and [29] are also displayed in open symbols.

2.4 Magnetic structure

Neodymium gallate, $NdGaO_3$, was considered a rather stable and inert compound from the magnetic point of view since the only magnetic interaction, Nd-Nd interaction, was believed to be too weak to provide collective magnetic ordering of the Nd sublattice [30]. However, low temperature specific heat measurements showed that, as mentioned in Section 2.1, a collective antiferro-

magnetic ordering of Nd at $T = 0.97$ K, evidenced by a sharp lambda anomaly, is present [10].

In that work, Bartolomé et al. suggested an antiferromagnetic ordering of Nd magnetic moments and an accurate prediction of the observed low temperature specific heat was provided by an XY model on a simple cubic lattice. However, neutron diffraction measurements pointed to a c_z configuration of the Nd moments [25]. Moreover, the obtained g tensor was nearly isotropic, a result incompatible with a XY model. Later susceptibility measurements [31] confirmed the c_z configuration proposed by Marti et al. As can be observed in Fig. 2.5, in this structure Nd magnetic moments are ordered ferromagnetically inside a column parallel to c axes, and antiferromagnetically between adjacent columns. As Luis at al. [31] pointed in their article, in this configuration Nd exchange interaction is strongly direction dependent, unlike in the simple cubic lattice where all Nd six nearest neighbours are equivalent. They argue that this result can be expected, since only two nearest Nd neighbours are equivalent due to the low crystallographic symmetry of Nd sites have (only a horizontal mirror plane), In Ref. [31], susceptibility and heat capacity data are explained by the same set of parameters within the $S = 1/2$, Ising 2D to 3D crossover model.

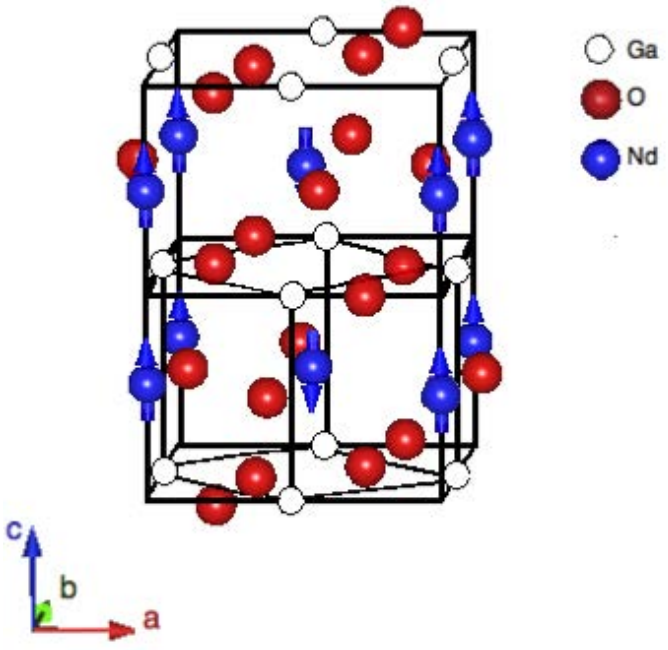

Figure 2.5: Crystallographic and magnetic structure of $NdGaO_3$ at very low temperature.

Similar results were found in other $NdMO_3$ systems where M was a non magnetic metal, such as $NdCoO_3$(where Co ions are in low-spin non-magnetic state) [32], $NdScO_3$ [33] and $NdInO_3$ [34]. In the first case, the same c_z magnetic structure for Nd ordering as $NdGaO_3$ was found, while the other two compound order in a $g_y a_x$ magnetic mode.

As discussed in Section 2.1, when M is a $3d$ magnetic metal as Fe, Ni or Cr, the M sublattice orders at high temperature T_{N1} due to M–M interaction. According to previous studies, order of iron spins in $NdFeO_3$ corresponds to an antiferromagnetic structure with a weak ferromagnetic component $G_x F_z$ (irreducible representation Γ_4) [35]. Below T_{N1} the anisotropic Fe-Nd exchange induces spin reorientation transitions of the M sublattice. In this region, marked by a double peak in susceptibility measurements, the iron spins rotate continuously in the *ac* plane , from $G_x F_z$ to the low temperature configuration $G_z F_x$ (irreducible representation Γ_2) [36, 37], being both configurations observed by neutron measurements (see Fig. 2.6). Moreover, at low temperatures this configuration induces, via Nd–Fe exchange, a Nd polarisation of the same symmetry ($c_y f_x$) that becomes noticeable in neutron measurements below 25K [16]. As mentioned above the Nd^{3+} ion occupies a low-symmetry position, being its $^4I_{9/2}$ ground multiplet fully splited into five Kramers doublets by the $C_s - m$ low-symmetry crystal field [22]. At low temperatures only the ground doublet is populated and the Nd polarisation can be observed in heat capacity measurements since it splits the ground doublet of Nd^{3+} ion due to Zeeman effect, producing a Schottky anomaly [32].

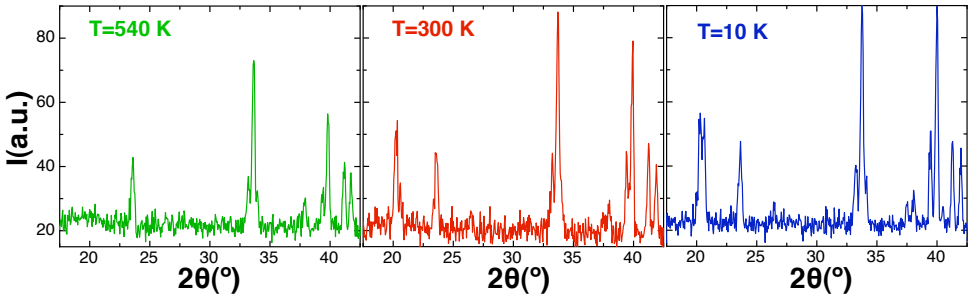

Figure 2.6: Neutron diffraction patterns for $NdFe_{0.8}Ga_{0.2}O_3$ (left panel): $T \gg T_{N1}$, (center panel): $T \gg T_{SR1}$, and (right panel): $T \ll T_{SR2}$.

Thus, the Nd momenta behave as a paramagnetic system in an internal field of intensity H_{M-Nd}. Depending on the strength of this H_{M-Nd}, cooperative order of Nd sublattice may appear, f.e. in $NdFeO_3$ [16] or $NdNiO_3$ [17], at a lower temperature as in the case where M is a non magnetic metal, evidenced by a small lambda peak superimposed on the Schottky anomaly. In other cases, such as in $NdCrO_3$ [18] or $NdMnO_3$ [19], no λ peak is found, indicating

than Nd cooperative ordering is fully inhibited.

In this context, the introduction of a non-magnetic atom in $RFe_xM_{1-x}O_3$ can be considered as the introduction of a magnetic vacancy in the Fe sublattice. In this case, the compensation of the isotropic exchange interaction on R^{3+} sites is destroyed and an extra isotropic exchange field acting on both R and Fe sublattices arises. The effect of this dilution is not negligible even for a small concentration of vacancies and depends on the rare-earth, as already mentioned in Section 2.1, being the net effect on the magnetic ordering of the rare earth dependent on the competition between the crystal electric field and the exchange field.

In following chapters we study the effect of magnetic vacancies on the magnetic ordering of the Fe sublattice and in the polarisation and magnetic ordering of the Nd sublattice in $NdFe_xGa_{(1-x)}O_3$. Some studies on $NdFe_xCo_{(1-x)}O_3$ for $x > 0.5$, have already been performed [22, 38]. The motivation to use Ga instead of Co as diamagnetic ion is, that it has a similar ionic radius to that of Fe (76 and 78.5 pm respectively). Moreover, it avoids deviations of the actual x value from the nominal one, because Co^{3+} ion may change its spin configuration depending on neighbouring defects, oxygen vacancies, etc., making difficult to control the paramagnetic fraction in the high x side.

As already mentioned, the Fe sublattice orders antiferromagnetically at $T_N \sim 700$ K [11], and therefore, the magnetic dilution of the Fe sublattice will provoke the lowering of T_N until the percolation limit is reached $x \approx 0.33$. Regarding the Fe sublattice two different situations are faced. For $x < 0.33$, Fe moments are paramagnetically disordered, generating a random H_{M-Nd} over Nd sites, while for $x > 0.33$, Fe moments will be ordered, but due to the magnetic vacancies still H_{M-Nd} will also be random. Both situations will be studied from the Fe sublattice point of view. Regarding Nd ordering, since the high Fe content region has already been studied, by substituting Fe ions by Co instead of Ga ions, [22, 38], in this work we shall mainly focus on the low Fe content region.

Chapter 3

Calorimetric study of the inhibition of Nd magnetic order in $NdFe_xGa_{(1-x)}O_3$

3.1 Introduction

As already discussed, due to the low intensity of the Nd-Nd exchange interaction –when it is in isolation, as in $NdGaO_3$, Nd sublattice orders antiferromagnetically at 1K–, the Nd cooperative order is not always present in the $NdMO_3$ compounds. When M is a magnetic ion, such as iron, Nd ordering takes place depending on the ratio between H_{M-Nd} and H_{Nd-Nd}. In $NdFeO_3$ this ratio is found just below the critical value which would inhibit Nd cooperative ordering. Thus, the study of the $NdFe_xGa_{(1-x)}O_3$ family, provides the opportunity to study the effect of magnetic vacancies on this ratio, and how it affects the ordering of the Fe and Nd sublattices. In this chapter we will focus on the effect of Fe dilution on the polarisation and magnetic ordering of the Nd sublattice. To do so, heat capacity measurements on $NdFe_xGa_{(1-x)}O_3$ compounds were performed. The reason to choose this technique is that, as already shown in previous studies [10, 18, 22, 30, 39], the magnetic features we are interested in are easily observed by specific heat measurements.

This chapter is organised as follows: in Section 3.2 a description of the measurement system and procedure is provided. In Section 3.3 experimental results are described; while in Section 3.4 a detailed analysis of the experimental data is performed to extract the information on the different observable contributions. Finally, in Section 3.5 the main results presented in this chapter are summarised.

3.2 Experimental details

Heat capacity measurements discussed in this chapter were performed in the Quantum Design PPMS (Physical Property Measurement System) located at the Servicio de Medidas Físicas of the University of Zaragoza[1]. When the PPMS Heat Capacity option is combined with the Helium-3 System, high sensitivity thermal-relaxation calorimetric measurements can be performed between 0.35 and 350 K, with a measurement accuracy better than 2%. The system also allows to apply a magnetic field as high as 9 T with a longitudinal uniformity of 0.01% over 5.5 cm x 1 cm diameter cylindrical volume.

Samples are mounted on to a platform of 3 x 3 mm^2 suspended by 4 thin wires. These wires are used as thermal connection between the platform and the bath, and as electrical connection for the heater and thermometer. Sample powder is pressed into pellets well below 1mm thick. To provide a compact piece, sample powder is combined with ethylene glycol, pressed and then dried in an oven at $\sim$200 °C for several ours. The samples are thermally contacted to the platform with Apiezon-N grease.

Among the different methods for calorimetric measurements the thermal-relaxation method developed by Bachmann et al. [40] is designed to study small samples at low temperatures. In this method the sample specific heat is determined by measuring the thermal response of the calorimeter to a heat pulse [41, 42]. The heat-flow diagram of the total system- sample, platform and heat bath- is displayed in Fig. 3.1a. The whole system consists of a sample of unknown heat capacity, C_s at a temperature T_s, connected to the platform with a grease of thermal conductance K_2. C_a is heat capacity of the total addenda (platform, Apiezon-N grease, thermometer and heater). This ensemble has a temperature of T_p. Finally, the platform is thermally connected to a heat bath at T_0 through K_1.

The heat balance in the system can be described by the following coupled differential equations [41]:

$$\begin{aligned} P &= C_a\frac{\mathrm{d}T_p}{dt} + K_2(T_p - T_s) + K_1(T_p - T_0) \\ 0 &= C_s\frac{\mathrm{d}T_s}{dt} + K_2(T_s - T_p) \end{aligned} \tag{3.1}$$

When a heat pulse, P, is applied to the heater, the platform and the sample are warmed to a temperature $T_0+\Delta T$, where $\Delta T = P/K_1$. Ideally, the thermal

[1] *http : //wzar.unizar.es/invest/sai/ins_ele/ins_ele.html*

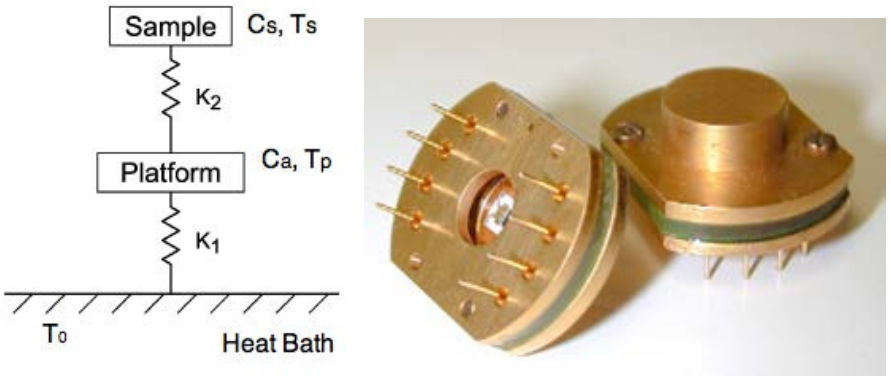

(a) (b)

Figure 3.1: (a) Heat flow diagram for a conventional thermal-relaxation calorimeter. (b) Picture of PPMS heat capacity sample holder.

connection between the sample and the platform will be good ($K_2 \gg K_1$, $T_s \sim T_p$), thus Eq. 3.1 simplifies to:

$$P = (C_a + C_s)\frac{\mathrm{d}T_p}{dt} + K_1(T_p - T_0) \tag{3.2}$$

When the heat pulse stops, both the platform and the sample cool down to the bath temperature T_0 following:

$$T_p(t) = T_0 + \Delta T \exp(-t/\tau) \tag{3.3}$$

with a time constant $\tau = (C_s + C_a)/K_1$. If $\Delta T/T \ll 1$, C_s, C_a and K_1 can be considered as temperature independent, thus, the sample heat capacity can be directly estimated from a measure of the temperature decay, once C_a and K_1 are determined. K_1 can be estimated by measuring ΔT for an applied power, since, as mentioned above, $\Delta T = P/K_1$; while C_a can be obtained from a temperature decay measurement of the system without sample.

However, if the condition $K_2 \gg K_1$ is not fulfilled, one can not consider $T_s = T_p$, and the thermal decay of T_p is the sum of two exponentials:

$$T_p(t) = T_0 + A\exp(-t/\tau_1) + B\exp(-t/\tau_2) \tag{3.4}$$

Usually, one of the time constants is much shorter than the other, τ_2, and corresponds to the thermal relaxation process between the sample and the platform; while the other, τ_1, correspond to the thermal relaxation between the platform and the bath.

The PPMS heat capacity software uses two separate algorithms to determine which of the two cases above described- Eq. 3.3 or Eq. 3.4 best fits the measured data. The chosen fit provides information such as the sample heat capacity, the addenda heat capacity, the thermal coupling between the sample and the platform or the thermal time-constants.

The sample $NdFe_{0.3}Ga_{0.7}O_3$ was further characterised by Marco Evangelisti and Fernando Luis in a Kelvinox 25 dilution fridge located at the Low Temperature Laboratory of the Instituto de Ciencia de Materiales de Aragón (ICMA). In this system, a heat-relaxation calorimeter compatible with the one available in the PPMS system has been installed, allowing us to extend the temperature range down to 100 mK. Data are calibrated using higher temperature measurements taken at the PPMS system.

3.3 Experimental results: specific heat measurements

Fig. 3.2 shows the results of the specific-heat experiments on $NdFe_xGa_{(1-x)}O_3$ with $0.05 \leqslant x \leqslant 0.5$, while in Fig. 3.3a these data are shown together with specific heat data of $NdGaO_3$ from Ref. [10]. In $NdGaO_3$ specific heat data, the Nd cooperative order is marked by a sharp peak at T=0.97 K, over the lattice contribution, being these two features the only observed contributions.

X ray diffraction analysis on $NdFe_xGa_{(1-x)}O_3$ series showed that no significant structural changes among the series take place as iron content increases, being *Pbnm* the space group in all cases . Therefore, as shown in Fig. 3.3a, the lattice contribution, dominant above 10 K, is expected to be approximately the same for all the samples, including $NdFeO_3$ and $NdGaO_3$. Below this temperature the lattice specific heat is mostly negligible. As already mentioned, Nd^{3+} in the family $NdMO_3$ is a $^4I_{9/2}$ ion fully split into five Kramers doublets by the $C_s - m$ low-symmetry crystal field. Inelastic neutron scattering at T=4.2 K [43] and specific heat measurements [18] on $NdCrO_3$ showed that the energy of the first Nd excited doublet is ∼127 K. Therefore the maximum of its Schottky contribution would be at $T \sim 50$ K and, since the low temperature part of a Schottky anomaly decay exponentially with temperature, no crystal field contribution is expected in the temperature range of study, $0.3 < T < 30$ K. Moreover, since $NdFe_xGa_{(1-x)}O_3$ compounds are dielectric and do not present superconductivity effects, crystallographic transitions, etc., below 10 K, all the observed features can be ascribed to the magnetic contribution, that can be considered practically isolated.

The sharp peak corresponding to the Nd magnetic ordering is still present in $x = 0.05$ ($T_N = 860$ mK), but it is strongly rounded in $x = 0.1$ ($T_N = 740$

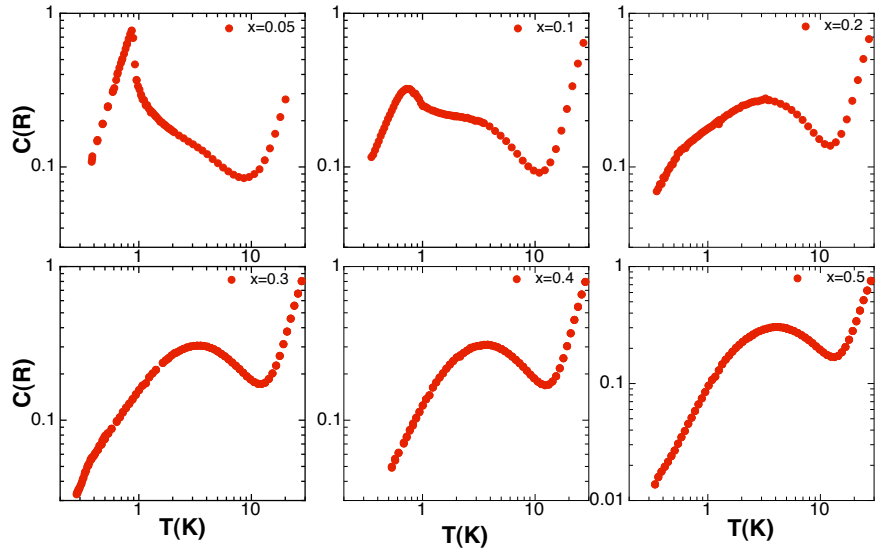

Figure 3.2: Low-temperature specific-heat measurements of the $NdFe_xGa_{(1-x)}O_3$ system for $0.05 \leqslant x \leqslant 0.5$.

mK). Moreover, its height is reduced by a factor of 3 in $x = 0.05$ and a factor of 10 in $x = 0.1$. The peak is substituted in $x = 0.2$ and $x = 0.3$ by a kink at T=520 mK and 350 mK respectively, while no trace of order can be found for $0.4 \leqslant x \leqslant 0.96$. As can be clearly observed in Fig. 3.3a, not only the height of the ordering peak is reduced by increasing Fe concentration, its position is also shifted towards lower temperatures, following a nearly linear dependence.

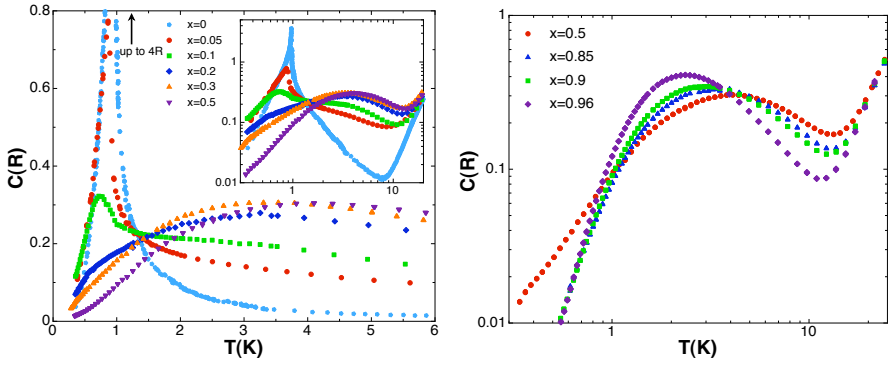

(a) (b)

Figure 3.3: (a) Low-temperature specific-heat measurements of the $NdFe_xGa_{(1-x)}O_3$ system for $0 \leqslant x \leqslant 0.5$. Inset shows the data in double-log scale up to 30 K. (b) Low-temperature specific-heat measurements of the $NdFe_xGa_{(1-x)}O_3$ system for $0.5 \leqslant x \leqslant 0.96$.

As x increases a rounded bump between 1K and 10 K appears, being

slightly visible for x=0.05, since the sharp ordering peak tends to hide it. As x increases, both the intensity and the bump position increase till x=0.5. As already mentioned the Nd^{3+} ion its a $^4I_{9/2}$ ground multiplet, fully split into five Kramers doublets by the low-symmetry crystal field [22]. At low temperatures only the ground doublet is populated, and when the non magnetic Ga ions are substituted by Fe ions, Nd ones are polarised by the H_{Fe-Nd}. This field splits the ground doublet of Nd^{3+} ion due to Zeeman effect, producing a Schottky anomaly [32] that can be observed in heat capacity measurements through a rounded bump. For higher values of iron concentration (x>0.5) the observed feature shifts again towards lower temperatures, while the intensity increases slightly and the bump becomes narrower, as displayed in Fig. 3.3b, achieving a shape similar to that of a two-level Schottky anomaly. For $x \leqslant 0.5$, the bump seems to correspond to a distribution of Zeeman splittings of Nd^{3+} ions.

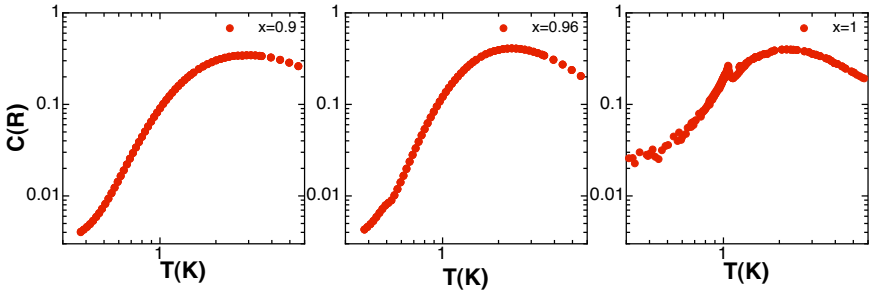

Figure 3.4: Low-temperature specific-heat measurements of the $NdFe_xGa_{(1-x)}O_3$ system for $0.9 \leqslant x \leqslant 1$.

On the other side of the $NdFe_xGa_{(1-x)}O_3$ series as x increases above 0.95 the Nd cooperative order is recovered –see Fig. 3.4–. For $x = 0.96$ a small round shoulder at T=490 mK can be observed over the Schottky hump. This peak is considerably smaller than the Nd ordering peak in $NdGaO_3$, shown in Figs. 3.2 and 3.3a. Specific heat data for this compound are taken from Ref. [22]. It must be noted that, although Nd cooperative order is clearly present for Fe concentrations ~ 0.1, the ordering on the other side of the series is more *"fragile"*, being only slightly observed for $x \sim 0.95$, a concentration of Ga twice smaller (0.05).

Although the kink observed in the specific heat measurements of samples x=0.2 and 0.3 seems to be some sort of remnant of the Nd cooperative magnetic order, its nature is not evident from specific heat measurement only. To provide more information, specific heat measurements were performed in the x=0.2 sample under different applied magnetic fields, being these results depicted in Fig. 3.5. For $H \leqslant 1$ T the kink observed in specific heat measurements is still

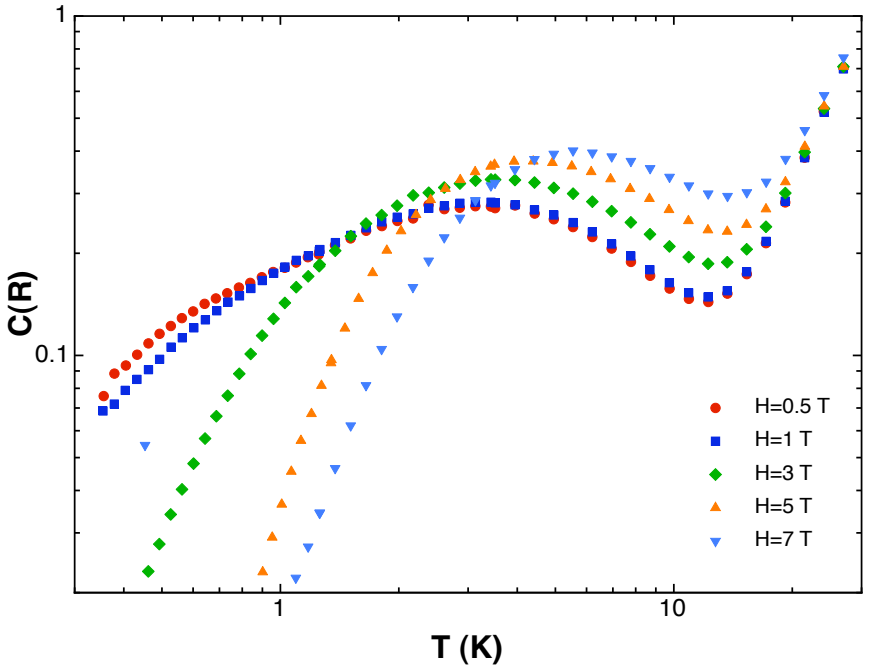

Figure 3.5: Low-temperature specific-heat measurements of $NdFe_xGa_{(1-x)}O_3$ for different applied magnetic fields.

present, although its shape softens and it is shifted towards lower temperatures. For $H > 1$ T, the kink is no longer present; moreover as the applied field increases the Schottky anomaly increases in height and temperature, while the shape becomes similar to the two-level Schottky shape.

3.4 Analysis of the experimental specific-heat data

3.4.1 Study of the different specific-heat contributions

Fig. 3.6 shows a detailed analysis of some of the doped samples –x=0.05, 0.1, 0.2, 0.3, 0.4, 0.5, 0.9, and 0.96–. The specific heat above T∼1 K has been remarkably well fitted (thick red lines in Fig. 3.6) by a sum of three contributions, which have been fitted jointly to reduce the number of free parameters. First, a lattice specific heat, $C_l \sim 3.2 \cdot 10^{-5} \cdot T^3$, which is approximately equal for all x. This contribution is shown isolated in all panels of Fig. 3.6 by a dotted line.

As already discussed, the Schottky anomaly observed in most of the samples cannot be ascribed to a single two-level Schottky anomaly, as expected from

a single doublet, like the Nd ion in this case. This broadening of the typical Schottky contribution indicates a distribution of Zeeman splittings of Nd^{3+}. In the $NdFeO_3$ case, a combination of isotropic and anisotropic Fe-Nd exchange interactions, originated by the weak ferromagnetic and the antiferromagnetic M order, creates an effective field on Nd sites, the internal field H_{Fe-Nd}. This field, that polarises the Nd moments, is responsible of the Zeeman splitting of the Nd ground doublet. The introduction of magnetic vacancies in the Fe sublattice destroys the nearly complete antiferromagnetic compensation around the neighbouring Nd^{3+} ions, introducing a large, extra isotropic exchange field to H_{Fe-Nd}, that modifies its intensity. Due to the random distribution of these vacancies, the internal field on every Nd site would be different, thus generating a different Zeeman splitting in every case. To account for this distribution of H_{Fe-Nd} internal fields acting on Nd ions, a Schottky distribution is introduced. We have limited the number of Schottky anomalies in the fit procedure to 2, with common splittings for all the samples, as a very satisfactory fit is reached already within these constraints. This second contribution, $C_{Sch} = \sum p_i \cdot Sch(\Delta_i)$, where $Sch(\Delta_i)$ is the Schottky specific heat for a two-level system with splitting Δ_i, is represented by a continuous blue line in Fig 3.6. A green dashed-dotted line represents $p_1 \cdot Sch(\Delta_1)$, while a red dashed line represents $p_2 \cdot Sch(\Delta_2)$. p_1 and p_2 values for every sample are provided in Fig. 3.6 and Table 3.1.

Finally, an empirical $C_{ht} = \beta \cdot T^{-2}$ contribution has to be included in x =0.05 and 0.1. This is the dominant term due to short-range order of the high-temperature expansions of the specific heat above a phase transition [31], in our case, the onset of the Nd-Nd cooperative order. The obtained β values resulting from the fits are given both in Fig. 3.6 and Table 3.1, being significantly lower than the result found for $NdGaO_3$, $\beta \sim 0.7$ [10].

As pointed out in the previous section, for $x \leqslant 0.5$, the Schottky contribution increases with the Fe concentration, and so does its temperature position. Looking at Fig. 3.6, this translates into an increment of p_1 and p_2 as x increases, but also into a reduction of the ratio p_1/p_2, being this value smaller than the unit for x=0.5. This enhancement of the Zeeman splitting of the Nd ground doublet is indicative of the increase of the internal field acting on the Nd sublattice. Thus, for $x \leqslant 0.5$, the introduction of uncompensated magnetic moments increases the H_{Fe-Nd}. This effect is observed even below Fe sublattice percolation limit –$x \sim 0.3$ [44]– where Fe ions are paramagnetic in the whole temperature range. However, above $x = 0.5$ the behaviour is reverted and the Schottky contribution shifts toward lower temperatures. As can be observed in Fig. 3.6, for $x = 0.96$, $Sch(\Delta_2)$ is negligible, being p_1 nearly equal to 1. Thus, the observed bump is almost equal to only one Schottky contribution: the one expected from the Nd ground doublet in $NdFeO_3$, $\Delta_1 \sim 6K$ [38].

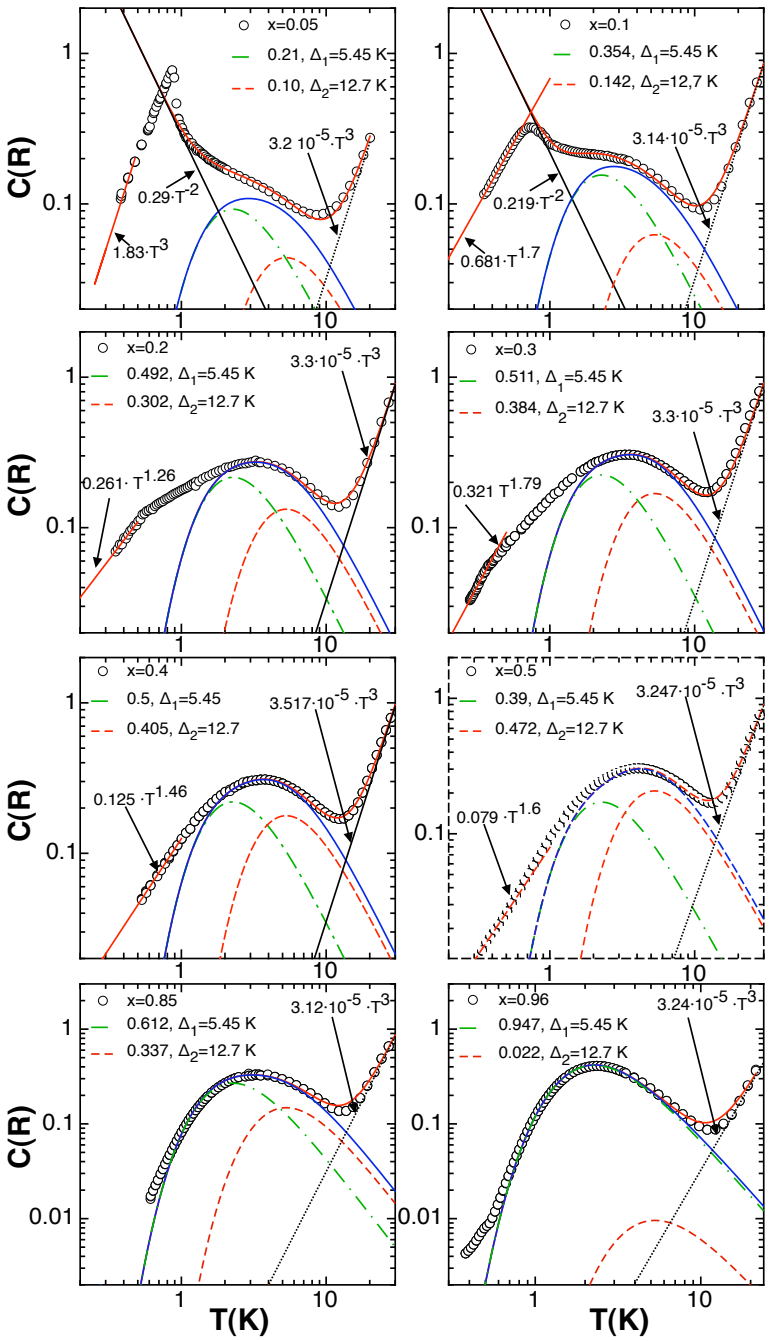

Figure 3.6: Analysis of the low temperature specific-heat contributions of $NdFe_xGa_{(1-x)}O_3$ compounds for x=0.05, 0.1, 0.2, 0.3, 0.4, 0.5, 0.9, and 0.96.

As Fe concentration is reduced, p_2 increases, and so does H_{Fe-Nd}.

The substitution of Fe ions by non-magnetic Ga atoms in $NdFeO_3$ is, there-

Table 3.1: Magnetic entropy, p_i, β, and ε parameters obtained from the analysis of specific-heat measurements in $NdFe_xGa_{(1-x)}O_3$ compounds.

x	$\Delta S(R)$	p_1	p_2	β	ε
$x = 0.05$	0.74	0.21	0.1	0.29	3
$x = 0.1$	0.76	0.354	0.142	0.219	1.7
$x = 0.2$	0.75	0.492	0.302	–	1.26
$x = 0.3$	0.76	0.384	–	–	1.79
$x = 0.4$	0.70	0.50	0.405	–	1.46
$x = 0.5$	0.64	0.39	0.472	–	1.6
$x = 0.85$	0.64	0.612	0.337	–	–
$x = 0.96$	0.64	0.947	0.022	–	–

fore, somehow equivalent to the introduction of magnetic Fe ions in $NdGaO_3$. This can be more clearly seen by observing the neighbourhood of a Nd ion –see Fig. 3.9a–. As already discussed, Fe magnetic moments in $NdFeO_3$ order antiferromagnetically with a weak ferromagnetic component [35], thus, Nd-Fe exchange interaction is nearly cancelled out due to the antiferromagnetic ordering of Fe ions.

However, the substitution of one of these magnetic moments produce an uncompensated magnetic moment in the Fe sublattice that increases considerably H_{Fe-Nd}. The absolute value of the uncompensated magnetic moment is, therefore the same that in the case of the introduction a Fe magnetic moment in a $NdGaO_3$ Nd site. In both cases the isotropic H_{Fe-Nd} can be considered more or less the same, if we neglect the contribution of the weak ferromagnetic component.

As already mentioned, the Nd cooperative order is observed on $NdMO_3$ perovskites depending on the ratio H_{M-Nd}/H_{Nd-Nd}. Thus, the increase in H_{Fe-Nd} that we have found when changing x, does not only affect the polarisation of Nd, as shown by the Schottky contribution in our compounds, but also the Nd-Nd magnetic ordering. We have seen that the introduction of magnetic ions on Ga sites in $NdGaO_3$ generates an H_{Fe-Nd}. This field polarises Nd sublattice, thus reducing the magnetic entropy available for cooperative ordering. This effect is shown in specific-heat measurements through the reduction of both T_N and the intensity of the ordering peak, till, eventually H_{Fe-Nd} is so high that the Nd collective order is inhibited for $x = 0.4$, as observed in Fig. 3.6. In $NdFeO_3$, the isotropic field generated by the introduction of magnetic vacancies is added to the already existing internal field H_{Fe-Nd}, thus Nd ordering is fully inhibited for smaller concentrations of magnetic vacancies than the Fe concentration required in the case of $NdGaO_3$, as depicted in Fig. 3.6.

Similar results were found in $NdFe_xCo_{(1-x)}O_3$ for $x > 0.5$ by Bartolome et al. [22]. In that case, experimental data were reproduced by a theoretical mean field model, that included the modification of H_{Fe-Nd} by the introduction of magnetic vacancies on $NdFeO_3$. For this analysis, it was assumed that the vacancies do not modify the symmetry of the Fe sublattice above percolation. Thus, the contribution due to the uncompensated Fe moment was assumed to conform to the same Fe sublattice symmetry (G_zF_x) than in $NdFeO_3$. Therefore, Nd was considered to be polarised with the same Nd configuration as the $x = 1$, i.e., the c_yf_x configuration. Although it is a reasonable assumption, to our knowledge, no measurements have been performed to corroborate the magnetic structure of $NdFe_xM_{(1-x)}O_3$ compounds, being M a non-magnetic ion, such as Ga or Co.

The hyperfine contribution is negligible above $T > 0.3$ K compared to the spin wave contribution, both in $NdGaO_3$ [10, 31] and in $NdFeO_3$ [16]. Indeed we have not observed the Nd hyperfine contribution to the specific heat –which is a Schottky contribution due to the Zeeman splitting of nuclear spin levels– in any of the samples displayed in Fig. 3.6. Nd in $NdGaO_3$ is known to order in a c_z configuration (antiferromagnetic arrangement of ferromagnetic chains along the c axes) below T_N [25]. Thus, the simple antiferromagnetic T^3 behaviour within the range $0.3 < T < T_N$, is expected in the low-temperature part of the specific heat. As can be seen in Fig. 3.6, this $\sim T^3$ dependence is also found in $NdFe_xGa_{(1-x)}O_3$ compounds for $x \leqslant 0.05$. Nevertheless, for higher values of x, low temperature specific-heat data no longer follow this power law.

To analyse the low temperature part of our specific-heat measurements we have limited ourselves to fit this part of the curves to a power law, to compare them qualitatively. The ε values from the fitting to $C = a \cdot T^{\varepsilon}$ are given in Table 3.1. A continuous tendency toward $\varepsilon = 1$ is found as the Fe content increases, till $x = 0.2$. After this value is reached, $\varepsilon \sim 1$ is obtained for $x \leqslant 0.5$. No fitting results are provided for $x = 0.85$ and $x = 0.96$ since, in the latter, the Nd ordering peak is placed in the middle of the studied region; while for $x = 0.85$ the exponential decay of the Schottky contribution becomes dominant below $T = 1$ K, thus preventing any further analysis.

A linear dependence of C with T is the behaviour expected for spin glasses below their freezing temperature [45]. $NdGaO_3$ has been shown to behave as a quasi-2D Ising system [31]; it is worth noting that low-dimensionality favours frustration, one of the ingredients that originates spin glasses [45]. Unfortunately, the possible presence of some kind of non-canonical spin glass in our samples is obscured by the other magnetic contributions to the specific-heat. Only at low temperatures, below the Nd ordering temperature, where those magnetic contributions are less important, a trace of *"spin glass"* like

behaviour can be observed.

As shown in Fig. 3.8b, in x=0.2 and 0.3, C/T is almost constant at temperatures below the kink. This is similar to the behaviour found in $Sr_2Fe(Mo_{1-y}W_y)O_6$ (SFMWO) [39], a re-entrant spin-glass system (RSG) showing a continuous variation $1.7 < \varepsilon < 2.6$ as a function of y. This system has been interpreted in terms of a random mixture of ferromagnetic and weak antiferromagnetic segregated ordered regions giving rise to RSG. SFMWO and $NdFe_xGa_{(1-x)}O_3$ do have important similarities: in both cases a glassy behaviour is induced in an undoped magnetic sublattice (Nd in $NdFe_xGa_{(1-x)}O_3$, Fe in SFMWO) by means of diluting a partially magnetic interspersed lattice (Fe–Ga in NFGO, Mo–W in SFMWO). However, an important difference must be pointed out: Fe is ordered at temperatures above the freezing in SFMWO, while Nd is not ordered in $NdFe_xGa_{(1-x)}O_3$, because Nd–Nd interaction provokes ordering only around $T \sim$1K. Moreover, Fe has been found to generate cluster-glass (CG) behaviour in $(Sr_{1-x}La_x)Ru_{1-x}Fe_x)O_3$ (SLRFO) for $x \sim$0.2 at temperatures below 50K [46].

Therefore, we attribute the anomalous ε values observed in the low temperature specific heat of $NdFe_xGa_{(1-x)}O_3$ to the interaction between a glassy Fe sublattice interspersed on the Nd one, which is likely to be frustrated by the random H_{Fe-Nd} internal field. As displayed in Fig. 3.6, for $x \geqslant 0.85$, the Schottky contribution from the Nd polarisation, together with the Nd ordering peak, remain the only low temperature contributions. Thus, the glassy behaviour of the Fe sublattice seems restricted to x values close to percolation, $x_c = 0.33$, although its origin and nature cannot be fully elucidated from our specific-heat measurements only.

3.4.2 Specific-heat response of the $NdFe_{0.2}Ga_{0.8}O_3$ sample as a function of an applied field

In order to further analyse the nature of the kink observed in $NdFe_{0.2}Ga_{0.8}O_3$ specific-heat measurement and the possible presence of glassy effects, $x = 0.2$ sample specific-heat was studied under different applied magnetic fields. To do so, the same fitting procedure that was described in Section 3.4.1, has been applied to the data displayed in Fig. 3.5. Fitting results are shown in Fig. 3.7.

For applied magnetic fields $H \leqslant$1 T, no significant changes in the lattice or Schottky contribution are observed; while appreciable changes occur in the low temperature part of the specific heat measurements. As the applied magnetic field increases, the kink softens acquiring a more rounded shape; moreover, its temperature position decreases. This temperature dependence is opposite to the behaviour expected from a spin-glass system [45]. Hence, although the

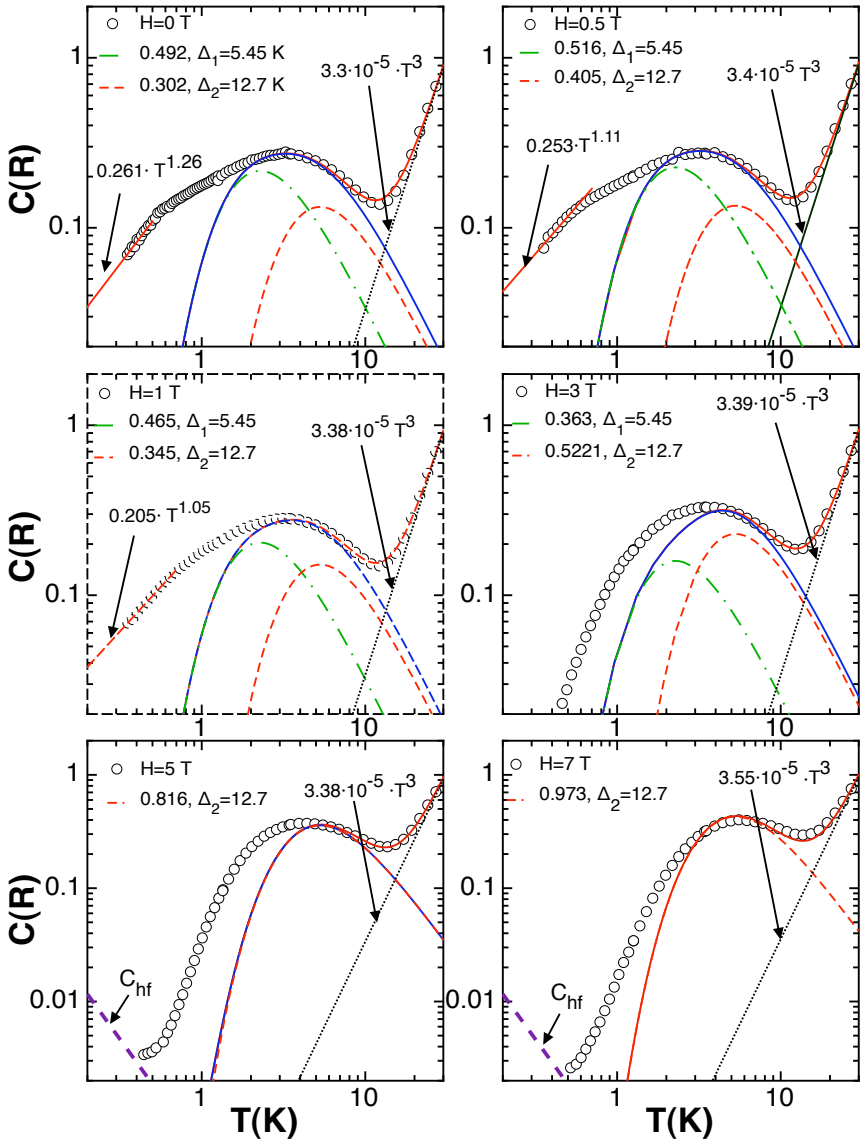

Figure 3.7: Analysis of the low temperature specific-heat contributions of $NdFe_{0.2}Ga_{0.8}O_3$ compounds for different magnetic fields.

low-temperature measurements point to the presence of some kind of glassy response, the kink itself cannot be considered a spin-glass feature.

Due to its field dependence, one can consider it to be related with a weak Nd cooperative order, that is finally destroyed as the Nd polarisation by the external magnetic field increases. As shown in Ref. [22], in $NdFe_xCo_{1-x}O_3$, an increment in H_{Fe-Nd} of $\sim$1T, is enough to destroy Nd cooperative order. In this scenario, once the remnants of Nd ordering are removed by the applied

field, only the *"spin-glass-like"* contribution remains, as highlighted by the linear dependence of $C(T)$. Therefore, these data suggest again the existence of some type of glassy state in our system for $x \lesssim 0.5$.

For H$\geqslant$ 3 T, the applied magnetic field is so high that those effects become less noticeable, and the specific heat measurements move towards a single Schottky contribution. The application of an external field of intensity comparable to the H_{Fe-Nd} in $NdFeO_3$, 5.9 T, seams to affect Nd polarisation, shifting the Schottky contribution, increasing its intensity and narrowing its shape. The effect is equivalent to the reduction of the dispersion of Zeeman splittings values, to a value centred in a higher effective field, generated by the combination of the external field and the internal H_{Fe-Nd}.

As the external magnetic field increases above 1T, the specific heat contributions associated with some kind of Nd ordering process –short-range order, *"cluster-glass-like"* phase – are inhibited. This process considerably reduces the specific heat signal, enabling us to slightly observe the hyperfine contribution originated by the nonzero magnetic moments of ^{143}Nd and ^{145}Nd. This hyperfine contribution, $C_{hf} \propto T^2$, estimated by Bartolome et al. [18] for the $NdCrO_3$ compound, is represented in Fig. 3.7 by a purple dashed line. Overlapped to the Schottky anomaly, this contribution explains the slope change observed at very low temperature in the specific heat curve.

3.4.3 Estimation of the total magnetic entropy

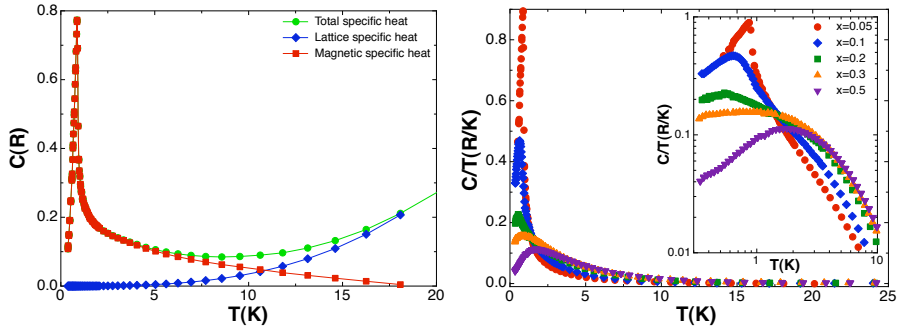

(a) (b)

Figure 3.8: (a) Example of the specific-heat magnetic contribution estimation for x=0.05. (•)corresponds to the total specific-heat measurement, (♦) corresponds to the estimated lattice contribution, and (▪) corresponds to the magnetic contribution. (b) C/T measurements of some $NdFe_xGa_{(1-x)}O_3$compounds. Inset displays the same data on a double-log plot.

The entropy of an ordering transition, such as the Nd one analysed in this

chapter, can be calculated by direct integration of the quantity C/T, being C the anomalous heat capacity. That means that the lattice contribution has to be subtracted from the experimental data to obtain the magnetic specific heat.

As already discussed on the previous section, the lattice contribution, common for all x values, can be estimated as $C_l \sim 3.2 \cdot 10^{-5} \cdot T^3$. The subtraction of this contribution is the first step towards the estimation of the magnetic entropy of the studied transition. In Fig. 3.8a an example of the result of this procedure is shown for x=0.05. To properly obtain the total magnetic entropy, the C/T curves have to be extrapolated at higher and lower temperatures than those of the experimental limits. For this we use the fitted curves shown in Fig. 3.6. Results are displayed in Fig. 3.8b. The high-temperature, $T > 30$ K, contribution is negligible, but the low-temperature region, $T < 0.35$ K, contributes as much as 15% of the entropy, depending on the sample. The values obtained for the total magnetic entropy are given in Table 3.1 and depicted in Fig. 3.9b.

In the microcanonical formalism, for fixed energy, the entropy of a system is given by:

$$\Delta S = k_b \cdot N_A \cdot ln\Omega \tag{3.5}$$

with Ω being the degeneracy of the magnetic state. Thus, when the entropy is estimated in R units, the ΔS of the Nd ground doublet can be assumed to be $\ln 2 \sim 0.693$. The entropy content obtained in $x = 0$ is in excellent agreement with this expected value. The values obtained for the doped samples present a systematic excess of the order 10–15 % with respect to $\ln 2$ for $x \leqslant 0.3$. At least a part of this excess must be attributed to Fe magnetic moments, although it is difficult to determine how much of the expected Fe entropy should be observed within the range of temperature studied.

For $x > x_c = 0.33$, Fe magnetic moments are ordered at the working temperatures. The ordering process reduces the Fe available entropy at low temperatures; thus, the Fe sublattice contribution to the entropy in the studied range is expected to decrease. This effect can be clearly observed in Fig. 3.9b, where already at $x = 0.4$, still too close to percolation to ensure that all Fe moments are ordered, Δ S is reduced from ~ 0.75, to 0.70. For x values well above the percolation Δ S decreases to a value ~ 0.64, differing only a 8% of the theoretical value. In any case, it is evidenced that the whole entropy of the Nd ground doublet is exhausted below $T < 30$ K.

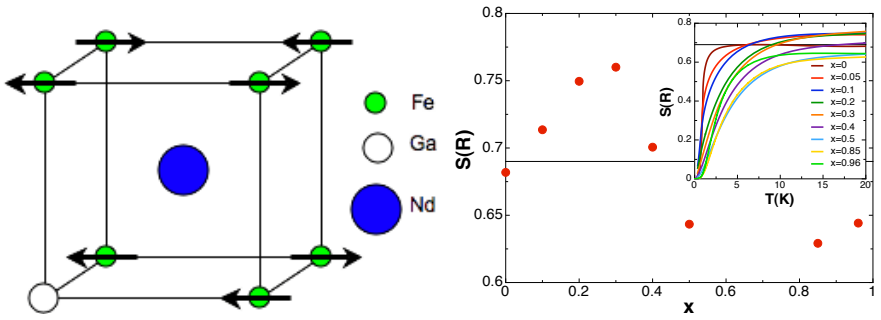

(a) (b)

Figure 3.9: (a) Squematic representation of the first neighbours of a Nd ion in a $NdFe_xGa_{1-x}O_3$ compound. (b) Entropy curves of the $NdFe_xGa_{1-x}O_3$ series calculated as described in the text.

3.5 Conclusions

Calorimetric measurements on the $NdFe_xGa_{1-x}O_3$ series clearly show that the substitution of non- magnetic Ga ions by Fe ions inhibits Nd long-range cooperative order for $x \gtrsim 0.3$. Our analysis shows that the inclusion of magnetic moments in the neighbourhood of Nd sites generates an effective field that polarises Nd atoms. This polarisation is reflected in our specific-heat measurements by the appearance of a Schottky contribution, associated to the Zeeman splitting of the Nd ground doublet. The random localisation of the Fe atoms generates a distribution of Zeeman splittings that slightly distort the Schottky contribution shape. As x increases, the effective field H_{Fe-Nd} also increases until $x = 0.5$ is reached. This increment reduces the available magnetic entropy for cooperative order. This reduction translates in a reduction of both T_N and the peak intensity as x increases, until the Nd long-range order transition is inhibited. Remnants of these transitions appear to be present in x=0.2 and 0.3 data. Although its response to magnetic field has been studied, results show that calorimetric measurements are not enough to fully elucidate the nature of this feature.

To interpret our data, it has been assumed that the introduction of magnetic moments into the system does not modify the symmetry of the different sublattices. Nd sublattice is considered to order in a c_z mode and to be polarised, when Fe sublattice is magnetically ordered, into a c_y mode. While Fe sublattice is considered to order into a G_zF_x mode. However, to our knowledge, no measurements on the magnetic structure of these compounds have been performed. To do so, and to further research into the nature of the specific-heat kink observed in x=0.2 and 0.3, neutron diffraction experiments of the $NdFe_xGa_{1-x}O_3$ series were performed. Results will be discussed in

Chapters 5 and 6.

Finally, for Fe concentration below or close to percolation, low temperature specific-heat measurements suggest the existence of a glassy Fe sublattice embedded into the Nd one. Given that other phenomena in our samples –such as Nd cooperative ordering and Nd polarisation–, produce specific-heat contributions in the same range of temperatures, $T \lesssim 1K$, the possible *"spin-glass contribution"* is difficult to distinguish. Specific heat measurements are not among the most sensitive techniques for the study of spin-glasses. Furthermore, among the different parts of a spin-glass specific-heat contribution only the low temperature part, $C \propto T$ for $T \lesssim T_f$, remains in this case. Thus, our specific-heat results cannot be regarded as conclusive. To study the presence of glassy behaviour in our samples and, if present, to elucidate its origin and nature, further analysis will be required. Ac-susceptibility measurement analysis will be explained in Chapters 5 and 6. However, before reaching that point and trying to offer a full description of the magnetism of $NdFe_xGa_{1-x}O_3$, the Fe sublattice behaviour must be fully characterised as a function of x down to low temperatures.

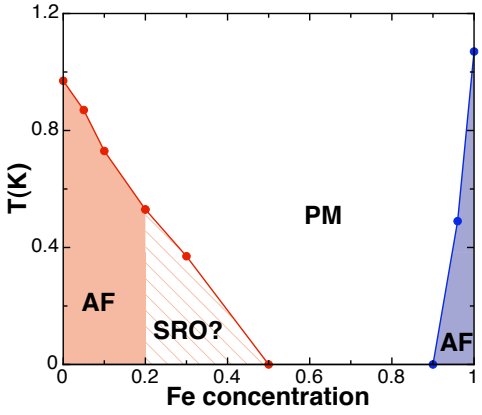

Figure 3.10: Low temperature phase diagram of Nd ordering in $NdFe_xGa_{1-x}O_3$ series after the experimental results. Red and blue areas correspond to cooperative order on the Nd sublattice, while the white area corresponds to the region where Nd cooperative order is inhibited. The shadowed region corresponds to Fe concentrations where specific heat measurements are not enough to elucidate the nature of the Nd order, possible Nd short-range order (SRO).

Results obtained from specific-heat measurements on $NdFe_xGa_{1-x}O_3$ compounds allow us to draw the preliminary phase diagram of the Nd ordering that is displayed in Fig. 3.10. This diagram, along with the Fe ordering phase diagram, would be completed in the following chapters so as to achieve a full understanding on the magnetic ordering processes in the $NdFe_xGa_{1-x}O_3$ series.

Chapter 4

Complementary experimental techniques

4.1 Introduction

As discussed in Chapter 3, low temperature calorimetry measurements provide useful information on the magnetic ordering of the Nd sublattice in the $NdFe_xGa_{(1-x)}O_3$ series and how the substitution of Ga atoms by magnetic ions affects this cooperative order. However, no conclusive results on the presence of Nd long range order for $x \geqslant 0.2$ can be achieved with these measurements. Moreover, to fully characterise the system, other experimental techniques are required. In this way, we would be able to, for instance, study the ordering of the Fe sublattice in the different compounds, its influence on Nd sites, or the magnetic structure of the series.

This chapter contains a short description of the experimental techniques that, besides calorimetry, have been applied to the study of the $NdFe_xGa_{(1-x)}O_3$ series. In Section 4.2 magnetisation and susceptibility measurements required for the magnetic analysis of the compounds are described. The magnetic structure of the samples was determined by neutron diffraction measurements performed in different instruments, as described in Section 4.3. Finally, in Section 4.4 a X-ray magnetic circular dichroism facility is described. This element-selective magnetometry is used to determine the magnetic orientation of the Fe and Nd net moments in the $NdFe_xGa_{(1-x)}O_3$ series, after a field-cooled process in which negative magnetisation takes place for $0.5 \leqslant x \leqslant 0.9$.

4.2 Magnetic analysis: magnetisation and susceptibility

In order to determine the magnetic ordering of the Fe sublattice in the whole series magnetisation and susceptibility measurements were performed in the two Quantum Design MPMS magnetometers (Magnetic Property Measurement System) located at the Servicio de Medidas Físicas of the University of Zaragoza[1] and shown in Fig. 4.1a.

These systems, based in Superconducting Quantum Interference Device (SQUID) technology, allow us to obtain magnetisation and magnetic susceptibility in a temperature range between 1.9 K and 400 K. The applied magnetic field can be as high as 5 T, with a magnetic field uniformity of 0.001% over 4 cm. MPMS systems are designed to measure magnetisation DC signals with a sensitivity of $1 \cdot 10^{-8}$ emu and susceptibility AC signals with sensitivity of $2 \cdot 10^{-8}$ emu. When the Sample Space Oven option is used, the temperature range is increased to 800 K. For dynamic susceptibility measurements, the amplitude of the excitation field can reach $\sim$ 4.5 Oe with excitation frequencies between 0.005 and 1500 Hz.

(a) (b)

Figure 4.1: (a) Picture of the two MPMS systems located at the Physical Measurement Service of the University of Zaragoza. (b) Picture of the susceptometer connected to the dilution fridge.

The magnetic ordering of the Nd sublattice that, as already discussed in Chapter 3, is observed for some of the compounds in the $NdFe_xGa_{(1-x)}O_3$ series, takes place at temperatures below the limits of the measurement system described above. Therefore, susceptibility measurements in these samples was completed with measurements taken by Enrique Burzurí and Fernando Luis in a Kelvinox 25 dilution fridge located at the Low Temperature Laboratory

[1] *http://wzar.unizar.es/invest/sai/ins_ele/ins_ele.html*

of the Instituto de Ciencia de Materiales de Aragón (ICMA). In this system, susceptibility measurements in a temperature range between $\sim$ 80 mK and 3.5 K and a frequency range between 10 and 10000 Hz were performed in an AC susceptometer developed at Kammerlingh–Onnes Laboratory in the Leiden Institute of Physics[2].

This AC low temperature susceptometer is based in the principle of coaxial mutual inductance. A primary coil is used to generate an AC magnetic field on a secondary coil. The voltage measured across the latter, conformed by two oppositely wound coils, will be zero in the absence of a sample. When a sample is placed in the centre of one of the secondary coils, a non-zero voltage signal will appear, directly proportional to the AC susceptibility amplitude. A picture of this susceptometer can be seen in Fig. 4.1b. These data are calibrated using measurements taken at the same frequency as those used at the MPMS systems.

Although both magnetisation and susceptibility are powerful tools to determine the magnetic ordering of samples, the information they provide is macroscopic, since they measure the collective behaviour of the molecules in the sample. In the studied case, to fully characterise the competing interactions that take place in the $NdFe_xGa_{(1-x)}O_3$ series and how they affect the magnetic ordering of Fe and Nd ions, the determination of the magnetic structure of the $NdFe_xGa_{(1-x)}O_3$ compounds is required.

4.3 Magnetic structure: neutron diffraction

4.3.1 Why to use neutrons?

Neutron scattering is one of the most powerful and versatile experimental methods to study the structure and dynamics of materials on the nanometer scale [47]. Before the eighties neutron scattering measurements were applied only to solid state physics and crystallography, while at present they are extensively used in fields as different as biology, earth science or nanoscience, that is, in all scientific fields dealing with condensed matter. In this technique, as in the case of X-ray diffraction, the change in energy and momentum of the probe particle is used to provide information of a certain sample. The scattering of a neutron beam is described by the neutron scattering cross section, σ, that defines the ability of the system under study to scatter neutrons. Considering the neutron beam flux, Ψ, the number of neutrons reaching a surface per second and per surface area perpendicular to the neutron beam direction, the differential cross

[2] *http://www.nanowerk.com/nanotechnology/labs/Leiden_Institute_of_Physics_Kamerlingh_Onnes_Laboratory.html*

section corresponds to Eq. 4.1

$$\frac{d\sigma}{d\Omega} = \frac{N^{\circ}\, of\, scattered\, neutrons\, per\, second\, in\, a\, solid\, angle\, d\Omega\, in\, the\, direction\, \theta,\, \phi}{\Psi d\Omega} \tag{4.1}$$

where the different angles and directions are presented in Fig. 4.2a. Thus, the scattering cross section will be the integral of Eq. 4.1 over the solid angle. The total cross section corresponds to the sum of the cross section associated with all the possible interactions neutron-matter. However, in the energy range of thermal neutrons –the ones used in condensed matter physics–, only two processes are relevant: scattering and absorption. In some cases the latter is small enough to be considered it as a correction factor of the scattering cross section. The analysis of the relation between the scattering cross section and the neutrons dispersed by the sample provide information about the sample itself.

Neutrons used in this technique have a wavelength similar to inter-atomic distance and an energy similar to elementary excitations in solids, allowing to study the structure and dynamics of materials and excitations. Moreover, neutron scattering cross section depends strongly on the nuclei under study, allowing us to distinguish between isotopes.

However, among the different capabilities of neutron diffraction measurements, in this work we are mostly interested in neutron penetration and neutron interaction with magnetic atoms. Neutrons do carry a magnetic moment, that interacts with unpaired electrons in magnetic atoms , generating an extra scattering term, that reveals information of the magnetic structure of the sample. Moreover, as they are neutral particles, they penetrate deeply in the material, interacting with nuclei and probing the bulk of the sample and not only its surface. These characteristics enable neutron scattering measurements to be performed in all sort of sample environments, from cryostats to furnaces or pressure cells. In our case, this deep penetration will allow us to determine the magnetic structure of our samples in wide temperature range, from 50 mK to 600 °C, since different systems such as dilution refrigerator, ^{4}He cryostat or cryofurnaces can be easily combined with neutron diffraction measurements.

The macroscopic understanding of the sample magnetic behaviour provided by magnetisation and susceptibility measurements on $NdFe_xGa_{(1-x)}O_3$ compounds will be complemented by the results from neutron diffraction measurements. The microscopic information provided by the latter cannot replace macroscopic measurements. Due to time and cost constrains, diffraction patterns can not be acquired at every temperature, applied field or pressure. Magnetisation and susceptibility measurements are not only cheaper and faster, but

also they should be used to determine the measurement conditions for neutron diffraction measurements. Moreover, without an understanding on the macroscopic behaviour of the studied samples, neutron diffraction pattern would be nearly impossible to interpret.

Only two types of neutron sources provide flux densities adequate for neutron scattering investigations: conventional fission reactor or spallation sources, where neutrons are produced by bombarding heavy elements with high-energy particles. To obtain neutrons with wavelength comparable to the interatomic space in solids, in both cases neutrons are moderated to thermal velocities, and only then, transported to the measurement instruments in neutron guide systems. A description of the neutron powder diffractometers used in our case to elucidate the magnetic structure of Nd and Fe sublattices in $NdFe_xGa_{(1-x)}O_3$ is provided in the next Section 4.3.2.

4.3.2 Description of neutron powder diffractometers

A complete study of the $NdFe_xGa_{(1-x)}O_3$ samples magnetic structure was performed through neutron diffraction experiments developed at the Institut Laue–Langevin (ILL). ILL[3] is an international research center located at the European Photon and Neutron Science Campus (EPN Campus), in Grenoble (France) that operates the most intense neutron source on Earth; a neutron reactor that feeds beams of neutrons to 40 different instruments. This institute, funded and managed by France, Germany and the United Kingdom in partnership with other 11 European countries –Spain among them– receives more than 800 experiments per year, from so different fields as condensed matter physics, chemistry or biology.

Neutron powder diffraction experiments in our samples were performed in three different instruments: D1B, D2B and D20. D1B is a two-axis high intensity diffractometer funded and managed by CNRS (France) and CSIC (Spain). This instrument, dedicated to experiments where a high neutron flux and high spatial resolution is needed, is equipped with a ^{3}He/Xe position sensitive detector composed of a system of multi-electrodes with 400 cells, that span a 2θ range of 80°, expandable to 160° by moving the detector. The monochromator is composed of three pyrolitic graphite monochromators and provides $\lambda = 2.52$ Å. A second wavelength of 1.28 Å is available by using a germanium monochromator, although the flux in this case is reduced by a factor of 16. When combined with a cryostat, a thermal variation of the diffraction patterns between 1.5 K and 300 K can be achieved. This instrument is one of the

[3] http://www.ill.eu/

most powerful powder diffractometer for magnetic structure studies [4].

Do to its high flux and high detector efficiency, diffraction patterns with sufficient statistics can be acquired in minutes. In our case, this instrument was used to scan in temperature the magnetic structure of our samples, obtaining a complete thermal variation of the diffraction patters in $NdFe_xGa_{(1-x)}O_3$ samples with $0.3 \leqslant x \leqslant 0.8$. Since temperature was limited to the range 1.5 K- 300 K, only the magnetic ordering of the Fe sublattice in some compounds and the Fe spin reorientation were studied in this diffractometer. A schematic view of D1B diffractometer is shown in Fig. 4.2b

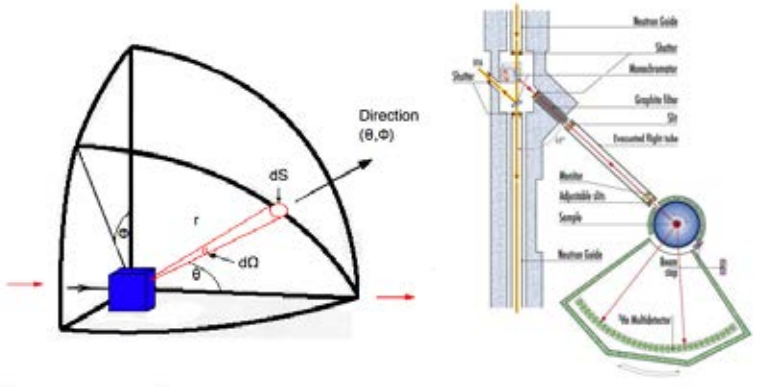

(a) (b)

Figure 4.2: (a) Typical geometry of a neutron scattering event. *Credit: Adapted from [48]* (b) Schematic layout of D1B two-axis diffractometer. *Credit: ILL.*

D2B is a very high-resolution two-axis powder diffractometer designed to achieve a resolution only limited by powder particle size. However, when -as in our case- high neutron flux is needed, it can operate with a resolution similar to that of other instruments but with a much higher flux. This diffractometer, shown in Fig. 4.3a, is characterised by a very high take-off angle for the 28 germanium crystal monochromator (135°). The detector is formed by 128 ^{3}He counting tubes spaced at 1.25° intervals, that allow obtaining a complete diffraction pattern ($5° < 2\theta < 165°$) after ∼100 steps of 0.005° in 2θ. D2B can operate with wavelengths in the range between 2.4 and 6 $\mathring{A}$ by rotating the Ge crystals, however its optimum working λ is 1.59 $\mathring{A}$, the value used in our case. D2B instrument was combined with a cryofurnace to obtain diffraction patterns for temperatures between 1.5 K and 525 K [5].

D2B provides a better resolution than D1B does, thus allowing to study more precisely ordering effects observed in D1B measurements, such as the Fe

[4] http://www.ill.eu/instruments-support/instruments-groups/instruments/d1b/more-about-d1b/

[5] http://www.ill.eu/instruments-support/instruments-groups/instruments/d2b/characteristics/

spin reorientation. Since D2B diffraction patterns take longer to be obtained, a thermal scan like the one performed in D1B is not possible in this case. Thus, D1B measurements were used to choose the acquisition temperatures of the D2B diffraction patterns. Moreover, since the temperature range was increased till 525K, in this case all the Fe magnetic ordering phenomena for $0.3 \leqslant x \leqslant 0.8$ were analysed.

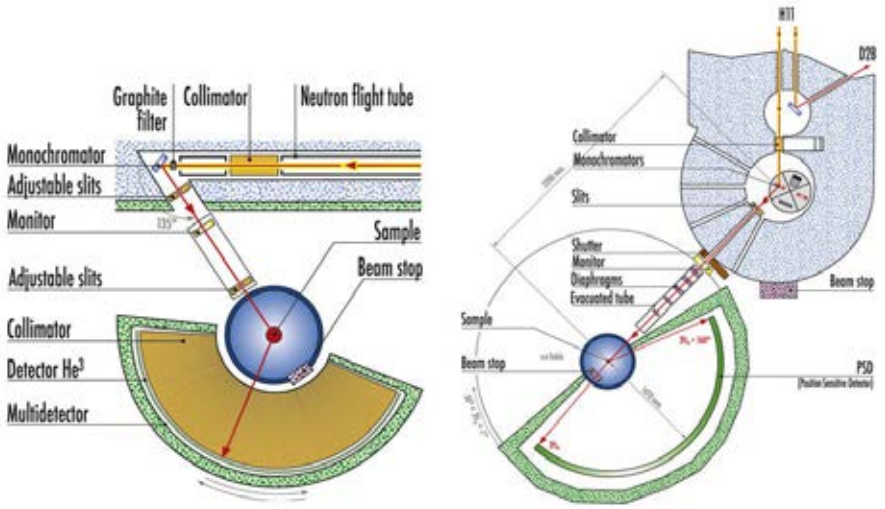

(a) (b)

Figure 4.3: (a) Schematic layout of D2B high-resolution two-axis diffractometer. *Credit: ILL.* (b) Schematic layout of D20 high-intensity two-axis diffractometer. *Credit: ILL*

Finally, D20 is a high-intensity two-axis diffractometer with variable resolution. The detector is a large microstrip position sensitive detector, filled with ^{3}He and CF_4 bars. Micro-strip gas chambers are made of sputtered chromium onto electronically conducting glass plates, covering 153°. Depending on the working wavelength one can choose between a pyrolitic graphite (HOPG) or a copper monochromator. In our case, where λ=2.4 $\AA$, the HPOG monochromator was used, offering a take-off angle of 42°. This system is combined with a pryolitic graphite filter to suppress second harmonics. Additionally, a variable vertical focussing Germanium monochromator increases resolution at higher take-off angles. This instrument, whose scheme is shown in Fig. 4.3b, was combined with a dilution fridge refrigerator, allowing us to study the temperature range between 50 mK and 4 K [6].

The high resolution and high intensity of D20 instrument make D20 diffractometer ideal to study the magnetic ordering of Nd, since, as found in calori-

[6] http://www.ill.eu/instruments-support/instruments-groups/instruments/d20/characteristics/

metric measurements for $x \geqslant 0.2$, the intensity of this signal is not expected to be very high. Like D1B, this instrument is equipped with a high neutron flux, thus, allowing us to obtain a complete thermal variation of the diffraction patterns in a completely different range of temperatures. The magnetic ordering of the Nd sublattice for $0.05 \leqslant x \leqslant 0.3$ was studied, concluding the determination of the $NdFe_xGa_{(1-x)}O_3$ series magnetic structure.

4.4 X-ray magnetic circular dichroism

4.4.1 Why to use XMCD?

Synchrotron radiation is the electromagnetic radiation emitted by charged particles moving at relativistic speed following a curved trajectory with a radius of curvature long enough to make quantum effects negligible. These conditions are fulfilled by particles moving inside accelerators. From an experimental point of view, this electromagnetic radiation was first observed in 1946 in General Electric Laboratories [49], the results being in good agreement with the theoretical predictions made by Schwinger or Ivanenko [50]. A comparison between the electromagnetic radiation distribution emitted by a particle moving in a circular orbit at relativistic and non-relativistic speed is displayed in Fig. 4.4a. Synchrotron radiation was identified as one of the sources limiting the energy of the particles in accelerators such us the betatron, and was not considered a useful tool till the work of Tomboulian and Hartman in 1956 [51]. In this work they pointed out the wide spectral emission range of synchrotron radiation–from X-ray to γ-ray–, its high intensity concentrated in a small area and its polarisation.

X-ray and ultraviolet radiation are specially important since their wavelengths are comparable to the planar distances in crystals, and to the size of large molecules, proteins, etc. Moreover, their energies excite electronic transitions inside the atoms. X-ray radiation produced in this type of systems provides a flux, an energy range and a resolution unachievable in conventional X-ray radiation sources, what allows resolving the structure of matter to its lowest level. Applications range from life sciences –crystallography of protein and large molecules, for instance–, to earth science or material science.

Electron packages are emitted in a linear accelerator (linac) and transmitted to a circular accelerator (booster) where they are accelerated until they reach energies between 2 and 8 GeV, and finally injected in the storage ring. In Fig. 4.4b a simplified outline of a synchrotron can be found. Experiments are placed at the end of the beam lines, that are located all along the ring, tangent to the electron trajectory, so that radiation can reach the experiments.

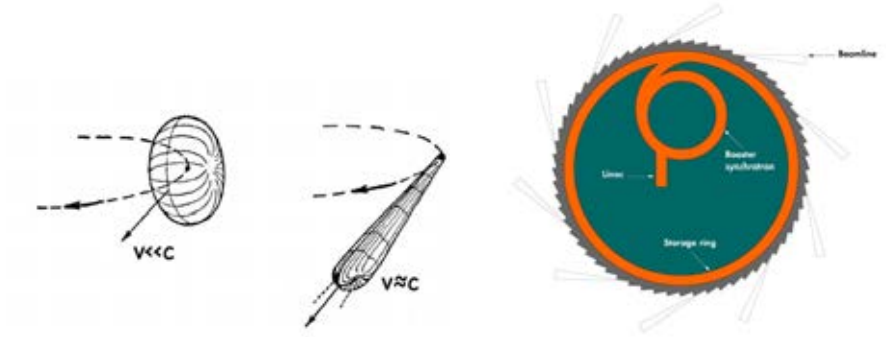

(a) (b)

Figure 4.4: (a) Qualitative representation of the radiation distribution emitted by a non-relativistic particle and a relativistic particle. *Credit: Adapted from [51].* (b) Outline of a synchrotron. *Credit: ESRF*

An example of this distribution is displayed in Fig. 4.6b, where the ESRF beamlines at the end of 2010 are represented.

Each beamline is dedicated to a specific technique. In our case, the chosen technique is the X-ray magnetic circular dichroism (XMCD), the effect originated by the different absorption of left and right circularly polarised light that takes place in a sample under a strong magnetic field oriented parallel to the direction of light propagation. For transition and rare earth metals, like those in our compounds, the typical photon energies required to observe magnetic circular dichroism are in the X-ray range. The comparison of the two XMCD spectra provides information on the magnetic properties of each component, such as spin or orbital magnetic moment, and also about the chemical environment of the atoms. A description on how information is extracted from XMCD measurements is provided in the next section.

4.4.2 Brief theoretical basis of XMCD

As already indicated, magnetic dichroism consists of a change in the light polarisation when it goes through a magnetic sample. In the case of X-ray Magnetic Circular Dichroism, the light absorption occurs at the resonant absorption energies, that are characteristic of the different electronic layers of every element. Thus, by selecting the energy of the incident light, XMCD measurements provide atomic and layer selectivity.

The effect of the magnetic circular dichroism can be described by a two step model [52]. In the first step one considers the initial states involved in the absorption process once the spin-orbit splitting has been applied. In the

second step the cross sections that could provide the transition to the final state are determined. There are different models to describe the initial and final states, but, in the case of L_2 and K edges of the transition metals –the ones we are interested in [19]– a one electron model, where only a core electron is involved in the transition, provides a simple vision of the existence of XMCD signal.

Magnetic properties of transition metals are mostly due to their d electrons. This together with the fact that X-ray absorption spectra are governed by dipole selection rules, makes the study of the $L_{2,3}$ absorption edges, where p core electrons are excited to the d band by dipole transitions, one of the most interesting applications of XMCD to 3d metal systems. That is the reason why in this section the combination of the simple one electron model with the Stoner model of a solid will be used to provide an intuitive explanation of the origin of the XMCD signal in the $L_{2,3}$ edges.

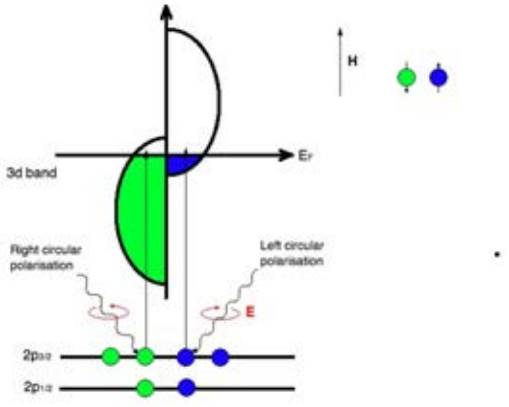

Figure 4.5: XMCD absorption sketch of the $L_{2,3}$ edges in a Stoner model.

As said above, $L_{2,3}$ absorption spectra are governed by excitations of the p core electrons to the empty states above the Fermi level. The spin-orbit interaction couples the initial state electrons into states of total angular moment $j = 3/2$ ($2p_{3/2}$ level) and $1/2$ ($2p_{1/2}$ level). Considering a Stoner model with total orbital degeneration, the d band will be split into a spin up band and a spin down band. In a magnetic system both bands will have a different density of empty states (ρ), being the magnetisation of the band given by $M = \rho_\uparrow - \rho_\downarrow$.

The interaction of circularly polarised X-rays with these electrons in the p shell leads to the excitation of spin-polarised electrons, being this polarisation dependent on the edge and on the polarisation of the light. At the L_2 edge

left circular polarised light (LCP) excites 25% spin up and 75% spin down electrons; while right circular polarised light (RCP) does the opposite. A the L_3 edge, 62.5 % spin up and 37.5% spin down electrons are excited by LCP, and vice-versa for RCP [53]. In a non magnetic material, since $\rho_\uparrow = \rho_\downarrow$ the transition intensities are the same for LCP as for RCP. However, when $\rho_\uparrow \neq \rho_\downarrow$ the absorption of the two polarisation will be different, with a difference which is opposite at the L_2 and L_3 edges. This difference will be proportional to $\rho_\uparrow - \rho_\downarrow$ and, thus, to the magnetisation of the studied d band, more precisely to the M projection over the applied magnetic field direction.

4.4.3 Description of the Circular Polarisation Beamline

Measurements described in this work have been performed in the European Synchrotron Radiation Facility (ESRF). This institution, funded by 19 countries is located in Grenoble, France, and houses one of the largest and most powerful synchrotrons in the world, together with the Advance Photon Source (APS) in USA and Spring-8 in Japan. ESRF, as ILL, is located at EPN-Campus, hosting 3500 visiting scientists per year. A picture of the Campus is shown in Fig. 4.6a. In this facility, the storage ring consist of a 844 metres circumference, and feeds 48 beam lines[7], whose distribution on 2010 is shown schematically in Fig. 4.6b.

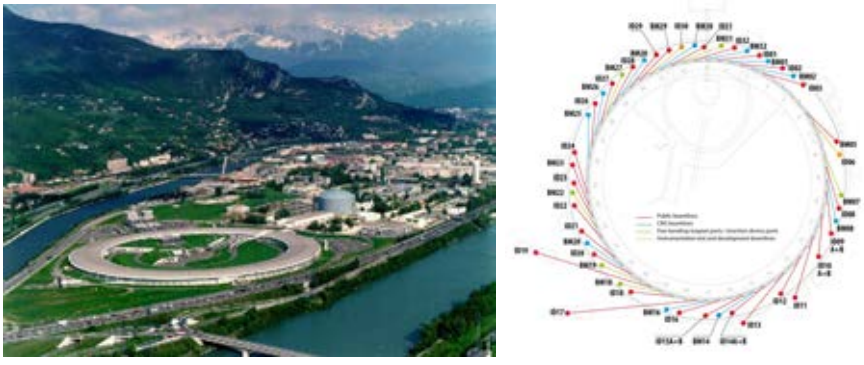

(a) (b)

Figure 4.6: (a) Picture of the European Photon and Neutron Science Campus. *Credit: http://www.saxier.org/aboutus/saxs.shtml.* (b) Schematic layout of ESRF beamline distribution. *Credit: ESRF*

ID12 beamline was used to determine the ordering of the different magnetic ions when cooled with or without applied magnetic field, looking at the possible formation of magnetically coupled clusters. The ID12 beamline is dedicated to

[7] www.esrf.eu

polarisation-dependent X-ray absorption and excitation spectroscopies in the energy range between 2 and 20 keV, and provides the user with a full control of the polarisation stated of the X-ray beam. Both circularly and linearly polarised X-ray photons can be generated by one of the three helical undulators installed in ID12. The beamline is equipped with a UHV compatible double crystal, fixed-exit monochromator with a pair of Si (111) crystals, and ion implanted silicon photodiodes, that work as intensity monitors, beam position monitors or fluorescence detectors, as in our case: TFY(total fluorescence yield)[8]. In this system the sample was pressed into a pellet and combined with boron nitride to provide a compact piece. As in the case of neutrons the sample was cooled down into a cryostat between 10 and 300 K under an applied magnetic field of 300 Oe and 1T. ID12 beamline allow to perform measurements between 2 and 300 K with an the applied magnetic field can be as high as 17 T.

[8]http://www.esrf.eu/UsersAndScience/Experiments/ElectStructMagn/ID12/

Chapter 5

Fe magnetic ordering in $NdFe_xGa_{(1-x)}O_3$

5.1 Introduction

As explained above, Fe ion substitution by non magnetic atoms, such as Ga, will affect all the magnetic interactions in the system, Fe-Fe, Fe-Nd and Nd-Nd. In the first case, Fe dilution will cause a lowering of T_{N1} until ordering disappears, for x below the percolation threshold. In the second case, randomly distributed magnetic vacancies will destroy Fe antiferromagnetic compensation generating an extra isotropic exchange field acting on both Fe and Nd. Furthermore, depending on the strength of this new interaction, cooperative order of the Nd sublattice might be fully inhibited. Therefore, in order to understand how magnetic dilution affects Nd collective ordering in the series $NdFe_xGa_{(1-x)}O_3$, it is necessary to fully characterise Fe sublattice behaviour and how its interactions, change with Ga magnetic vacancies concentration.

Although no competing interactions are inherently present in $NdFe_xGa_{(1-x)}O_3$, the random distribution of diluted Fe atoms magnetic moments is likely to generate clusters inside the sample. Moreover, these randomly allocated magnetic vacancies will cause disorder in the antiferromagnetic system, leading to uncompensated moments inside the clusters. Therefore, intrinsic frustration of the exchange interactions (isotropic, anisotropic and antisymmetric) between cluster net moments is induced. In addition, the Nd lattice enhances the anisotropy of the system, and so does the randomness induced by vacancies on the internal Fe-Nd exchange field at low-temperatures.

It is common knowledge that frustration and disorder may originate short-

range order and a rich variety of magnetic behaviours related to clustered magnetic states. The latter are manifest by puzzling effects such as mictomagnetism [45], superparamagnetism [54], magnetic phase coexistence [55], parimagnetism [56] and negative magnetisation [19, 57], among others. In particular, the role of the cluster glass formation on percolative scenarios has been recently studied in relation with Kondo effect on strongly correlated electron systems [58–60] and the formation of metallic Griffiths phases [61, 62]. In oxides, the formation of magnetic clusters due to chemical disorder within a non-magnetic or antiferromagnetic matrix has been related with the onset of Griffiths singularities, invoked as a mechanism of explanation of colossal magnetoresistance in manganites [63, 64].

The formation of magnetic clusters is especially interesting in connection with the problem of percolation. In $NdFe_xGa_{(1-x)}O_3$, by varying the Fe concentration from lower to higher, we can study the formation of small, unconnected Fe islands to the slightly vacancy doped Fe-rich system, which can be related with previous studies [19–21, 23, 38], through the range below and above the percolation concentration.

Indeed, diluted magnetic lattices are physical realisations of the magnetic percolation problem. As the Fe concentration x diminishes, T_{N1} decreases continuously until the percolation threshold $x = x_c$ is reached, at which $T_{N1} = 0$. In general, x_c depends on the lattice and spin dimensionality and the sign of the magnetic interaction (ferro- or antiferromagnetic). In our case, the Fe subsystem can be treated as a Heisenberg antiferromagnetic simple cubic lattice of $S = 5/2$ spins. There have been both experimental studies and theoretical predictions for this model. Although early theoretical predictions give a value of $x_c = 0.21$ [65], experimental studies on the $S = 5/2$ simple cubic Heisenberg antiferromagnet $KMn_xMg_{1-x}F_3$ [66] find $x_c = 0.31$. This value coincides with the most general value $x_c = 0.31$ predicted for the percolation problem by Monte Carlo simulations [67, 68]. The Fe concentrations near x_c are particularly interesting. Below x_c, the magnetism of finite clusters may dominate the behaviour of the system, behaving as a distribution of paramagnetic entities with different sizes and uncompensated moments. In contrast, above x_c the infinite cluster would have regions with large, uncompensated moments [66]. Moreover, the possibility of a quantum phase transition has been predicted for diluted magnets for x values close to percolation [69, 70]. Following previous results on $La_{2/3}Ca_{1/3}Mn_{1-x}Ga_xO_3$ manganites, where a quantum critical point (QCP) associated to the metal-insulating transition induced by Ga doping has been theoretically predicted [71] and claimed experimentally [72], it is interesting to explore the possibility of a quantum phase transition in $NdFe_xGa_{(1-x)}O_3$. The possible QCP would be a second-order phase transition occurring at the percolation limit and zero temperature.

The chapter is organised as follows; in Section 5.2 and 5.3 we study the macroscopic magnetic properties of these compounds, while in Section 5.4 we focus on the complete determination of the magnetic structure of our samples in a wide range of temperatures. Finally, in Section 5.5 we summarise the main results obtained.

5.2 Magnetisation measurements

Previous studies on $NdFeO_3$ [11, 73] showed that, in this structure, iron atoms order magnetically at high temperature ($T_{N1} \sim 700$ K) and undergo a spin reorientation transition between $T_{SR1} = 190$ K and $T_{SR2} = 80$ K. Temperature dependent magnetisation measured under an applied field of $H = 500$ and 1000 Oe of the $NdFe_xGa_{(1-x)}O_3$ compounds is reported in Fig. 5.1. T_{N1} decreases with decreasing x due to Fe dilution, and the same holds for T_{SR1} and T_{SR2}. As can be seen in Fig. 5.1 for some selected examples ($x = 0.8, 0.7, 0.6$), the same transitions can be observed in $NdFe_xGa_{(1-x)}O_3$, provided that x values are well above percolation ($x \geqslant 0.5$). T_{N1} is clearly observed in $x = 0.8$ and 0.6 as the onset of spontaneous magnetisation, due to canted antiferromagnetism as will be demonstrated later by the analysis of neutron diffraction data. The highest temperature reached in the experiment for $x = 0.7$ was below its T_{N1}, but without any doubt, a similar behaviour as that observed in $x = 0.8$ and 0.6 can be foreseen. On cooling, magnetisation displays a clear upturn followed by a strong decrease which coincides with the spin reorientation transition of the Fe magnetic moments. Below $T \sim 40$ K, the magnetisation curves for every x exhibit a paramagnetic-like contribution down to the lowest temperatures studied which can be ascribed mainly to the paramagnetic Nd moments.

The right-bottom panel of Fig. 5.1 illustrates the comparison between the magnetisation measurements of $x = 0.4$ and $x = 0.3$. These two samples are above and below the percolation limit x_c, respectively. The magnetic ordering for $x = 0.4$ is not clearly observed below 200 K, although a peak that in principle can be identified with the spin reorientation transition is present at $T_{SR} = 52$ K. The magnetisation of $x = 0.4$ above $T = 52$ K is rather unexpected, and clearly different from that of a paramagnetic sample, as it is the case for $x = 0.3$. We have prepared different batches with iron content $x = 0.4$ (with longer calcination times and finer intermediate grinding before pressing the material into pellets) with similar results. Evidently, the ceramic route used to prepare the samples does not ensure the exact nominal stoichiometric throughout the whole sample at local scale. Indeed, the magnetisation results presented in Fig. 5.1 suggest the presence of different minority phases with a slightly higher (and also lower) iron content which undergo a contin-

uous appearance of magnetic order. This interpretation is supported by the temperature dependence of neutron diffraction data, as will be later shown.

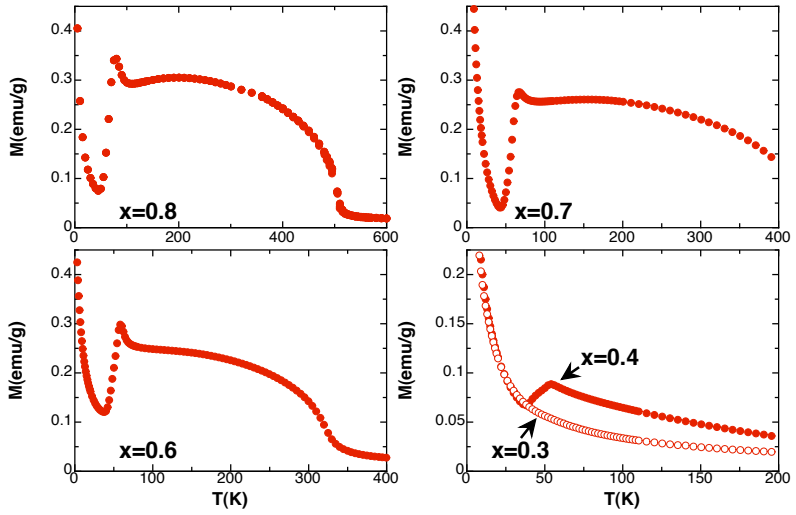

Figure 5.1: Magnetisation as a function of temperature measured at $H = 1000$ Oe of $NdFe_0.8Ga_{0.2}O_3$, $NdFe_{0.7}Ga_{0.3}O_3$, $NdFe_{0.6}Ga_{0.4}O_3$, and at $H = 500$ Oe of $NdFe_{0.4}Ga_{0.6}O_3$, and $NdFe_{0.3}Ga_{0.7}O_3$.

5.3 Susceptibility measurements

Susceptibility measurements on the same samples are displayed in Fig. 5.2. For samples with iron concentration $x = 0.8$ or higher, the observed behaviour is similar to that of $NdFeO_3$ [11]. As represented in Fig. 5.1, these compounds present a magnetic order transition at high temperature T_{N1} and a spin reorientation process between two lower temperatures T_{SR1} and T_{SR2}. This reorientation process exhibits a double peak in the susceptibility measurement that, in the case of $NdFeO_3$ was assigned to the onset (T_{SR1}) and termination (T_{SR2}) of the reorientation [11]. As the iron concentration decreases, the difference of temperature between the two peaks ($\Delta T = T_{SR1}$-T_{SR2}) also decreases, being approximatively equal to $\Delta T = 40$ K, 25 K and 20 K for $x = 0.95$, 0.9 and 0.8 respectively. For $x \leqslant 0.7$ these two peaks merge into one, being the spin reorientation nearly unnoticeable for $x = 0.4$.

For $0.2 \leqslant x \leqslant 0.3$, i.e. at $x \lesssim x_c$, the ac-susceptibility measurements at three different excitation frequencies are plotted in Fig. 5.3. Although the real part of χ_{ac} is dominated by the Nd paramagnetic contribution, a small shoulder can be identified near $T = 6$ K and $T = 15$ K for $x = 0.2$ and 0.3 respectively. This shoulder is more clearly resolved when subtracting the highest frequency

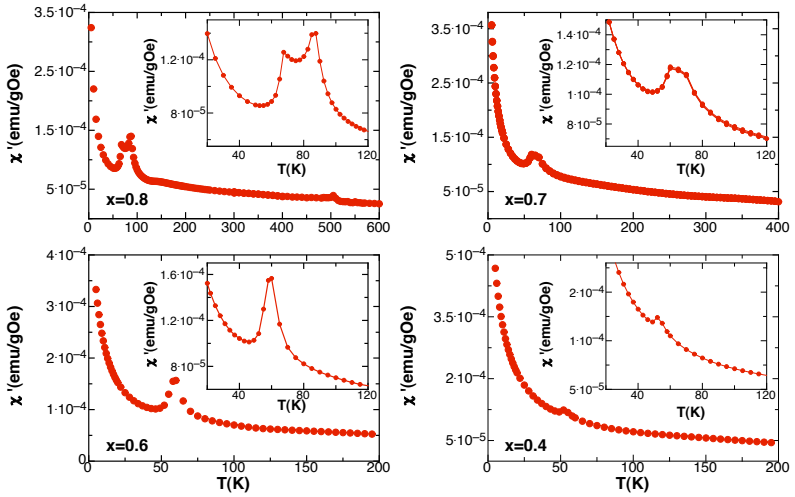

Figure 5.2: ac magnetic susceptibility as a function of temperature of $NdFe_xGa_{(1-x)}O_3$, for $x = 0.8$, 0.7, 0.6, and 0.4. The excitation frequency used was 9 Hz.

measurement to the other susceptibility curves, as displayed in Fig. 5.3 (Right column). In this Fig. a maximum at $T_f \simeq 6$ K is present in the real part of χ_{ac} for $x = 0.2$ and two maxima at $T_f \simeq 6$ K and $T_f \simeq 15$ K are evident for $x = 0.3$. The intensity of these maxima decreases as the frequency increases and the temperature at which it appears increases with frequency, resembling the frequency dependence of a spin-glass. The magnitude of this temperature shift provides a good criterion for distinguishing a canonical spin glass from a spin-glass-like material or from a superparamagnet [45]. A quantitative measurement of the frequency shift of the susceptibility peak is given by $(\Delta T_f/T_f)$ per decade ω, where ΔT_f is the difference between the position of the peak at a given frequency and the value at the lowest frequency, ν=12 Hz, being this value $\delta = 0.05$ both for x=0.2 and 0.3. This result is intermediate between the values reported for canonical spin-glasses ($\delta = 0.005$ for CuMn [74]) and for superparamagnets ($\delta = 0.28$ [45]); therefore, the observed susceptibility shoulders seem to be associated to interacting magnetic clusters, i.e. a cluster-glass state. Similar values of δ where found in other cluster-glass systems such as $CeNi_{1-x}Cu_x$ ($\delta = 0.06$) [58] or $Co_{0.2}Zn_{0.8}Fe_2O_4$($\delta = 0.032$) [75]. If one tries to explain the frequency shift of the χ' maxima by a thermal activation process over anisotropy barriers E_a (equation 5.1 Arrhenius law),

$$\frac{1}{\omega} = \tau = \tau_0 exp\Big[\frac{E_a}{kT_f}\Big] \tag{5.1}$$

the obtained parameters, $\tau_0 = 0.9310^{-23}$ and 410^{-25} and $E_a = 254$ K and

591 K (for x=0.2 and 0.3 respectively), are unphysical. This simple model only holds for superparamagnetic systems, where τ_0 has values between 10^{-10} and 10^{-13} and $E_a/\mathrm{k}\sim 25T_f$ [45]. However, for a canonical spin-glass system $\tau_0 = 10^{-200}$ values are expected to be much shorter than those in our results, thus pointing again to the existence of magnetic intercluster interactions.

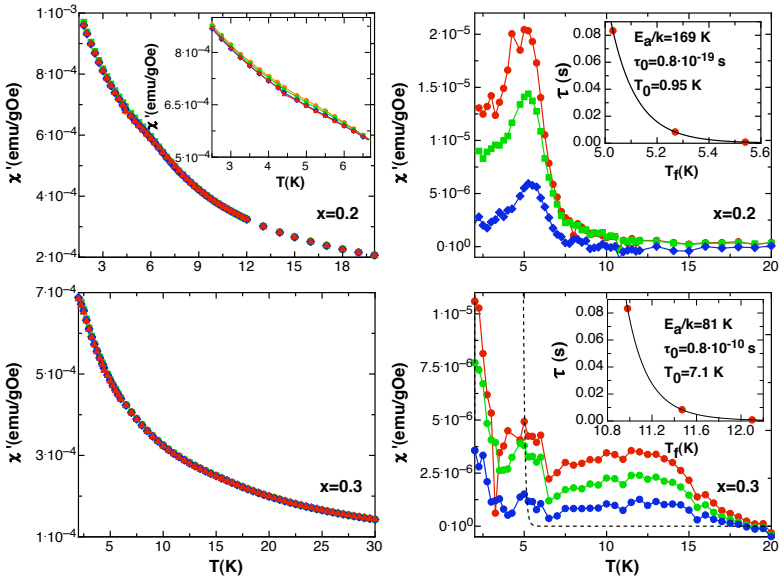

Figure 5.3: (Left column): Real part of the ac-susceptibility as a function of temperature measured at different frequencies on $NdFe_{0.2}Ga_{0.8}O_3$ (upper panel) and $NdFe_{0.3}Ga_{0.7}O_3$ (lower panel). Full circles are χ' values at ν=1.2 Hz, full squares are values at ν=12 Hz, full diamonds are values at ν=120 Hz, and full triangles at ν=1200 Hz. (Right column): χ' as a function of temperature at different frequencies of $NdFe_{0.2}Ga_{0.8}O_3$ and $NdFe_{0.3}Ga_{0.7}O_3$ minus χ' at ν=1200 Hz. Dash line is the fit of χ' data of x=0.2 shoulder with the Vogel-Fulcher law plot on the first feature of x=0.3 χ' data. Insets detail the fit of the experimental data of $T_f(\omega)$ with the Vogel-Fulcher law.

For magnetically interacting particles, a Vogel-Fulcher law was proposed by Shtrikman et al. [76] and applied to spin-glass systems by Tholence [77] ,

$$\frac{1}{\omega} = \tau = \tau_0 exp\Big[\frac{E_a}{k(T_f - T_0)}\Big] \tag{5.2}$$

being only valid if $T_f > T_0$. Although a physical interpretation of this phenomenological relation is still lacking [45, 78], it provides a more physical set of parameter values and a criterion to distinguish spin glasses and superparamagnetic-like systems through the ratio $(T_f - T_0)/T_f$ [79]. Insets in Fig. 5.3 show the fit of the experimental data of $T_f(\omega)$ with the Vogel-Fulcher law, in both cases, the condition $T_f > T_0$ is fulfilled. Although the

noise in the χ' measurements of the x=0.3 sample does not allow fitting the first bump data, however, it seems to follow the same $T_f(\omega)$ dependency than the one observed for x=0.2, as can be seen by overplotting the fitting results of x=0.2 χ' data on x=0.3 data –see Fig. 5.3–. From these fits, the ratio $(T_f - T_0)/T_f$ is 0.8 and 0.3 for x=0.2 and 0.3 respectively, being these values an order of magnitude higher than those reported for canonical spin glasses (CuMn$\sim$0.02) [45], but still too low to be considered a superparamagnetic system ($La_{0.994}Gd_{0.006}Al_2\sim$1[80]). Again, our data are intermediate between those of spin-glasses and superparamagnets, and are comparable to the ones obtained for systems displaying evidences of a progressive freezing of clusters, $ZnCr_{1.6}Ga_{0.4}O_4\sim$0.4 [80].

Another paradigmatic characteristic that clearly marks the presence of spin-glass is a deviation in the susceptibility ZFC and FC curves below T_f, which allows us to differentiate between canonical spin glasses and cluster spin glasses [45, 58]. Unfortunately, in our case the Nd paramagnetic contribution, superimposed to the Fe one, is dominant at low temperatures, thus making impossible to detect any significant difference between FC and ZFC measurements in the temperature range where the maxima in the *ac* susceptibility curves was observed.

However, the strong χ' frequency dependence (δ) of our data, along with the unphysical results of the Arrhenius fits and large values of the ratio $(T_f - T_0)/T_f$ allow us to suggest that the maxima in the *ac* susceptibility curves have their origin in a cluster freezing process. As iron concentration for these compounds is below, but close to percolation, we ascribe this cluster-glass-like behaviour to the presence of cluster regions with slightly higher-than-nominal iron content. These clusters, with a net magnetic moment, will behave as interacting particles which became frozen below a certain temperature mainly given by their size. A mainly bimodal distribution of sizes in the $x = 0.3$ sample may originate the χ_{ac} experimental curve. Indeed, the same kind of clusters would explain the continuous increase in magnetisation observed in Fig. 5.1 for x=0.4.

The results obtained from magnetic measurements can be summarised in the phase diagram depicted in Fig. 5.4. For the sake of clarity, Fig. 5.4 includes information obtained by neutron diffraction, which will be presented in the next section.

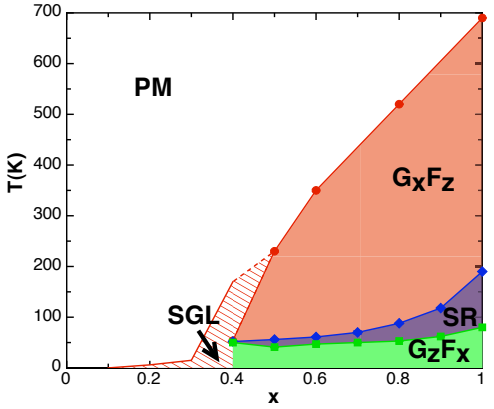

Figure 5.4: Phase diagram of $NdFe_xGa_{1-x}O_3$ series. The different represented regions are the paramagnetic phase (PM), the Γ_4 high temperature configuration (G_xF_z), the spin reorientation region (SR), the Γ_2 low temperature configuration (G_zF_x) and the cluster-spin-glass phase (SGL). Data of x=1 are taken from [11].

5.4 Neutron measurements

In order to determine the magnetic structure of our samples in the range of study presented in Figs. 5.1 and 5.2, neutron diffraction experiments were performed. According to previous studies, iron spins in $NdFeO_3$ order correspond to an antiferromagnetic structure with a weak ferromagnetic component G_xF_z (irreducible representation Γ_4) [35]. In the spin reorientation region, marked by the double peak in susceptibility measurements (Fig. 5.2), the iron spins rotate continuously in the ac plane, from G_xF_z to the low temperature configuration G_zF_x (irreducible representation Γ_2) [36, 37]. At low temperatures this configuration induces, via Nd-Fe exchange, a Nd polarisation of the same symmetry (c_yf_x) that becomes noticeable below 25K [16]. In our case, the same iron spin configurations are observed for x above percolation, but we have not detected the (100) diffraction peak due to Nd polarisation. For $x = 1$, the isotropic Nd-Fe exchange interaction is nearly cancelled out due to the antiferromagnetic ordering of Fe ions. However, for $x \lesssim 1$, an extra isotropic, random exchange field is generated on Nd sites by uncompensated iron spins due to the substitution of some iron by diamagnetic gallium. This field could be expected to be rather strong, due to the nearly compensated antiferromagnetic structure of the Fe lattice in $NdFeO_3$. This random field would polarise the neighbour Nd ion breaking the Γ_2 symmetry, thus preventing the collective antiferromagnetic polarisation to be observed. The existence of this random field was already revealed by the calorimetric measurements described in Chapter 3, where the distribution of the H_{Fe-Nd} produces a broadening of the corresponding Schottky anomaly. It is worth to mention that for $x = 0.9$ already $\sim$ 50% of Nd

ions are affected by a random field due to some degree of uncompensation of their first Fe neighbours [22].

In Fig. 5.5 we display, as an example of the analysis, the measured and calculated diffraction patterns obtained at the D2B high-resolution diffractometer of the ILL at T=38 K for $NdFe_{0.6}Ga_{0.4}O_3$. The starting structural parameters were taken from our previous X-ray analysis, reported in Chapter 2. No significant difference is observed between structural parameters determined by X-ray and neutron diffraction. Since the temperature is lower than the spin reorientation temperature of this compound (T_{SR}=60 K), the intensity of the diffraction pattern is calculated considering a G_zF_x configuration for the iron spins.

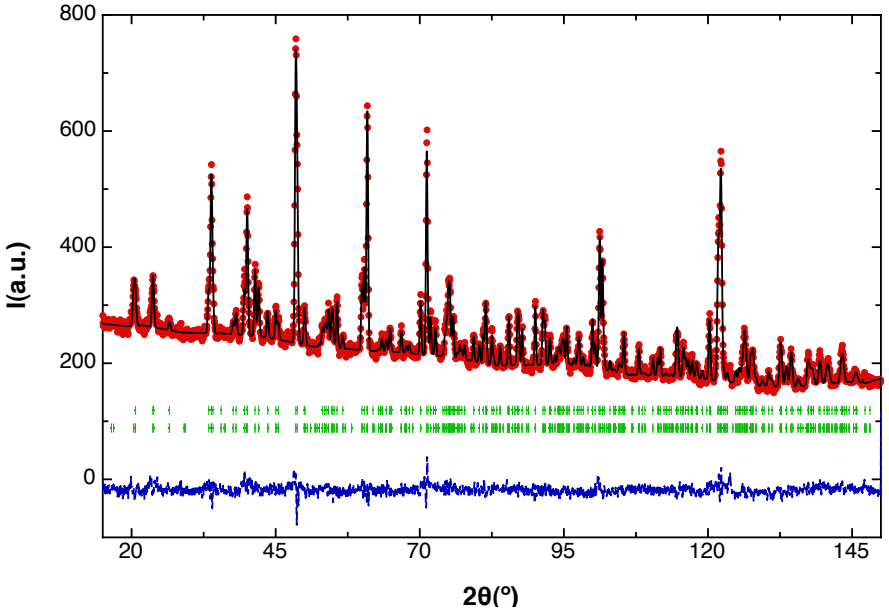

Figure 5.5: Neutron diffraction pattern of $NdFe_{0.6}Ga_{0.4}O_3$ at T=38 K. Full circles represent the observed intensity, solid line represents the calculated intensity, bars represent allowed Bragg reflections for the structural phase (up) and the magnetic phase (down) and dotted line (bottom) represents the difference between the observed and the calculated intensities.

An example of the crystallographic and magnetic structure obtained from the neutron diffraction analysis using FullProf Studio tool [28] is shown in Fig. 5.6, also displayed in Chapter 2. For $NdFe_{0.8}Ga_{0.2}O_3$ and T=94 K the magnetic configuration of iron spins displays an antiferromagnetic structure along the a axis and a weak ferromagnetic component along the c axis (G_xF_z). In Fig. 5.7 the diffraction peaks due to iron magnetic ordering obtained at the ILL-D1B diffractometer are displayed. The upper panel display the (011) and

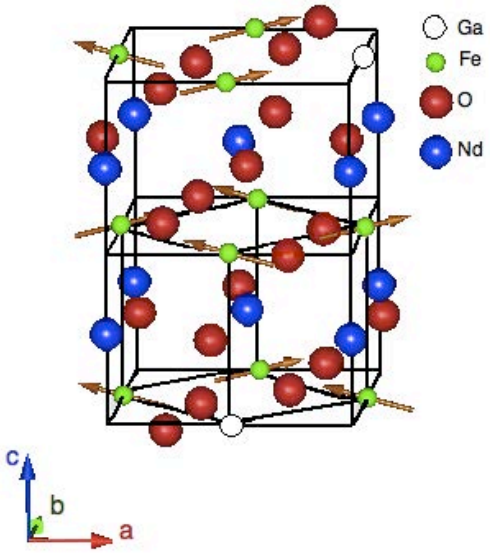

Figure 5.6: Crystallographic and magnetic structure of $NdFe_{0.8}Ga_{0.2}O_3$ at T=94 K.

(101) reflections for different iron concentrations at temperatures above T_{SRT}. The intensity of (101) and (011) peaks strongly diminishes as the iron concentration decreases, resulting the first one almost indistinguishable from the corresponding structural peak for $x = 0.4$. This evolution holds for all studied temperatures. As expected, the intensities of the (101) and (011) reflections change significantly from above T_{SR1} and below T_{SR2}. In the reorientation region $T_{SR2} < T < T_{SR1}$ the iron spin rotates continuously from the high temperature structure to the low temperature one and, therefore, it is not possible to fit these reflections with the spin configurations corresponding to either Γ_4 or Γ_2 representations.

The rotation of the four iron magnetic moments present on a unit cell is graphically illustrated in Fig. 5.8. The results of the Rietveld refinement for the magnetic moment of the ordered Fe^{3+}ions are depicted in Fig. 5.9

Although some works suggested that the ferromagnetic component is too small to give a measurable contribution to the neutron powder diffraction patterns in $NdFeO_3$ [81], several authors have demonstrated that a pure G_x or G_z mode cannot explain the ratio between the obtained intensity of (011) and (101) reflections in this material [35, 37], both above and below the spin reorientation transition. Moreover, the magnetisation measurements reveal a non

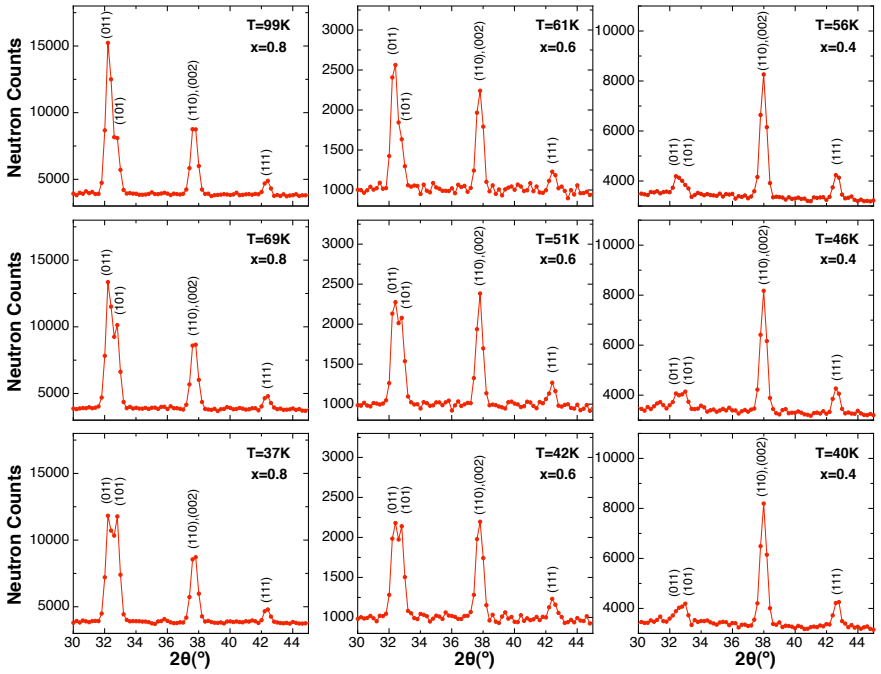

Figure 5.7: Neutron diffraction patterns for (left panels): $NdFe_{0.8}Ga_{0.2}O_3$, (center panels): $NdFe_{0.6}Ga_{0.4}O_3$, and (right panels): $NdFe_{0.4}Ga_{0.6}O_3$ at three different temperatures; (upper panels):$T > T_{SR1}$; (center panels): $T_{SR1} > T > T_{SR2}$ and (lower panels): $T < T_{SR2}$.

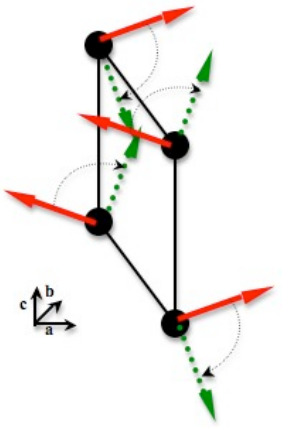

Figure 5.8: Spin reorientation of iron magnetic moments. Solid line arrows reproduce magnetic moments orientation at high temperature phase (Γ_4) and dotted line arrows the magnetic moments orientation at low temperature phase (Γ_2)

negligible magnetisation signal, easily observed in a SQUID magnetometer for $0.5 < x < 1$, as illustrated in Fig. 5.1. Therefore, we performed our Rietveld

refinement assuming a G_xF_z ordering for $T>T_{SR}$ and G_zF_x for $T<T_{SR}$. In the spin reorientation region the magnetic moment was allowed to rotate between both configurations by using polar coordinates in the refinement. Neutron powder diffraction measurements do not allow us to discriminate between the spin rotation of a single phase and a "phase coexistence model" in which a G_zF_x phase grows at the expenses of the G_xF_z one. Therefore our results can not be distinguished in principle from those obtained for $NdFeO_3$ in [82] and [81], where the refinement of neutron powder diffraction patterns of $NdFeO_3$ is performed assuming a G_xG_z ordering in all the temperature range. Although the results are indistinguishable, our treatment has the formal advantage of being compatible with the symmetry of the system along the whole temperature range.

Fig. 5.9 depicts the values of the magnetic moment per Fe^{3+} atom resulting from our Rietveld analysis (upper panel), the staggered magnetisation M_x and M_z with the signs corresponding to the iron atom occupying the (1/2, 0, 0) position (central panel) and the angle θ formed by the iron spin at position (1/2, 0, 0) with the z axis as a function of temperature (lower panel) for the samples $x = 0.9$ (left column), $x = 0.8$ (center column), and $x = 0.6$ (right column). The thermal evolution of θ exhibits a continuous spin reorientation process for $x \geqslant 0.6$ as observed in the non diluted x=1 compound [81, 82]. Moreover, no discontinuities in the total magnetic moment are observed during the spin reorientation transition.

As it was already displayed in Fig. 5.2, the temperature range at which the spin reorientation occurs decreases as the iron concentration diminishes. According to Ref. [11], the onset and termination of the spin reorientation process were associated with a double peak in the susceptibility measurements that is no longer detected in our experiment for $x \leqslant 0.6$. However, neutron diffraction on the $x = 0.6$ sample shows that the spin reorientation process is not that sharp, although the temperature range is only 14 K wide (see Figs. 5.7 and 5.9). Since the high temperature peak in the susceptibility curve is higher and wider than that of the low-temperature, for low x values the spin reorientation region becomes too narrow to distinguish T_{SR1} and T_{SR2} in a χ_{ac} measurement.

The effect of the substitution of Fe by a non magnetic ion in spin reorientation processes has been studied in different rare-earth orthoferrites, as mentioned in Chapter 2, concluding that a small concentration of non magnetic ions has an important effect on the magnetic properties of these compounds. The presence of a magnetic vacancy destroys the compensation of the $R - Fe$ isotropic exchange interaction, generating an isotropic exchange field that creates an additional anisotropy.

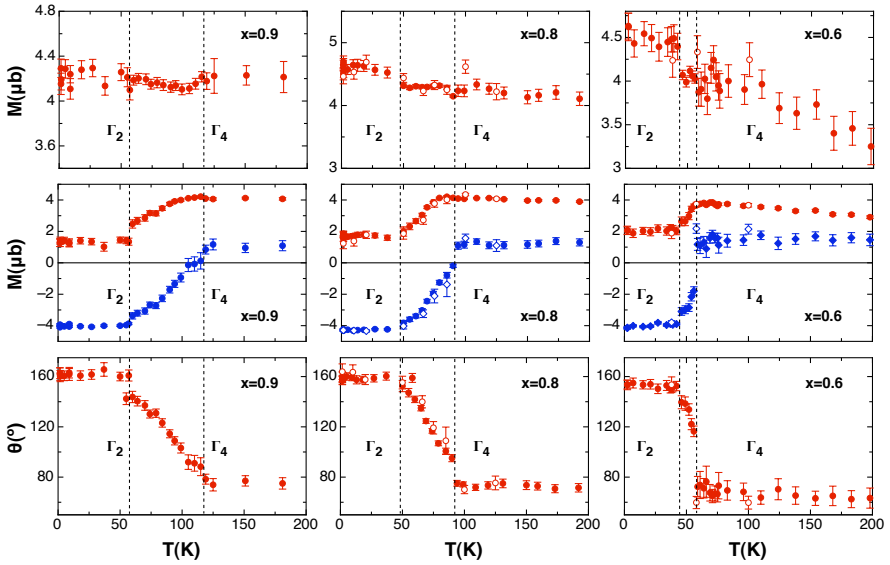

Figure 5.9: (Upper panel): magnetic moment per Fe^{3+} atom obtained from the Rietveld fit. (Central panel): Magnetic moment components per iron atom. Circles correspond to M_x component and diamonds to M_z. (Lower panel): Obtained values of the angle between magnetic moments and c axis. Full symbols are results obtained from measurements performed at the D1B diffractometer while empty symbols correspond to the high-resolution D2B diffractometer.

In a non-diluted RMO_3 system the isotropic exchange interaction $R-M$ plays no role in the SR process, since the effective field acting on M^{3+} spins due to R^{3+} ions is along the weak ferromagnetic moment. The antisymmetric exchange and the anistropic-symmetric exchange interactions tend to make the M^{3+} and the R^{3+} subsystems perpendicular to each other, generating an effective field on the M^{3+} spins in the direction perpendicular to that of the G_x component:$+H_z$ for up-spins and $-H_z$ for down-spins, that tends to rotate the spins, keeping the antiferromagnetic configuration. As the temperature is lowered, this effective field increases due to R^{3+} moment enhancement. When the interaction created by this field on M^{3+} becomes larger than the anisotropy energy of the metal ions, the spin reorientation transition takes place [83]. In $NdFe_xGa_{(1-x)}O_3$, as in $TbFe_xAl_{1-x}O_3$ [21], the presence of magnetic vacancies increases the Fe ion anisotropy, thus stabilising the Γ_4 configuration and lowering the temperature at which the spin reorientation transition starts.

The magnitude of the total magnetic moment of Fe^{3+} well above percolation ($x \geqslant 0.6$), both above and below the spin reorientation process, is in good agreement with previous neutron powder diffraction studies on $NdFeO_3$ [37, 73, 81, 82, 84] and so are the values of the canting angles. All these data, together with the spin reorientation process data and magnetic ordering of Fe

spins are given in Table 5.1. It is interesting to note that the canting angle, both above and below the reorientation transition increases with the gallium concentration. The antiferromagnetic component of iron moments becomes uncompensated by substituting iron atoms by gallium. Therefore, the average strength of the exchange interaction decreases allowing iron spins to rotate slightly, thus, decreasing the effective magnetic moment in the G mode. This effect is specially remarkable for $x = 0.4$, where the canting angle is increased by a factor of three with respect to that of $NdFeO_3$, as can be seen in Table 5.1. Moreover, in $x = 0.4$ the magnetic moment per Fe obtained from the Rietveld refinement is only $\sim 2.4\mu_B$ in comparison with $\sim 4.2\mu_B$ for $x = 0.9$. This indicates that only a half of the iron spins in the $x = 0.4$ sample are ordered, consistently with the scenario suggested by the magnetisation measurements on this sample represented in Fig. 5.1: in $NdFe_{0.4}Ga_{0.6}O_3$ iron atoms are not equally distributed through the sample, with Fe-rich and Fe-poor regions in which iron concentration vary. Iron atoms in Fe-poor regions, where effective x is below percolation, would not be ordered, and, therefore, would not contribute to the measured intensity of the G and F modes.

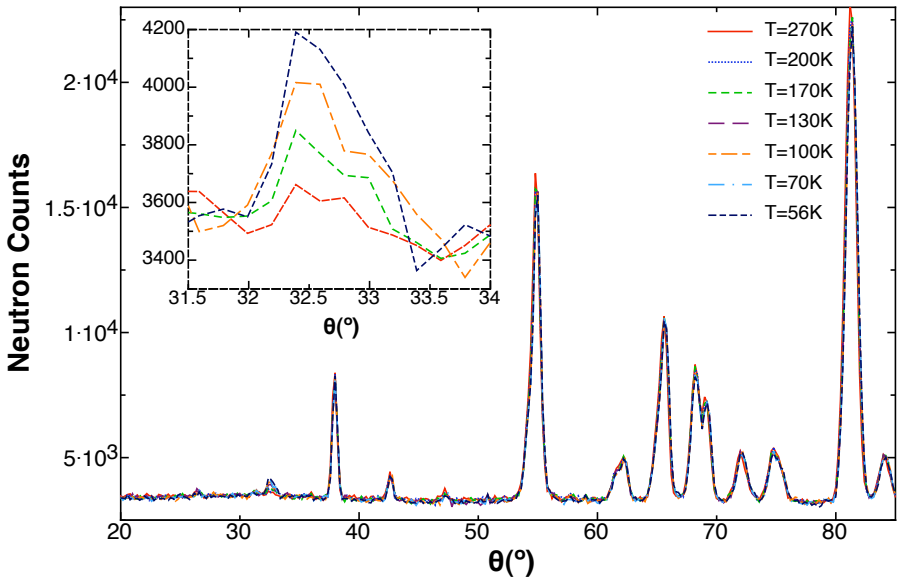

Figure 5.10: Neutron diffraction patterns of $NdFe_{0.4}Ga_{0.6}O_3$ at different temperatures, above spin reorientation. Inset displays a zoom on the (0 1 1) (1 0 1) peaks for some selected temperatures.

The experimental evidence of this different concentration regions is observed in Fig. 5.10. The neutron diffraction pattern of the $x = 0.4$ sample exhibits a continuous increase with temperature of the (1 0 0) and (1 0 1) peaks, while in magnetisation and susceptibility measurements displayed in

Figs. 5.1 and 5.2 no order transition is observed, besides the spin reorientation process. Note that $T_{SR1}^{x=0.4} \approx 52$ K is lower than the temperatures at which the diffraction patterns in Fig. 5.10 have been recorded. However, magnetisation measurements did not allow us to identify the ordering temperature above $T_{SR1}^{x=0.4}$. The continuous enhancement of the (1 0 0) and (1 0 1) peaks in a wide range of temperatures (from ∼200 K) starts at temperatures close to the magnetic order of $NdFe_{0.5}Ga_{0.5}O_3$. The magnetisation measurement also manifests the continuous appearance of a net magnetic moment above the paramagnetic background below $T = 200$ K. These results suggest that, even for crystallographically monophasic samples, one cannot avoid a certain chemical distribution, that originates regions with Fe concentrations slightly different from the nominal one. Usually, the effect of these small regions is not predominant, since the effect of the majority phase dominates the system, especially below its order transition. However, for iron concentrations just above percolation, where the long range ordering contribution is very low, the effect of these Fe-rich regions is no longer negligible, generating an observable extra contribution to the sample magnetisation. Our results suggest that intrinsic disorder –leading to clusterisation of the sample is always present– for concentrations close to percolation with the ceramic fabrication route described in Chapter 2. The small fraction of the sample with iron concentration slightly different from the nominal one can be minimised by repeating the sinterisation process, but it appears to be always present in our samples. The relaxation processes taking place at different low temperatures in the $x = 0.3$ sample is consistent with the presence of Fe clusters with a distribution of sizes, or magnetic "*rare regions*", a term coined by Vojta in [85].

One may wonder whether Fe in $NdFe_xGa_{(1-x)}O_3$ is an appropriate system to test quantum phase transitions at concentrations close to percolation, as suggested by Vojta [85]. Two problems arise in this system to compare experimental results with theoretical predictions. First, the presence of paramagnetic Nd in the background makes extremely difficult to obtain critical exponents from magnetic susceptibility measurements in samples near $x = 0.312$ [66–68], as evidenced in Figs. 5.1 and 5.2. Second, the percolative quantum phase diagram suggested by Vojta [70, 85] indicates that the effect of quantum fluctuations would be a higher than expected critical temperature for concentrations near (and higher than) percolation. This may appear to be the case in $NdFe_{0.4}Ga_{0.6}O_3$ as magnetisation and neutron diffraction experiments show. However, the experimental results could also be simply due to the ordering of a wide distribution of Fe-rich regions, with higher than nominal concentrations and therefore, higher than expected critical temperatures. Evidently, this *"compositional distribution"* deters the study of quantum phase transitions at concentrations close to percolation. The use of non-magnetic rare earth, as

in the $LaFe_xGa_{1-x}O_3$ series, may pave the way to future (quantum) critical exponents search.

5.5 Conclusions

In this chapter we have verified that Fe ions in $NdFexGa_{(1-x)}O_3$ compounds order magnetically for $x \geqslant 0.4$ in the same configuration as that observed in $NdFeO_3$, Γ_4, but at a lower temperature due to Fe dilution. The Fe ion anisotropy increase due to the substitution of Fe by a non magnetic metal depresses the spin reorientation temperature of the metal sublattice. However, the effect is not as large as those described in other systems such as $TbFe_{1-x}Al_xO_3$ [21], in which the spin reorientation process is fully inhibited by a 2.5% aluminium concentration, due to the strong Ising character of the Tb ion. The lowest doublet of the Nd^{3+} in $NdGaO_3$ has been proved to be slightly Ising-like [31]. However, the high temperatures at which the spin reorientation takes place in $NdFeO_3$ ensures the thermal population of several crystal field doublets of the Nd ion [10], reducing even more the weight of its Ising ground doublet. Therefore, the Fe spin reorientation is not inhibited even for Ga concentrations as high as 60%. The reduction of T_{SR1} and T_{SR2} is found to narrow the reorientation temperature range, being nearly negligible for $x = 0.4$, for which a sharp Γ_4-Γ_2 transition is observed in less than $\Delta T = 2$ K. These results are summarised in Table 5.1 and in Fig. 5.4

The uncompensated isotropic exchange field generated by the Fe magnetic vacancies on Nd sites magnetize Nd ions along G_zF_x for $T<T_{SR}$, and therefore even at the higher Fe concentrations no peak due to Nd polarisation is observed in neutron diffraction measurements. Magnetic vacancies induce an increase in the canted angle of the Fe spins both in the high- (Γ_4) and in the low-temperature (Γ_2) phases. However, for Fe concentrations well above percolation these canted angle values are in good agreement with previous results on $NdFeO_3$ and so are the Fe magnetic moments, ensuring that magnetic vacancies do not influence the ordering type found for Fe in the diluted phase.

Indeed, for $x = 0.4$, our fits to neutron diffraction data indicate that the ordered magnetic moment per Fe ion is 2.4 μ_B, which amounts only to 60% of the value for the pure $NdFeO_3$, pointing along a canting angle which is almost twice that found in the pure compound. Moreover, no Néel temperature is clearly observed on the $x = 0.4$ sample, and the ordering appears to be distributed below $T = 170$ K and $T = 52$ K, both in magnetisation and neutron diffraction experiments. All these facts indicate a strong magnetic disorder in this system. In $x = 0.2$ and 0.3, the magnetic susceptibility data indicate the presence of relaxation processes that seems to be related with the presence of

Table 5.1: a, b, and c lattice parameters at room temperature, temperature at which the spin reorientation begins, temperature of spin reorientation termination,ΔT_{SR}, T_C, canted angle at $T>T_{SR}$, canted angle at T=1.5 K, $|\mu_{Fe}|$ at $T>T_{SR}$ and at T=1.5 K of all compounds analysed in this work. Data of $NdFeO_3$ from [11, 37, 81] are also represented.

	a	b	c	T_{SR1} (K)	T_{SR2} (K)	ΔT_{SR} Δ(K)	T_C (K)	θ_1 (°)	θ_2 (°)	$\lvert\mu_{Fe}\rvert_1$ (μ_B)	$\lvert\mu_{Fe}\rvert_2$ (μ_B)
[81] - $x = 1$	5.451 02	5.588 08	7.761 65	190	100	90	-	13	20	3.87(5)	4.18(5)
[11] - $x = 1$	-	-	-	190	80	110	690	-	-	-	-
[37] - $x = 1$	-	-	-	-	-	-	-	-	20.6	-	4.12(5)
$x = 0.9$	5.4459	5.5759	7.7522	118±1	62.0±1	56±1.4	-	13±4	18±5	4.22±0.14	4.16±0.1
$x = 0.8$	5.4448	5.5676	7.7495	88±1	53±0.5	35.0±1.1	520±1	19±3	22±3	4.1±0.05	4.46±0.12
$x = 0.7$	5.4430	5.5591	7.7437	70±3	50±1	20±3	-	-	-	-	-
$x = 0.6$	5.4426	5.511	7.7409	61±1	47±1	14.0±1.4	350±2	21±8	26±3	4.00±0.18	4.62±0.14
$x = 0.5$	5.4393	5.541	7.7327	56±1	51±1	4.0±1.4	230±2	-	-	-	-
$x = 0.4$	5.4385	5.5354	7.7304	52±1	50±1	2.0±1.4	52±2	37±12	31±9	2.42±0.13	2.74±0.22

cluster-glass-like phases. Both samples present a common feature at $T \sim 5$ K, while $x = 0.3$ has another one at $T \sim 12$ K. The strong dependence of these maxima freezing temperatures with frequency (δ) and the magnitude of the ratio $(T_f - T_0)/T_f$ given by fitting our data to Vogel-Fulcher law, suggest the freezing of magnetic moments of Fe clusters of different sizes and momenta, whose concentration obviously depends on x.

Near percolation ($0.2 \leqslant x \leqslant 0.4$), three related dilution effects will influence the magnetism of the system. First, above percolation the fractal nature of the infinite cluster [66, 86] induces the presence of magnetically uncompensated regions, which are expected to have a paramagnetic behaviour, thus reducing the ordered magnetic moment per Fe. Second, both above and below percolation, even in a chemically perfect distribution, the presence of finite clusters is ensured. The random net magnetic moment, interactions and anisotropy of these entities will reduce the ordered magnetic moment per Fe atom, as well as give raise to glassy behaviour. Third, a chemical concentration distribution of Fe and Ga is intrinsically related to the ceramic fabrication route, generating regions with local Fe concentrations higher and lower than nominal, which seems to induce a distribution of magnetic properties, and in particular, the T_N of the $x = 0.40$ system observed both in macro- and microscopic magnetic measurements.

The random isotropic exchange field created by Fe on the Nd system as a result of Ga dilution inhibits the Nd polarisation in $NdFe_xGa_{(1-x)}O_3$, as observed in neutron diffraction. The influence of Ga dilution and Fe magnetic disorder on the cooperative ordering of Nd taking place in the pure compounds [10, 32] at $T = 1K$ has been discussed in Chapter 3, and will be further analysed in Chapter 6.

Chapter 6

Nd magnetic ordering in $NdFe_xGa_{(1-x)}O_3$

6.1 Introduction

On Chapter 3 we analysed in detail the effect of magnetic ions introduction on the Ga sublattice in the polarisation and magnetic ordering of the Nd sublattice in $NdGaO_3$. Although interesting information on Nd ordering inhibition and changes in Nd polarisation was obtained, specific heat measurements were proven insufficient to fully solve the nature of all the different components that are manifested in the $NdFe_xGa_{(1-x)}O_3$ series.

As a first step to understand the different processes taking place in the Nd sublattice as x is modified, the Fe sublattice behaviour was fully characterised as a function of x down to low temperatures, and the results discussed in Chapter 5. In this chapter, we will focus on the unexplained features observed in specific heat measurements and related to the Nd sublattice, such as the Nd magnetic structure in $0.05 \leqslant x \leqslant 0.1$, the possible existence of Nd cooperative order in $x = 0.2$ and 0.3 or the appearance of a *"glassy"* state in $x = 0.1$, 0.2 and 0.3 at very low temperatures. In this way, we hope to achieve a full description of the magnetism of the $NdFe_xGa_{(1-x)}O_3$ series.

This chapter is divided into two sections. In Section 6.2, the magnetic structure of the Nd sublattice of $0.05 \leqslant x \leqslant 0.3$ is discussed by means of neutron diffraction measurements, focusing on the different types of ordering undergone by the Nd ions. In Section 6.3, the nature of the *"glassy"* state observed in specific heat measurements in $0.1 \leqslant x \leqslant 0.3$ at very low temperatures will be further analysed from very low temperature ac susceptibility. The results obtained and conclusions drawn are summarised in Section 6.4

6.2 Neutron diffraction measurements

According to previous neutron diffraction [25] and susceptibility [31] studies, Nd^{3+} ions in $NdGaO_3$ order magnetically at $T_N \sim 1K$ in the c_z mode. In this magnetic structure each Nd^{3+} magnetic mode is coupled antiferromagnetically in layers and ferromagnetically in columns. To study how this structure might be distorted by the introduction of magnetic ions in $NdFe_xGa_{(1-x)}O_3$ compounds below Fe percolation, $x \leqslant 0.3$, neutron diffraction experiments were performed.

As an example of the analysis, in Fig. 6.1 we display the measured and calculated diffraction patterns obtained at the D20 high-resolution diffractometer of the ILL at T=55 mK for $NdFe_{0.05}Ga_{0.95}O_3$. The starting structural parameters were taken from our previous X-ray analysis, reported in Chapter 2. No significant difference is observed between structural parameters determined by X-ray and neutron diffraction. Since the temperature is lower than the ordering temperature obtained by calorimetric measurements, the intensity of the diffraction pattern is calculated considering a c_z configuration for the Nd spins, the same obtained for $NdGaO_3$. The good agreement between experimental and calculated pattern leads us to conclude that, in $NdFe_{0.05}Ga_{0.95}O_3$, Nd^{3+} cooperative order follows the same magnetic configuration as the pure compound.

The presence of a Schottky anomaly on the calorimetric measurements in this compound, showed that Nd ions were polarised by the presence of Fe magnetic moments, through a H_{Fe-Nd} exchange field. However, since Fe concentration is well below percolation, no cooperative ordering can be found in the Fe sublattice. Therefore, the exchange field in every Nd site is expected to be random and different, depending on the number and orientation of Fe magnetic moments in their neighbourhood, as shown by the broad Schottky peak put on in Chapter 3. Thus, no diffraction peak due to Nd polarisation by the iron sublattice is expected in this case.

An example of the crystallographic and magnetic structure obtained from the neutron diffraction analysis using FullProf Studio tool [27, 28] is shown in Fig. 6.2b. For $NdFe_{0.05}Ga_{0.95}O_3$ and T=55 mK the magnetic configuration of Nd spins displays an antiferromagnetic structure in the $a-b$ plane axis and a ferromagnetic structure along the c axis (c_z). Fig. 6.2a depicts the values of the electronic magnetic moment per Nd^{3+} atom resulting from our Rietveld analysis. The thermal evolution of M exhibits an ordering transition at $T \sim 890$ mK, similar to the one obtained from calorimetric measurements, $T = 860$ mK. Moreover, the magnitude of the total electronic magnetic moment of Nd^{3+}, $\mu_{Nd} = 0.99 \pm 0.04$, is in good agreement with previous neutron

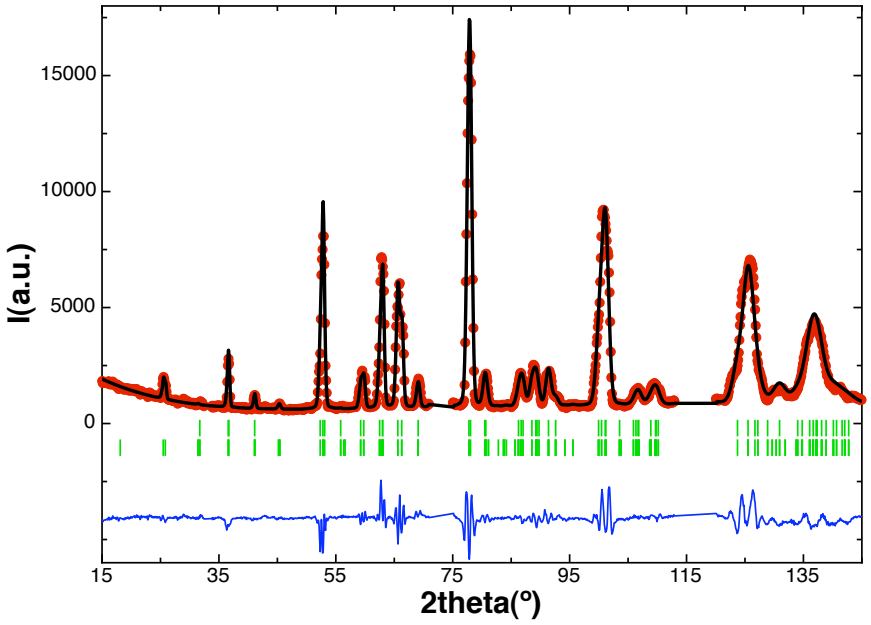

Figure 6.1: Neutron diffraction pattern of $NdFe_{0.05}Ga_{0.95}O_3$ at T=55 mK. Full circles (○) represent the observed intensity, black solid line(−) represents the calculated intensity, bars (|) represent allowed Bragg reflections for the structural phase (up) and the magnetic phase (down) and blue solid line (−), at the bottom of the graph, represents the difference between the observed and the calculated intensities.

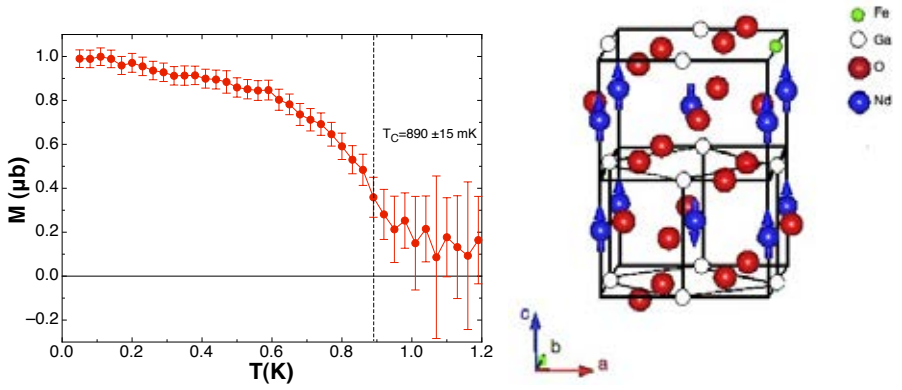

(a) (b)

Figure 6.2: (a) Magnetic moment per Nd^{3+} atom obtained from the Rietveld fit. (b) Crystallographic and magnetic structure of $NdFe_{0.05}Ga_{0.95}O_3$ at T=55 mK.

diffraction studies on $NdGaO_3$: $1.1 \pm 0.1\ \mu_B$ [25]. Thus, the introduction of magnetic ions in the Ga sublattice reduces T_N, leaving the intensity of the Nd magnetic reflections unaffected.

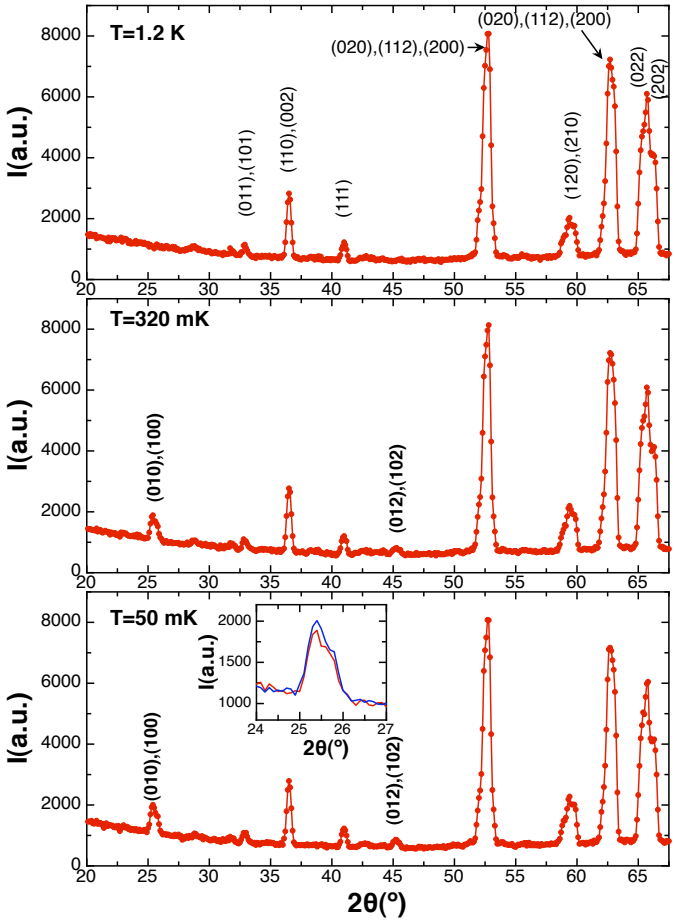

Figure 6.3: Neutron diffraction pattern of $NdFe_{0.05}Ga_{0.95}O_3$ at different temperatures. Inset displays the comparison between the intensity of the (010)+(100) magnetic reflection at $T = 320$ mK(–) and $T = 50$ mK (–).

Marti et al. [25] showed that below 300 mK an enhancement of the magnetic reflection could be clearly observed in their neutron powder diffraction measurements in $NdGaO_3$. They found that the intensity of magnetic peaks doubled its value when temperatures of the order of 10 mK were reached. They ascribed this enhancement to the polarisation of the ^{143}Nd and ^{145}Nd nuclear spins in the hyperfine field created by the Nd electronic moments. As can be seen in Fig. 6.3 and 6.5a, this enhancement is also noticeable in our case, although it is less intense. For $NdFe_{0.05}Ga_{0.95}O_3$, the integrated intensity of the principal magnetic reflection [(010)+(100)] does not display an abrupt change in its slope at $T \sim 300$ mK, after reaching a constant value right below the transition. Instead, as shown in Fig.6.5a, the integrated area increases continuously below T_N as the temperature decreases until $\sim$ 400 mK; after

this temperature the integrated intensity remains constant and, below $\sim$ 300 mK, the intensity slightly increases again. The effect is even less evident when neutron diffraction patterns are compared, as in the inset of Fig. 6.3.

When our diffraction data are compared to those of $NdGaO_3$ in Ref. [25], it is evident that the latter holds a better statistics due to much longer measurements –$\sim$40 hours compared to 20 minutes–, thus, relative variations in the peak intensities due to thermal variation are expected to be smaller in the first case. Moreover, thermal stabilisation in $NdGaO_3$ measurements was ensured by condensing liquid helium into the sample container, reducing the temperature gradient between the cryogenic mixture and the sample; while a bit of ^{3}He was used in our case as exchange gas. A not so a good thermal contact, combined with not long enough acquisition time might be the cause of a less intense neutron response for Nd hyperfine polarisation. Since the effect of the hyperfine-enhanced nuclear polarisation in our data is negligible compared to the long range Nd-Nd ordering contribution, it has not been considered to perform Rietveld refinements.

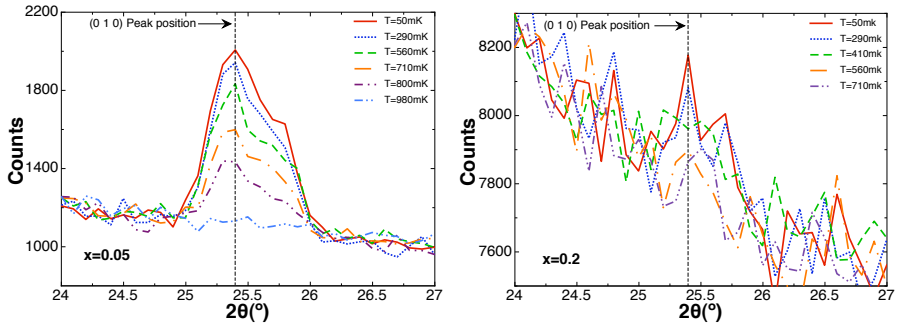

(a) (b)

Figure 6.4: (a) (010)+(100) neutron diffraction peak of $NdFe_{0.05}Ga_{0.95}O_3$ at different temperatures. (b) (010)+(100) neutron diffraction peak of $NdFe_{0.2}Ga_{0.8}O_3$ at different temperatures.

A peak corresponding to Nd magnetic ordering is also clearly present in $x = 0.1$ specific heat measurements, although less intense and at a lower temperature than in $x = 0.05$ and $x = 0$. Because no significant difference with $x = 0.05$ regarding Nd magnetic structure is expected, this sample was not characterised using neutron diffraction measurements. In contrast, $x = 0.2$ and $x = 0.3$ specific heat measurements displayed a distinctive feature, a *"kink"* instead of a ordering peak, whose nature was not clear.

Neutron diffraction measurements on $x = 0.2$ show a small peak, nearly indistinguishable from the background, in the magnetic position (010)+(100). This peak appears at temperatures below $T = 540$ mK, approximately the

same temperature of the kink in specific-heat measurement. Besides its extremely small intensity, its width suggests that Nd cooperative order still exist in $NdFe_{0.2}Ga_{0.8}O_3$. The small size of the associated magnetic diffraction peak could be explained by the fact that, for x=0.2, already most of Nd sites have Fe neighbours. These neighbours have been shown to generate a high H_{Fe-Nd} field when the antiferromagnetic component of Fe magnetic moment is not compensated, which inhibits Nd-Nd ordering. Indeed, the percentage of Nd ions with no Fe neighbours or surrounded by nearly compensated antiferromagnetic moments is found to be close to percolation –∼0.33–. Besides the small percentage of Nd ions contributing to the cooperative order, the random H_{Fe-Nd} on the collectively ordered Nd ions, although small, will perturb Nd magnetic moments reducing even more the contribution of percolated Nd ions to the c_z mode, what would explain the intensity of the observed neutron diffraction peak.

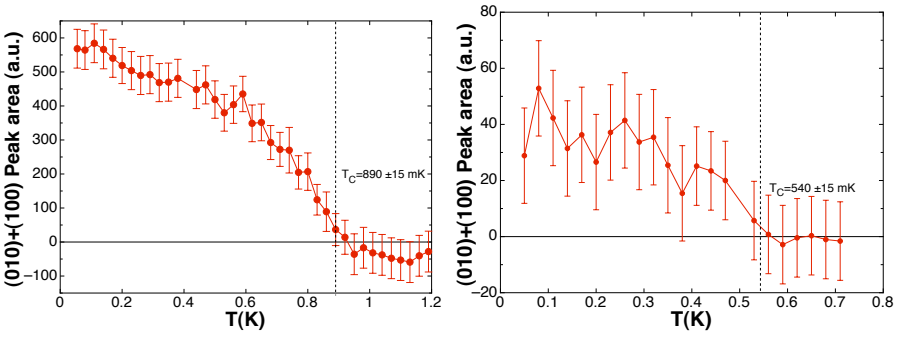

(a) (b)

Figure 6.5: (a) Estimated area of the (010)+(100) peak of $NdFe_{0.05}Ga_{0.95}O_3$ at different temperatures. (b) Estimated area of the (010)+(100) peak of $NdFe_{0.2}Ga_{0.8}O_3$ at different temperatures.

In Fig. 6.5 the integrated area thermal evolution of the most intense magnetic reflection on $NdFe_{0.05}Ga_{0.95}O_3$ –(010)+(100)– is compared with the integrated area of the (010)+(100) magnetic peak on $NdFe_{0.2}Ga_{0.8}O_3$. Due to the extremely low intensity of this peak, measurements on x = 0.2 sample were taken during 55 minutes, instead of 20 minutes, as can be observed in Fig. 6.4 by looking at the background level. To obtain Fig. 6.5b, $NdFe_{0.2}Ga_{0.8}O_3$ neutron diffraction data were normalised to the intensity of $NdFe_{0.05}Ga_{0.95}O_3$ neutron diffraction data. As displayed in Fig. 6.5, the estimated intensity of the main magnetic peak in $NdFe_{0.2}Ga_{0.8}O_3$ is ten times smaller than in $NdFe_{0.05}Ga_{0.95}O_3$. The low intensity of the magnetic peak and thus, its high relative error on the area estimation, prevent any further analysis, like the estimation of Nd magnetic moment or possible Nd nuclear moment polarisation. Nevertheless, this graph confirms that, despite being highly depressed by Fe

ions, Nd cooperative order in $NdFe_{0.2}Ga_{0.8}O_3$, takes place below $T = 540$ mK.

Regarding $x = 0.3$, although the same type of feature than in the $x = 0.2$ sample, appears in specific-heat measurements, no trace of magnetic order can be found in our neutron diffraction patterns. In this case, the acquisition time and, therefore, the statistics are 10 times lower, due to a much smaller sample mass and a reduced counting time. Nevertheless, the fact that the percentage of Nd affected by a H_{Fe-Nd} field low enough to allow cooperative order is found to be below percolation for $NdFe_{0.3}Ga_{0.7}O_3$, suggests that no long range order takes place in the sample. Non-percolative clusters of cooperatively ordered Nd are expected in this samples. This type of *short range* order could be the origin of the *"kink"* in $x = 0.3$ specific heat measurements.

6.3 Susceptibility measurements

On the previous section Nd magnetic structure modification by the dilution of Fe^{3+} ions on the Ga sublattice in $NdGaO_3$ was studied. Results allow us to determine the nature of all features related with Nd cooperative ordering observed by specific heat measurements for $x \leqslant 0.3$. However, no information on a possible spin-glass like behaviour for $0.1 \leqslant x \leqslant 0.5$ was obtained from neutron diffraction measurements. To elucidate the presence of such a state, evidenced by the low temperature part of the specific heat measurements of these samples, ac susceptibility measurements were performed on samples x =0.05, 0.1, 0.2 and 0.3. As shown in the previous chapter, ac susceptibility is one of the most powerful techniques to analyse spin glass systems, due to its characteristic response to frequency variations of the exciting field on ac susceptibility measurements.

Since no evidence of *"spin-glass-like"* behaviour on $x = 0.05$ was found in specific heat measurements, ac susceptibility measurements were acquired at a single frequency. In this case, the objective was to provide an example of a Nd ordering peak, to serve as reference for the analysis of the signals acquired for the other samples. As shown in Fig. 6.6, the real part of the ac susceptibility in $NdFe_{0.05}Ga_{0.95}O_3$ displays a sharp lambda peak at T_N=0.92 K –Nd ordering temperature–; while no signal is obtained in the imaginary part.

In Fig. 6.7, ac susceptibility measurements of samples x =0.1, 0.2 and 0.3 at different frequencies are displayed. Plotted data are obtained by combining measurements from the PPMS system and the dilution fridge as described in Chapter 4. In all the samples, the main contribution above 2 K is the Nd paramagnetic one. Below that temperature, different contributions are found. In the $NdFe_{0.1}Ga_{0.9}O_3$ case, the Nd magnetic ordering peak can be observed

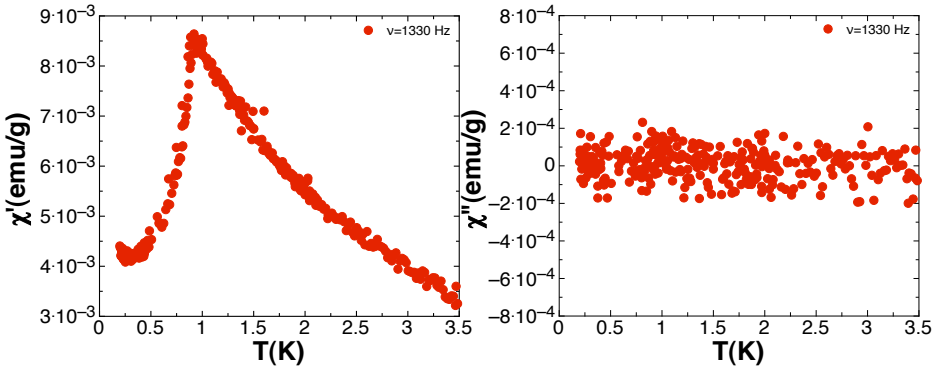

Figure 6.6: χ' and χ" as a function of temperature of $NdFe_{0.05}Ga_{0.95}O_3$ at $\nu = 1330$ Hz.

at $T \sim 950$ mK, a temperature slightly higher than the value obtained from calorimetric measurements, $T_N = 740$ mK. As in this case, the ordering peak on $x = 0.1$ is strongly rounded and lower than the one found for $x = 0.05$. Moreover, at very low temperatures χ' values tend to saturate into a plateau whose value decreases as frequency increases.

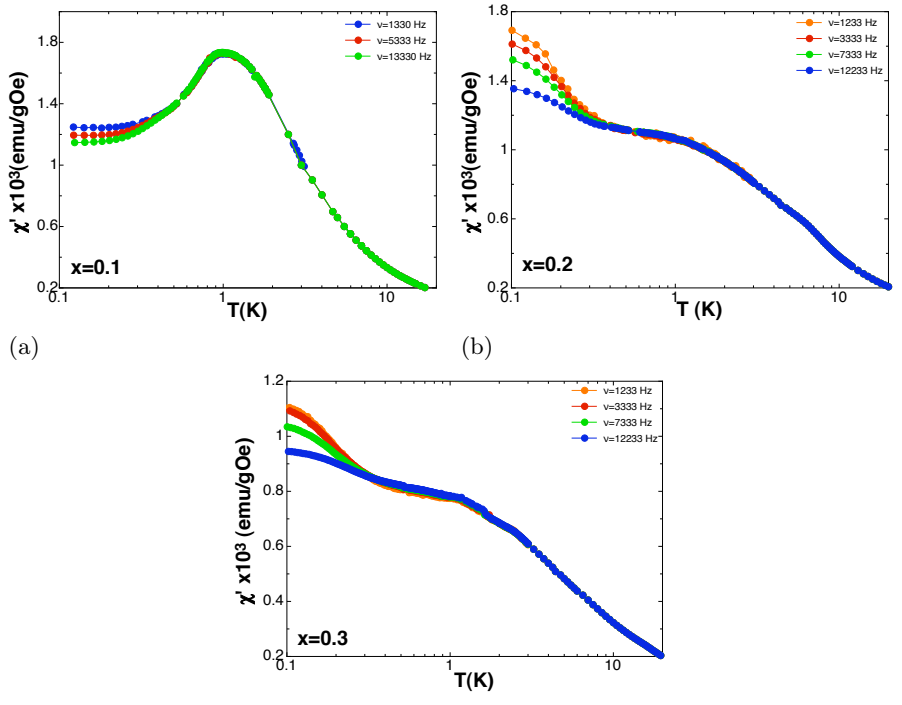

Figure 6.7: ac magnetic susceptibility as a function of temperature at different excitation frequencies of (a) $NdFe_{0.1}Ga_{0.9}O_3$. (b) $NdFe_{0.2}Ga_{0.8}O_3$. (c) $NdFe_{0.3}Ga_{0.7}O_3$.

This very low temperature frequency dependence is also found in the $x = 0.2$ case –Fig. 6.7b–. Although, as in the specific heat measurements, no distinct Nd ordering peak can be found in the $NdFe_{0.2}Ga_{0.8}O_3$ susceptibility data. Between 400 mK and 1K, χ' changes from the Nd paramagnetic contribution to a rounded plateau. Both specific heat and neutron diffraction measurements showed a weak long-range order of the Nd sublattice in this temperature range. The small susceptibility signal of this feature, combined with the high temperature tale of the frequency dependent bump observed on Fig. 6.7b could explain this plateau. The origin of the *"glassy"* bump will be discussed later.

The same features as in $x = 0.2$ are found in $NdFe_{0.3}Ga_{0.7}O_3$ susceptibility measurements, although in this case, between 400 mK and 1K, a change in χ' slope, more than a plateau is observed at lower χ' values. This difference might be ascribed to the expected reduction of the short-range order contribution, as found in specific heat and neutron diffraction measurements. For $x = 0.3$, an extra contribution overlapped to the slope change is found between 0.5 and 1.5 K. This contribution generates a *shoulder* that, as the frequency increases, shifts toward higher temperatures. Similar features were obtained in this sample and in $x = 0.2$ at higher temperatures, as shown in Fig. 5.3. In those cases, this contribution was isolated by subtracting the highest frequency measurement to the other susceptibility curves and its T_f *vs.* τ relation studied with different models. These analysis led us to suggest that the maxima in the *ac* susceptibility curves might have their origin in a cluster freezing process. As iron concentration for these compounds is below, but close to percolation, we proposed that this cluster-glass-like behaviour was due to the presence of clustered regions with slightly higher-than-nominal iron content. These clusters, with a net magnetic moment, will behave as interacting particles which became frozen below a certain temperature mainly given by their size. In the present case, such analysis was not possible because of the width of the observed shoulder and the noise intrinsically associated with its low χ' signal. However, the similarity of the bumps observed in Fig. 5.3 and in Fig. 6.7c, and its freezing temperature $T_f \sim 1$ K –well above the Nd long range order for $x = 0.2$–, leads us to consider that the shoulder observed in Fig. 6.7c between 0.5 and 1.5 K is originated by Fe clusters of smaller size than the ones detected in Fig. 5.3.

In Fig. 6.8 χ' and χ" values of $x = 0.1$, $x = 0.2$ and $x = 0.3$ samples obtained in the dilution refrigerator at different excitation frequencies are represented. The appearance of an imaginary component of the ac susceptibility means that relaxation processes are taking place in the sample and, by decoupling the spins from the lattice, causing absorption [45]. Thus, for spin glasses, there is a sudden onset of the imaginary component near T_f. These

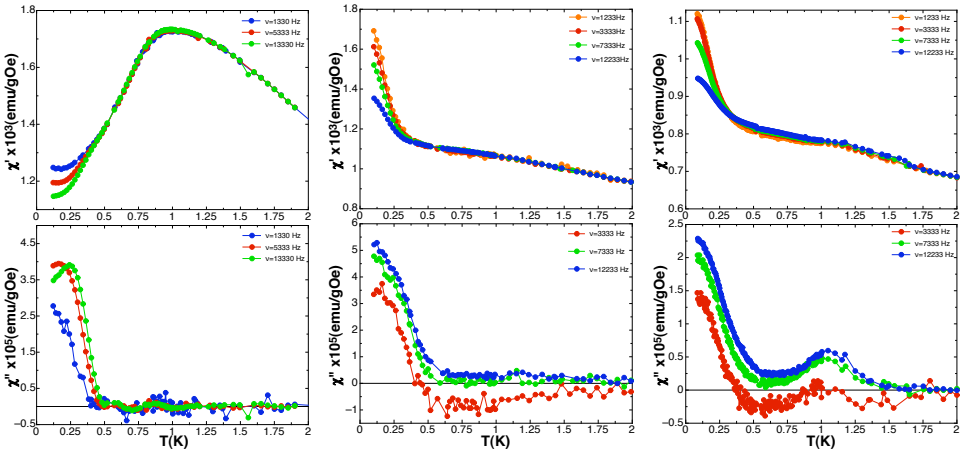

(a) (b) (c)

Figure 6.8: χ' and χ" as a function of temperature at different excitation frequencies of (a) $NdFe_{0.1}Ga_{0.9}O_3$. (b) $NdFe_{0.2}Ga_{0.8}O_3$. (c) $NdFe_{0.3}Ga_{0.7}O_3$.

effects are not found in magnetic transitions, except when hysteresis appears. As can be seen in Fig. 6.8c, $x = 0.3$ χ" measurement displays a rounded peak around T_f=1 K, indicating, as already suggested, the freezing of Fe clusters of smaller size than the ones detected on Chapter 5. Again, not enough data are available to further characterise this *"glassy"* state. No trace of similar features are found for $x = 0.1$ and $x = 0.2$, what could be explained by the lower Fe concentration in those cases.

At lower temperatures –$T < 500$ mK– a peak whose intensity is reduced as the frequency increases can be observed both in χ' and χ" data for the three studied samples, although its maximum is only visible in $x = 0.1$. χ" measurements in Fig. 6.8a show that this maximum shifts toward higher temperatures with frequency, this behaviour being, as in the χ' case, indicative of a spin-glass-like state. As already mentioned, T_f decreases as the iron concentration increases. Since the presence of more Fe ions enlarges the average cluster size and, consequently, the associated freezing temperature, Fe clusters can be discarded as the cause of the low temperature peaks. Seeing that the maximum of the low temperature peak of Fig. 6.8 is below the experimental temperature range, no analysis on the nature of this susceptibility feature can be performed with our data. However a speculative discussion on its possible origin can be conducted.

Ac susceptibility measurements on $x = 0.2$ and 0.3 at $T > 1.8$ K, together with magnetisation and neutron diffraction measurements on $x = 0.4$, pointed at the formation of interacting magnetic clusters on the Fe sublattice. In these cluster regions, Fe concentration would be slightly higher than the nominal

value, ensuring Fe magnetic order and producing a net magnetic moment inside the cluster. These magnetic moments would polarise Nd^{3+} ions inside the cluster, preventing their cooperative ordering. For small iron concentration, such as $x = 0.1$, these Fe clusters would be scarce and small, what would limit the number of polarised Nd ions. Therefore, although not all Nd ions take part in the Nd-Nd order, as shown by the reduction of both T_N and the order peak intensity in specific heat and susceptibility measurements, the concentration of non-polarised Nd ions is high enough to allow Nd cooperative magnetic order. Then, a possible origin for the observed *glassy* behaviour might be the presence of regions with polarised Nd ions that could lead to the isolation of some sample areas where Nd^{3+} ions are ordered. These areas could be considered to behave as Nd clusters with net magnetic moment that, similarly to the Fe case, would become frozen below a certain temperature given by their size. As Fe concentration increases, more Nd ions become polarised, what would reduce the size of the Nd ordered clusters and would increase the distance among them, thus explaining the reduction of T_f as x become larger, observed in Fig. 6.8.

6.4 Conclusions

In this chapter the different order processes involving Nd^{3+} ions in $NdFe_xGa_{(1-x)}O_3$ compounds with $x < x_c$ have been studied by means of neutron diffraction and ac susceptibility measurements.

As displayed by neutron diffraction experimental data from $NdFe_{0.05}Ga_{0.95}O_3$ sample, the dilution of Fe^{3+} ions does not modify the Nd ordering configuration, c_z. Since in this case iron concentration is well below percolation, no magnetic order in the Fe sublattice does appear. Thus, although specific heat measurements showed Nd polarisation by the H_{Fe-Nd}, the random distribution of exchange fields on Nd sites prevents any collective contribution to the neutron diffraction pattern. Although measurements have not enough statistics to estimate the polarisation of the ^{143}Nd and ^{145}Nd nuclear spins in the hyperfine field of the Nd electronic moments, the effect can be qualitatively observed in the thermal evolution of the neutron diffraction pattern. This fact, together with the good agreement between T_N values from specific heat and neutron diffraction data, ensures a good thermalisation of the samples in the neutron diffraction experiments.

Neutron diffraction measurements showed that, for x =0.2, the number of Nd ions affected by a nearly zero H_{Fe-Nd} internal field is just above the percolation limit, while for $x \geqslant 0.3$, the introduction of magnetic ions on the Ga sublattice does not destroy Nd order completely. Indications of short-range

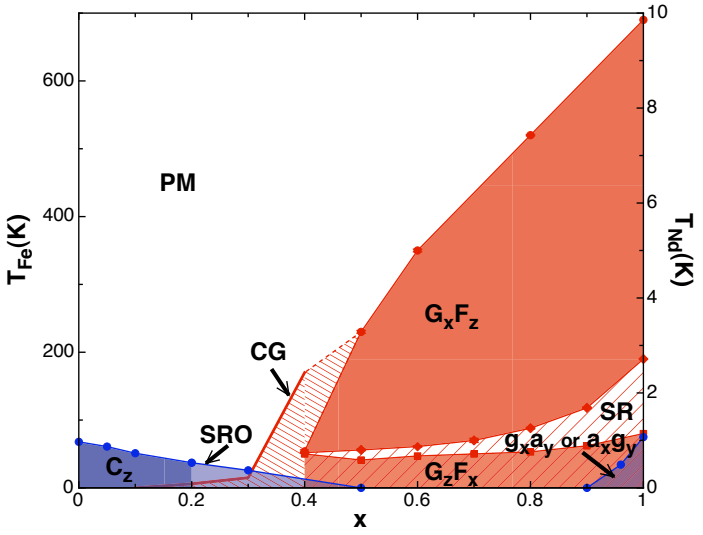

Figure 6.9: Phase diagram of $NdFe_xGa_{1-x}O_3$ series. Red areas correspond to the different ordering phases in the Fe sublattice, while the blue ones correspond to the different ordering phases in the Nd sublattice. The different represented regions are the paramagnetic phase (PM), the Fe sublattice high temperature configuration (G_xF_z), the Fe spin reorientation region (SR), the Fe sublattice low temperature configuration (G_zF_x), the Fe cluster-spin-glass phase (CG), the Nd sublattice c_z configuration, the Nd short range ordering region (SRO) and the Nd sublattice g_xa_y or g_xa_y configuration. Data of x=1 are taken from [11], and data of $x-0$ from [10]

order in $NdFe_{0.3}Ga_{0.7}O_3$ are found at very low temperatures, both in specific heat and ac susceptibility measurements.

Although ac susceptibility measurements corroborate the presence of some kind of Nd-Nd cooperative order in $x = 0.2$ end 0.3, they do not provide an estimation of T_N due to the overlapping of this contribution and a *"glassy"* state inside the Nd sublattice. Due to its higher iron content, close to percolation, evidences of a cluster-glass state into the Fe sublattice, similar to the ones discussed in Chapter 5 but of smaller size, are found in $x = 0.3$. No traces of iron clusters are found in $x = 0.1$ and 0.2 in the temperature range of study 80 mK$\lesssim T \lesssim$2 K, since one would expect them to be smaller and located far away from each other. The polarisation of Nd ions inside these Fe clusters is likely to prevent their cooperative ordering, what might generate clusters of magnetically order Nd. The size of these clusters would be bigger for small Fe concentration, just as the intensity of the interaction among them. A cluster-glass system as this one, where a clustered Fe sublattice is interspersed on the Nd one, could explain both the specific heat and ac susceptibility features that pointed to a *"spin-glass-like"* behaviour.

The results obtained in this chapter allow us to complete the phase diagram of the $NdFe_xGa_{(1-x)}O_3$ series. The main results from Chapters 3, 5 and 6 can be summarised in Fig. 6.9, where the ordering phases of both Nd and Fe sublattices in the whole temperature range are displayed using different colours and on different y axes. The Nd clusterisation induced at very low temperatures by the Fe sublattice for $x < 0.5$ is not shown as a separate region of the phase diagram because of its rather speculative nature and the impossibility to determine T_f from our data for $x > 0.1$. However, due to its origin, it can be considered to be more or less superimposed to the Nd short-range order phase.

Chapter 7

Negative magnetisation on the $NdFe_xGa_{(1-x)}O_3$ series

7.1 Introduction

As already mentioned, complex oxides of transition metals with perovskite structure have been extensively studied due to the combination of the wide range of physical properties displayed –from high temperature superconductivity to ferroelectricity– and their relatively simple structure. Among this unique properties, several groups have reported negative magnetisation when cooling these samples in an external magnetic field (FC). This anomalous magnetisation has been observed in vanadites [87, 88], cromites [89–91] or manganites [57, 92, 93], among others. Indeed, this type of reversed magnetisation (opposed to the applied magnetic field) after a field-cooling process was first described in some spinel ferrites [94], and then found in other complex ferrimagnetic systems such as molecular magnets [95], “fanned" amorphous alloys [96] or irradiated garnets [97].

All the systems enumerated above have in common a complex ferri- or antiferromagnetic order with at least two magnetic sublattice and some degree of chemical or structural disorder. In most of the cases, the behaviour of the FC curves is the following: for high enough magnetic fields, no difference between FC and zero field cool (ZFC) measurements is found; below a critical field value, however, a negative magnetisation appears at some point below the ordering temperature, T_N, in the FC curve, instead of a compensation point. Thus, at least two ingredients are needed for negative magnetisation to appear: competition between two antiferromagnetically coupled systems and an energy barrier high enough to avoid the magnetisation components to

change direction and follow the external field. Thus, several mechanisms can cause negative magnetisation to arise, such as a structural phase transition [98], a negative coupling between sublattices of $3d$ and $4f$ ions [89, 90] or a phase separation process [22]

Although no reversed magnetisation can be observed in the pure compounds $NdFeO_3$ and $NdGaO_3$, the random dilution performed in the transition metal sublattice in $NdFe_xGa_{(1-x)}O_3$ introduces a chemical disorder. This, combined with the antiferromagnetically coupling of the Nd and the Fe sublattice that generates a compensation point at low temperatures, might give rise to such phenomenology.

The main objective of this chapter is to determine whether a negative magnetisation contribution can be found for some x and, if so, to establish its origin in this case. In Section 7.2, ZFC-FC measurements of the $NdFe_xGa_{(1-x)}O_3$ for $0.4 \leqslant x \leqslant 1$ will be displayed and analysed. In Section 7.3, the possible freezing of magnetic moments and glassy phenomena needed for negative magnetisation will be studied by means of *ac* susceptibility. Detailed measurements on $NdFe_xGa_{(1-x)}O_3$ will be examined by different thermal relaxation models to gain insight on the nature of the observed thermal relaxation process. In Section 7.4 the results obtained so far will be summarised and discussed in order to confront them to the XMCD experimental results offered in Section 7.5. Finally, the main conclusions of the study will be presented in Section 7.6.

7.2 Magnetisation measurements

Magnetisation after a field cooling process (FC) in $NdFe_xGa_{(1-x)}O_3$ compounds with iron concentration above percolation ($x \geqslant 0.4$) was measured. These data are shown in Fig. 7.1 together with the zero field cool (ZFC) measurements discussed in Chapter 5. As can be observed, no significant difference between the ZFC and the FC data is found above the Fe spin reorientation temperature. However, after this process, both signals start to diverge.

In ZFC data, below T_{SR}, magnetisation rapidly reduces to a nearly zero value, because of the increase of the paramagnetic moment of the Nd^{3+} spin system. As already discussed on previous chapters, Nd ions are polarised by the Fe sublattice antiparallel to the Fe^{3+} weak magnetic moment. At low temperatures a compensation point occurs when both contributions to the total moment are equal [11].

That is not the case for the FC measurement, where below T_{SR} magnetisation shows no compensation point, but a continuous decrease, becoming even negative for $0.5 \leqslant x \leqslant 0.9$ at temperatures lower than 20K.

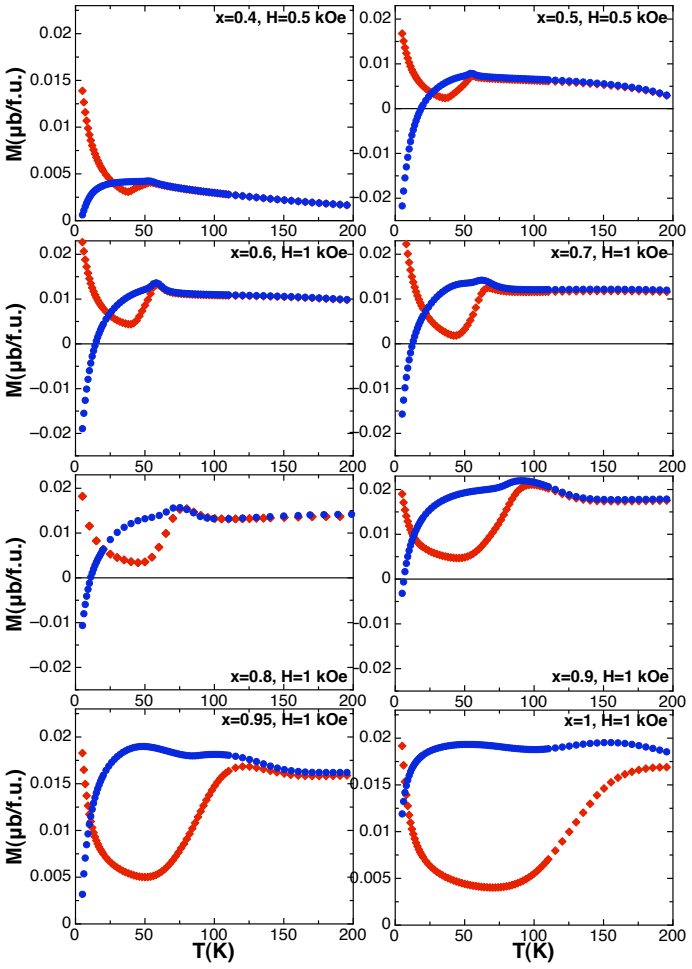

Figure 7.1: Magnetisation measurements of $NdFe_xGa_{(1-x)}O_3$ compounds with $0.4 \leqslant x \leqslant 1$ as a function of temperature. (♦) correspond to Zero Field Cooled Magnetisation measurements, while (•) are data from Field Cooled Magnetisation measurements.

Fig. 7.2 shows the magnetisation value at low temperature (T=5K) and the temperature at which magnetisation value becomes zero in the $NdFe_xGa_{(1-x)}O_3$ family as a function of x, to allow a more detailed discussion on how the negative magnetisation depends on the Fe concentration. As already pointed out, no negative magnetisation can be observed for $x = 0.4$ in the whole temperature range of study. For $x > 0.4$ the magnetisation value at $T = 5$ K increases with x, reaching a final value of M=0.012 $\mu_B/f.u.$ for $x = 1$. Due to this increase, for $x \geqslant 0.95$ magnetisation is no longer negative in any point of the measurement range. Therefore, negative magnetisation seems to be related with disorder in the Fe sublattice: the higher the Ga concentration, the lower the magnetisation value at low temperatures. Although $x = 0.4$ suddenly

breaks the trend. The same conclusion can be drawn from the plot of the crossing temperature as a function of x –also in Fig. 7.2–. As x increases, the temperature at which $M = 0$ decreases too. Thus, for small Fe concentration values, the temperature region where magnetization is negative is wider.

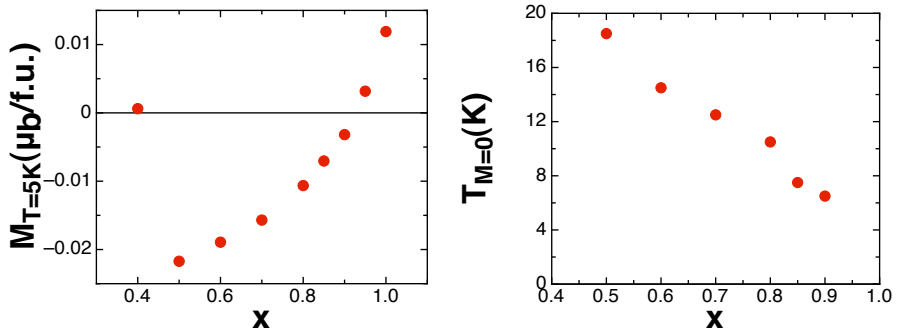

(a) (b)

Figure 7.2: (a) Magnetisation at very low temperature (T=5 K) as a function of iron concentration (x). (b) Crossing Temperature at M=0 as a function of iron concentration.

The origin of the observed magnetisation reversal cannot be elucidated by means of magnetisation measurements only. The same holds for the reason why, if this behaviour is related to the introduction of magnetic vacancies on the Fe sublattice, no trace of this negative magnetisation is displayed in $x = 0.4$, where the magnetic disorder is expected to be maximum. However, further analysis on magnetisation measurements can be performed by comparing FC–ZFC curves acquired with different applied magnetic fields.

In Fig. 7.3 $NdFe_{0.8}Ga_{0.2}O_3$ FC–ZFC curves with $H = 30$, 100 and 3000 Oe are depicted. Since, as shown in Chapter 5, this compound displays a Fe sublattice ordering transition at $T_N \sim 500$ K, to ensure a truly Zero Field Cool process, $NdFe_{0.8}Ga_{0.2}O_3$ powder sample was separated in different batches that were heated in a muffle furnace at temperatures above T_N. Each of these batches was used once for magnetisation measurements under a different value of the applied magnetic field.

For $H = 30$ and 100 Oe, the shape of the magnetisation curves is similar to the one observed with $H = 1000$ Oe and displayed in Fig. 7.1. The increase of the applied magnetic field does not reduce, as one might expect, the magnitude of the negative magnetisation component. On the contrary, all the magnetisation components increase with the external field, including the negative one.

As can be observed on the inset of Fig. 7.3, at low temperatures the ZFC

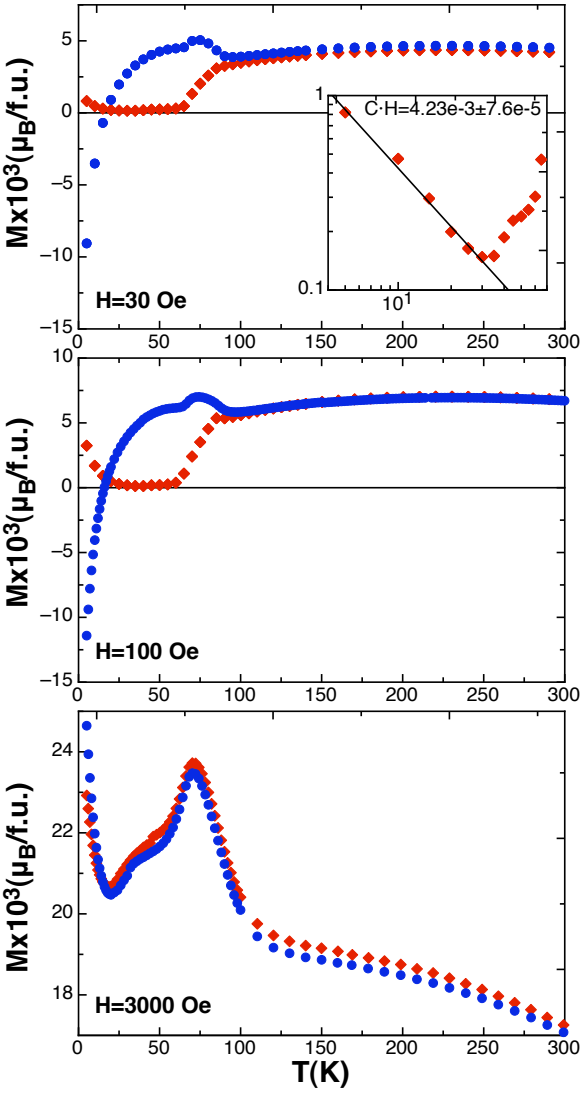

Figure 7.3: Magnetisation measurements of $NdFe_{0.8}Ga_{0.2}O_3$ as a function of temperature for different applied magnetic fields. (♦) correspond to Zero Field Cool Magnetisation measurements, while (•) are data from Field Cool Magnetisation measurements. Inset displays the power fit to the magnetisation signal from the Nd paramagnetic low temperature phase.

magnetisation signal displays a dependence T^{-1}, as corresponds to a paramagnet under such a low value of the applied field. In this range of temperature the weak ferromagnetic component of the Fe sublattice is negligible when compared to the polarised Nd magnetic moment, responsible of the paramagnetic signal. For very low applied magnetic fields- as in the case of H=30 Oe- the magnetisation of a paramagnet follows Curie's law [3]. Being only valid well

below saturation, as in our case, when increasing the applied magnetic field translates into an increment of the total magnetisation:

$$M = C \cdot \frac{H}{T} \tag{7.1}$$

where

$$C = \frac{N_A}{3k_B}\mu_{eff}^2 \tag{7.2}$$

and μ_{eff} is the effective magnetic moment per paramagnetic ion. Assuming that Nd electronic magnetic moments are polarised by the weakly ferromagnetic component of the Fe sublattice, and that this component is approximately constant in the $NdFe_xGa_{(1-x)}O_3$ compounds, as long as $x > 0.5$, –see Table 5.1–, Nd polarised magnetic moment in $NdFe_{0.8}Ga_{0.2}O_3$ can be considered as equal to that of $NdFeO_3$, $\mu_{Nd} = 0.9\ \mu_B$ [16]. Considering this value and the results of fitting ZFC magnetisation measurements at H=30 Oe to Eq. 7.1 one obtains that the magnetic field acting on Nd ions is $H \sim 1800$ Oe, considerably higher than the applied field. Thus, although no Nd polarisation peak was observed in the neutron diffraction measurements performed in this compound –see Chapter 5–, Nd ions are polarised by an internal field H_{Fe-Nd}, in agreement with calorimetric measurements.

Finally, when a higher magnetic field is applied –$H = 3$ kOe– the negative component of the FC magnetisation is overcomed, and both FC and ZFC magnetisation measurements are equivalent. This last measurement gives us an idea of the magnitude of the interaction inside the sample that produces the negative magnetisation of these compounds.

7.3 Susceptibility measurements

7.3.1 Description of $NdFe_xGa_{(1-x)}O_3$ χ_{AC} measurements

With the aim of elucidating the origin of the anomalous magnetisation found in the $NdFe_xGa_{(1-x)}O_3$ family of compounds, *ac* susceptibility measurements at three different frequencies were performed in all the compounds with $x > x_c$. Since similar results were obtained in all cases, data from only three of these samples are depicted in Fig. 7.4 –$x = 0.6$, 0.8 and 0.9–. As can be observed, besides the reorientation peak –which, as expected, is not affected by frequency–, only a small frequency dependent bump is present. This feature, although more clearly noticeable for x=0.8, is found in all the samples at the

same temperature range ($100K \leqslant T \leqslant 160K$). Indeed, for x=0.9 it appears nearly superimposed to the Fe spin reorientation peak. From magnetisation measurements the negative values obtained seem to be related to the spin reorientation process, the onset of the divergence between the ZFC and the FC curves, and the Fe concentration. However, the temperature of the feature observed in *ac* susceptibility is constant for all the samples independently of both the T_{SR} and the Fe concentration. The small signal of the frequency dependent bump, compared to the spin reorientation transition, might indicate that not all the magnetic moments in the sample are involved in the corresponding process.

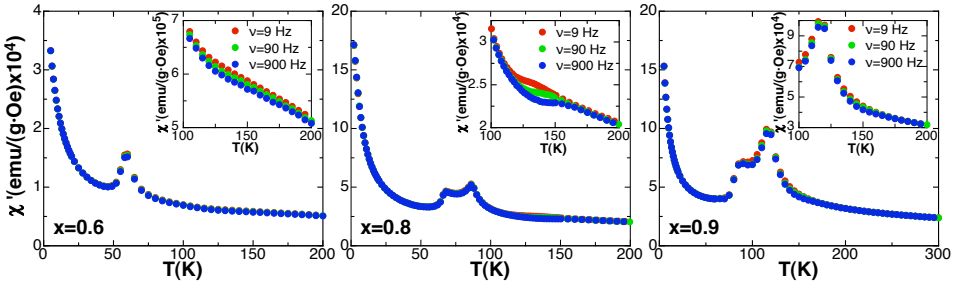

Figure 7.4: Real part of $NdFe_xGa_{(1-x)}O_3$ compounds susceptibility measurements with x =0.6. 0.8, 0.9 as a function of temperature for different frequencies.

This feature and its frequency dependence is more clearly revealed by looking at the imaginary part of the χ_{AC} measurements displayed in Fig. 7.5, especially for $x = 0.8$ and 0.9. In these plots a peak in the temperature range between 100 K and 160 K comes clearly into sight. As the frequency increases, it shifts toward higher temperatures and its intensity is reduced, as expected from a freezing process [45]. A similar dependence was found in the peak observed in samples with $x < x_c$, as described in Chapter 5, although in the present case the imaginary signal is considerably higher.

The formation of a cluster-glass segregated phase –as our susceptibility measurements may suggest for $x > x_c$ samples– is known to originate negative magnetisation in manganites [19]. Thus, if the reversed magnetisation observed in our samples is related with the freezing process revealed by χ_{AC} measurements, the fact that the blocking process takes place above the ordering temperature of the Fe sublattice in $x = 0.4$ would explain why no negative magnetisation is observed in this sample. As already discussed, experimental results on this sample suggest the presence of different minority phases with an iron content slightly different from that of the nominal value which undergo a continuous appearance of magnetic order. Therefore only the minority phases with a T_N higher than 160 K would be expected to display negative magnetisation, since a paramagnetic phase can not be affected by the freezing process.

The contribution of these minority phases would not be enough to generate a net negative signal for the whole sample.

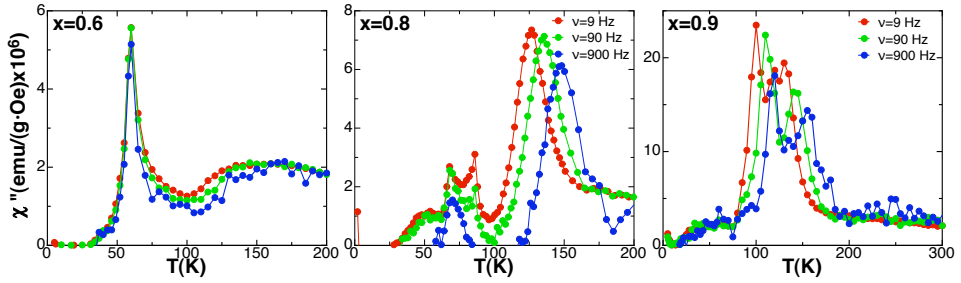

Figure 7.5: Imaginary part of $NdFe_xGa_{(1-x)}O_3$ compounds susceptibility measurements with x =0.6. 0.8, 0.9 as a function of temperature for different frequencies.

In the low Fe concentration samples analysis, we showed that information about the intensity and relaxation time of the blocking process and, therefore, its origin, can be extracted from the relation between the exciting frequency and the freezing temperature. However, in the $NdFe_{0.9}Ga_{0.1}O_3$ sample the maximum of the χ" is masked by the superposition of this feature to the Fe spin reorientation transition. Therefore, $NdFe_{0.8}Ga_{0.2}O_3$ sample appears as the best choice to perform additional susceptibility measurements designed to provide extra information on the blocking process observed in the $NdFe_xGa_{(1-x)}O_3$ series for $x > x_c$.

7.3.2 Detailed study of $NdFe_{0.8}Ga_{0.2}O_3$ *ac* susceptibility measurements: Experimental results

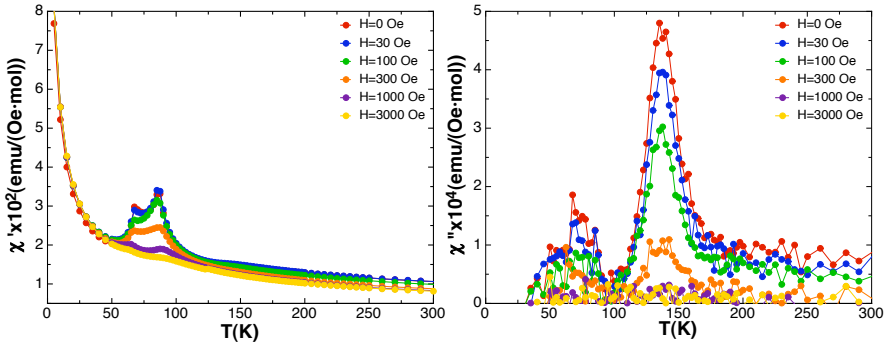

Figure 7.6: $NdFe_{0.8}Ga_{0.2}O_3$ susceptibility measurements as a function of temperature at ω=90 Hz for different applied magnetic fields.

As in the case of magnetisation measurements, *ac* susceptibility measurements in $NdFe_{0.8}Ga_{0.2}O_3$ sample are repeated under different applied fields.

In all the cases the sample was heated in a muffle furnace till $T > T_N$ before every measurement to eliminate any trace of the previously applied magnetic field. Results are displayed in Fig. 7.6. It can be observed that for $H < 300$ Oe no significant change on the reorientation peak intensity can be observed, while the intensity of the frequency dependent peak is reduced by nearly a factor of 2. For $H = 300$ Oe the reorientation contribution is reduced to half its original value, while the freezing peak nearly disappears. For higher magnetic fields, the spin reorientation process is still noticeable while the other one is completely destroyed. The extreme sensitivity of the *"extra"* peak even to small external magnetic fields has been related to a *"spin-glass-like"* state [45].

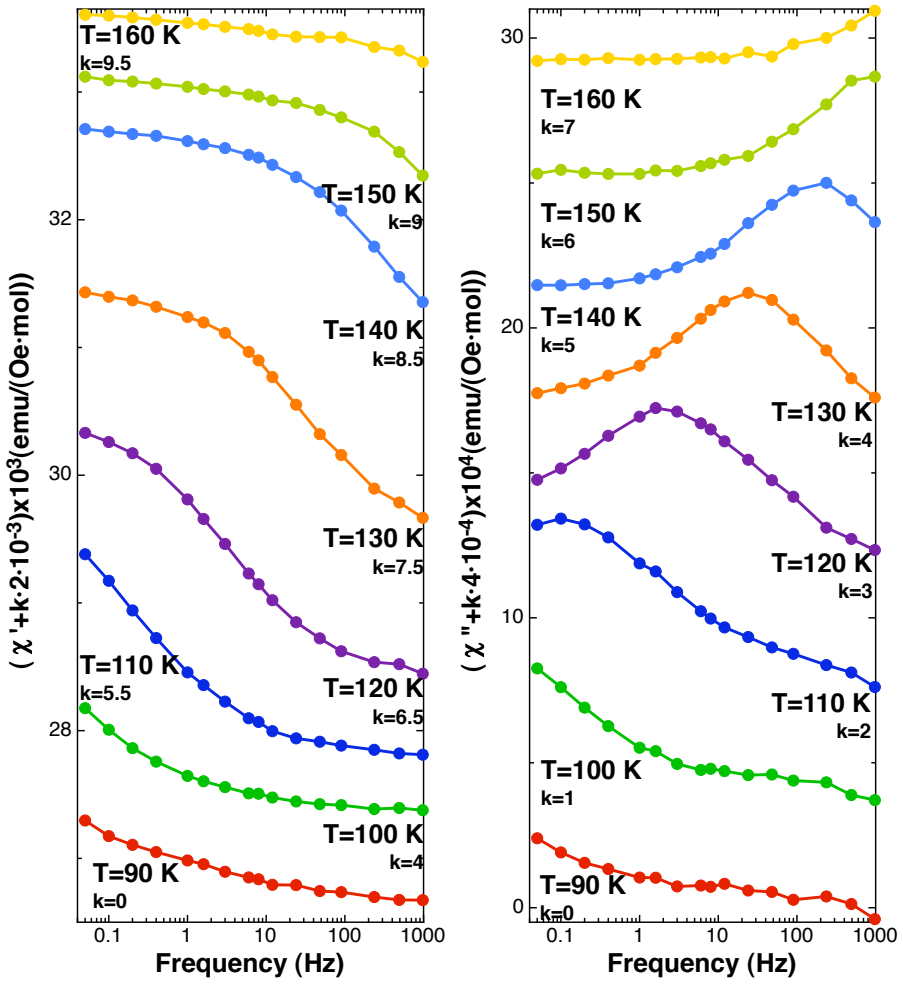

Figure 7.7: (a) Real part of $NdFe_{0.8}Ga_{0.2}O_3$ $\chi_A C$ at different temperatures. (b) Imaginary part of $NdFe_{0.8}Ga_{0.2}O_3$ $\chi_A C$ at different temperatures.

To study in an accurate way the dynamic response of the freezing process observed in the $NdFe_xGa_{(1-x)}O_3$ series, its dependence with the exciting frequency is analysed. *ac* susceptibility measurements are performed at $H = 0$, temperatures between 80 and 200 K and frequencies between 0.05 and 1000 Hz.

In the chosen temperature range (80K$<T<$200 K), the susceptibility signal beside the freezing process contribution can be considered as approximately constant, since the Fe sublattice order is saturated ($T \ll T_N$) and the spin reorientation starts at lower temperatures. Thus, when temperature is fixed and frequency is swept, only the blocking process that we want to observe varies its contribution from one measured temperature to another. In this way the *"glassy"* behaviour can be more easely identified than by fixing the frequency and changing the temperature.

In Fig. 7.8 the thermal evolution of the real (Fig. 7.7a) and imaginary (Fig. 7.7b) parts of the susceptibility as a function of frequency is displayed. χ' measurements show an intensity decreasing with frequency and a shoulder that swifts toward higher frequencies as the temperature increases. While in χ" a non symmetric peak is observed and, as in the χ' case, the frequency at its maximum increases with temperature.

Magnetic susceptibility is defined as the rate of change of magnetisation of a material in response to an applied magnetic field. Since magnetisation follows the direction of the magnetic field, when magnetic field direction is changed with a certain frequency, as in χ_{AC} measurements, the magnetisation is forced to change its direction too. Typically in *"glassy"* states, above a certain frequency the system is not able to overcome the associated energy barrier Q and it can no longer follow the magnetic field, what produces a delay between the magnetisation and the applied field. This effect is observed in Fig. 7.8, where for lower temperatures, the impossibility to follow the field appears at lower frequencies since the system has less available thermal energy. The characteristic time for the magnetisation to change its direction is the relaxation time, τ, and it depends on the energy barrier, Q, and, therefore on the system. Thus, the determination of this characteristic time provides information about the system and its dynamic properties. In the next subsection different susceptibility models are described, while in Section 7.3.4 *ac* susceptibility data discussed above are analyse in the framework of these models in order to extract information on the possible origin of the observed freezing process.

7.3.3 Magnetic relaxation models

Debye model

The frequency dependence of the complex dielectric constant was represented by P. Debye [99] by means of an empirical model that considers that the orientation of polar molecules in an alternating-current field was opposed by the effects of thermal disorder and molecular interaction. This last effect was represented as spherical molecules inside a viscous medium, what provides a viscous damping. This model has been successfully applied to other types of dispersion phenomena. Indeed, since the imaginary part of the permitivity is related to the dissipation or adsorption of energy within the medium and the real part is related to the stored energy, an analogy with the susceptibility is straightforward. Therefore, the same expression can be applied to the paramagnetic dispersion by changing only the significance of the involved parameters [100, 101].

In this way, the complex magnetic susceptibility of a system of independent spins under an applied magnetic field can be expressed as:

$$\boldsymbol{\chi} = \chi_0 + \frac{\chi_{eq} - \chi_0}{1 - i\omega\tau} \tag{7.3}$$

where ω is the frequency of the applied magnetic field, τ is the relaxation time, χ_0 is the susceptibility value at infinite frequency (adiabatic susceptibility: no heat exchange between the spins and the lattice phonons takes place) and χ_{eq} is the susceptibility value at zero frequency (isothermal susceptibility: spins and lattice are at the same temperature).

From Eq. 7.3, the imaginary and real parts of the susceptibility can be expressed as:

$$\chi' = \chi_0 + \frac{\chi_{eq} - \chi_0}{1 + (\omega\tau)^2} \qquad \chi" = \omega\tau\frac{\chi_{eq} - \chi_0}{1 + (\omega\tau)^2} \tag{7.4}$$

A usual representation of χ' and χ" consists of plotting the imaginary part against the real part. In this representation, known as Cole–Cole plot, the Debye model corresponds to a perfect semicircle centered on the χ' axis at $(\chi_{eq} + \chi_0)/2$ and with a radius $(\chi_{eq} - \chi_0)/2$. When a semicircle with radius equal to the maximum value of χ" is plotted together with some isothermal *ac* susceptibility measurements –see Fig. 7.8a– it is evident that our data cannot be fitted with the Debye approximation. Besides being depressed, susceptibility curves shown in Fig. 7.8a are not symmetric, what suggests that our data do not correspond to a single relaxation time process. A more complex model will be required.

Davidson-Cole model

Among the different generalisations of the Debye model, we will focus on the Davidson-Cole model [102], that has been successfully applied to a large variety of relaxing magnetic systems such as cluster-glass in spin ice systems [103], Griffiths like-phases [104] or ferrofluids [105]. The complex *ac* susceptibility is written in this model as:

$$\boldsymbol{\chi} = \chi_0 + \frac{\chi_{eq} - \chi_0}{(1 - i\omega\tau)^\gamma} \tag{7.5}$$

The case $\gamma = 1$ yields the standard Debye law with just one relaxation frequency. For lower values of γ, the predicted susceptibility curves become more asymmetric and flattened, just as in our measurements. Other models, such as the Cole-Cole one [106], although widely applied to spin-glass systems [107–109], were discarded since they are not able to reproduce the asymmetry of our results that is more clearly shown in Fig. 7.9 for T=139 K.

In order to fit our data to this empirical model Eq. 7.5 is expanded to:

$$\begin{aligned} \chi' &= \chi_0 + Re\Big(\frac{\chi_A}{(1 - i\omega\tau)^\gamma}\Big) = \chi_0 + \frac{\chi_A r^\gamma cos(\gamma\theta)}{r^{2\gamma}(cos^2(\gamma\theta) + sin^2(\gamma\theta)))} \\ \chi" &= Im\Big(\frac{\chi_A}{(1 - i\omega\tau)^\gamma}\Big) = \frac{-\chi_A r^\gamma sin(\gamma\theta)}{r^{2\gamma}(cos^2(\gamma\theta) + sin^2(\gamma\theta)))} \end{aligned} \tag{7.6}$$

where

$$\begin{aligned} \chi_A &= \chi_{eq} - \chi_0 \\ r &= \sqrt{1 + (\omega\tau)^2} \\ \theta &= arctag(-\omega\tau) \end{aligned}$$

Due to the asymmetry of our measurements, poor results are obtained when using only one relaxation time. Therefore, two Davidson-Cole functions (Eq. 7.6) are needed to reproduce the mainly bimodal relaxation time distribution observed in our measurements (Fig. 7.9).

7.3.4 Detailed study of $NdFe_{0.8}Ga_{0.2}O_3$ susceptibility measurements: Analysis of χ_{AC} measurements

Data displayed in Fig. 7.8 are fitted using two Davidson-Cole functions as shown in Fig. 7.9. Best results are obtained when fitting the imaginary part

instead of the real part, since one parameter less is needed. Therefore, the analysis procedure consists of fitting χ" data to the two Davidson-Cole equations and use the obtained parameter to fit χ' data and get χ_0. The same γ value was used for both relaxation processes, being its value $0.07 \leqslant \gamma \leqslant 0.3$, far away from the value expected for a Debye relaxation process $\gamma = 1$.

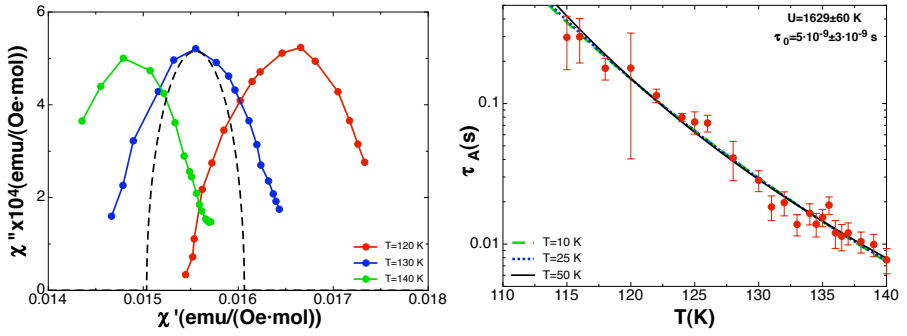

(a) (b)

Figure 7.8: (a) χ" *vs.* χ' for different temperatures. Dash line represents a circumference as expected from a Debye model. (b) Dependence of τ_A- defined in Eq.7.6- as a funtion of temperature. Dashed lines corresponds to the fitting of τ_A values to Eq. 5.2 with different T_0

.

In Fig. 7.9 the fitting results of one isothermal –T=139 K– susceptibility measurement is shown, together with the original data. The two contributions of the Davidson-Cole functions can also be found in this graph, each one with a different relaxation time – τ_A and τ_B. In all the studied temperatures at least a bimodal distribution of relaxation times is found, being τ_A the dominant one in all the studied cases.

As already discussed in Chapter 5, a thermal activation process over an anisotropy barrier E_a –as the one we are assuming here– is usually described by an Arrhenius law–Eq. 5.1–. The temperature dependence of τ obtained from a Debye model follows this law. As in the case of the cluster-glass state found in the x region close to percolation, when fitting the thermal evolution of the dominant τ_A to this equation, the obtained parameters are unphysical –$\tau_0 = 1.1 \cdot 10^{-10}$ and $E_a = 2500$ K. This result is not unexpected since the data shown in Fig. 7.8 do not follow a Debye single relaxation process.

Usually, in systems with a broad distribution of relaxation times, such as a spin-glass system, τ follows a Vogel–Fulcher law [45] –also discussed in Chapter 5–, Eq. 5.2. When fitting the three available parameters –τ_0, E_a and T_0– similar results to the ones obtained with the Arrhenius equation are found for τ_0 and E_a. Moreover, an unphysical negative value of T_0 is found. To

avoid this result the experimental data were analysed by means of the Vogel–Fulcher law with different values of T_0, always fulfilling the condition $T > T_0$ in the whole temperature range. The best agreement between the quality of the fit and the physical meaning of the results is obtained for $T_0 \sim 25K$. The parameters obtained in this case are shown in Fig. 7.8b, while the ratio $(T - T_0)/T$ is similar to 0.8 in the whole temperature range.

Unlike the results observed near percolation, no unambiguous conclusion on the nature of the $NdFe_{0.8}Ga_{0.2}O_3$ frequency dependent susceptibility peaks is achieved by means of its relaxation time analysis. Although its frequency and temperature dependence points to a *"glassy"* behaviour and its $(T-T_0)/T$ ratio suggest a cluster-glass origin [80], the characteristic relaxation process is too slow to be ascribed to a cluster-glass, being closer to a superparamagnetic system. The unphysical high value of the energy barrier also contradicts the assumption of an interacting particle system.

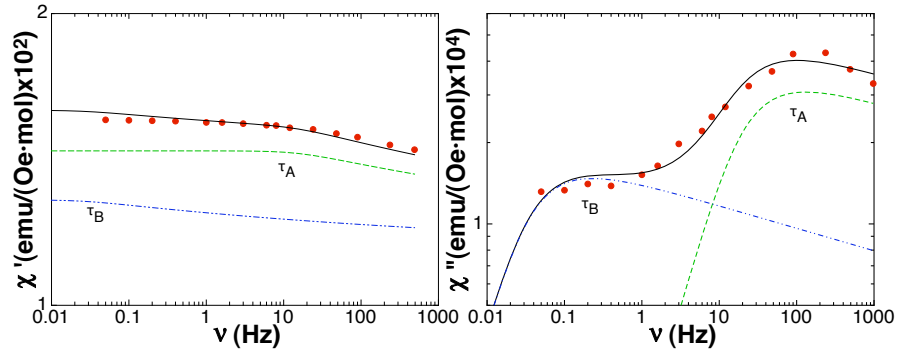

Figure 7.9: Example of susceptibility data fitting to Eq.7.6 in $NdFe_{0.8}Ga_{0.2}O_3$ at T=139 K. • are the original data, the solid line shows the fitting results, while the dashed and the dashes-dotted line represent each one of the Davidson-Cole functions.

7.4 Possible origins of negative magnetisation in $NdFe_xGa_{(1-x)}O_3$ series

From the available data presented on the previous sections, some comments on the observed negative magnetisation and its origin arise.

From magnetisation measurements it is clear that the magnetisation reversal is induced by the applied magnetic field, since no sign of negative values can be found in the ZFC measurement. Susceptibility measurements have shown a relaxation process at a temperature range between 100K and 160 K. Moreover, in all the cases, the onset of the divergence between the ZFC and the FC measurement is the Fe spin reorientation, while the observed relaxation ap-

pears at a different temperature. This freezing temperature is constant for all the samples, being independent of T_{SR} or x, what suggests that the negative magnetisation in all the observed samples has a common origin.

As already discussed, in $NdFeO_3$ [11] and in the other compounds of the $NdFe_xGa_{(1-x)}O_3$ series, Nd ions are polarised by the Fe sublattice antiparallel to the Fe^{3+} weak magnetic moment. The Nd magnetic moment increases and when both contributions are equal, a compensation point occurs, changing both contribution its sign. This type of process is shown in Fig. 7.10a.

When the components are blocked by an energy barrier greater than k_BT, the compensation cannot occur and, therefore, a net negative magnetisation might appear, as in Fig. 7.10b. This is the usual origin of a negative magnetisation, although another option is also possible.

In manganites, such as $NdMnO_{3+\delta}$, the random distribution of excess oxygen ions generates clusters of ferromagnetically ordered Mn in the regions with higher oxygen concentration. Since Mn ions in $NdMnO_3$ order in the same configuration as Fe in $NdFeO_3$ –although ferromagnetically coupled to Nd ions–, ferromagnetic clusters emerge inside a canted antiferromagnetic matrix. Even though these clusters were shown by low angle neutron diffraction measurements [57], the origin of the negative magnetisation in this compound was solved by using X-ray Circular Magnetic Dichroism (XMCD), an element-specific magnetometry that allowed us to identify the relative sign of the Nd and the Mn net moments [19]. This experiment showed that when the system is cooled under an external field, the matrix net magnetic moment orders in the direction of the field, while the clusters, due to an antiferromagnetic interaction with the matrix, are oriented in the opposite direction. As the temperature is reduced, the magnetic moment of the clusters increases overcoming the matrix contribution, thus generating a negative magnetic moment. This process is summarised in Fig. 7.10c.

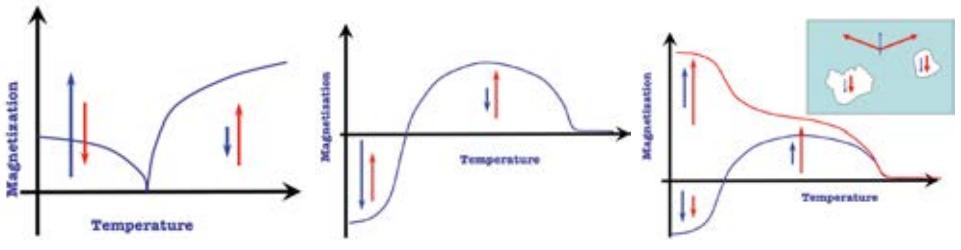

(a) (b) (c)

Figure 7.10: (a) Squematic representation of a normal compensation point. (b) Squematic representation of a standard negative magnetisation. (c) Squematic representation of a negative magnetisation originated by a cluster-glass phase.

The existence of a compensation point in ZFC magnetisation measurements of the $NdFe_xGa_{(1-x)}O_3$ compounds, together with the extra anisotropy induced in the system by the introduction of magnetic vacancies in the Fe sublattice, would suggest an explanation like the one displayed in Fig. 7.10b for the observed negative magnetisation in $NdFe_xGa_{(1-x)}O_3$ FC curves. However, susceptibility measurements discussed above do not allow ruling out a *cluster-glass* state, similar to the one found in $NdMnO_{3+\delta}$, as the possible origin of the reversed magnetisation in these samples.

In order to univocally determine which of the mechanisms depicted in Fig. 7.10 is behind the anomalous magnetisation observed in the $NdFe_xGa_{(1-x)}O_3$ samples, XMCD measurements were used, as in the case of $NdMnO_{3+\delta}$, to determine the relative sign of the Nd and Fe net magnetic moments in different points of the ZFC-FC magnetisation curves. Results are discussed in the next section.

7.5 Selective magnetometry by X-ray Magnetic Circular Dichroism (XMCD) in $NdFe_{0.8}Ga_{0.2}O_3$

$NdFe_{0.8}Ga_{0.2}O_3$ sample was studied by means of XMCD experiments where the circularly polarised light absorption on both Nd L_2 and Fe K edges was measured. The experiment was performed by recording the total fluorescence yield in backscattering geometry. Since we are mainly interested in the orientation with respect to the applied magnetic field of the magnetic moment of each sublattice and not in their respective magnitude, the analysis of the acquired data is relatively simple. In all the studied edges (Fe K- edge and Nd L_2-edge), the absorption of $NdFe_{0.8}Ga_{0.2}O_3$ is measured with circularly positive (μ_+) and negative (μ_-) polarised light. After separately normalising the absorption of each polarisation, XMCD signal is obtained as the difference $\mu_- - \mu_+$.

In Fig. 7.11 a schematic representation of $NdFe_{0.8}Ga_{0.2}O_3$ magnetisation curves at an applied magnetic field of $H = 300$ Oe and 3000 Oe is shown together with the three points –labelled from A to C– at which XMCD spectra were acquired. In the A state, the sample was cooled down under an applied field of 3 kOe down to 2K, where the XMCD measurement were taken. B and C points are measured over the 300 Oe FC magnetisation curve, being B acquired at 2 K and C at 60 K, well below the Fe spin reorientation transition and the relaxation process observed in susceptibility measurements. Between every measurement, the sample was heated to reset it magnetically.

The XMCD signals measured in state A at the Fe K and Nd L_2 edges are shown in the upper panes of Fig. 7.12. Both curves show the typical shape of

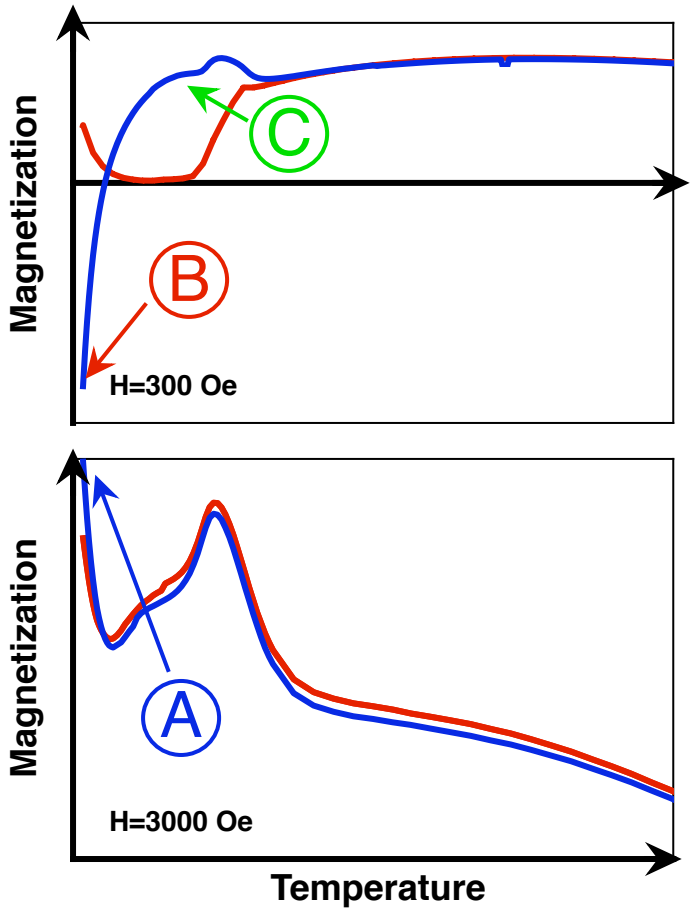

Figure 7.11: Squematic representation of magnetisation points at which XMCD measurements are taken.

the XMCD at the Fe K and Nd L_2 edges, with positive sign for Nd and negative sign for Fe. The sign of each sublattice can be easily identified with the help of references, such as the perovskite compound $NdMnO_{3+\delta}$ [19] and $Nd_2Fe_{14}B$ [110]. This result is coherent with the magnetisation measurements discussed earlier in this chapter, where no difference between FC and ZFC curves was observed for $H = 3000$ Oe. As already mentioned, the magnetisation of the $NdFe_xGa_{(1-x)}O_3$ compounds display a compensation point at low temperatures when Nd polarised magnetic moment – antiferromagnetically coupled to the weak ferromagnetic moment of the Fe sublattice– overcomes the Fe contribution. Since the $H = 3000$ Oe FC measurement is indistinguishable from that of the ZFC, at temperatures below the compensation point, Nd ions are expected to display a positive sign with respect to the applied magnetic field, while Fe ions are expected to display a negative one.

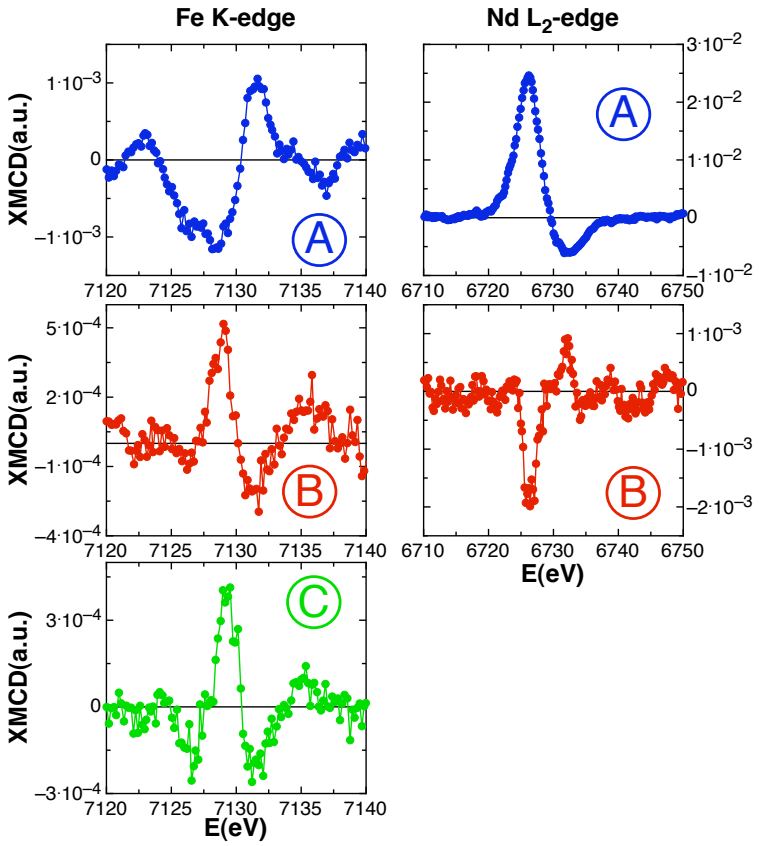

Figure 7.12: XMCD measurements at the Fe K-edge (Left) and at the Nd L_2-edge in $NdFe_{0.8}Ga_{0.2}O_3$ (Right). A, B, D, and D points measurement conditions correspond to the points in Fig. 7.11

In the central panels of Fig. 7.12, B and C states are depicted. B data clearly show that both Nd and Fe magnetic moments are reversed when the sample is cooled under a 300 Oe external field, being Nd sign negative and Fe sign positive in this case. C measurement was acquired at $T = 60$ K, a temperature at which Nd sublattice is paramagnetic. XMCD at the Nd L_2-edge was not acquired in this case since its contribution is negligible in this temperature range. As in the B case, Fe sign reveals that Fe magnetic moments are oriented parallel to the applied magnetic field.

XMCD results turns out to be incompatible with the cluster-glass state suggested by the *ac* susceptibility measurements. This explanation would require that the contribution of these clusters to the total magnetization at low temperatures was the dominant one, so that the positive contribution of the canted antiferromagnetic matrix can be overcomed. This is the case of the $NdMnO_{3+\delta}$, where Mn ferromagnetic clusters are formed inside the canted an-

tiferromagnetic matrix and coupled antiparallel to it [19]. It can be easily seen that a similar situation in our samples would imply opposite directions at low temperatures that the ones found in the B state depicted in Fig. 7.12, both for Fe and Nd moments. Fe magnetization at this temperature would be given by the cluster magnetic moments, oriented antiparallel to the matrix and, thus, also to the applied magnetic field; while the Nd magnetic moments would be located antiparallel to Fe ones and parallel to the external field. No significant minority phases or impurities were found in the $NdFe_xGa_{(1-x)}O_3$ samples both by X-ray and neutron diffraction [111], being the develpment of Fe clusters inside the matrix very unlikely due to the high value of Fe concentration, well above percolation ($x_c \sim 0.33$). This, combined with XMCD results lead us to discard the presence of Fe clusters inside the sample.

By contrast, the obtained results correspond to the scenario where a *"normal"* compensation point is inhibited by the presence of an external magnetic field, Fig. 7.10b. In our case, we assume that in a $NdFe_xGa_{(1-x)}O_3$ compound cooled down under an external field, when Fe spins are reoriented, the F_x direction parallel to the applied magnetic field will be favored, generating anisotropy on the sample. As it was already shown in Chapter 5, the random disorder induced by Ga ions in the Fe sublattice also increases its anisotropy. As the temperature decreases, the Nd polarized magnetic moment increases, antiferromagnetically ordered with respect to the Fe magnetic moment. The increase in the Fe anisotropy, together with the presence of non magnetic ions in the Fe sublattice that could act as pinning centers, lead to a freezing of the weak ferromagnetic domain walls. Once the domain walls are blocked, a reversal of the magnetic moment is prevented, unless a sufficiently high magnetic field is applied, as observed in XMCD measurements. For high applied magnetic fields, as shown by XMCD results in A, the external field provides enough energy to the ions to move the domain walls and overcome the anisotropy. This translates in a recovery of the normal compensation point observed in ZFC magnetization measurements. The same origin for the negative magnetization found in samples with $0.5 \leqslant x \leqslant 0.9$ can be assumed, explaining the common temperature range and frequency dependence of the χ_{ac} features.

The reason why the negative magnetisation appears at higher temperatures for lower x values and why its intensity is higher also for low x values can be explained by the temperature difference between the freezing of the domain walls and the reorientation process. As shown in Fig. 7.13, for $x \geqslant 0.95$, T_f is slightly below T_{SR}, thus not all the domain walls will be blocked when the Fe spin reorientation takes place. This will allow some of the domain walls to move, reducing the number of Nd magnetic moments oriented antiparallel to the external field. This effect will be larger for $NdFeO_3$, since the spin reorientation transition takes place even at higher temperatures and there is

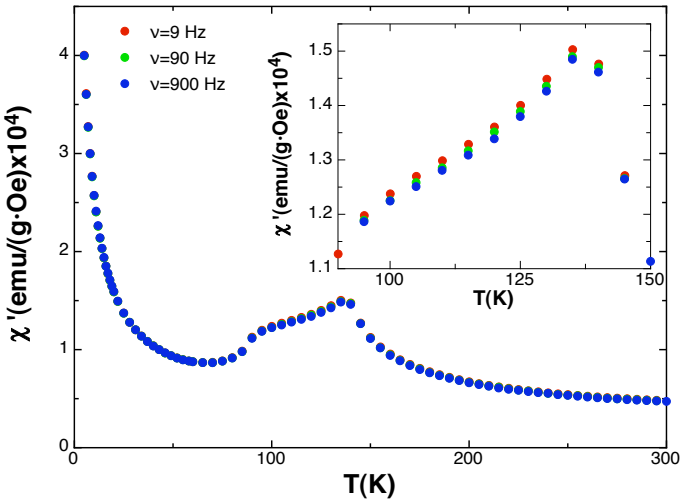

Figure 7.13: χ' as a function of temperatures for $NdFe_{0.95}Ga_{0.05}O_3$ for different frequencies. Inset displays a zoom around the reorientation peak.

no Ga ions that could act as pinning centres for the domain walls. As the number of magnetic vacancies increases, the anisotropy on the Fe sublattice increases and T_{SR} is reduced, and so is the available thermal energy to overcome the anisotropy barrier associated with the blocked domain walls once the Fe ions reorient. Moreover, magnetic vacancies will act as pinning centers for the domain walls. As already mentioned, for $x = 0.4$, Fe ions are not ordered at the blocking temperature, thus domain walls can not be frozen, since they have not yet be formed. The consequence, as observed in Fig. 7.1 is that no reversed magnetisation appears in this sample.

Thus, the introduction of magnetic vacancies on the Fe sublattice of $NdFeO_3$ induces a negative magnetisation on the FC measurements for $H < 3$ kOe, through the reduction of the temperature of the Fe spin reorientation transition, and the introduction of magnetic defects which act as pinning centers for weak ferromagnetic domain walls.

7.6 Conclusions

FC-ZFC magnetisation measurements performed on the $NdFe_xGa_{(1-x)}O_3$ series show that the dilution of Ga ions in the Fe sublattice generates a non-intrinsic negative magnetisation on the FC curves between $0.4 < x < 0.95$. The absolute value of the magnetisation at low temperatures decreases as the Fe concentration increases until positive values of M are recovered for $x = 0.95$. The temperature range at which M display negative values is also reduced as

x increases. In all the cases FC and ZFC curves diverge just below the spin reorientation.

ac susceptibility measurements on the same samples showed a relaxation process at a common temperature independent of x or T_{SR}. This process seems to be related with a mainly bimodal distribution of relaxation times of the order of $5{\cdot}10^{-9}$ s. This feature, associated with the negative magnetisation, seems to behave as some kind of *"glassy"*-state, although its detailed analysis by different models does not allow us to draw a clear conclusion on its possible origin.

With the help of XMCD measurements, the presence of Fe clusters, similar to the ones found near percolation, has been ruled out. These measurements allow us to associate the thermal relaxation process observed in χ_{AC} experiments to the freezing of the sample domain walls. This freezing would not only explain the obtained XMCD data, but also the variation of the negative magnetisation throughout the series while T_f remains mostly unchanged. The reduction of the Fe spin reorientation transition by the introduction of magnetic vacancies, also reduces the thermal energy available to unblock the domain walls right bellow T_{SR}. The associated impossibility of Fe and Nd magnetic moments to rotate translates into a negative magnetisation, with an absolute value that increases with $T_f - T_{SR}$.

Chapter 8

Part I Final Conclusions

On the previous chapters we have studied in detail the magnetic behaviour of the $NdFe_xGa_{(1-x)}O_3$ family of compounds, analysing how the interplay between the different magnetic interactions in the sample – Nd–Nd, Fe–Fe and Fe–Nd – are modified by the Fe concentration. In this chapter, the main conclusions drawn in the first part of this thesis are presented.

- The magnetic ordering of the Fe sublattice in $NdFe_xGa_{(1-x)}O_3$ compounds has been determined in the whole Fe concentration range by means of magnetisation, susceptibility and neutron diffraction measurements as a function of temperature.
  - X-ray and neutron diffraction data demonstrate that the introduction of magnetic vacancies in the Fe sublattice of $NdFeO_3$ do not change the structure of the sample that it is shown to be *Pbnm* in all the cases. Moreover, for iron concentrations above percolation, Fe ions in $NdFe_xGa_{(1-x)}O_3$ samples order magnetically in the same configuration observed in $NdFeO_3$, but at a lower temperature. The dilution of Ga ions in the Fe sublattice enhances the Fe ion anisotropy, thus depressing the spin reorientation temperature of the metal sublattice. This reorientation is not inhibited even for Fe concentrations as low as 40%. Both canted angles and Fe magnetic moments obtained for $x > 0.5$ are in good agreement with previous results on $NdFeO_3$.
  - For iron concentrations close to percolation the presence of cluster-glass-like phases was detected. For x=0.4, neutron diffraction data and magnetisation measurements evidence the existence of sample regions with iron concentration slightly above and below the nominal value. Susceptibility measurements on x =0.2 and 0.3 reveal frequency dependent features with a behaviour corresponding to a cluster-glass.

Our results suggest the formation of Fe clusters of different sizes and net magnetic moments. The random distribution of magnetic vacancies in $NdFe_xGa_{(1-x)}O_3$ enhanced by a chemical concentration distribution intrinsically related to the ceramic fabrication route will generate magnetically uncompensated regions and finite clusters for x values close to percolation.

- The detailed analysis of the Fe sublattice order led us to determine the phase diagram of the series for temperatures $T > 2$ K. Since Nd–Nd is the weakest interaction among those taking place in $NdFe_xGa_{(1-x)}O_3$, the study of the Fe sublattice ordering is the key point that enables us to face the study of how the introduction of magnetic vacancies affects the Nd sublattice through the change of H_{Nd-Fe}.

- Calorimetric measurements on $NdFe_xGa_{(1-x)}O_3$ compounds, together with neutron diffraction and ac susceptibility data on samples with iron concentration below percolation were performed to fully characterise the studied series of compound from the magnetic point of view. With these techniques, the Nd cooperative order and its inhibition due to the generation of magnetic disorder in the Fe sublattice was examined.

  - Neutron diffraction, χ_{AC} and calorimetric measurements on the $NdFe_xGa_{(1-x)}O_3$ series clearly show that the substitution of non-magnetic ions by Fe ones in $NdGaO_3$ inhibits Nd long-range cooperative order for $x > 0.2$. Equivalently, the substitution of Fe ions in $NdFeO_3$ by Ga ones destroys Nd–Nd order for $x \leqslant 0.96$. Results show that the inclusion of unpaired Fe magnetic moments in the neighbourhood of Nd sites generates an effective field that polarises Nd atoms. This polarisation reduces the entropy available for cooperative order, and thus T_N, until the Nd-Nd long range order becomes impossible. However, the dilution of Fe^{3+} ions does not modify the Nd ordering configuration displayed in $NdGaO_3$.
  - The Nd polarisation by the Fe sublattice is observed by specific-heat measurements through a Schottky contribution. Its temperature dependence corresponds to the variation of H_{Nd-Fe} with Fe concentration, as expected from the increment of unpaired antiferromagnetic Fe moments near Nd sites.
  - Specific heat measurements identify what appears to be remnants of the Nd order transition for $x = 0.2$ and 0.3. These features, also visible in ac susceptibility measurements in these samples, are identified as Nd short-range order by neutron diffraction measurements in $x = 0.3$ sample, while for x=0.2 the number of Nd ions affected by a nearly zero H_{Fe-Nd} internal field is just above the percolation limit.

  - As it was found at higher temperatures, spin-glass-like behaviour is detected both in calorimetry and susceptibility measurements for x values below, but close to percolation. A possible origin for this *"glassy"* state is proposed: the polarisation of Nd ions inside this Fe clusters, preventing their cooperative ordering, might generate clusters of magnetically order Nd, isolated by regions of polarised Nd. A cluster-glass system as this one, where a clustered Fe sublattice is interspersed on the Nd one, could explain both the specific heat and ac susceptibility features that pointed to a "spin-glass-like" behaviour.
  - Specific-heat, neutron diffraction and susceptibility measurements performed on $NdFe_xGa_{(1-x)}O_3$ compounds with Fe concentration below percolation were used to complete the phase diagram of the $NdFe_xGa_{(1-x)}O_3$ series that summarised the ordering phases of both Nd and Fe sublattices in the whole temperature range. The results presented in this thesis provides a complete study of the effect of magnetic vacancies on the magnetic ordering of the Fe sublattice and in the polarisation and magnetic ordering of the Nd sublattice in $NdFe_xGa_{(1-x)}O_3$.

- Finally, ac susceptibility measurements and XMCD data are combined to examine the origin and nature of the negative magnetisation found in the FC-ZFC curves of the $NdFe_xGa_{(1-x)}O_3$ series above percolation.

  - Magnetisation measurements on $NdFe_xGa_{(1-x)}O_3$ compounds proved that the introduction of magnetic vacancies generates a non-intrinsic negative magnetisation on the FC curves between $0.4 < x < 0.95$, whose intensity decreases with Ga concentration.
  - Ac susceptibility measurements on the same samples showed a relaxation process at the same temperature for all the samples, even for $x \geqslant 0.95$.
  - By means of XMCD measurements, it was found that the extra anisotropy introduced in the Fe sublattice by the randomly distributed Ga ions, prevents Nd and Fe net moment from rotating when both become equal at the compensation point. This anisotropy originates a negative magnetic moment with an origin clearly different from that found in other perovskites such as the $NdMnO_{3+\delta}$.

Final comment: The rich phenomenology displayed by the family of compounds $NdFe_xGa_{(1-x)}O_3$ combined with its simple structure, has allowed us to explore a large variety of techniques in order to achieve a full understanding of the magnetic properties of the series. Although the study of this type of compounds might not be a burning issue at present, its study from a basic science

point of view has provided the thesis defendant with an excellent knowledge of the available set of tools for magnetic analysis, their use, strengths and limitations, turning out an unbeatable training topic. Moreover, besides its apparent solely academic interest, fascinating and uncommon behaviours appear in the $NdFe_xGa_{(1-x)}O_3$ family: from cluster-glass formation inside a non-frustrated system, its connection with the percolation problem or the effect of cluster formation in one sublattice in the other one, to the existence of negative magnetisation for some compounds of the series.

Part II

Calorimetry as a detection tool. TES based bolometers and calorimeters for radiation detection

Chapter 9

Calorimeters and bolometers based in superconducting materials

9.1 Superconducting cryogenic detectors for astronomical applications

The enormous success of astronomy during the last quarter of the century has improved our understanding of the Universe in a way that leads us to face questions that a few years ago seemed impossible to achieve. Some of those questions are gathered together in the objectives of the ESA Cosmic Vision 2010-2025[1], the long-term planning for space science missions of the European Space Agency –ESA–.

To address them, detectors of extremely high spectral and spatial resolution are needed in the different frequency ranges. Among the various radiation detectors, cryogenic ones are the most suitable candidates, since they provide high sensitivity in a wide range of frequencies due to their low thermal noise. Cryogenic detectors include Superconducting Tunnel Junctions (STJ), Kinetic Inductance Detectors (KID), Magnetic Microcalorimeters (MMC), Quantum Capacitance Detectors (QCD), Si-thermistors and Transition Edge Sensors (TES). While KID's, QCD's and MMC's have already shown excellent performance, they are still under development, what rules them out for most of the space missions applications. Calorimeters based on Si-thermistors do not match the spectral resolution requirements of the missions under study inside Cosmic Vision, neither do STJ sensors. On the contrary, TES are among

[1] http://sci.esa.int/science-e/www/area/index.cfm?fareaid=100

the most sensitive radiation detectors working in any frequency range, from sub-mm and FIR astronomy [112–114] to γ-rays [115–117], being their sensing capability already established beyond any doubt. Their unbeatable characteristics explain why they have been selected to be the base for the next generation of ultra-sensitive detectors required for future space based telescope missions, such as the SAFARI instrument on SPICA [2] and the X-ray Microcalorimeter Spectrometer (XMS) on IXO [3], two of the ESA missions competing for launch opportunities in the future.

Regarding the X-ray Microcalorimeter Spectrometer, the extremely high energy resolution required –2.5 eV in 6 keV– can only be achieved by TES microcalorimeters, for which values as low as $\sim$2 eV have been already proven in this energy range [118], while the best results on STJ's and Si-thermistors are limited to $\sim$ 10 eV resolution at 6 keV [119, 120]. The sensitivity requirement for SAFARI is given by a Noise Equivalent Power (NEP) $\leqslant 3 \cdot 10^{-19}$, still away from the results obtained so far –NEP$\sim 1 \cdot 10^{-17}\ W/\sqrt{Hz}$ [121]–. However, researchers claim that TES bolometers might approach the sensitivity required for these missions [122].

Besides astrophysics, TES have been applied to other fields such as spectroscopy or metrology [123]. Moreover, TES based detectors have been applied for particle detection such as dark matter [124], weakly interacting particles [125], biomolecules [126, 127] and heavy ions and α particles [128]. This vast collection of uses is leading to the development of a large variety of TES applications such as non-proliferation of nuclear weapons and defence applications that can unambiguously discriminate between radioactive isotopes, X-ray microanalysis systems for microchips characterisation or the improvement of the security of quantum communications [129].

Among their different applications, in this thesis we will restrict our selves to the use of TES as radiation detectors in the sub-mm, FIR and X-ray regimes. More specifically, we deal with the development and characterisation of TES for the already mentioned SPICA and IXO missions. In Chapters 10, 11 and 12 we focus on the development of TES for X-ray applications, while in Chapters 13 and 14 the complete characterisation of TES for the mentioned SAFARI and XMS instruments will be described. But before reaching that point, in this chapter a description of what is a TES and how it is operated will be provided.

[2] http://sci.esa.int/science-e/www/object/index.cfm?fobjectid=42281
[3] http://sci.esa.int/science-e/www/area/index.cfm?fareaid=103

9.2 Transition edge sensors

Superconductivity was discovered in 1911 by Heike Kamerlingh Onnes when, measuring the electrical resistance of mercury at low temperatures, its value abruptly dropped to zero, below 4.2 K [130]. After this discovery, superconductivity was found in several other materials, showing a logarithmic sensitivity with temperature in the superconducting transition –$\alpha = dlogR/dlogT$– that can be two orders of magnitude higher than that of semiconductor thermistors [131]. This is the reason behind the development of the so called Transition Edge Sensors, where a superconducting film operated at the transition temperature is used as a radiation detector. In 1941 and 1949 D.H. Andrews implemented the first demonstration of a TES bolometer and a TES calorimeter respectively, by detecting IR radiation with a fine tantalum wire [132], and alpha particles with a niobium nitride stripe [133]. Besides these promising early developments, it wasn't until the end of the century that TES were used in practical applications due to the impossibility to match their noise to FET amplifiers and to the instability associated with the narrow transition. The solutions taken to solve these problems, together with a brief summary of the physics of the superconducting transition are given in the following sections.

9.2.1 Superconductivity

Below a certain temperature –known as the critical temperature T_C–, in some materials an attractive electron-electron interaction appears, leading to the formation of Cooper pairs. These Cooper pairs act as bosonic particles and condense into the ground state forming a superfluid. Cooper pairs have a much larger length scale than conduction electrons, since the energy binding the two electrons prevents them from scattering. This originates the zero electrical resistivity displayed by superconductors. John Bardeen, John Schrieffer and Leon Cooper developed the first microscopic theory for the superconductivity, the BCS theory [134], associating its origin to the formation of Cooper pairs [135].

Although Cooper pairs are quantum particles, their origin can be explained from a classical point of view. An electron moving inside a material will interact with positive ions in the lattice, moving these ions forward as it travels through the sample. This will generate a cloud of positive charge around the electron that could attract another electron, binding the two of them together into a Cooper pair. This effective attraction results into the establishment of an energy gap –known as the *"superconducting energy gap"*–, a temperature dependent value that at $T = 0$ is written as $E_{gap} \approx 3.5 k_B T_C$. The size of the Cooper pair, given by its coherence length, $\xi(T)$, also depends on the

critical temperature and has a zero temperature value that is expressed as $\xi_0 \equiv \xi(0) \approx 0.18 v_f/(k_B T_C))$. As the temperature increases the superconducting gap is reduced and, above T_C the thermal fluctuations can provide enough energy to break Cooper pairs, destroying superconductivity.

Another characteristic length of superconductors in the BCS theory is the penetration depth, $\lambda_{eff}(T)$, that is associated with the Meissner effect, i.e. the expulsion of magnetic field from a superconductor during the superconducting transition. $\lambda_{eff}(T)$ is the distance from the superconductor surface where the magnetic field is not fully cancelled, being its value at $T = 0$ known as the London penetration depth $\lambda_L(0)$.

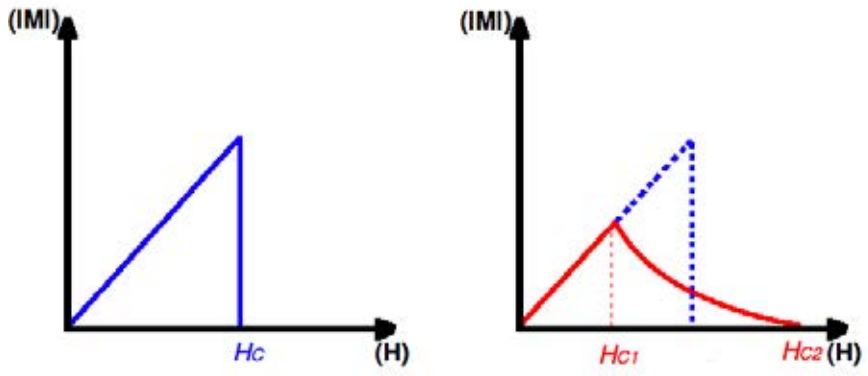

(a) (b)

Figure 9.1: (a) Magnetisation in a Type I superconductor as a function of magnetic field. (b) Magnetisation in a Type II superconductor as a function of magnetic field.

While the microscopic BCS theory provides an explanation of the origin of superconductivity, the Ginzburg-Landau theory succeeded at properly describe the physics of a superconductor from a macroscopic point of view [136]. The behaviour of a superconductor with respect to an external applied field allows to divide these materials into two types on the basis of Ginzburg-Landau theory. If the dimensionless Ginzburg-Landau parameter $\kappa \equiv \lambda_{eff}(T)/\xi(T)$ is smaller than $1/\sqrt{2}$, the superconductor is of Type I, i.e. when the external magnetic field reaches the critical value H_C superconductivity is fully destroyed. While for $\kappa > 1/\sqrt{2}$, the superconductor is of Type II, when H rises above a certain value H_{C1}, magnetic flux can penetrate the material being separated into individual flux quanta that repel each other. This mixed superconductor-normal state is destroyed for $H > H_{C2}$ –see Fig. 9.1–. The physical properties of a TES will depend on the type of superconductor, since it will influence not only the physics of the transition, but also the noise behaviour, the current-carrying capability and the sensitivity to magnetic field. Thus, the determination of the

superconducting lengths will be a key point to understand and improve the final TES performance, as it will be shown in Chapter 10.

9.2.2 Proximity effect

T_C of the final TES is a critical parameter that determines its final energy resolution and time response through the dependence of heat capacity, thermal conductance, thermal noise, among others, with the temperature of operation. A trade-off between sensitivity, cryogenic effort and count rate is usually made, what leads to operational temperatures of $T_C \sim 100$ mK or 400 mK, above the base temperature of the different types of refrigerators: dilution or adiabatic demagnetisation refrigerators in the first case, and ^{3}He refrigerators in the second case. As it will be discussed later, TES with the appropriate critical temperature can be achieved using different approaches: selecting a superconducting material with a T_C in the proper temperature range, using magnetic dopants to suppress the T_C of the superconductor or, the most commonly used solution, applying the proximity effect in a normal/superconductor bilayer to decrease T_C.

The proximity effect is the effective reduction of a superconductor T_C by placing it into contact with a normal metal through a sufficiently clean interface. In this way, some Cooper pair penetrate into the metal inducing superconductivity in it. The total bilayer exhibits a reduced T_C when compared to the individual superconductor. For a bulk superconductor, the contact with a normal metal layer slightly reduces T_C, but, for thinner films $-d_S < \xi_0-$ T_C is depressed as the normal metal layer thickness $-d_M-$ increases, until a critical value $-\xi_M-$ is reached. For $d_M > \xi_M$ no further suppression of T_C is found, where the normal metal coherence length, ξ_M, is the distance inside the normal metal where the superconductivity propagates.

The proximity effect was first observed by Meissner [137] and was intensively studied in the 1960's [138–141], however, it was not applied to TES until the 1990's by Nagel et al. [142]. Different approximations allow to analytically determine the critical temperature of a normal/superconductor bilayer as a function of the individual layers thickness, as long as these values are less than the respective coherence lengths (Anderson limit) [143–147]. However, different combinations of thickness values can be used to obtain the same T_C, as shown in Fig. 9.2, where a schematic illustration of the influence of the proximity effect on the bilayer final T_C is depicted. Moreover, since the quality of the interface will also influence T_C, from a experimental point of view, the easiest approach to obtain a TES bilayer with the desired T_C consists of choosing the normal metal thickness to adjust the resistance of the system to

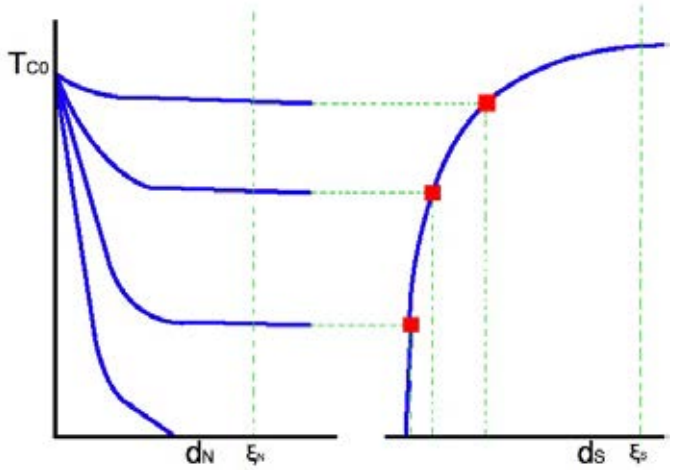

Figure 9.2: Schematic representation of the proximity effect on a superconductor/normal bilayer. Left curves correspond to fixed values of d_S and different normal metal thickness while the curves on the right correspond to fixed values of d_M and different values of d_S. *Adapted from [123]*

the required value, and then varying the superconducting layer thickness to tune the T_C. If $d_M > \xi_M$ no variation in T_C will be found when changing d_M, what allow us to fabricate sensors with the desired T_C and different resistivity values without determining again the $T_C(d_M)$ characteristic curve showed in Fig. 9.2.

9.2.3 Voltage bias and negative electro-thermal feedback

As mentioned above, one of the problems limiting the application of TES to radiation detection was that, due to the sharpness of the superconducting transition, even small signals could saturate the TES response. In 1995, Irwin proposed to use a feedback circuit to avoid this limited dynamic range, as it was common practice in electrical circuits to face analogous limitations [148].

In a TES, the electrical and the thermal response are related. As shown in Fig. 9.3b when a heat pulse reaches the system the temperature of the TES increases, what translates into a change in the resistance of the detector. Equivalently, an electrical signal will modify the temperature of the sensor through Joule heating. This interrelationship can be used to hold the TES temperature constant.

TES, as any other electrical device can be either voltage or current biased. Assuming a sensor with a positive α value, the resistance of the system will

increase with its temperature. Thus, if the detector is current biased, an enhancement of T and R will produce an increase of the Joule dissipated power $P_J = I^2R$, leading to a positive electro-thermal feedback. On the contrary, when TES is voltage biased, the expression for the Joule power dissipated in it will be $P_J = V^2/R$, thus, an increase of T will reduce P_J and, consequently T, forcing the sensor to recover its operational temperature. This negative electro-thermal feedback (ETF), as in the case of transistors or amplifiers, avoids the instabilities that a positive feedback can cause, linearising the output signal and increasing the dynamic range. Moreover it reduces the time response of the TES to a heat pulse [148–151], increasing the count rate and the bandwidth.

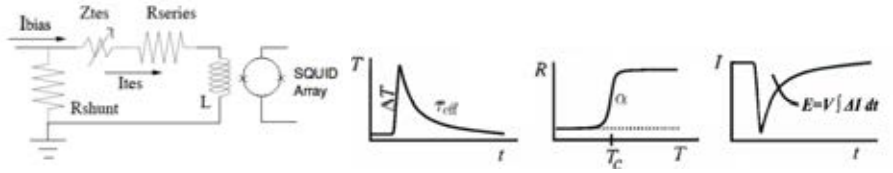

(a) (b)

Figure 9.3: (a) Squematic of a TES readout system with electro-thermal feedback . (b) Squematic representation of TES response to heat pulses.

With these considerations, the TES readout circuit is established as depicted in Fig. 9.3a. A shunt resistance –$R_S \ll R_{TES}$– is used so that nearly all the current will be carried by this resistance, and the TES can be considered as voltage biased with $V_{TES} \approx I_{bias}R_S$. All the parasitic resistances in the circuit are included in R_{series}, and L is the inductance used to couple the TES output to the input of the amplification chain. Under this configuration, when a heat pulse reaches the detector its resistance increases and then, due to the ETF circuit it slowly returns to its equilibrium value. Since V_{TES} is assumed to be constant, initially the current going through the TES will be drastically reduced, and its initial value recovers with the same characteristic time constant experienced by the temperature of the sensor. This current variation, is thus, proportional to the energy of the detected event.

This signal is too low to be directly detected, usually of the order of μA, thus requiring amplification to be acquired. However, the low resistance of TES, typically $\sim 10 - 100\ m\Omega$ prevent the use to FET amplifiers due to noise mismatching. In most cases, TES signals are amplified by means of SQUID sensors operated at low temperatures, as the sensor itself.

In this configuration, the current-to-voltage TES response is characterised by sweeping the bias current –I_{bias}– and measuring the output of the SQUID –V_{out}–. The typical result is displayed in Fig. 9.4a. When the sensor is in the normal state, it behaves as a resistance of constant value R_N – the

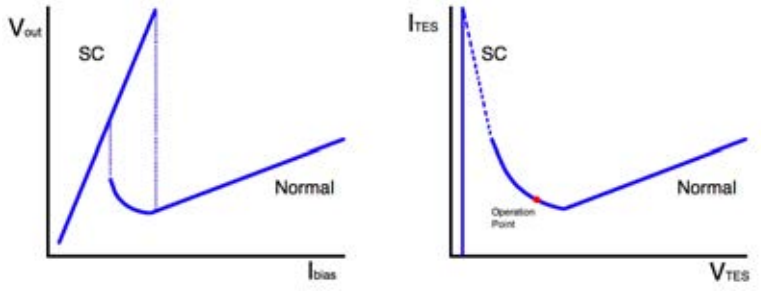

(a) (b)

Figure 9.4: (a) SQUID output signal as a function of the bias current of a TES. (b) Typical current to voltage response of a TES. (•) represents the operation point of the TES.

residual resistance of the TES at low temperatures–, thus, V_{out} displays a linear dependency with the bias current. As the current through the sensor is reduced, the temperature of the sensor decreases and, when T_C is reached, R_{TES} starts to decrease as well. Since the TES is voltage biased, this reduction of the TES resistance translates into an increase of the current running through it and of the output signal. At $R_{TES} = R_{Load} = R_S + R_{series}$, the current through the TES is no longer capable of keeping the TES warm, and the superconducting state is reached. Once in the superconducting state, the TES can only come back to the normal state when I_C is achieved, what leads to the hysteresis of V_{out} with respect to I_{bias} shown in Fig. 9.4a

When the transfer function between the SQUID and the L of the TES bias circuit is known, the output of the SQUID can be easily translated into the current running through the TES. In order to determine the voltage across the sensor an estimation of the parasitic resistance is required. This value can be obtained from a linear fit of the superconducting and the normal branches of the $I_{bias} - I_{TES}$ curve, since $(I_{bias} - I_{TES})R_S = I_{TES}(R_{TES} + R_{series})$. The resulting I-V curve, shown in Fig. 9.4b is the basis for the TES complete characterisation, that will be described in Chapters 13 and 14.

9.2.4 Different parts and requirements of TES

Radiation detectors based on TES can be developed both as bolometers and microcalorimeters. In the calorimeter case, the average time between arrival of the individual quanta should be bigger than the characteristic time constant of the system, what allow the user to detect individual photons or heat pulses. This is the case discussed above. In the case of TES bolometers, the sensor is not used to detect individual heat pulses, but variations in the energy levels.

Thus, the TES time constant should be bigger than the time between photon arrival. Therefore, changes in the incident power are translated into changes in I_{TES} by the sensor, providing information on the energy of the particle flux reaching the detector. Besides the characteristic time ratio and the type of radiation detected, no difference between bolometers and calorimeters can be found –indeed, a device designed as a bolometer can be used as a calorimeter and vice versa– therefore, in both cases the same readout and bias circuit described in Fig. 9.3a is used.

(a) (b) (c)

Figure 9.5: (a) Squematic of an ideal calorimeter. (b) Example of a Ti/Au TES bolometer. *Credit: SRON-Utrecht.* (c) Example of Ti/Au TES microcalorimeter. *Credit: SRON-Utrecht.*

Bolometers and calorimeters are thermal radiation detectors, thus, they are basically formed by three parts: an absorber or thermal mass that absorbs the incident radiation and transforms it into heat, a thermometer that measures the temperature increase in the absorber and a weak thermal link to a heat bath that allows the absorber to relax into the initial state. Therefore, the system can be characterised by the absorber heat capacity –C–, the thermal link conductivity –G– and the bath temperature T_0, as shown in Fig. 9.5a.

In a TES bolometer or calorimeter the superconducting layer of critical temperature T_C acts as the system thermometer, perfectly coupled to an absorber whose nature, shape and dimensions depend on the type of sensor we are dealing with –bolometer or calorimeter–. Since the thermal link will also vary between bolometers and calorimeters, the superconducting thermometer remains as the common point in TES based thermal detectors.

Examples of how TES bolometer and microcalorimeter are implemented are displayed in Figs. 9.5b and 9.5c respectively. In both cases thermometers are formed by a Ti/Au bilayer of thickness $\sim 20/50$ nm deposited over a 1 μm thick SiN suspended membrane that acts as the thermal link to the bath. In order to reduce G to achieve the required value for a bolometric application, some parts of the membrane are removed by lithographic techniques, until supporting legs of a few μm wide are obtained, reducing G from 0.36 nW/K [152] to 370 fW/K [153]. As mentioned above, the design of the absorber

depends on the application. In the case of the bolometer show in Fig. 9.5b, aimed for FIR detection, a 8 nm thick Ta film is deposited over the same membrane as the TES and close to it [154]. In the case of the calorimeter shown in Fig. 9.5c, aimed for X-ray radiation detection, a 1 μm thick Cu absorber is deposit over the TES thermometer [152]. These are just some examples of TES radiation detectors but, as mentioned above, depending on the design and chosen materials, this type of sensors can be applied as radiation detector to a wide range of frequencies from millimetre waves, through gamma-rays, or even as particle detection such as dark matter [124], weakly interacting particles [125] or heavy ions and α particles [128].

Chapter 10

Materials for TES: structural and functional characterisation

10.1 Introduction

The expected performance of a TES is strongly dependent on the quality and properties of the involved materials such as stress or functional properties, like its critical superconducting temperature, T_C, the logarithmic sensitivity of superconducting transition, α and the residual resistance, R_N. Those will limit detector performance through energy resolution or noise. Thus, care should be taken in selecting the most adequate materials for each application.

In our case, TES are aimed to fabricate high resolution X-ray detectors. Since the energy resolution in this type of microcalorimeters is $\Delta E \propto \sqrt{4k_B T_C^2 C}$, a good energy resolution requires low T_C and heat capacity, C. On the other hand, another important feature of TES for X-ray detection is that they will be used as "photon counters", i.e. they will be used to detect individual photons, therefore a fast response is required. Time response in these sensors is mainly due to the thermal time constant, $\tau = C/G$, the time that an excited TES needs to thermalise to the heat bath. This thermalisation process takes place through a thermal conductance typically due to the Kapitza boundary resistance between the bath and the sensor, $G \propto T^3$. This means that, although reducing T_C will improve TES energy resolution, it will also reduce the number of counts per second achievable by our sensor. Moreover, even though low C materials can be used in order to improve energy resolution, sensor volume cannot be arbitrary reduce to reduce C, since reducing absorber volume could compromise TES quantum efficiency [155].

X-ray TES fabrication requires a compromise between energy resolution,

cryogenic effort and count rate. Usually T_C is selected to be around 100 mK to enable its operation with adiabatic-demagnetization and dilution refrigerators. To reach these values, superconducting elements with T_C less than 2 K are used, mainly Ir [156], Al [157, 158], Ti [159], and Mo [158, 160, 161]. Iridium bilayers are not widely used despite its good performance, due to the difficulty of fabrication process, that requires electron-beam evaporation onto high-temperature substrates (700 C) and ultra-high vacuum chambers ($<1 \cdot 10^{-10}$ Torr) [156]. Moreover, its critical temperature is too low for many TES applications ($T_C = 0.112$). Although Al/Metal bilayers are easy to fabricate through electron beam evaporation, and display good performance as X-ray detectors [157], the combination of Al and any noble metal is not chemically stable and presents many intermetallic phases at high temperatures [162], what destroys proximity effect. Ti/Au detectors have shown excellent performance [159], however they suffer ageing effects [163] and, as in the Al case, form intermetallic phases with noble metals at high temperatures [162].

For all these reasons, we decided to focus our work in Mo-based TES. Due to its high melting point (2623 °C), similar to the Ir one, evaporated Mo films show the same fabrication difficulties [158]. To avoid these problem Mo films deposited in this work are fabricated through sputtering processes. To reduce as much as possible detector residual resistance, while tuning T_C through the proximity effect, Mo is combined with noble metals. Among them we choose Au and Cu, since excellent results have being already achieved [158, 160, 161], obtaining energy resolutions as high as 1.8 eV for Mo/Au sensors [118] and 2.4 eV for Mo/Cu ones [164] at 6 keV. Moreover Mo/Au and Mo/Cu configurations are less diffusive even at high temperatures [158, 162] than Al/Ag, for instance. No intermetallic compound formation at the interface for temperatures below 800 °C and diffusion for temperatures below 300 °C are expected [162]. Specially appealing is the combination Mo/Au, since Au is highly resistant to corrosion and more easily lithographed, as shown in Chapter 12.

The quality and reproducibility of the superconducting transition are essential for the performance of the TES. Although these strongly depend on the properties of each layer, very little is known about the correlation of stress and morphology with Mo functional properties such as T_C and R_N, key parameters that will heavily affect TES performance. Since only a few papers on the subject are available [158, 160, 161, 165–167], a systematic study on how Mo superconducting behaviour relates to deposition is needed to ensure the best possible performance of our superconducting Mo-based devices.

In this chapter, the dependence of the functional properties of both layers with deposition parameters will be analysed to ensure a good fabrication control. The optimum deposition conditions will be determined to achieve high

resolution X-ray detectors. In Section 10.2 deposition systems together with characterisation tools used to study the material behaviour are described. In Section 10.3 the effect of deposition parameters on morphology, stress, resistivity and critical temperature in Mo thin films is analysed. Mo standard deposition conditions are determined, ensuring the best Mo film performance: low stress, low R_N and T_C as close as possible to the bulk value. Moreover the minimal thickness for negligible size-effects is also found. Finally, in Section 10.4, the quality of both Cu and Au normal metal layers is studied for different deposition methods.

10.2 Experimental techniques

All samples studied in Chapters 10, 11 and 12 have been fabricated at the Instituto de Microelectrónica de Madrid (IMM) in the group of Dr. Fernando Briones. Mo, Cu and Au thin films were deposited on the top of Si single crystal substrates covered by a 300 nm LPCVD Si_3N_4 layer. The deposition was carried out by Radio Frequency (RF) magnetron sputtering in the case of Mo, and by DC triode sputtering for Au and Cu layers. In all cases, deposition took place at room temperature in an Ultra High Vacuum (UHV) system with a base pressure of 10^{-7} Pa, depicted in Fig. 10.1. The Ar working pressure was kept constant at 0.5 Pa during sputtering. Typical growth conditions for the Au and Cu layers were a target potential of 1.0 kV, and a plasma-confining magnetic field of a few Oe. For Mo layers, the RF power was varied between 25 and 213 W. Typical deposition rates were of the order of 0.1-0.2 nm/s, 0.05 nm/s (Cu) and 0.22 nm/s (Au). The distance between substrate and target was 8 cm in all cases. The purity of Mo target was 99,95 %. Additionally Au layers were also evaporated by electron beam in a different chamber, with a growth rate of 0.2 nm/s.

So as to optimise the different material properties to make them suitable for TES fabrication, the layers performance was characterised mainly by analysing the dependence of their resistivity and critical temperature with the deposition parameters.

The temperature dependence of the resistance and the critical temperature of the different layers was measured using the four-point resistance method, in a commercial Physical Property Measurement System (PPMS) from Quantum Design, at the Servicio de Medidas Físicas of the University of Zaragoza. This system, shown in Fig.10.2, allows us to perform resistivity measurements down to 350 mK.

Structural properties, such as morphology or stress were studied in the

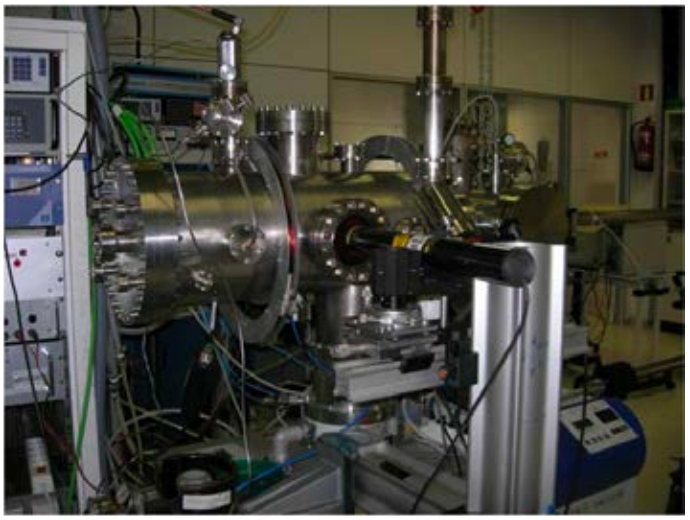

Figure 10.1: Picture of magnetron sputter deposition system at the IMM (Instituto de Microelectrónica de Madrid). *Credit: Raquel González-Arrabal.*

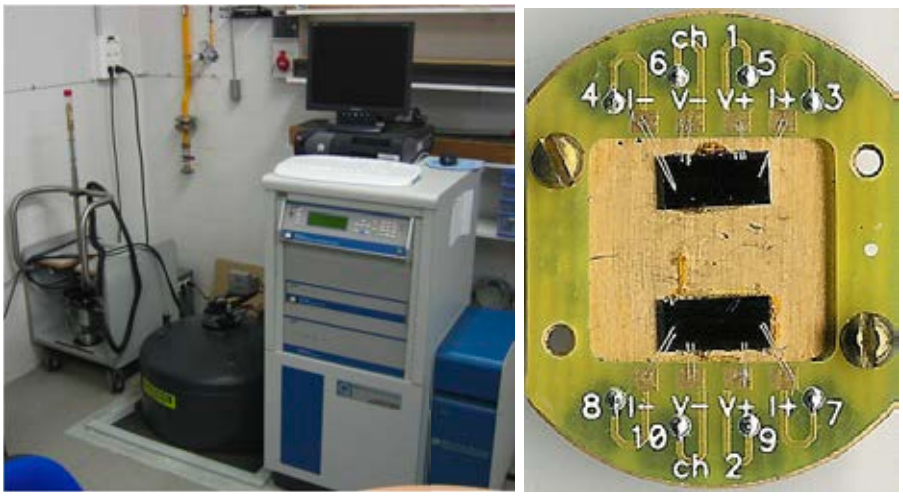

(a) (b)

Figure 10.2: (a) Picture of the Physical Property Measurement System (PPMS) of the Physical Measurements Service. (b) PPMS holder for resistivity measurements.

group of Dr. Lourdes Fàbrega at the Institut de Ciencia de Materials de Barcelona (ICMAB). To do so, X-Ray diffraction, Transmission Electron (TEM), Scanning Electron (SEM) and Atomic Force (AFM) microscopies were used, as described in [168].

10.3 Superconducting material: Molibdenum

Due to its chemical and mechanical inertness, high conductivity and high melting point, molybdenum has been extensively used in various technological areas. Molybdenum thin films are applied as diffusion barriers in microelectronics [169], high-temperature coating [170, 171], X-ray mirrors [172] and as the bottom electrode in solar cells [173]. The Mo deposition technique will depend on its function; in our case, to develop Mo-based transition edge sensors, the most commonly used techniques are DC and RF sputtering [160, 174, 175] and electron-beam evaporation [161, 176–178]. In most cases the substrate is heated above 500 °C to improve the superconducting properties of the film [166] and to reduce the stress [158, 178], so as to ensure sharp and reproducible transitions when fabricating TES. Mo is a highly refractory metal which oxidises easily. Thus, waiting time between Mo deposition and the next steps in the fabrication process, due to the required sample cooling down, may lead to irreproducibility problems in the bilayer properties, since the quality of the interface can be degraded [176]. Therefore, achieving good quality Mo layers growth at room temperature is specially appealing. This quality, represented by the layer functional properties (T_C and resistivity) and the substrate adherence are strongly related with the film stress. Thus, when molybdenum is grown at room temperature, a full understanding of the effects of deposition conditions on stress is required in order to reduce it.

10.3.1 Properties dependence on deposition conditions

When thin films are deposited by RF magnetron sputtering, their properties are governed by the RF power, W. Changes in W are always associated to changes in the DC bias, V_C, and therefore on the deposition rate, G_r. This variation of both the energy of the atoms reaching the substrate and its rate will affect the stress, defect structure and morphology of the films. However, as can be seen in Fig. 10.3, the three parameter determining the growth conditions- W, V_C and G_r- can be considered nearly proportional for the range studied in this work. Thus, in this section, only the dependence of T_C, ρ and stress with one of these parameters, V_C, will be considered. We choose V_C because, once the pressure and target substrate distance are fixed, the initial energy of the atoms ejected from the target is mainly determined by this parameter, and we have obtained more reproducible films when fixing its value during the deposition process.

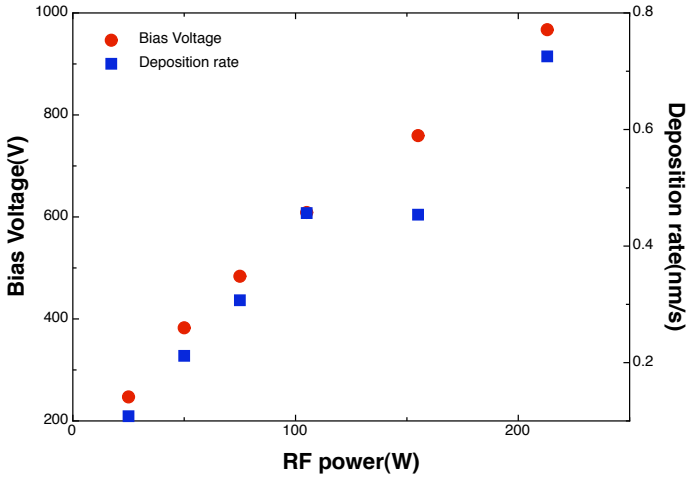

Figure 10.3: Bias voltage and deposition rate as a function of the RF power to the target, for the films studied.

Variations in stress and morphology

Typically, metal films grown at temperatures much lower that their melting temperature present a columnar structure. This is also the case of Mo films, as reported for sputtered layers, and also for the ones deposited by e-beam [179, 180]. Planar TEM and SEM images reveal that the films studied in this work are very flat –with an average roughness smaller than a nanometer– but, indeed, quite granular (Fig. 10.4). Moreover, transversal TEM images in similar films, as the one presented in Fig. 10.5a, have shown that they are made of tightly packed columns with height equal to the thickness of the films [181].

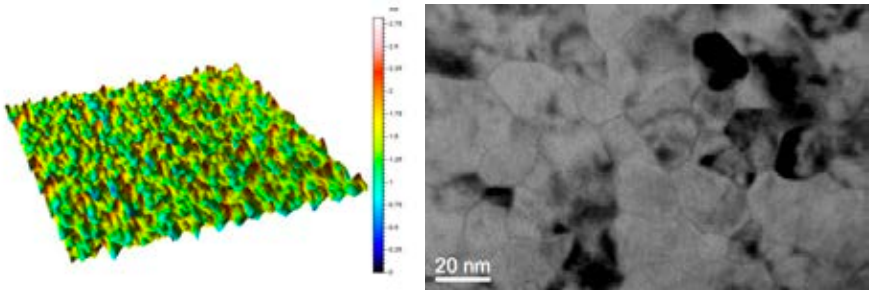

(a) (b)

Figure 10.4: (a) Planar AFM image of a 50 nm Mo film deposited at V_C=248V. (b) Planar TEM image of the film deposited at V_C=248V. *Credit: Lourdes Fàbrega and Oscar Gil.*

The surface morphology of the films does not seem to display a clear de-

pendence on V_C, in the studied range. On the contrary, as shown in Fig. 10.5b, stress is enhanced when increasing the DC bias. The stress values shown in Fig. 10.5b agree with those reported in other studies [160, 165, 180, 182–184]. Residual stress of the layers was determined with the so-called $\sin^2 \Psi$ technique [185] from X-ray diffraction data (XRD). These data, also allow us to study the crystal structure and preferential orientations of the films, revealing a preferential orientation along the (110) direction for all the samples [168, 181]. Thus, we are able to control the stress status of Mo layer without affecting the morphology just by changing a deposition parameter, in this case V_C. This control will allow us to ensure a good TES performance without heating the substrate to reduce the residual stress, as needed in films grown by e-beam [161, 186].

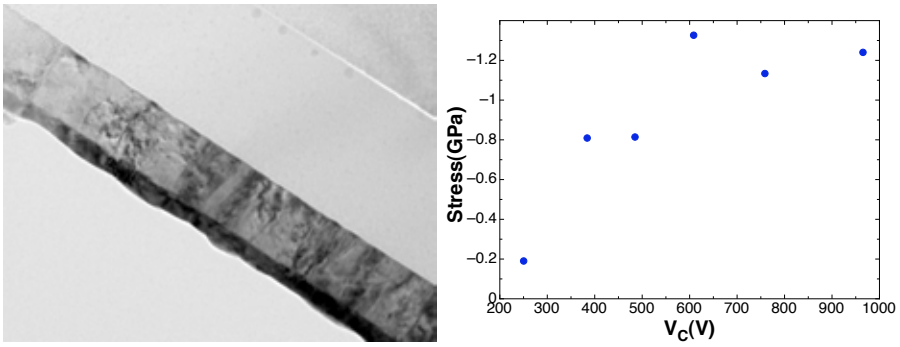

(a) (b)

Figure 10.5: (a) Transversal TEM image of a 50 nm Mo film deposited at V_C=248V with a 15 nm Au layer that prevents Mo degradation. *Credit: Oscar Gil.* (b)Residual stress of the films as a function of bias voltage V_C. The vertical axis is reversed to emphasise that the compressive stress increases with V_C.

Variations in the normal state resistivity

The variation of both resistivity and critical temperature when V_C is changed from 250 to 960 V is shown in Fig. 10.6. This figure shows ρ values for temperatures below 1.3 K of a set of Mo films with a thickness of 50 nm. This is a typical thickness value for Mo-based TES developed for X-ray detection [158, 160, 176]. As can be observed in Fig. 10.6, the residual resistivity, R_N and T_C increase as the DC bias voltage increases.

The analysis of the resistivity in a wider temperature range shows that the Residual Resistance Ratio (RRR) decreases as V_C increases, as displayed in Fig.10.7a. As it is well known, the resistivity of a metal has two components: the electron scattering with phonons and that with lattice imperfections. The first one, typically proportional to temperature, mainly depends on the phonon concentration; the second one, known as residual resistivity ρ_N, is the

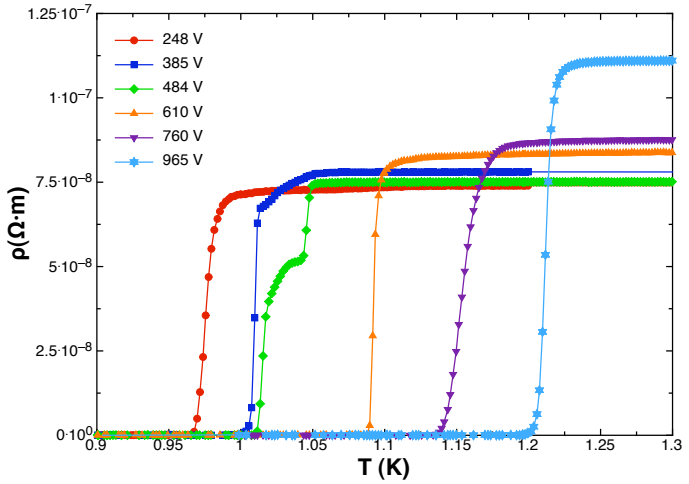

Figure 10.6: Variation of the resistivity with temperature for various films grown at different V_C.

one which dominates the low temperature behaviour. Therefore RRR, calculated as the quotient between the resistance at room temperature and the low temperature value, R_N, is an indicator of the material quality: the higher RRR, the lower R_N.

As above stated, Mo films present a columnar structure. Thus, in the films studied here, R_N is not only originated by electron collision with impurities or physical defects in the lattice, but also with grain boundaries.

In this case, the reduction in RRR values observed as V_C is increased, is exclusively caused by the degradation of the residual resistivity depicted in Fig.10.6. This can be easily checked by comparing the temperature dependent part of the various samples. As shown in Fig. 10.7b, after normalising this part to the room temperature value in order to eliminate geometrical factors, no variation of the resistance temperature dependent part with bias voltage is observed.

Since the residual resistivity is originated by electron scattering with lattice imperfections, the defects whose density is susceptible of increase with V_C will be examined, looking for the origin of changes in R_N.

In sputtered films, incorporation of impurities during deposition is possible either 1) from the residual gas or 2) from the sputtering gas (Ar). In the first case, a low deposition rate will favour the addition of impurities, therefore increasing V_C will reduce R_N, just the opposite behaviour than observed in Fig. 10.7a. In the second case, Ar concentration should increase when raising the energy of the atoms ejected from the target (i.e., increasing V_C), thus displaying

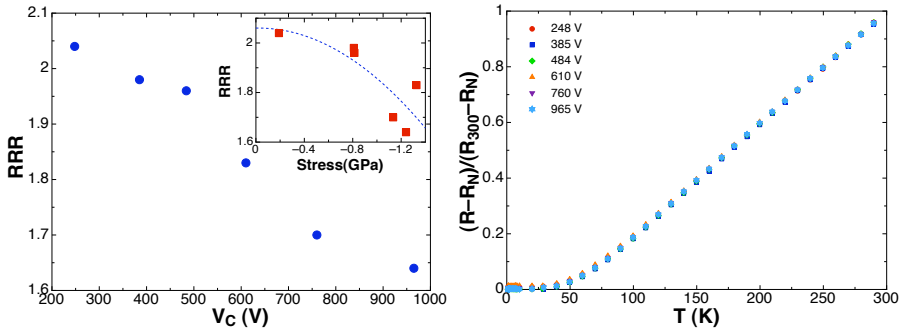

(a) (b)

Figure 10.7: (a) Residual resistance ratio RRR as a function of bias voltage Vc. Inset displays the residual resistance ratio –RRR– as a function of stress (b) Temperature dependent part of the normal state resistance for different bias voltage V_C values

a tendency similar to the dependency measured for $R_N(V_C)$. However, since no impurity traces, other than an atomic percentage of argon (<2%), have been detected by RBS in this type of samples [187] –see Section 11.7–, and the density of incorporated Ar atoms is too small, the impurities originated by the sputtering gas cannot be considered the main responsible of the observed changes in R_N (This change reaches 55% when comparing the lowest and highest V_C values: 248 and 965 V). Moreover, an atomic percentage of impurities in metals has been reported to produce a resistivity enhancement of the order of $1{\cdot}10^{-8}\Omega$m [188], several times smaller than the changes in resistivity shown in Fig. 10.6.

Another possible cause of the observed dependence of $R_N(V_C)$, once the impurities incorporated during the sputtering process have been excluded, is a change in grain boundaries. This is a well known phenomena in granular metal thin films. When the average grain size is approximately equal to the thickness of the film, one can estimate the resistivity of a granular disordered film, ρ_{film}, using the Mayadas-Shatzkes expression [189] presented in Eq. 10.1. This equation relates ρ_{films} to the bulk resistivity ρ_{bulk}.

$$\rho_{bulk} = \rho_{film} 3[1/3 - a/2 + a^2 - a^3 ln(1 + 1/a)] \tag{10.1}$$

The parameter a is defined as $\frac{R}{(1-R)}\frac{\ell_0}{D}$, where D is the average grain size in the film, R is a factor corresponding to the fraction of electrons reflected specularly at the boundary, and ℓ_0 is the electron mean free path of the metal. That means that, when D approaches ℓ_0, the resistivity of the film is very sensitive to D and can suffer a significant enhancement. For granular Mo films, ℓ_0 is 40 nm [188]. The lateral grain size of the columns in our films has been determined with TEM images at ICMAB. As displayed in Fig. 10.4b,

a considerable distribution in the lateral size and shape of the columns is observed within each film. Most of the grains are of about ∼20 nm, but there are larger ones, of the order of 35-40 nm, as well as a few even larger (∼70 nm). The boundaries of the grains are sometimes diffuse or difficult to discern; it might very well be that these larger grains are in fact an agglomeration of smaller ones. Thus, on average, lateral grains size is of the order of ℓ_0 or smaller, what makes grain boundary scattering a plausible explanation for the observed increase of ρ_N. Moreover, an increase in the growth rate should reduce grain size and therefore, make grain boundary scattering more relevant. However, since no clear variation of grain size distribution as a function of V_C has been observed, likely due to the large dispersion in grain sizes, it was not possible to directly corroborate this hypothesis from experimental data.

Nevertheless, some estimates can be done, in order to deduce if variations in D within the observed dispersion could account for the changes measured in the resistivity. Using D=25 nm and ρ corresponding to the film grown at the lowest V_C, Eq. 10.1 allows to estimate R ∼0.4, a value consistent with literature [179, 190]. Assuming R constant, a grain size of D=20 nm would explain the resistivity of the film grown at the highest V_C, thus proving that ρ is very sensitive to small changes –within our experimental dispersion– in the grain size D. It must be noted that, as it will be explained later, in our films ℓ_0 is limited by the lateral grain size, being the estimated mean free path ∼ 20 nm, smaller than the one used here. However, when considering $\ell_0 = D$ the estimated R is also ∼ 0.4, thus the above conclusion on the possible origin of ρ enhancement remains valid. Finally, even though the resistivity of metals is quite insensitive to stress, because it produces tiny changes of the lattice parameters, it may have indirect effects. An example of these effect is the possible increase in the density of structural defects and morphology changes, including a reduction of grain size. Therefore, although grain boundary scattering can be assumed to be a good candidate to account for the behaviour observed in Fig. 10.7a, the observed increase of stress with V_C can also contribute to explain the enhancement of residual resistivity discussed above.

Variations in the superconducting critical temperature

As shown in Fig. 10.6, in all the cases T_C values are higher than the one corresponding to bulk Mo (T_C^{bulk} = 915 mK). Moreover a gradual enhancement of T_C is observed when raising V_C. To understand the mechanism responsible of the observed T_C changes, one need to focus on the different factors that vary with V_C, that is, the stress and RRR, as depicted in Fig. 10.7a and 10.5b. From Fig. 10.8, one can conclude that, the enhancement of T_C may be originated by an increase of the residual stress or a reduction of RRR. However, since within

the BCS theory, changes of T_C –either enhancement or suppression–are the result of changes in the density of states or in the electron-phonon coupling, it is necessary to establish what are the consequences of the changes in RRR and stress.

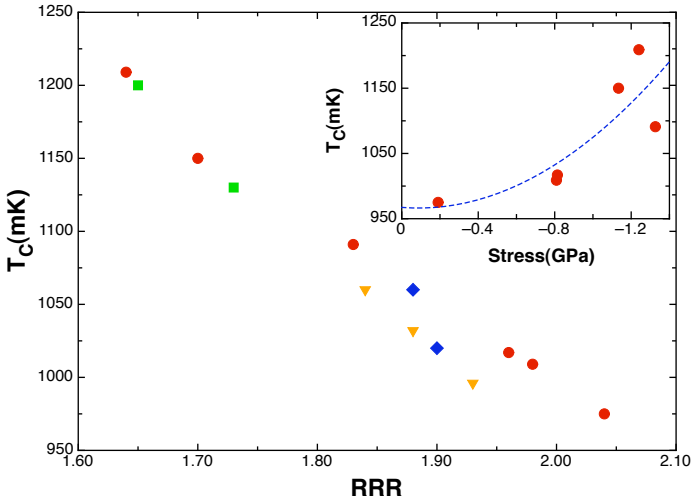

Figure 10.8: Variation of the critical temperature with RRR for various films grown at different V_C. Each type of symbol stands for a series of samples grown changing V_C. Inset: Variation of the critical temperature with stress for sample series represented by •.

Regarding the stress, it is well known that it can produce large changes in T_C, since it may change both the electronic structure and the phonon spectrum of a material [191–194]. Previous studies have emphasised its influence in Mo films T_C. For films deposited by e-beam, T_C and RRR rise as tensile stress is suppressed [158, 161, 165–167]. For DC magnetron sputtered films, reports stated that the best T_C (∼1-1.4 K) and reproducibility are obtained for slightly compressed films (σ ∼ -100 MPa) [160, 165].

However, as depicted in Fig.10.8 the existing dependence of T_C with stress is less neat than the dependence on RRR. Moreover, Fig. 10.8 shows that this dependence is highly reproducible, being the same for different series of samples grown changing V_C while keeping the other parameters constant. However, such dependence is found to be quite anomalous among classical metal superconductors. Indeed, the T_C of most of them (Nb,Ta, V, Al...) gets lower when increasing residual resistance (mainly because of impurity incorporation), which has been explained by a reduction of the mean free path [191, 195]. It should be stated, however, that a rise of T_C with increasing ρ_N is possible, depending on the origin or type of defects dominating the residual resistance and their influence in the density of states or the electron-phonon

coupling. McMillan [143] showed that metals with weak electron-phonon coupling and low T_C, like Mo, could display large increases in T_C upon decreasing the average phonon frequency. In fact, Kar'kin et al. [196] have reported that binary superconducting compounds with Mo or Nb, behave in different way under pressure. While for Nb compounds T_C clearly increases with RRR, Mo compounds display a less clear trend, with a tendency of T_C to increase for decreasing RRR; the authors have argued that this different behaviour must be related to distinct changes of the electron and phonon spectra of Nb and Mo associated to microstresses, which could also explain the anomalous $T_C(RRR)$ in our Mo films.

As it is the case of $\rho_N(V_C)$, the percentage of Ar impurities incorporated during deposition is too small to explain the significant rise of T_C with V_C. But there is still another possible origin of this dependence that need to be examined: the granular character of the films, which we have considered as a very likely cause for the changes of ρ_N. It has been argued [197] that, in granular films the average ionic vibration amplitude increases because the ionic restoring forces are weaker at the grain surfaces, due to reduced symmetry. This effect implies an increase of the phonon amplitude and a reduction of their average frequency, causing an increase of the electron-phonon coupling and therefore an increase of T_C. As above explained lattice disorder also leads to changes in the electronic band structure, modifying T_C. However, this effect, specially relevant in amorphous films and alloys of simple metals, is negligible compare with the enhancement of the electron phonon coupling for granular films [197].

In summary, both the enhancement of T_C in comparison to Mo bulk and the $T_C(RRR)$ dependence could be explained by changes in the electronic density of states caused by compressive stress, or by an increase of electron-phonon coupling associated to stress or to progressively reduced grain size.

Standard deposition conditions

The results discussed in this section, allow us to establish the optimum deposition conditions for Mo thin films of 50 nm thickness intended for TES fabrication. As explained above, this includes minimising stress and ρ_N, and ensuring a T_C value as close as possible to the bulk one. These conditions are fulfilled by a V_C value of 248 V, thus a RF power of 25 W, and an argon pressure of 0.5 Pa. Results from samples prepared in different moments along 2 years and, therefore with different Mo targets, are shown in Fig. 10.9. In all the cases T_C reproducibility is high, a maximum deviation of 50 mK has been found, although some transitions are quite broad, due to the wide extent

of the samples studied in this section, $\sim$ 2.5mm. To avoid a possible masking by chemical processes of the effect that different deposition parameter have on Mo properties, these films where not lithographed to reduce the sensed area. Thus, inhomogeneity effects due to the relatively big studied areas are found. Changing Mo targets and some improvements performed in the sputtering system have, however, an effect on the resistivity of the samples, originating a distribution of ρ_N values, ranging from 4 $\mu\Omega$cm to 8 $\mu\Omega$cm. This distribution is translated to ρ_{300} from 10$\mu\Omega$cm to 15 $\mu\Omega$cm, values that agree quite well with those typically reported for Mo thin films [158, 160, 161, 165–167, 181] and are up to a factor of 3 higher than those for bulk Mo, ρ_{300}^{bulk}=5.3 $\mu\Omega cm$.

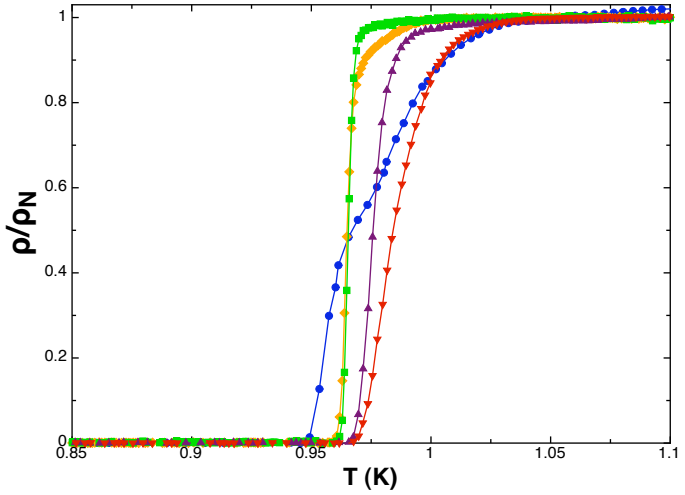

Figure 10.9: $\rho/\rho_N(T)$ curve of 50 nm Mo films deposited at V_C=248V and Ar pressure of 0.5 Pa.

10.3.2 Size effects in Molybdenum layers.

Since Mo thickness will be changed when fabricating Mo/Au TES to tune the T_C of future devices, we need to ensure that no effects on Mo functional properties –ρ_N and T_C– due to thickness reduction are found in the working values ($\sim$ 50 nm). This reduction has been previously observed in metallic samples having some physical dimension comparable to the electron mean free path [198, 199]. Since precedent works on Mo granular films suggested a ℓ_0 of 40 nm [188], similar to the depth of samples studied in Section 10.3.1, these size-effects cannot be obviated.

Even when superconductivity in Mo was discovered, nearly 50 years ago [200], the superconducting properties of this metal have been poorly investigated. According to existing studies, Mo has been shown to be a classical type

I superconductor extremely sensitive to impurities [201, 202], weakly coupled, with critical temperature T_C= 915 mK and critical field H_C= 98 Oe [203–206]. Nevertheless, as far as we know, no experimental data on fundamental parameters such as penetration depth (λ) and coherence length (ξ) are available in literature for Mo thin films. These parameters have only been estimated for Mo bulk to be $\lambda \approx$96 nm and $\xi \approx$271 nm by French [207], from indirect calculations using other reported data [188, 204, 205]. The uncertainty in these estimates is high, and the reported values can be considered an upper and a lower limit of λ and ξ, respectively, since, as the author states, surface roughness or a high resistivity surface layer will lead to an alteration of both λ and ξ.

In granular films, a transition 3D-2D character has been reported to occur when the film thickness becomes equal to the coherence length [208]. Since the disorder both enhances λ and reduces ξ [209, 210],the granular character may affect the dimensional crossover and the onset of finite thickness effects. Moreover, for type I superconductors, as Mo is reported to be, a transition from type I to type II may occur for thin enough films. The changes in dimensionality and superconductivity type can result in significant modifications of the behaviour of the superconducting thin films under magnetic field, since the critical fields can considerably change. Moreover, a 2D superconductor displays the Kosterlitz-Thouless transition [211, 212], which demarks the spontaneous generation of vortex-antivortex pairs in zero field, due to fluctuations. In fact, it has been shown very recently that vortex motion is one of the fundamental processes responsible for excess noise in TES devices [213]. Therefore, a clear determination of the superconductivity character in Mo thin films is crucial to understand the different noise sources of our future Mo-based TES.

Mo thin films with thickness (d) ranging from 13 to 83 nm were analysed by measuring $\rho(T)$ and T_C both with or without applied magnetic field. X-ray reflectometry measurements performed by Lourdes Fàbrega were used to determine film thickness. Structural characterisation, as explained in the previous section was performed by X-ray diffraction. Both grain size and texture degree do not depend on width: all films are textured along the (110) crystallographic direction and display columnar growth, with a column width of about 20 nm.

Influence of thickness in Mo functional properties

As shown in Fig. 10.10, residual resistance is enhanced for $d \leqslant 30$ nm when reducing d, and the opposite behaviour is observed for T_C. For $d > 30$ nm the thickness dependence saturates to the values reported on the previous section as the optimum ones. The room temperature resistivity (not shown

here) displays nearly the same dependence as ρ_N, indicating that ρ_N is the responsible of the observed variation in resistivity. As explained in Section 10.3.1 this can be checked by comparing the resistance temperature dependent part of the various samples, after eliminating geometrical factors. As expected, no variation of this resistance part with d is observed.

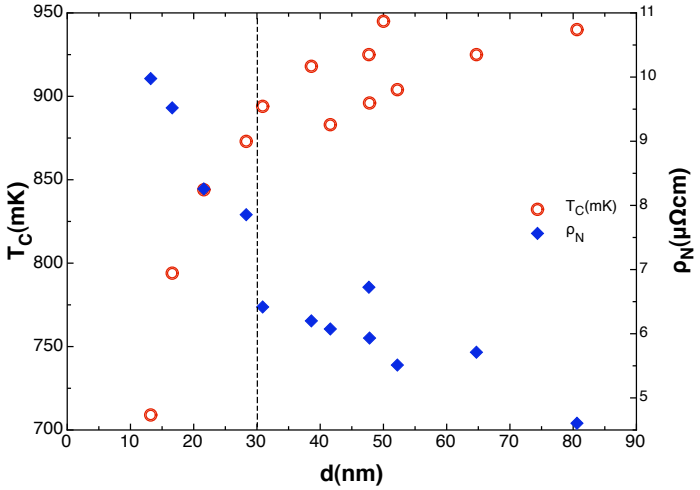

Figure 10.10: Variation of critical temperature and residual resistivity with film thickness d.

The measured changes in ρ_N and T_C might have several origins beside thickness effects, such as stress and impurities. To exclude the last two, their possible contribution needs to be analysed. The evolution of the lattice strain and that of the residual resistance ratio, RRR, with thickness for some of the samples are depicted in Fig.10.11a. Regarding stress, for films thinner than ∼25-30 nm, a rather high in-plane tensile strain is found, which relaxes when increasing d until thickness values ∼50 nm are reached, where samples are nearly relaxed. It must be noted that deposition conditions, as described in Section 10.3.1, were selected to optimise functional properties of 50 nm Mo films, this includes minimising the strain state. For films thicker than ∼50 nm stress changes sign and a compressive in-plane strain is found.

The RRR curve shows the opposite behaviour: its value monotonously increases with d until thickness close to 50 nm, where RRR shows a maximum, for $d > 50$ nm RRR decreases as thickness increases. This last dependence has been already explained in Section 10.3.1, where RRR and stress are related through the enhancement of electron scattering. Nevertheless, when plotting the dependence of T_C with RRR and stress (Fig. 10.11b) the behaviour is completely different from the one observed in Fig. 10.8. In the present case, T_C increases with RRR reaching a saturation value for RRR$\geqslant$2, while it decreases as stress increases, without a net dependence. In the case discussed in Section

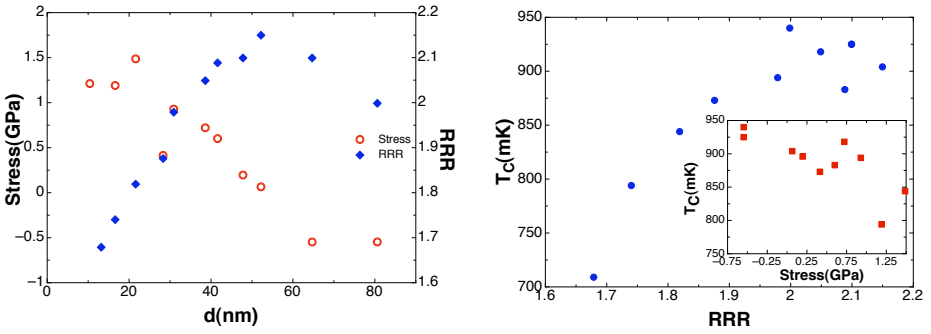

(a) (b)

Figure 10.11: (a) Variation of stress and residual resistance ratio with film thickness, d. (b)Variation of the critical temperature with RRR for various d. Inset: Variation of the critical temperature with stress.

10.3.1, $T_C(RRR)$ is a nearly linear decreasing function without a tendency to saturate; dependency that could be explained by an increase of electron-phonon coupling associated to stress, as displayed by the exponential increase of T_C with stress. The remarkably different behaviour of Mo functional properties in both cases - changing V_C or d- leads to the conclusion that the observed changes in T_C and ρ_N for films thinner than $\sim$ 50 nm have an origin completely different than those due to stress.

Regarding impurities, as above discussed, no other components beside argon were found when analysing this type of layers by RBS, being this quantity too small to produce any remarkable change in T_C or ρ_N.

All these arguments evidence that the clear changes of both T_C or ρ_N observed for films thinner than $\sim$30 nm should be associated to size-effects, as expected for samples having some physical dimension comparable to the electron mean free path [198, 199]. No thickness effects are observed for d >30 nm, thus our 50 nm optimised Mo films are suitable for TES fabrication, anyhow, a more detailed analysis on the possible causes of ρ_N and T_C changes with thickness is described in following subsections, for the shake of completeness.

Influence of thickness in Mo $\rho_N(d)$: As it is known, the resistivity depends on sample dimensions when the contribution to the resistivity arising from surface scattering of conduction electrons can no longer be ignored. For films in which the thickness dependence has been attributed to surface scattering, experimental data have been commonly analysed on the basis of Fuchs theory, that determines the total resistivity of a film by imposing a boundary condition on the electron-distribution function, which enhances the thickness-independent bulk resistivity [198]. This theory does not consider grain boun-

daries effect on resistivity, since usually the grain size is much larger than the mean free path, limited by other scattering processes, and thus, grain boundary contribution can be neglected. However, for polycrystalline films, Mayadas et al. [189] showed that a strong thickness dependent resistivity, comparable in magnitude to the Fuchs effect, exist if $D \approx d$. Since, in the present case, the average grain size and the thickness of the film are considered as equal, a parameter in Mayadas-Shatskes resistivity (Eq. 10.1) can be also written as $\frac{R}{(1-R)}\frac{\ell_0}{d}$. Moreover, in our case the expected mean free path - Mo ℓ_0 of 40 nm [188]- is of the same order of magnitude as d, even smaller in some samples, thus, assuming $R \sim 0.4$, as estimated in Section 10.3.1, and $a \lesssim 1$ [214], Eq. 10.1 can be approximated as:

$$\rho = \rho_\infty(1 + \frac{3a}{2}) = \rho_\infty(1 + A\frac{\ell_0}{d}) \tag{10.2}$$

Where A is a factor equal to $\frac{3R}{2(1-R)}$ and of the order of the unit, R is the reflection coefficient, ρ_∞ is the resistivity of thick enough films (notice that this value may differ from that corresponding to the bulk metal, ρ_{bulk}, if the films are granular, because of the resistivity enhancement due to grain boundary scattering [199]. The dependence of ρ_N on the reciprocal thickness is shown in Fig. 10.12, where data clearly follow the behaviour expected from Eq.10.2. Moreover, assuming $A \sim 1$ –as expected from theory and from our estimated R value, $R \sim 0.4$– from the linear fit, ℓ_0 is estimated to be ∼19 nm, thus the mean free path value is very close to the column width of the films. This result points out that the resistivity in room temperature sputtered Mo films is dominated by grain boundary scattering, as argued in Section 10.3.1, and consequently finite thickness effects in resistivity become relevant when d is comparable to the grain size.

Influence of thickness in Mo $T_C(d)$: In Fig.10.10, it was shown that not only ρ_N changes with thickness, also T_C is strongly reduced for films thinner than ∼ 30 nm. The T_C suppression due to finite thickness effects can be due to two mechanisms: the weak localisation effects due to surface scattering [215], or the contribution to the superconducting free energy of the surface term, which becomes relevant for thin films when surface-to-volume ratio is dominant [216]. To determine which of these two mechanism is the main responsible for the observed T_C suppression, experimental data were interpreted in terms of both models. According to the Maekawa and Fukuyama theory, the localisation reduces T_C because the Coulomb repulsive interaction between electrons is enhanced and the electronic density of states depressed. This theory, only valid for 2D superconductors, like the films discussed here, allows us to estimate the critical temperature as a function of the sheet resistance –$R_\square$– and the effective

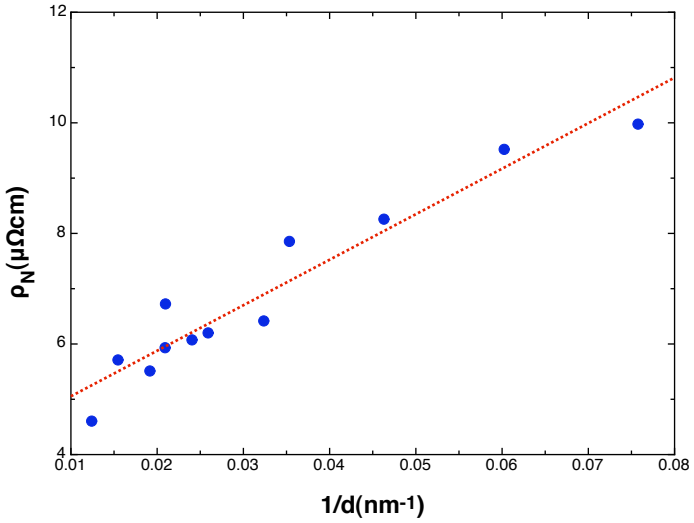

Figure 10.12: Linear dependence of ρ_N with $1/d$. Dash line is the fit of $\rho_N(1/d)$ to Eq. 10.2

coupling constant $g_1 N(0)$, the only fitting factor in the model:

$$ln\left[\frac{T_C}{T_{C0}}\right] = -\frac{1}{2}\frac{g_1 N(0) e^2 R_S}{2\pi^2\hbar}\left[ln\left(5.5\frac{\xi_0}{\ell_0}\frac{T_{C0}}{T_C}\right)\right]^2 - \frac{1}{3}\frac{g_1 N(0) e^2 R_S}{2\pi^2\hbar}\left[ln\left(5.5\frac{\xi_0}{\ell_0}\frac{T_{C0}}{T_C}\right)\right]^3 \quad (10.3)$$

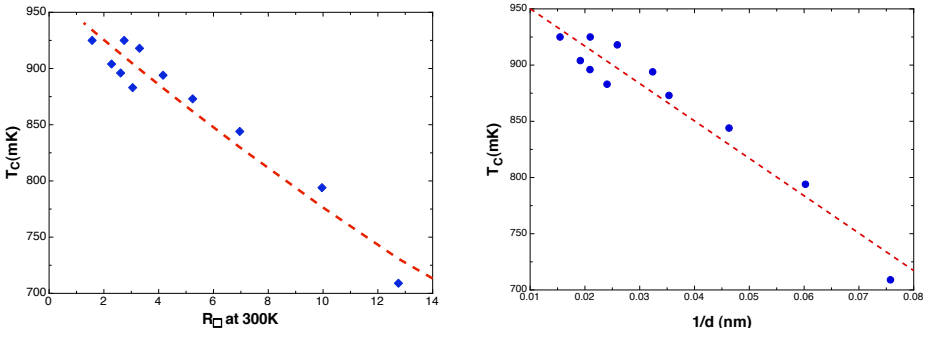

(a) (b)

Figure 10.13: (a) Solid points represent variation of critical temperature with sheet resistance for different film thickness, d, dash line is the fit of $T_C(R_\square)$ to Eq. 10.3. (b) Solid points represent variation of critical temperature with film thickness, d, dash line is the fit of $T_C(d)$ to Eq. 10.5

with T_C0 the bulk critical temperature and ξ the BCS coherence length, estimated by French et al. to be $\xi \approx 271$ nm [207] for Molybdenum, being this value, as above explained, a lower limit due to uncertainty in the estima-

tion. In this expression the first term is due to the reduction of the density of states because of localisation and second term is the vertex correction to the electronic interaction. The effect of localisation is specially important in the dirty superconductor limit, as in our case, since $\xi_0 >> \ell_0$ makes the first term in the bracket negligible, and a nearly linear dependence of T_C is expected [217, 218]. As shown in Fig.10.13a, the measured $T_C(R)$ curve can be fitted to this dependence but the slope obtained from the fit, when using ξ_0= 271 nm and ℓ_0 = 20 nm, provides an unphysical $g_1N(0)$ value –$g_1N(0)$=4–, while it should be similar to one. Therefore, the weak localisation effect cannot be considered to be the main responsible for the observed suppression of T_C at small d.

Initially, the suppression of T_C observed in different materials as aluminium or niobium when thickness decreases was explained by the presence of a proximity effect caused by a normal-metal layer on top of the superconductor sample [219, 220]. To do so the model developed by Cooper [221] for films thinner than the superconducting coherence length was used.

$$T_C = T_{C0} e^{\frac{-2a}{N(0)Vd}} \tag{10.4}$$

However Simonin [216] showed that a similar expression for $T_C(d)$ could be obtained by introducing an extra term for surface contribution to the Ginzburg-Landau free energy. This allows to obtain the same decrease of the density of states near the surfaces as in Cooper's law without introducing an extra "non-superconductive" layer. Moreover, Cooper's law cannot explain the dependence of T_C with $1/d$ for small d values and the sample response to applied magnetic fields.

In Simonin model expressed as Eq. 10.5, a_F is the Thomas-Fermi screening length and $N(0)V$ is the bulk interaction potential.

$$T_C = T_{C0}\big(1 - \frac{2a_F}{N(0)Vd}\big) \tag{10.5}$$

The T_C as a function of the reciprocal thickness for all characterised films is depicted in Fig. 10.13b. A nearly linear dependence of T_C on $1/d$ is observed. To fit these data to Eq.10.5 an estimated value of $N(0)V$ is needed. T_C/θ_D in Mo is equal to 0.002, according to Mallon et al. [203], where θ_D is the Debye temperature, defined as $\theta_D = \hbar\omega_D/k_B$. Thus, since in the BCS theory the critical temperature can be expressed as a function of the electron-phonon coupling as presented in Eq.10.6

$$T_C = 1.14\frac{\hbar\omega_D}{k_B} e^{-\frac{1}{N(0)V}} \tag{10.6}$$

one can assume that $N(0)V$ =0.157 for Mo. Using this value, the Thomas-Fermi screening length is calculated to be 0.3 nm; a value in excellent agreement with that reported by Boucher et al. [222], λ_F=0.365 nm. Thus, data analysis evidence that the reduction of the order parameter near the superconductor surfaces seems to be the main responsible for the finite thickness effects in the T_C suppression mechanism for the studied films.

Magnetic field effects in Mo thin films.

Previously, on this section, we have been focusing on how Mo functional properties (T_C, ρ_N or transition sharpness) are affected by size effects, since they will limit the detector performance. All of them are directly related to the electric and superconducting properties of layers, thus, a deep understanding of the fundamental physics that governs the superconducting-to-normal transition of these devices is essential for optimising their design.

In order to investigate the critical field and to find out if Mo thin films are type I or type II superconductors, their electrical and superconducting properties were investigated as a function of an external magnetic field, H. Magnetic fields have been applied both perpendicular an parallel to the film plane, to the sample series described at the beginning of Section 10.3.2.

In Fig.10.14a resistive superconducting transition for a film with $d \approx 80$ nm, under several magnetic fields applied perpendicular to the film plane are displayed. As expected, the transition shifts towards lower temperatures when increasing the magnitude of the external magnetic field. According to literature, the thermodynamic critical field of bulk Mo, which is known to be a type I superconductor, is ∼98 Oe [203–206, 223]. However, Fig.10.14a shows that superconductivity is still present in the film up to 370 mK for an applied field of 220 Oe.

As it is well known the superconductor type depends on the ratio between the penetration depth and the coherence length, $\kappa \equiv \lambda/\xi$. Moreover, the superconducting purity may affect these characteristic lengths. Since for the analysed films ℓ_0 has been estimated to be ∼20 nm, and the lower limit of the Mo coherence length has been reported to be ξ_0 ∼271 nm [207], one can conclude that these Mo films are in the dirty limit ($\ell_0 << \xi_0$). For dirty superconductors, the fundamental superconducting lengths must be renormalised according to the following expressions [224]:

$$\xi(0) \approx 0.85\sqrt{\xi_0 \ell_{eff}} \qquad \lambda_{GL} \approx \lambda_L(0)\Big(\frac{\xi_0}{1.33\ell_{eff}}\Big)^{1/2} \tag{10.7}$$

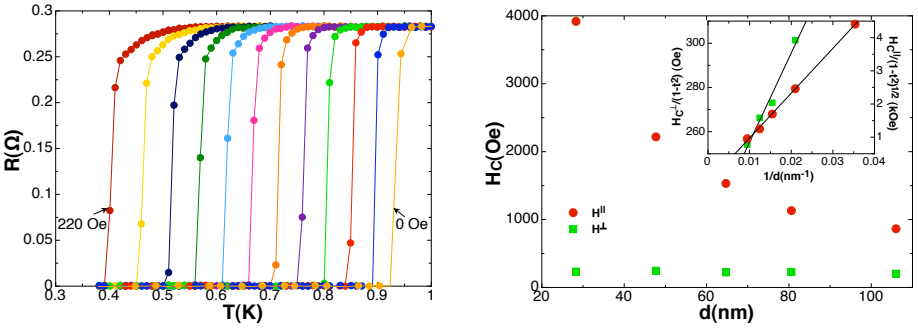

(a) (b)

Figure 10.14: (a) R(T) curves under magnetic field applied perpendicular to the film with thickness $d = 80.6$ nm. Curves were measured between 0 and 220 Oe with increases of 20 Oe. (b). Critical fields measured parallel (•) and perpendicular (▪) to the film surface as a function of the thickness. Inset: Corrected parallel (•) and perpendicular (▪)critical fields as a function of the reciprocal thickness.

where $\xi(0)$, $\lambda_{GL}(0)$ and $\lambda_L(0)$ are the zero temperature Ginzburg-Landau coherence length, the penetration depth and the London penetration depth respectively, and ℓ_{eff} is the effective mean free path. These equations evidence that, for a dirty superconductor, the coherence length and the penetration depth are correspondingly directly and inversely proportional to $\ell_{eff}^{1/2}$. Thus, an enhancement in the κ parameter value is expected when reducing the mean free path according to:

$$\kappa \approx 0.74\lambda_L(0)/\ell_{eff} \tag{10.8}$$

By inserting in Eq. 10.8 the λ_L value reported for Mo ($\lambda_L(0) = 96$ nm) [207], which was argued to correspond to an upper limit, we obtain that, when ℓ_{eff} is lower than ~ 140 nm, Mo should behave as a type II superconductor. Therefore, Mo films studied in this work are expected to behave as type II superconductors, and consequently the critical field obtained from $R(T, H)$ measurements should correspond to the upper critical field H_{c2}.

In Fig. 10.14b, the critical field values obtained for H applied perpendicular ($H^{\perp}$) and parallel ($H^{\parallel}$) to the film plane, are plotted as a function of d. The critical fields $H_C^{\perp}$ and $H_C^{\parallel}$ were determined from the middle point of the $R(H)$ transition recorded at 400 mK. The graph evidences that the critical field is highly anisotropic and thickness dependent, and that for both directions superconductivity persists up to fields much higher than the earlier reported thermodynamic critical field.

Since the critical fields were measured at different reduced temperatures

($t = T/T_C$) because of the different T_C's of the films, the experimental values presented in Fig. 10.14b need to be corrected. For a film in the perpendicular orientation, the upper critical field H_{c2} can be written as [224]:

$$H_{c2}^{\perp}(T) = \sqrt{2}H_C(T)\kappa \approx H_C(T)\lambda_L(0)/\ell_{eff} \tag{10.9}$$

where $H_C(T)$ is the thermodynamic critical field of the superconductor. Thus $H_C^{\perp}(d)$ data can be corrected by using the conventional Ginzburg-Landau approximation, $H_C(T) \propto (1-t^2)$.In the case of a film in the parallel orientation, H_{c2} expression depends on the superconductivity character. Considering the earlier reported lower limit for the coherence length value of Mo, $\xi_0 \approx$271nm [207], Eqs. 10.7 indicate that for the studied thickness range, $\xi(T) > d$, which points out that the analysed films might be 2D superconductors. In that case H_{c2} can be defined as [208]:

$$H_{c2}^{\parallel}(T) = \frac{\sqrt{12}\phi_0}{2\pi\mu_0\xi(T)d} \tag{10.10}$$

In this case, data are corrected considering the approximation for the Ginzburg-Landau temperature dependence of $\xi(T) \propto \sim (1-t^2)^{-1/2}$. The corrected data are depicted in the inset of Fig.10.14b. Both $H_C^{\perp}$ and $H_C^{\parallel}$ display a linear dependence on $1/d$, but with quite different slopes.

As shown by Eq.10.2 and [198], the effective mean free path –ℓ_{eff}– is thickness dependent and can be approximated to:

$$\frac{1}{\ell_{eff}}(d) = \frac{1}{\ell_0} + \frac{A}{d} \tag{10.11}$$

where ℓ_0 is the mean free path of an infinitely thick film. By linearly fitting data presented in Fig. 10.14b an estimation of $A\ell_0 \sim 21$ nm is obtained, in excellent agreement with that previously found from the $\rho(d)$ dependence. Also, by assuming $H_C =$ 98 Oe [203–206], the fit provides an estimate of 44 nm for $A\lambda_L(0)$, somehow smaller than the value derived by French [207] which was in fact considered an upper limit for the penetration depth, as argued at the beginning of Section 10.3.2.

Focussing on the data for magnetic field applied parallel to the film, the linear fit to Eq. 10.10 provides $\xi(0) \approx 85$ nm. Inserting this value in Eq. 10.7 and using $\ell_{eff} \approx \ell_0 \approx 20$ nm, an estimate for $\xi_0 \approx 500$ nm is obtained. This value is larger than the reported $\xi_0 \sim$271 nm [207], which was argued to correspond to a lower limit, and corroborates the assumed 2D character of the Mo films.

10.4 Normal metal materials: Copper and Gold

Besides superconducting material properties, the normal metal layer deposited on top of it will also govern the TES final performance, not only through its functional properties –mainly residual resistance– but also through the proximity effect, limited by the quality of the superconducting-metal interface. As described above, both gold and copper are good candidates for Mo-based TES, since no intermetallic phases or interdiffusion when combined with molybdenum is expected at working temperatures. Moreover, Au is highly resistant to corrosion [158].

A key point for TES fabrication is to achieve a low R_N value. Reducing this value will reduce noise in our device by reducing thermodynamic fluctuations associated with electrical resistance (Johnson noise, which is proportional to R_N) and, therefore, increase the energy resolution of the final sensor.

Moreover, a low R_N will also provide a better stability to phase separation. Every resistance has an associated Joule heating, that could create a set of different temperatures across the film, generating larger transition widths and, thus reducing the TES sensitivity and affecting the time response. Moreover, if regions with different temperature are placed perpendicularly to the current flow, regions with higher temperature will have higher Joule power dissipation, which could lead to geometrical phase separation into superconducting and normal regions [131]. This self-heating effect depends on the residual resistance of the sensor through the thermal conductance, on sensor geometry and on the dominant thermal conductance process. When the heat flows uniformly from the TES to the heat bath, the condition for stability against phase separation in a rectangular film, like the one we are developing, can be approximated as Eq.10.12 [225]

$$R_N < \frac{L_n T_C n}{G\alpha} \tag{10.12}$$

where n is the exponent of power flow to the heat bath and depends on the dominant thermal flow process between the heat bath and the electrons in the sensor. G is the thermal conductance to the heat bath and α is the sensitivity of the superconducting transition, defined as $\alpha = dlogR/dlogT$. As reported by Irwin et al. [225], in a typical X-ray microcalorimeter, where the dominant thermal conductance is the electron-phonon coupling, $n \sim 4$, self heating effect should be negligible if $R_N < 0.1\Omega$ [225]. In this calculation, an α value of 100 and a G value of 1 nW/K were considered. However, typical α values are considerably higher. Taking the average α value obtained in our lithographed bilayers, 550, –see Chapter 12–, and $G = 0.3$ nW/K, the value of

membranes similar to the ones used in this work [152], the stability condition will be even lower: $R_N < 0.06\Omega$.

This low R_N value reduces the possible metals for the normal layer to one of the noble metals: Au, Ag or Cu. Among these metals, Au and Cu were chosen because of the extensive work already existing on both Mo/Au and Mo/Cu sensors with proved excellent results [158, 160, 161].

Given that both metals are better electrical conductors than Mo, the final device residual resistance will be mainly due to the metal layer ρ_N. For all the reasons above described, reducing normal metal layer residual resistance, and thus TES residual resistance, is crucial to ensure an optimal sensor performance. This key functional property, together with film stress and morphology will be analyse and discussed in Sections 10.4.1 and 10.4.2 for two different deposition methods: DC triode sputtering and electron beam, to secure that the required normal metal layer quality for TES fabrication is achieved.

10.4.1 Metal layer morphology

Metal layer morphology and stress were studied for normal layers deposited on top of 50 nm Mo layers grown at standard conditions, to ensure that the effect of deposition over a columnar metallic layer is taken into account and, therefore, observed results correspond to the ones of metal layer in final sensors. As in the Mo case, XRD data, obtained by Dr. Lourdes Fàbrega, allow us to determine crystal structure and preferential orientations of films. For Au films, both sputtered and deposited by e-beam films are partially textured, with the (111) planes along the growth direction. A loss of texture is appreciated for thicker films as shown in Fig.10.15a. In this plot samples with a 15 nm sputtered Au layer are covered by an extra gold layer deposited by electron beam, no change in crystal orientation is observed. Cu films were only deposited by sputtering, being fully polycrystalline with no preferential orientation along the growth direction (Fig.10.15b).

As shown in Fig. 10.5a, and in [181] both Cu and Au sputtered layers follow the columnar growth of underlying Mo films, whereas Au grown by e-beam usually displays twin boundaries parallel to the interface. Although Au layers display a weakly tensile residual stress ($\sim$ 70 MPa) and Cu one is higher ($\sim$400MPa) [181], no significant change in Mo stress state is observed when normal metal layers are deposited on top of superconducting layer. This ensures that good performance of Mo 50 nm grown under standard conditions is not compromise by normal layer deposition.

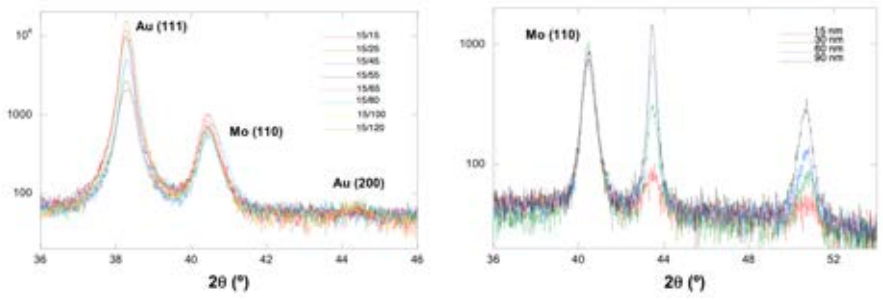

(a) (b)

Figure 10.15: (a) XRD ($\theta - 2\theta$ scan) for a Mo/Au series 50 nm of Mo and two different Au layers: a constant 15 nm sputtered layer and a thickness variable e-beam deposited Au layer. (b) XRD ($\theta - 2\theta$ scan) for a Mo/Cu series 50 nm of Mo and different thickness copper layers. *Credit: Lourdes Fàbrega.*

10.4.2 Metal layer normal resistance by sputtering and electron beam deposition

The gold resistivity in a bulk sample is expected to be ∼ 5.44 nΩm at 90 K [226]. This value is enhanced by various orders of magnitude for sputtered gold samples. Fig. 10.16a displays the resistivity of several 150 nm-thick Au films on Si substrates covered by a 300 nm Si_3N_4 layer, deposited at different conditions and with different techniques. For sputtered films deposited with a commercial magnetron at cathode voltages, V_C, ranging from 1 kV to 2 kV, the obtained ρ values at 90 K vary from 70 to 111 nΩm, being these results in good agreement with the ones reported by Toombs et al. [227]. To reduce this voltage as much as possible a specially designed magnetron was coupled to Au target reaching V_C=387 V and ρ_{90K}= 29 nΩm.

Considering that all the sensor designs analysed in this work are square shaped, –see Section 11–, that the usual Au thickness for Mo/Au TES reported in literature, ∼200 nm [161, 228] and that sensor R_N is mainly due to normal metal resistivity, the lowest residual resistance achievable with sputtered gold can be estimated as R_N= 0.11 Ω. Previous studies showed that resistivity in gold sputtered films does not display any thickness dependence for $d \gtrsim 40$ nm [229], thus one can assume the same resistivity value for 200 nm films as the one determine for our 150 nm films. As explained at the beginning of this section, this residual resistance is not low enough to neglect self heating effect and thus, phase separation could occur if sputtered gold was used to develop our sensors.

It has been found that Au films resistivity changes substantially with heat treatment [227], however the associated improvement is not enough to en-

sure the absence of self heating effect. In addition, although Mo/Au systems do not have intermetallic phases, annealing processes slightly modify bilayer functional properties T_C and R_N, as it will be discussed in Section 11.7, thus discarding the use of heat to achieve the required R_N. Gold layers with a good enough quality to be used as TES normal metal layer can be prepared with electron beam deposition, as shown in Fig. 10.16a. Resistivity in this case, $\rho_{90K} \sim 9$ nΩm, is equivalent to other evaporated films [230] and R_N is expected to be similar to 0.01 Ω. As in the sputtered case previous studies on evaporated gold films determined that no thickness dependence of resistivity is expected for $d > 60$ nm [229], allowing to estimate R_N for a 200 nm Au film from our data.

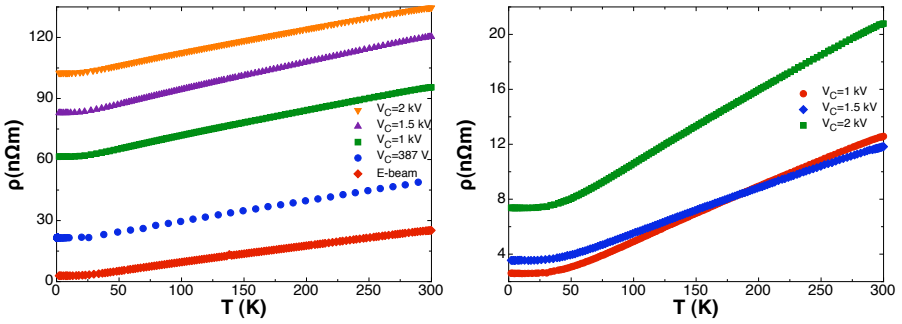

(a) (b)

Figure 10.16: (a) Resistivity of 150 nm Au layers sputtered at different V_C and grown by e-beam. (b) Resistivity of 150 nm Cu layers sputtered at different V_C

Regarding Cu layers, resistivity of sputtered films is significantly lower than Au layers, with a R_N value that, as in the case of Au, decreases with voltage bias. The difference between resistivity of our sputtered samples and bulk resistivity (17 nΩm at room temperature) is not as big as in the Au case. Resistivity of Cu sputtered layer is of the same order of magnitude as ρ_{bulk} and similar to those reported in literature [160]. In this case, no extra magnetron coupled to Cu target was needed, since for V_C=1 kV, residual resistivity was already ∼3 nΩm. Thus, assuming a Cu normal metal thickness ∼200 nm [160], TES residual resistance is expected to be R_N ∼0.01, very close to the Au e-beam one. As in Au case, no thickness dependence is reported for $d > 39$ nm, the bulk mean free path of copper [231].

10.5 Conclusions.

In this chapter a full characterisation of Mo, Au and Cu layers has been carried out to determine the optimum deposition parameters that will ensure quality

and reproducibility of TES functional parameters. In all three cases, the dependency of morphology, stress state, functional parameters and layer electric conductivity quality RRR with deposition parameters have been analysed.

In Mo films, although relations between stress, morphology and electrical resistivity are well known at room temperature, not enough information on their relation with superconducting properties was available in literature. Data presented on this chapter show that both residual resistance and critical temperature increase with deposition voltage bias, and relate to each other in a reproducible way. Changes in R_N are associated to enhanced electron scattering due to grain boundaries generated by increasing compressive stress. Changes in T_C can also be explained by stress and morphology changes through the specific electron and phonon spectra of Mo.

Lateral grain size, $D \sim 20$ nm, limits the electronic mean free path giving rise to finite size effects for $d \approx D$, both in R_N and T_C, since surface effects can no longer be neglected. The reproducibility of the functional parameter is ensured for our optimised films since $d = 50$ nm, well above the lateral grain size. Mo films are found to behave as 2D type II superconductors in the dirty limit. Moreover, our results point out that fundamental lengths of Mo are strongly affected by the grain size of the films –and thus by the fabrication conditions–. For highly disordered films, this would imply that transitions from type I to type II superconductor and from 3D to 2D behaviour might occur for Mo films with thickness close to those usually employed in proximity bilayers for TES (d$\sim$50 nm), what would affect possible noise sources, magnetic field sensitivity or current carrying capabilities.

Metal layers are deposited using different processes to compare electrical conductivity quality finding that, although Au films deposited by sputtering or electron beam display the same morphology, the high R_N value of sputtered films rules out this deposition technique for TES fabrication. On the other hand, Cu sputtered films show similar R_N and RRR values than Au films deposited by e-beam, therefore allowing both metals the fabrication of devices with acceptable TES R_N values.

Chapter 11

Bilayers: design and characterisation

11.1 Introduction

Elemental superconductors of low enough critical temperature, T_C, such as W and Ti can be used to fabricate TES [112, 232] –as described in Section 9.2.2–, but in general proximity bilayers are preferred. These sensors are based in the proximity effect: the reduction of T_C that a superconducting layer (S) thinner than its superconducting coherence length experiments when a normal metal layer (M) is deposited on top of it. The resulting bilayer, as a whole, behaves as a superconductor, with T_C determined by the ratio d_s/d_m.

As discussed in Chapter 10, TES performance is influenced or governed by the properties of the individual layers, like resistivity or stress, since they condition TES reproducibility or residual electrical resistance, R_N. However, other TES requirements depend on the proper combination of superconducting and metal layers and an optimum processing of the resulting bilayer to produce the final TES. A neat S/M interface determines the intensity of the bilayer coupling, thus fixing the ratio of S/M thickness required to reach the operation temperature of the sensor. Meanwhile the lithographic process establishes the sharpness of the TES transition –and thus the sensor temperature sensitivity– as well as the reproducibility of the functional properties. The different behaviour of Mo/Au and Mo/Cu bilayers and the influence of each fabrication step on final TES performance are discussed in this chapter.

As mention in Chapter 10, among the different S/M combinations studied, Mo-based bilayers are specially appealing, since its combination with noble metals display no intermetallic compound formation at the interface for tem-

peratures below 800 °C and for temperatures below 300 °C no diffusion at all is expected [162]. For Mo/Au bilayers, although no chemical interdifussion between Au and Mo layers is expected at temperatures below 300 °C, the extreme mobility of Au at temperatures as low as 200 °C, may lead to resistivity changes associated with grain size modification [230, 233]. However, to our knowledge, no systematic studies on the influence of temperature annealing on Mo/Au bilayers functional properties have been performed, except for some room temperature studies on microstructure and resistivity changes [234]. The same holds for the intensity of the coupling between Mo and Au. Despite the excellent energy resolution results on both Mo/Au –1.8 eV at 6keV [118]– and Mo/Cu –2.4 at 6 keV [164]–, no study on the sensitivity of T_C to layer thickness can be found, being this factor critical to T_C reproducibility.

In this chapter the different steps performed to develop and characterise Mo/Metal bilayers for its use as TES are described and its properties analysed. In Section 11.2 the different experimental techniques used in this work are described. Mo/Au and Mo/Cu sputtered bilayer characteristics are discussed in Section 11.3, in Section 11.4 our optimum solution for Mo/Au bilayers fabrication procedure is expound. Bilayer functional properties tuning and S/M coupling are presented in Section 11.5. In Section 11.6 Mo/Au bilayers with Mo deposited by DC sputtering instead of RF are analysed. While in Section 11.7, Mo/Au superconducting parameter stability as a function of annealing temperature is studied. Finally, in section 11.8 we summarise the main results obtained.

11.2 Experimental details

All samples studied in Chapters 10, 11 and 12 have been fabricated at the Instituto de Microelectrónica de Madrid (IMM)[1] by the group of Dr. Fernando Briones. Mo/Cu bilayers, with Mo films thickness, d_{Mo}=50 nm and Cu thickness ranging between 15 and 90 nm, and Mo/Au bilayers, with d_{Mo} ranging between 50 and 200 nm and Au thickness (d_{Au}) between 30 and 215 nm, were deposited on top of Si single crystal substrates covered by a 300 nm LPCVD Si_3N_4 layer. The deposition is carried out as described in Chapter 10.

The temperature dependence of the resistance down to 350 mK and the critical temperature of the different samples were measured using the four-point resistance method, in a commercial Physical Property Measurement System (PPMS) from Quantum Design, at the Servicio de Medidas Físicas of the University of Zaragoza. For temperatures in the range of 40 mK to 350 mK

[1] http://www.imm-cnm.csic.es/

a commercial dilution refrigerator (Kelvinox MX40) from Oxford Instruments with a refrigeration power of 80 mW at 100 mK, and an AVS-47 resistance bridge were used. This system is shown in Fig. 11.1a, while in Fig. 11.1b a picture of the holder for resistivity measurements is presented. This holder, designed to be compatible with Current-to-Voltage TES characterisation, allow us to measure 6 samples at the same time. Samples measured in the PPMS system where glued to the resistivity measurement holder with Ge-Varnish, since no fixing points are available in this commercial system. However, at temperatures as low as 40 mK this configuration cannot ensure good thermal contact between Mo/Au bilayers and sample holder. As depicted in Fig. 11.1b samples are hold tight to a oxygen free copper piece by two copper–beryllium flexible clamps. To avoid possible damages in free standing Si_3N_4 membranes caused by pumping the measurement area, samples are place over a thin 1x1.5 mm slit.

(a) (b)

Figure 11.1: (a) Picture of the commercial dilution refrigerator Kelvinox MX40 Resistivity at the ICMA Low Temperature Laboratory. (b) Holder for resistivity measurements.

Composition, areal density ($atoms/cm^2$), impurity concentration and mechanical interdiffusion on heated Mo/Au films interface was determined by Rutherford Backscattering Spectroscopy (RBS). These measurements were done using a He beam at the energy of 2.0 MeV in a high vacuum chamber which is connected to a 5 MV Tandetron accelerator at the Centre of Microanalysis of Materials (CMAM/UAM) by Raquel González-Arrabal. Backscattered ions were detected by a standard Si-barrier detector located at an angle of 170 °.

Morphology and structural characterisation of bilayers have been performed at ICMAB (CSIC) by the group of Lourdes Fàbrega. Structural and microstructural studies (texture, residual strain, grain size) were performed by X-ray diffraction and Scanning Electron Microscopy, using respectively a

Bruker D8 Advance diffractometer with a GADDS bidimensional detector and a QUANTA FEI 200 FEG-ESEM microscope. High Resolution Transmission Electron Microscopy (HRTEM) bright field images were obtained in a 200KV F20-sactem Tecnai microscope. Thin foils were prepared in cross section geometry (XTEM) by mechanical flat polishing down to 25 mm and final Ar^+ bombardment at 4 kV with an incidence angle of 7° using a PIPS-Gatan equipment. Interface compositional profiles were carried out in the same microscope using a beam of 1nm and an Energy Filter GIF-Tridiem spectrometer.

11.3 Sputtering samples: Mo/Au and Mo/Cu

Besides its electrical properties, discussed in Chapter 10, the choice of the normal metal layer will determine the final TES performance through superconducting functional properties. The metal and the deposition process will govern the transparency of the interface, that is, the intensity of the Metal/Superconductor coupling. Therefore, the thickness ratio between layers needed to achieved the working temperature, 100 mK, will depend on the metallic film. Although, as presented in Chapter 10, sputtered Cu and evaporated Au display similar residual resistivity values, the final R_N value could be different.

Other factor that could be affected by the chosen metal is the stability of TES behaviour when subject to temperature changes, corrosion effects, among others. While Au is highly resistant to corrosion, Cu can easily oxidised, specially in the presence of moisture, as could be the case due to water vapour condensation between different measurement cycles.

Some of these factors, together with the different lithographic requirements of Au and Cu when combined with Mo, are studied in this section.

As described in Chapter 10, sputtered Cu has a better quality than sputtered gold, being its residual resistivity significantly lower. Moreover, this value has been proven to provide a low enough R_N value for TES applications. Mo/Cu bilayers have been grown in-situ by sputtering at room temperature. As expected, Cu deposition over Mo layers reduce its critical temperature –T_C=915 mK– through proximity effect, as can be observed in Fig. 11.2a, where a 50/15 nm Mo/Cu bilayer is shown. Mo/Cu bilayers display sharp transitions –ΔT=25 mK– and a Residual Resistance Ratio –RRR– of 2. TEM images on Mo/Cu bilayers (not shown here) evidence sharp and flat interfaces between Mo and Cu, suggesting Mo flatness and absence of interdiffusion.

However, since copper is known to develop an oxide coating in contact with atmosphere, it is necessary to ensure that no degradation on bilayer due to age-

ing effects takes place. In Fig. 11.2a two resistance measurements performed on the same bilayer with 48 hours of difference are shown. No difference in residual resistance is observed, although T_C increases slightly. Similar results where found in other Mo/Cu samples.

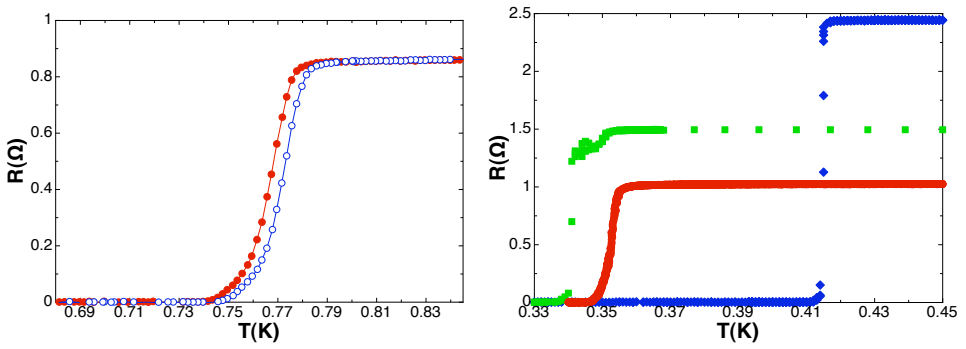

(a) (b)

Figure 11.2: (a) R(T) curve of a 50/15 nm Mo/Cu bilayer (•) and R(T) curve of the same sample after 48 hours (○). (b) Resistance as a function of temperature of non lithographed Mo/Au bilayers, with 25 nm Mo layer. (•) represent a sample with 75 nm Au sputtered layer, (♦) represent a sample with 80 nm Au sputtered layer deposited and (▪) represent a sample with 90 nm Au sputtered layer.

Moreover, Mo/Cu lithography process requires some extra steps, compare to Mo/Au, that will be described later on. As explained by Hilton et al. [160], Mo/Cu patterning leads to imperfections along the edges of the bilayers, what produce wider superconducting transitions with *"strange"* shape. To avoid these problems, an extra Cu layer deposition is needed to cover the future sensor boundaries. Finally, although as described in Chapter 10, no significant change in Mo stress is observed after metallic layer deposition, polycrystalline Cu layer display a tensile stress up to 6 times higher than Au layers. These problems, together with Au excellent performance, as resistance to corrosion, lead us to focus on Mo/Au bilayers.

The simplest deposition route consists in sputtering the Mo layer in the first place and then the Au layer in rapid succession. As shown in Fig. 11.2b Mo/Au bilayers deposited by sputtering display also sharp transitions (ΔT=10 mK), however RRR is lower, 1.3. As discussed above this poor quality of sputtered Au, makes unfeasible to fabricate TES based in these bilayers. To achieve Mo/Au bilayers with the required low R_N it is necessary to substitute sputtered Au layer by an evaporated one.

11.4 The trilayer solution

As above explained, Mo/Au bilayers require Au layer to be deposited by e-beam, to meet the R_N requirements for low noise and thermal stability. Since our e-beam deposition UHV chamber is not connected to the sputtering deposition one, Mo film will be exposed to air before metal layer deposition. This exposure could lead to contamination or oxidation of the superconducting layer, thus degrading Mo/Au interface and possibly leading to the destruction of the proximity effect.

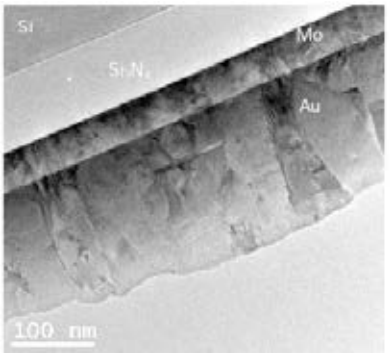

Figure 11.3: Cross-section TEM image of a 50 nm de Mo covered by a 15 nm sputtered Au and 200 nm evaporated Au.

To study this effect, e-beam Au layers of 50 and 125 nm thickness are deposited over bare 50 nm Mo layers and Mo layers covered by a protective thin 15 nm sputtered Au layer to prevent Mo degradation. In-situ measurements of stress during Au growth by sputtering on Mo reveal that coalescence of Au takes place for very low thickness, around 2 nm [181]. Therefore, a 15 nm-thick layer must be continuous across the film, isolating Mo layer completely from its surroundings.

In Fig. 11.3, a bright field cross-section TEM image of a Mo/Au bilayer, formed by 50 nm Mo, 15 nm Au deposited by sputtering and 200 nm Au deposited by e-beam can be seen. The thin Au layer grown by sputtering on top of Mo films reproduces the columnar grains of Mo; both Mo and Au columns are 20 nm wide. Moreover, it acts as a seed for the growth on its top of the thicker Au layer by e-beam. Due to this fact, it is difficult to distinguish the interface between both Au layers. The thick Au layers deposited by e-beam are quite disordered, with large grains –some of them reaching 70 nm, when the Mo thickness is 50 nm–, and often display other defects such as twin boundaries parallel to the interface, that are not seen in sputtered Au layers.

The interface between Mo and Au is quite visible and neat. Its roughness has been estimated of the order of 1 nm, by averaging distances between peaks

and valleys in different HRXTEM images; this value coincides with the average peak to valley distance obtained from AFM images of 50 nm Mo thin films, 1.1 nm, indicating that the interface roughness is due to the Mo layer roughness. Compositional profiles obtained by EELS provide also an average interface width of 1.1 nm$\pm$0.5 nm (see Fig. 11.11a) ; the error bar is given by the beam diameter used, which is a compromise between required sensibility and spatial resolution. It is therefore likely that the chemical interface detected by EELS is in fact due to the interface roughness.

RBS spectra for Mo/Au bilayers, similar to the ones reported here [187], illustrate that samples are constituted only by Mo and Au. Mo can easily combine with N or Si to form compounds of higher critical temperature than the one of Mo bulk. However no traces of these compounds or other impurities are appreciated with the exception of Ar (about 2%), which is incorporated during sputtering deposition. RBS measurements presented in Ref. [187] and Section 11.7 show no interdiffusion both in the Mo/Au and Mo/Si_3N_4 interfaces.

Resistivity measurements performed on these samples are depicted in Fig. 11.4b. These measurements are carried out in non lithographed samples where e-beam layers don't cover completely the bottom layers, due to the shadow effect of the sample holder. Thus, as shown in Fig. 11.4a, four points resistivity measurements can be performed connecting the measurement terminals to sputtered Au protective layer. This way we will be able to observe not only the superconducting transition of the Mo/Au *"trilayers"*, but also the transition associated to the sample part where Mo is covered only by sputtered Au layer. This double transition structure is also shown in Fig. 11.4b, where both "trilayer" samples have the same T_C=690 mK, corresponding to the Mo/$Au_{sputtering}$ bilayer transition, plus another transition at a lower temperature ascribed to the whole Mo/$Au_{sputtering}$/Au_{e-beam} sample. For the 50/15/120 sample, only the first transition is observed since, as it will be discussed later on, its critical temperature is expected to be $T_C \sim 100$ mK.

As can be seen in Fig. 11.4b the two samples without an sputtered Au protective layer display a superconducting transition at approximately the same temperature, a value close to the Mo critical one ($T_C \sim 900mK$). This clearly shows that the e-beam layer is not influencing the critical temperature of the Mo layer, leading to the conclusion that the proximity effect of the e-beam Au layer is inhibited when Mo layers are exposed to air before depositing Au layers. This fact is likely due to surface contamination of the superconductor, most likely surface oxidation, that degrades the quality of the interface. However, depth profile XPS measurements performed to study the chemical state of molybdenum did not evidence the presence of oxygen, within 1% resolution.

These results prove that the addition of a 15 nm sputtered gold layer pro-

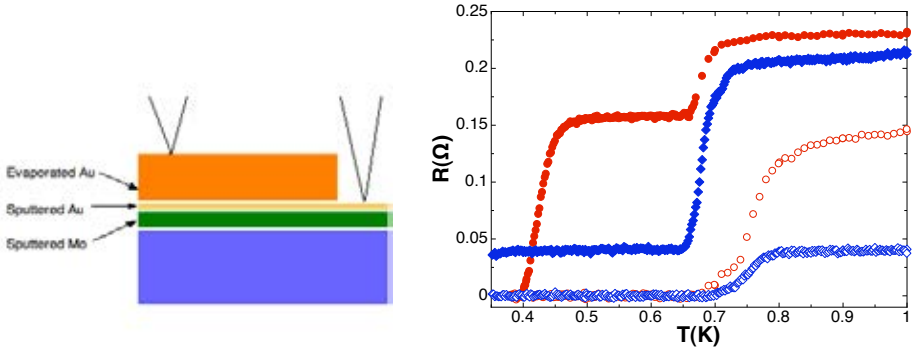

(a) (b)

Figure 11.4: (a) Schematic layout of sample connection for R(T) measurements displayed in Fig. 11.4b (b) Resistance as a function of temperature of non lithographed Mo/Au bilayers, with 50 nm Mo layer. Full circles represent a sample with 50 nm Au e-beam layer deposited over a protective 15 nm sputtered Au layer. Empty circles represent a sample with 50 nm Au e-beam layer deposited directly over Mo layer. Full diamonds represent a sample with 120 nm Au e-beam layer deposited over a 15 nm sputtered Au layer. Empty diamonds represent a sample with 120 nm Au e-beam layer deposited directly over Mo layer.

tects Mo layer from degradation ensuring clear and flat Mo/Au interfaces, and thus, sharp superconducting transitions. Moreover, TEM images show that no clear $Au_{sputtering}/Au_{e-beam}$ interface can be found. Since sputtered Au acts as a seed for e-beam Au layer no extra interface needs to be taken into account, studied Mo/Au samples can be considered bilayers with Au thickness equal to the sum of both Au layers.

11.5 Critical temperature as a function of Mo thickness

In order to tune the critical temperature of the bilayer, the normal metal layer thickness is kept constant (d_{Au}=215 and 115 nm) while Mo layer thickness, d_{Mo} is reduced. As already mentioned in Chapter 9, decreasing d_{Mo} will decrease T_C due to proximity effect. To avoid finite size effects that could affect Mo functional properties, mainly T_C, d_{Mo} reduction is limited to thickness values above 30 nm [235]. Critical temperature is estimated by linearly fitting the high temperature part of the superconductng transition, being T_C defined as the temperature at which the linear fit and $R(T)$ data diverge. T_C of various samples is displayed as a function of d_{Mo} in Fig.11.5. Full symbols correspond to Mo/Au bilayers with a normal layer thickness of 215 nm; empty symbols are associated with bilayers of d_{Au}=115 nm; while different symbols represent

sample series deposited within a few days. Despite having been deposited over a year, these samples display excellent T_C reproducibility for different values of d_{Mo}. T_C dispersion observed in these samples is similar to the one described in the previous section for sputtered Mo layers covered by a thin sputtered Au layer. With these results, a theoretical T_C = 100 mK will correspond with a 53 nm Mo layer, in good agreement with previous results in this material [160, 161]

The shape of the dependency of T_C with d_{Mo} seems to correspond to the one expected for a bilayer with the normal metal layer thicker than the metal coherence length, ξ_M [123, 138]. When $d_{Au} > \xi_M$, T_C no longer depends on normal metal thickness. This is the case observed in Fig.11.5, since T_C variation with d_{Mo} shows the same dependence for both d_{Au}= 115 nm and 215 nm. Thus, not only bilayer critical temperature will be insensitive to inaccuracies in deposited d_{Au}, but also R_N value of final TES could be tuned to fit application requirements. This result is coherent with the expected ξ_M, between 10 and 100 nm [138, 222, 236].

As it was mentioned in Chapter 9, when the thickness of the normal and the superconductor layers are less than the respective coherence lengths, different approximations permit to analytically determine the critical temperature of a bilayer as a function of the individual layer thickness. One of these approximations was developed by Martinis et al. [146], from Usadel equations [237]. According to it, one can find an expression to predict T_C from simple physical parameters, such as supenconducting layer thickness, d_s, normal metal layer thickness d_m or the quality of the interface, represented by a transmission parameter, t, ranging from 0 to 1. In the simple case where both layers can be considered thin- the function representing the superconducting state is assumed to be nearly constant across the film- T_C can be expressed as,

$$\begin{aligned} T_C &= T_{C0}\Big[\frac{d_s}{d_0}\frac{1}{1.13(1+1/\alpha)}\frac{1}{t}\Big]^{\alpha} \\ 1/d_0 &= (\pi/2)k_B T_{C0}\lambda_f^2 n_s \\ \alpha &= d_m n_m / d_s n_s \end{aligned} \tag{11.1}$$

where T_{C0} is the transition temperature of the bare superconductor, λ_f is the Fermi wavelength, n_m and n_s are the density of states in the normal and superconducting layer respectively. In our case, some of these values can be considered as n_{Mo}=0.29·10^{23}states/eVcm^3, [146] n_{Au}=0.107·10^{23}states/eVcm^3 [222] and λ_{fAu}=0.524 nm [222].

When only the superconducting layer can be assumed to be *"thin"*, $d_m > \xi_M$, an analytical solution of Usadel equation is still found by substituting $1/t$

by:

$$\frac{1}{t} + \frac{1d_m}{3\sigma_m}\frac{2G_K}{(\lambda_f/2)^2} \tag{11.2}$$

where $G_K = e^2/h$ is the conductance quantum and σ_m is the conductivity of the normal metal layer. In the general case –layers of arbitrary thickness– Usadel equations have to be solved numerically in order to get an expression similar to Eq. 11.1. In Ref. [146], authors show a numerical solution for the case of a thick superconducting Mo/Cu bilayer. This solution is similar to 11.2 but adding an extra term due to the resistance of the Mo film, as shown in Eq. 11.3

$$\frac{1}{t} \rightarrow \frac{1}{t} + \frac{1}{3}\Big(\frac{d_s}{0.0130\mu m}\frac{\rho_s}{\rho_{s0}} + \frac{d_m}{0.0405\mu m}\frac{\rho_m}{\rho_{m0}}\Big) \tag{11.3}$$

where ρ_{s0} and ρ_{m0} are the room temperature resistivity values of both layers, and ρ_s and ρ_m the residual resistivity values. As above explained, the second term in Eq. 11.3 corresponds to the analytical solution for *"thick"* normal metal layer, and, therefore is valid for all normal metals. Since $\lambda_f^{Au} = 0.524$ nm, in our case, 0.0405 μm has to be replaced by 0.153 μm. Moreover, the first term has been developed as a solution for sputtered Mo layers, thus, Eq.11.1 can be applied to our samples by using the proper substitution contained in Eq. 11.3.

Since $d_{Au} > 60$ nm, ρ_{Au} can be considered as independent of d_{Au} [229]. For our bilayers, $\rho_{s0} = 130 \cdot 10^{-9}\Omega$m and $\rho_{m0} = 10.5 \cdot 10^{-9}\Omega$m are metal room temperature resistivity values, and $\rho_s = 60 \cdot 10^{-9}\Omega$m and $\rho_m = 5.8 \cdot 10^{-9}\Omega$m are residual resistivity values. With these values, data presented in Fig. 11.5 can be adjusted to Eq. 11.1 to estimate the interface quality. However, this simple model leads to different t values for the two different normal metal layer thickness, even in the more general case of Eq. 11.3. Since this value represents the transparency of the interface, a parameter not related to the thickness of the layers, no difference between both sets of data should be found.

From data displayed in Fig. 11.5, it is found that, at some point around $d_{Au} \lesssim 115$ nm, a saturation point is reached, and the normal metal layer thickness can be increased arbitrarily without affecting T_C. Thus, when using the total d_{Au} in Eq. 11.1 and 11.3, t is being underestimated. Since the Au thickness above ξ_M is not influencing T_C, only the portion coupled to Mo layer has to be considered in order to estimate t. Extremely low values of t (less than 0.1), together with high values of d_m (greater than 200 nm) [161] may be related to overestimation of the *"active"* metal thickness.

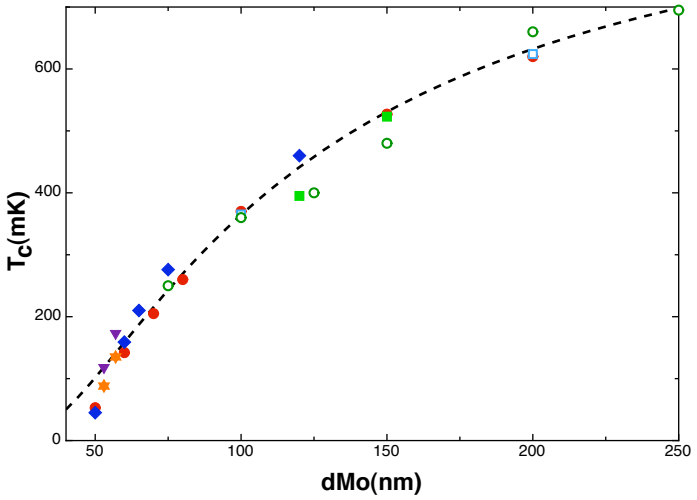

Figure 11.5: Influence of the proximity effect on the critical temperature of Mo/Au bilayer. T_C of Mo/Au bilayer as a function of the superconductor thickness for a normal metal thickness of 115 nm (empty symbols) and 215 nm (full symbols). Each symbol correspond to a set of bilayers.

When $d_m > \xi_M$, $T_C(d_s)$ dependence can be reproduced by an infinite number of t and ξ_M [238], thus no estimation of the normal metal coherence length can be obtained directly by fitting the data represented in Fig. 11.5 with Eq. 11.3. When, as in the gold case, microscopic parameters such as the Fermi velocity are known, ξ_M can be estimated as [239]:

$$\xi_M = \sqrt{\frac{\hbar v_M^f \ell_N}{6\pi k_B T_S}} \tag{11.4}$$

where $T_S \sim 980$ mK is the critical temperature of the superconducting layer and $v_M^f = 1.39 \cdot 10^6$ m/s is the Fermi velocity of gold [3] and ℓ is the mean free path. TEM measurements show that, for most of the samples the columns in the gold layer follows the ones of the Mo layer deposited underneath, with an average grain size $\sim$ 30 nm. As the thickness of the gold layer increases from 115 to 215 nm the dispersion in grain sizes increases reaching values as high as 70 nm. Assuming that, as in the case of Mo layer, ℓ is governed by the grain size, ξ_M will have a different value for every point plotted in Fig. 11.5. Thus, to apply Eqs. 11.1 and 11.3 an approximations has to be made: in our case, we have considered that the *"active"* gold layer is equal to an estimated ξ_M value of 130 nm $-\ell$ = 30 nm. To obtain this value it has been considered not only that the grain size in the Au layer is governed by the Mo layer, what suggest a similar value for the electron mean free path in both materials; but also that data shown in Fig. 11.5 indicate that ξ_M in our samples must be a

value lower or close to 115 nm, since no significant difference in T_C is found for samples with d_{Au}= 115 nm or 215 nm.

This theoretical result is in good agreement with the experimental data displayed in Fig. 11.6, where the dependence of T_C with Au thickness is plotted for samples with a fixed Mo thickness. The estimated $\xi_M = 130nm$ corresponds approximately with the d_{Au} value at which T_C can be considered nearly constant with Au thickness.

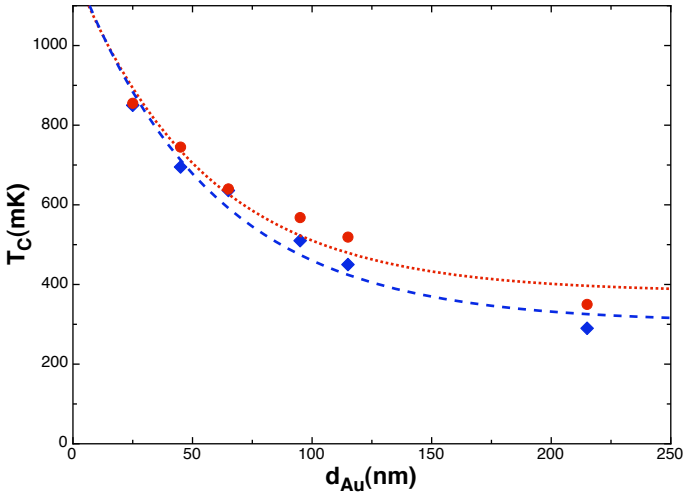

Figure 11.6: Influence of the proximity effect on the critical temperature of Mo/Au bilayer. T_C of Mo/Au bilayer as a function of the normal metal thickness for a superconductor thickness of 120 nm (•) and 70 nm (⬥) Dash line are guides for the eyes.

Adjusting data presented in Fig. 11.5 using Eqs. 11.1 and 11.3 allows us to estimate t and T_{C0} in our bilayers as $t = 0.33 \pm 0.08$ and $T_{C0} = 907 \pm 34$ mK considering data with d_{Au} =115 nm. While, when d_{Au} =215 nm, if only the *"active"* part of the gold layer is considered –d_{Au}^{eff}=ξ_M = 130 nm–, $t = 0.28 \pm 0.04$ and $T_{C0} = 914 \pm 24$ mK are obtained. Both T_C and t parameters obtained from the two different gold thickness can be considered as equal, within the estimated errors. It must be noted that our estimated T_C is in good agreement with previous results of critical temperature on bare sputtered Mo films [181] and with T_C of Mo bulk.

From Fig. 11.6, it can be seen that, as expected, the d_{Au} value at which T_C saturates depends on the superconducting layer thickness, being T_C strongly depressed for $d_{Mo} \ll \xi_S$, where the superconductivity eventually disappears [138]. This thickness dependency might explain why the fitting of the experimental data to Eq. 11.1 display a small divergence for $d_{Mo} < 60nm$, for these points.

Regarding interface transparency,the value determined in our case –$t \sim 0.3$– has to be considered a rough estimation, since ξ_M could not be accurately determined. In some cases, values similar to ours were found [160, 240], although usually proximity effect bilayers display a value, $t \sim 0.2$ [121, 146, 222]. Thus the deposition of a protective thin Au layer by sputtering seems not only to ensure reproducibility and avoid Mo degradation, but also to provide a clear interface that increases coupling between the two layers, as pointed out by a high interface transparency.

11.6 DC sputtered Mo in Mo/Au bilayers

RF sputtering deposition is specially suited for insulating materials, in DC systems, positive charge is build up in the cathode when an insulating target is used. Although Mo for TES bilayers was initially deposited by RF sputtering, there is no reason why DC sputtering deposition, the simplest one, cannot be used in this case.

In order to explore this possibility two Mo layers of 50 nm were deposited by RF and DC sputtering. In the first case the optimum conditions described in Chapter 10 were used, while in the second case a bias voltage of 330 V and a DC power of 35 W, what translated in a deposition rate $\sim 1\mathring{A}$ was used. Results are displayed in Fig. 11.7a, where it can be seen that no significant difference in T_C or transition width can be observed between both deposition techniques.

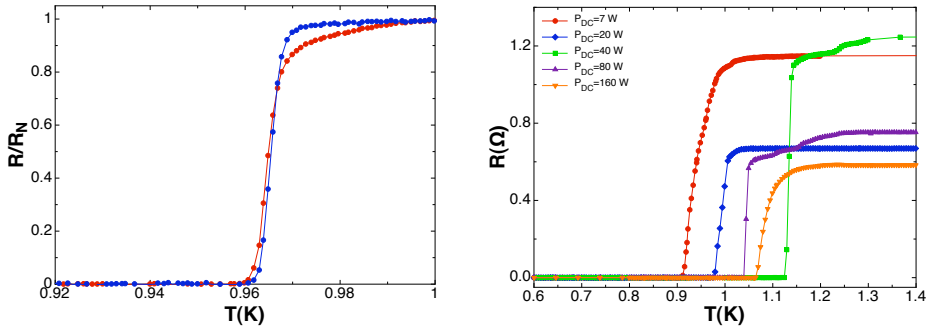

(a) (b)

Figure 11.7: (a) Resistance temperature dependency for 50 nm Mo layers deposited by RF sputtering (•) and DC sputtering (▪). b) R(T) measurement of 50 nm Mo layers deposited at different P_{DC} by DC sputtering.

The next step so as to obtain Mo-based sensors by DC sputtering consist in finding the optimum deposition conditions as it was done for the RF case –see Chapter 10–. In this case, the relevant parameter will not be the bias voltage,

since its change –from 275 V to 340 V– is insignificant when compare to the RF case –from 250 V to 1000 V–. In Fig. 11.7b a set of 50 nm Mo layers grown at different DC powers are shown. Contrary to the results found for RF sputtered samples, no direct relation between this parameter and T_C can be found. However, taking into account the Mo bulk critical temperature and the sharpness of the obtained transitions, the optimum deposition condition in the DC sputtering case is estimated to be $P_{DC} = 20W$. This selection is corroborated by the stress measurements performed in these samples, showing a tensile stress for low values of deposition powers, that change to compressive as the deposition rate increases, being the stress absolute value minimum for $P_{DC} = 20W$. XRD and SEM measurements show no difference in the morphology of Mo layers deposited by DC and RF sputtering, except for the fact that grain sizes appear to be slightly smaller ($\sim$ 17 nm) in the DC case.

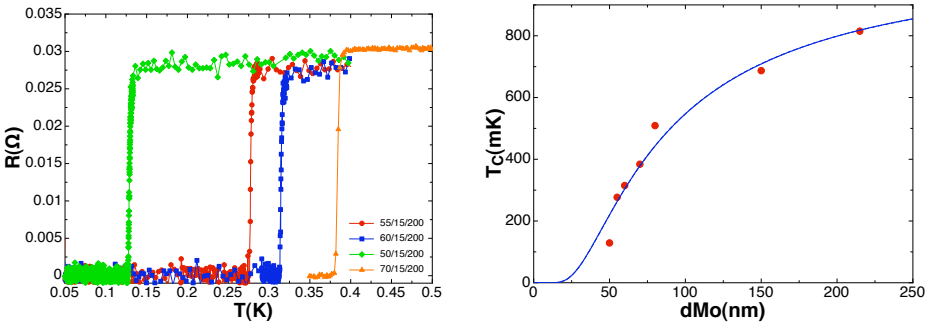

(a) (b)

Figure 11.8: (a) R(T) of some samples with Mo deposited by DC sputtering. (b) Influence of the proximity effect on the critical temperature of Mo/Au bilayer with DC sputtered Mo.

When the Au layer, deposited as described above in this chapter, is added to the DC sputtered Mo, transitions of similar characteristics to the ones obtained with RF sputtering are found. An example of some of these transitions is depicted in Fig. 11.8a, where some lithographed samples with a 200 nm Au layer and different d_{Mo} values are shown. R_N values of 30 $m\Omega$, quite similar to the ones that will be displayed in Fig. 12.4a for the RF case, are obtained. This is the expected result since, as already explained, the normal resistance of the bilayer is governed by the Au layer. Transition thickness is found to be $\sim$ 8 mK, again equivalent to the values that will be shown in Chapter 12 for lithographed RF sputtered Mo/Au samples.

However, that is not the case for the relationship $T_C(d_{Mo})$, as it can be clearly observed when comparing Fig. 11.5 with the results obtained for DC Mo layers displayed in Fig. 11.8b. Assuming a ξ_M value of 130 nm, somehow equivalent to the ones used in Section 11.5, since the Au layer remain

unchanged, the fitting parameters found in this case are $T_{C0} = 1024 \pm 71$ mK and $t = 0.15 \pm 0.04$. Although T_{C0} can be consider as equal to the one found in the RF case, within the error limits, the obtained t value is slightly lower. This correspond to the fact that, in the DC case, a bilayer of 50 nm of Mo instead of the 57 nm found in the RF case, is necessary to achieve $T_C = 130$ mK. The decrease in the transparency of the interface between DC and RF samples cannot be explained by any morphological difference, being its origin still under study.

11.7 Annealing effects on bilayer functional properties.

The absence of intermetallic Mo/Au compounds, plus the absence of interdifussion predicted for temperatures below 300 °C [162] and the excellent resistance to corrosion of Au, allow us to foreseen a better response to ageing effects or temperature degradation than other combinations, such as Ti/Au or Al/Ag bilayers.

Since Mo is a highly refractory material, annealing processes at temperatures below 600 K are not expected to affect the superconducting bilayer. However, due to the mobility of gold atoms, it cannot be ruled out that heating processes at temperatures well below both Au and Mo melting point, could affect functional properties of Mo/Au bilayer through changes in the normal metal layer.

Previous studies on Mo/Au bilayers showed that no degradation in T_C and α superconducting properties was observed for devices heated up to 700 K [178, 241]. These results are in good agreement with RBS measurements in our annealed samples, depicted in Fig. 11.9. Mo/Au samples of 25/140 nm thickness were heated up at different temperatures ranging from 50 °C to 300 °C, with heating times of 30 and 60 minutes. The sharp edges of Mo and Au features in the RBS spectra of our samples indicate absence of interdiffusion, within the resolution limits, for these annealed samples.

It is well known that resistivity of evaporated Au films is modified by annealing processes at temperatures as low as 150 °C [242]. Thus, further analysis are required to determine how the expected changes in Au layer functional properties affect Mo/Au TES performance. To do so, changes in bilayer superconducting properties, T_C and R_N are studied for 50/30 nm Mo/Au bilayers heated at different temperatures for different time periods, results are presented in Fig. 11.10a.

To discard that possible changes could be due to irreproducibility in the

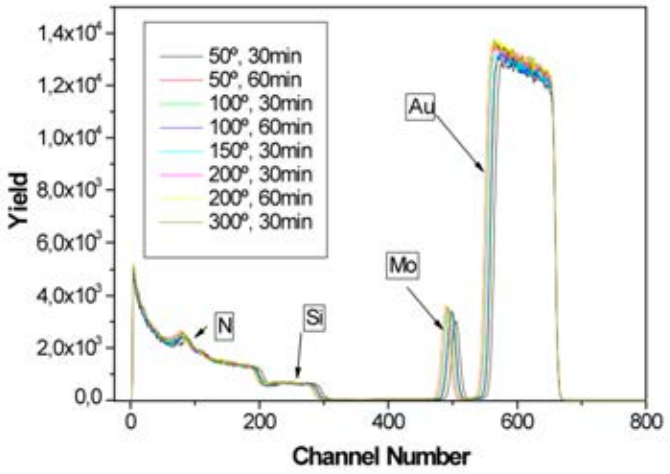

Figure 11.9: RBS measurements in annealed Mo/Au bilayers. *Credit: Raquel González-Arrabal.*

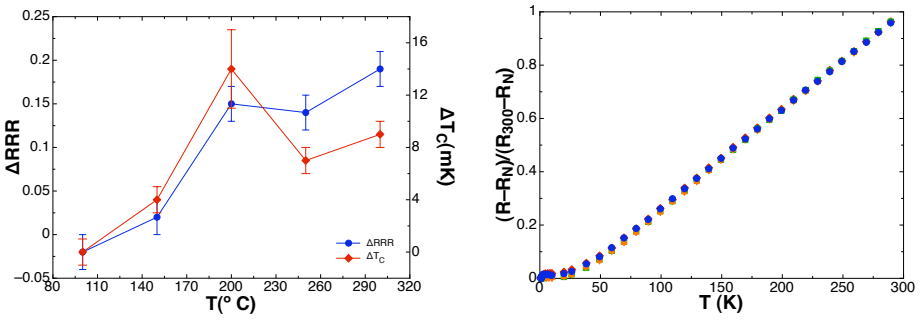

(a) (b)

Figure 11.10: (a) Observed changes in RRR and T_C as a function of the annealing temperature. All samples were heated for 30 minutes. ■ correspond to changes RRR values, while ♣ correspond to changes in T_C. (b) Temperature dependent part of the normal state resistance for control sample and bilayer heated at 200 ºC for 30 minutes.

measurement process or ageing effects, each sample was measured together with a control sample both before and after being annealed. In all the studied cases no change in control samples was observed between measurements.

No change is observed for temperatures $T \lesssim 100$ ºC, even for samples heated for 120 minutes. At T=150 ºC still no variations in resistivity are observed, however, T_C of the bilayer is slightly depressed by $4 \cdot 1$mK. For annealing temperatures $T \gtrsim 200$ ºC both resistivity and T_C decrease, being this change nearly independent of temperature. The change of the T_C and R_N with annealing processes also saturates with time, being both values nearly

constant for samples heated longer than 8 hours. In all cases the shape of the $R(T)$ curve remains nearly unaffected since no changes in the transition width are observed.

As mentioned above, the resistivity of a metal has two components: the electron scattering with phonons, a temperature dependent term, and that with lattice imperfections, such as impurities, physical defects in the lattice or grain boundaries. The first term of the bilayer heated at 200 °C for 30 minutes and its correspondent control sample is depicted in Fig. 11.10b after eliminating geometrical factors. Since no change is observed in this resistivity part, changes observed in RRR values are necessarily related to variations in the second component of the metal resistivity: the residual resistance of the Au layer. It has been already observed in evaporated Au films that annealing processes lead to increases in grain size, and, therefore, residual resistivity diminishes as a result of the reduction of the grain boundary scattering contribution [230, 233]. Indeed, both planar SEM and HRXTEM images of a 50/30 nm Mo/Au sample heated at 300°C for 30 minutes show that, when comparing this sample to its control bilayer (identical, same batch, without annealing) the average Au grain size increases, from 19 nm to 25 nm in the annealed one. As expected, no change in Mo average column width is observed at this temperature.

As discussed in Chapter 10, the influence of grain size on the residual resistivity of granular films, like our Au layers, can be expressed, according to Mayadas-Shatzkes [189], as Eq. 10.1.

Where , in this case ρ_{bulk} is the residual resistivity of a bulk sample and ρ_{film} is the residual resistivity of the film. As above explained, only the Au layer is considered to contribute to the sample resistivity. Assuming that $\rho_{bulk} = 0.022 \cdot 10^{-8}$ Ωm [243] and $\ell_0 = 30$ nm, as discussed in Section 11.5, the observed resistance changes are associated to the measured grain size change by a R value ∼0.5. Since this value is similar to other data found for (111) evaporated Au layers [230] one can concluded that, as expected, changes in RRR after annealing can be attributed to changes in grain size.

Regarding the observed change in T_C, we will first focus on the possible relation between this change and the obtained residual resistivity reduction. Taking up the interface transparency value obtained for our bilayers in Section 11.5 an the expressions 11.5 and 11.3, one can relate changes in resistivity to changes in critical temperature. With these elements, changes in resistivity can be ruled out as a cause for T_C variations, since variations twice as high as the measured residual resistivity will be required to account for the measured T_C.

From Eqs. 11.5 and 11.3, the other factor that could affect T_C besides resistivity is the quality of the interface. Fig. 11.11 displays an Electron

Energy Loss Spectroscopy (EELS) interface profile of a 50/30 bilayer annealed at 300° C for 30 minutes ant its control bilayer. The average interface roughness increases significantly, from 1.1 nm to 1.5 nm, and the chemical profile across the interface extends from 1.1 nm±0.5 nm to 2.1 nm±0.5 nm when annealing. EELS results clearly evidence that a diffusion has occurred at the interface during annealing. These results are not contradictory with RBS measurements; the absence of interdifussion between Mo and Au layer in RBS spectra is due to the resolution of this type of measurements –∼ 10 nm–, that cannot be compared with the atomic resolution of EELS.

Due to the refractory character of Mo and the high mobility of Au, we consider that the most likely scenario corresponds to a diffusion of Au atoms along the Mo grain boundaries in the interface. However, the small extension of the diffusion, together with the interface roughness and grain size, makes it impossible to verify this hypothesis.

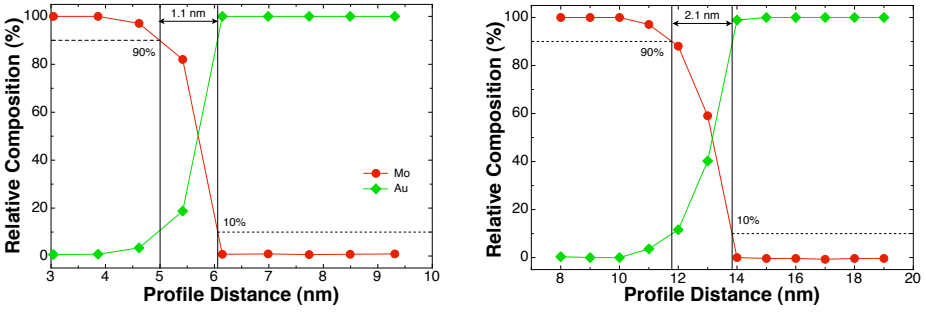

(a) (b)

Figure 11.11: (a) EELS profile of a 50/30 nm Mo/Au bilayer. (b) EELS profile of a 50/30 nm Mo/Au bilayer after heating the sample to 300 °C for 30 minutes.

11.8 Conclusions

We have grown Mo/Au and Mo/Cu bilayers for TES at room temperature by UHV sputtering and e-beam deposition. Mo/Cu bilayers are rejected for TES fabrication despite their good performance –sharp transitions and low residual resistance–, due to the observed ageing effects, high residual stress and lithographic difficulties. Mo/Au bilayers are actually made of three layers: a sputtered Mo layer, a 15 nm protective sputtered Au layer and an evaporated 200 nm Au layer. This extra Au layer, deposited by e-beam in a different chamber is needed to obtain low values of R_N, as required for TES applications. The thin sputtered gold layer (15 nm) prevents Mo degradation, improve T_C reproducibility and provides good coupling between layers. Structural and

compositional analysis showed the absence of an interface between Au layers, where sputtered Au layer acts as a seed for the evaporated Au. On the contrary neat interfaces of thickness similar to 1 nm are observed in Mo/Au boundary both by RBS and EELS techniques.

Excellent reproducibility allows us to accurately relate Mo layer thickness and bilayer T_C for samples with $d_{Au} \geqslant 115$ nm. Under this condition, $d_{Au} \gtrsim \xi_M$, thus, normal metal thickness can be choose to obtain the desired R_N value, without affecting T_C. $T_C(d_{Mo})$ results are analysed with equations developed by Martinins et al. [146] from Usadel theory; showing that the "trilayer" fabrication process provides good coupling between normal and superconducting layers, as reflected by the high transparency factor obtained, $t \sim 0.3$.

Finally, we presented a complete study on how Mo/Au superconducting properties are modified by annealing processes even at temperatures below the limit of interdifussion, 300 °C. Although previous studies suggested that Mo/Au bilayer functional properties remain unchanged for heating processes at temperatures below 700 °C our results show that R_N and T_C display small changes when heated above 150 °C, while α remains unchanged. R_N variations are associated with the reduction of the grain boundary contribution to resistivity, due to the increase in grain size associated with annealing processes. While changes in T_C can be associated to an improvement of t, due to Au atom migration through Mo grain boundaries. Although these changes are not extremely significant, the effects can be eliminated from Mo/Au sensors by annealing the bilayers at 200 °C for at least 8 hours.

Chapter 12

Towards a Mo/Au TES

12.1 Introduction

Thermal radiation detectors based in TES combine the TES with an absorbing element to convert radiation into heat and a thermal conductance to a heat sink. In this configuration TES is basically a thermometer [131, 142], therefore the study of its superconducting functional properties –T_C, R_N and temperature sensitivity– is crucial to ensure a good performance as radiation detectors.

In this chapter, we will focus on the transformation of Mo/Au bilayers into sensors by means of lithographic processes to improve their behaviour as detectors, and on the cryogenic characterisation of TES conceived exclusively as thermometers, a necessary first step for the development of TES for radiation detection. This preliminary characterisation will provide enough information to determine whether our Mo/Au bilayers are suited or not for TES applications.

The chapter is organised as follows: in Section 12.2 the characterisation set-up is described together with other experimental details, while in Section 12.3 the lithographic process is explained. The lithographed Mo/Au superconducting properties are discussed in detail Section 12.4. Finally, in section 12.5 the main results obtained are summarised.

12.2 Measurement system

As described in Chapter 11 in the case of bare bilayers, the preliminary cryogenic characterisation of Mo/Au sensors was performed in a commercial dilu-

tion refrigerator (Kelvinox MX40) from Oxford Instruments with a refrigeration power of 80 mW at 100 mK and a base temperature of 30 mK.

$R(T)$ curves were acquired using the four-point resistance method with an AVS-47 resistance bridge. To reduce heat load into the system temperature dependence of the resistance is acquired with the minimum available excitation voltage, $3\mu V$. Given the small R_N values displayed by our sensors, measurements were taken in the 0-2Ω resistance range, what translates in a final resistance resolution of 1 $m\Omega$. The same holder described in Chapter 11 is used in this case, thus samples are thermalise by tight contact to the cooper holder provided by copper-beryllium clamps. A picture of some Mo/Au sensors placed in the dilution fridge inset is displayed in Fig. 12.1a

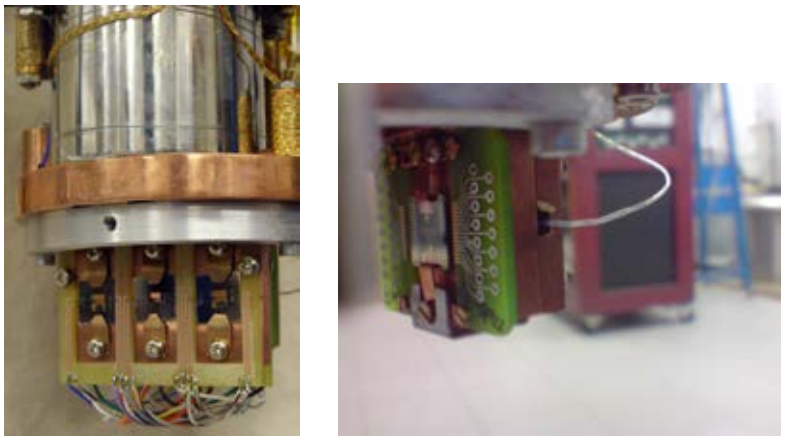

(a) (b)

Figure 12.1: (a) Picture of the Kelvinox MX40 mixing chamber with the mounted holder for resistivity measurements. (b) Picture of the Kelvinox MX40 mixing chamber with the current to voltage characterisation system mounted on it.

A dedicated control program was developed in order to control the increase of power supplied to the mixing chamber at the dilution refrigerator. This program enables us to achieve variations in the sample temperature as small as 1.7 mK per hour; thus, very sharp superconducting transitions can be characterised. Instead of using an extra heater placed close to the sample, the standard heater provided by Oxford Instruments in the mixing chamber is used to modify the temperature of the sample. In this way, temperature gradients inside the sample or the sample holder are avoided. For the same reason small power increases combined with long measurements are used.

Samples are fabricated as described in Chapters 10 and 11 on the top of Si single crystal substrates covered by a 300 nm LPCVD Si_3N_4 layer and over free standing 300 nm LPCVD Si_3N_4 membranes formed in it by KOH anisotropic etching of the Si underneath. These membranes are aimed to provide mecha-

nical support and a weak thermal connection to the TES.

12.3 Lithographic processes

After depositing the samples, as described in Chapter 11, Mo/Au bilayers are patterned using standard optical photolithographic techniques to get 200x200 μm and 300x300μm detectors. First, the gold layer is etched using a KI/I solution trough a photoresist mask. Later, the photoresist mask is removed by acetone and the Mo layer is etched in a $H_3PO_4/HNO_3/H_2O_2$/DI solution. This solution is selective to Au, thus Au layer can be used as a mask for Mo. Moreover, since Mo etching is about 20 times faster laterally than vertically, Au layer overhangs Mo and, when samples are taken out of the vacuum chamber these overhangs collapsed covering in a simple way Mo edges [167, 241]. This “normal metal" boundary condition has been proved to be a requirement for sharp and reproducible transitions [160, 175], since it eliminates edge effects and noise from quasiparticle and vortex fluctuations [146, 178].

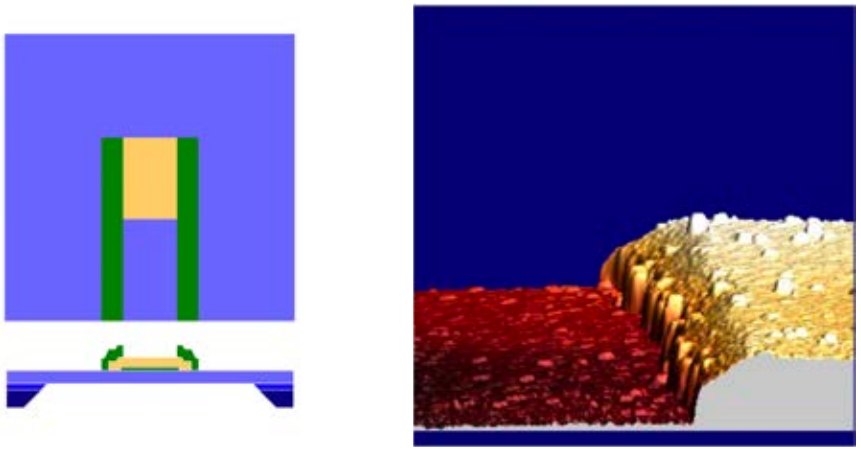

(a) (b)

Figure 12.2: (a) Schematic layout (not to scale) of a bilayer deposited over membrane and connected to the heat bath through Mo paths showing top view of the device and a cross section through the central point. (b) Profile of a 50 nm Mo film covered by a 60 nm Au film after a lithographic process. *Credit: Ivan Férnandez.*

As already discussed, Mo/Cu TES can be deposited in a single sputtering chamber, simplifying fabrication process and reducing waiting time between layer deposition. However, as mention in Section 11.2, for Mo/Cu bilayers the process to achieve normal metal edges is more complicated than the one described above, since Mo etchants also attack the Cu layer. An extra fabrication step is required to deposit Cu “sidebanks", covering superconducting

edges [160].

After pattering Mo/Au bilayers, a superconducting path from the sensor to the bias circuit is deposited. Since thermal connection is controlled by Si_3N_4 membrane, superconducting materials are used to ensure good electrical conductivity and thermal isolation. Nb –being the element with higher critical temperature, 9.3 K– is usually choose for TES wiring [160, 167, 177, 244]. To simplify fabrication root, in some cases Mo layer deposited at first place is also patterned into contact pads [161]. In our case, this simple idea is not feasible, since the wet Au etch also attack Mo. Thus, our approach consist in depositing an extra Mo layer of 175 nm thick by DC sputtering with a 35 W power over a photoresist mask, leading to Mo pads after lift-off. Mo/Au patterning can produce some residue that could affect affect superconducting pads by lowering its critical current or destroying its superconducting state. For this reason, an O_2 plasma etching process at a bias voltage of 30 V is performed after photoresist deposition and patterning to clean the region on Si_3N_4 where wiring is going to be deposited. The rest of the substrate will also be clear up with this plasma after Mo pads are lithographed. A schematic layout of the final sensor is depicted in Fig. 12.2a.

In Section 10.3.1 we showed that, when optimum deposition conditions are fulfilled, Mo T_C reproducibility is high (ΔT ∼50 mK). Covering the films in-situ with a thin 15 nm Au layer deposited by sputtering, to prevent contamination, decreases T_C due to the proximity effect, but also results in an improvement of T_C reproducibility. As plot in Fig. 12.3a this extra layer reduces T_C dispersion to ∼35 mK. By adding Au layer deposited by e-beam RRR factor increases from ∼ 1.9 in the case of the sputtered bilayer [181] to 4.2±0.6, without loosing reproducibility in T_C, as it will be shown later on.

12.4 Mo/Au TES thermometers: superconducting functional properties

Samples represented in Fig. 12.3a are non-lithographed bilayers deposited over 2.5x4.5 mm Si_3N_4/Si substrates. These bulk samples, display sharp transitions, ΔT∼20 mK. When size is reduce to micrometers (200x200 μm) by lithography, inhomogeneities are eliminated and transition widths are reduced to a few milikelvin. As an example, in Fig. 12.3b some bulk and lithographed Mo/Au bilayers are displayed, showing a reduce ΔT of 8 mK. This chemical process does not affect bilayer critical temperature, moreover, contrary to what was obtained by Olsen et al. [174] no difference, both in transition temperature and width, was observed when samples were deposited over freestanding Si_3N_4

membranes. As shown in Fig. 12.4a, transition width of the order of 1 mK are typically found for lithographed samples with 215 nm Au thickness. Their normal resistance is R_N ∼25 mΩ, similar to other TES with equivalent normal metal thickness [161, 175].

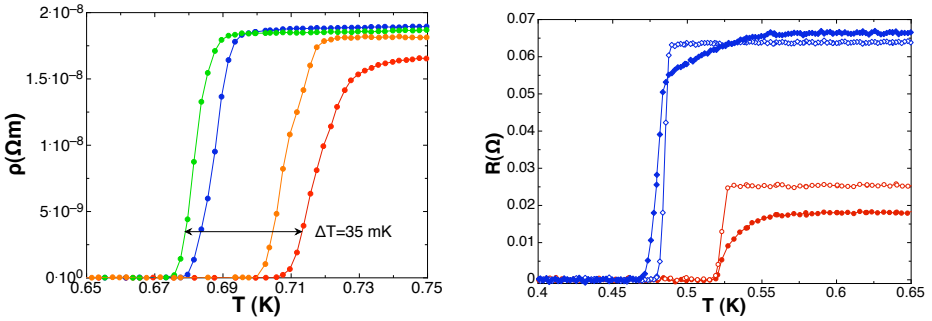

(a) (b)

Figure 12.3: (a) $R(T)$ of sputtered 50 nm Mo and 15 nm Au bilayer set of samples. (b) $R(T)$ of Mo/Au bulk samples (full symbols) and corresponding lithographed ones (empty symbols).

The excellent sensitivity of TES, associated with their sharp superconducting transitions is usually expressed by the parameter α:

$$\alpha = \frac{dlogR}{dlogT} = \frac{T}{R}\frac{dR}{dT} \tag{12.1}$$

being this value usually of the order of 2000 [163, 178, 241] for transition width ∼ 1 mK. The use of Eq. 12.1 on data presented in Fig. 12.4a give as a result similar values of α. In our case R_N=0.025 Ω, while R_N ∼1.5 Ω in Ref. [241] and ∼ 160Ω in Ref. [163]). The small current signal required to avoid self heating in Mo/Au sensors deposited over membranes, combined with their small resistance values will lead to a non negligible noise in the resistance determination. This noise, together with the sharpness of the transitions, results in a considerable uncertainty in α estimation using Eq. 12.4. To reduce the error bar in α estimation and compare in a more precise way how the bilayer sensitivity is increased by the lithographed process, the following analysis is performed. Critical temperature is estimated by linearly fitting the high temperature part of the superconductting transition, being T_C defined as the temperature at which the linear fit and $R(T)$ data diverge. For $T < T_C$, $R(T)$ curve can be expressed by Eq. 12.2.

$$R(T) = R_N \exp\frac{T - T_C}{\Delta T} \tag{12.2}$$

Since, at this low temperature part of the transition, $R(T)$ curve is expected to have a higher slope, α can be estimated as $T_C/\Delta T$, being this value temperature independent. With this consideration lithographic process increase α values from $\sim$ 220 to 605$\pm$140, being this the average α value from samples presented in Fig. 12.4a. An example of this estimation is depicted in Fig. 12.4b, where $\alpha = 596 \pm 84$ is obtained for a 75/215 nm lithographed Mo/Au bilayer.

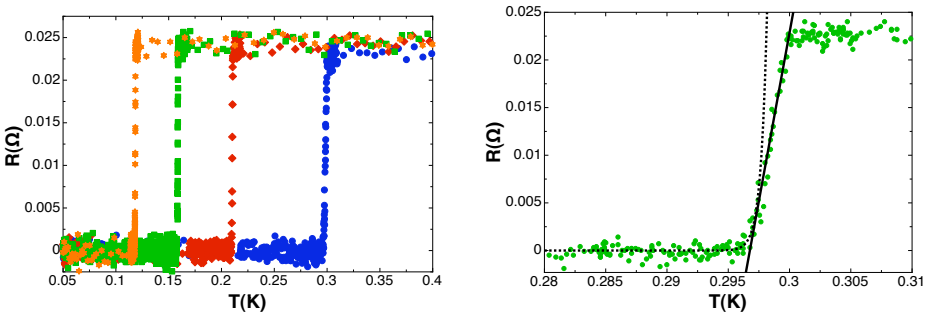

(a) (b)

Figure 12.4: (a) $R(T)$ of some lithographed bilayers (•75/215, ♦65/215, ▪60/215, ✶53/215). (b) Example of α calculation for a Mo/Au lithographed bilayer (75 nm/215 nm). Full symbols represent $R(T)$ measurements, solid line correspond to $T(C)$ calculation and dash line to the fit of experimental data to Eq.12.2 for $T < T_C$.

Combining these results with the dependence of the critical temperature with d_{Mo}, discussed in Chapter 11 we obtain the characteristics of our TES thermometers. Mo/Au TES with a working temperature $\sim$ 100 mK, a transition width of $\sim$ 3 mK, $\alpha \sim 600$ and $R_N \sim 25\ m\Omega$ are achieved for bilayers formed by 53 nm of Mo and 215 nm of Au. Among these parameters, R_N can be tuned depending on the application by changing the gold layer thickness, always above ξ_M, without affecting the other functional properties of the sensor.

12.5 Conclusions

A simple lithographic route is followed to achieve normal metal conditions on bilayer boundaries. Besides its simplicity, sharp edges are observed, ensuring a good coverage of Mo boundaries. Deposition over freestanding membranes instead of bulk substrates, and lithographic processes do not affect Mo/Au bilayers T_C, although, as expected, transition width is reduced.

Mo/Au TES basic functional properties –T_C, R_N and α– are determined showing results comparable to the ones found in literature for similar sensors

[160, 161]. The excellent reproducibility, the sharpness of the transitions and the low residual resistance make these thermometers ideal for radiation detection applications. As it will be discussed later on, TES can be used as bolometers or as microcalorimeters. Therefore, as already mentioned the enormous potential of TES can be applied in cryogenic radiation detectors in a wide range of frequencies. TES are the base for the next generation of ultra-sensitive detectors required for future space based telescope missions, being also ideal calorimeters for the next generation particle astrophysics experiments. Thus, the development of a Mo/Au TES is a key point for the development of a new type of technology for radiation detection in Spain. A development that could improve the quality of the Spanish contributions to the next generation of space missions and to reduce the huge gap between Spain and the leading countries in Europe developing cryogenic technologies for space.

In order to continue with this development a more complete characterisation, of TES, including current-to-voltage measurements, would be required. To do so a set up for Mo/Au I-V measurements is being developed an implemented. This system, formed by a SQUID sensor and the necessary polarisation circuit described in Chapter 14 is complemented by a small superconducting coil, placed right behind the sample holder, and a EM shield. This shield, formed by a lead and a μ-metal cans, is hold to the mixing chamber plate by an aluminium support, as shown in Fig. 12.1b. This system, currently under testing, will allow to further extent the study of our Mo/Au sensors and their applications to cryogenic radiation detectors.

Chapter 13

AC bias characterisation of a TES microcalorimeter

13.1 Introduction

Because of the success obtained by Chandra (NASA) and XMMNewton (ESA) missions, space agencies are studying and designing new missions involving detectors prepared to performed high resolution spectroscopy and X-ray imaging of extended sources. TES high sensibility place them among the best candidates to build the pixels of the cryospectrometric cameras required for these missions. In order to achieve the technical requirements in terms of energy resolution and count rate of this instrumentation, no signal degradation due to electronic readout will be allowed. Therefore, superconducting quantum interface devices (SQUIDs) are needed to amplify TES signal to match the noise and impedance level of TES to the room temperature electronics.

Given that the SQUID bandwidth is bigger than TES pulses bandwidth, a huge amount of sensors might be read by using only one SQUID amplifier. Thus, allowing to reduce the amount of cables and amplifiers needed for the read-out of large arrays and, therefore, the power dissipation of the system and the heat load onto the refrigerator. To do so, multiplexed read-out electronics is needed.

13.1.1 Frequency domain multiplexing versus time domain multiplexing

During the last years, two different multiplexing techniques have been developed for the readout of large imaging arrays: time-domain multiplexing

(TDM) and frequency-domain multiplexing (FDM). In both cases TES signals are multiplied by a set of modulating functions and summed by just one amplifier. One can recover each of these signals by multiplying the final signal by the correspondent modulating function and applying a low pass filter to remove the higher harmonics [245].

TDM was first developed at NIST, Boulder [246–249] in collaboration with GSFC, Greenbelt. In this multiplexing method, M column of N TES are read-out using M SQUID amplifiers. Each of these N sensors are switched on and off sequentially, and measured during 1/N of the total measuring time. This method is quite straightforward, and is the most mature multiplexing technique. However, it presents some problems and limitations. Switching from one sensor to the next one reduces the total signal bandwidth. This effect cannot be compensate by increasing the SQUID bandwidth, because this will also increase SQUID white noise, generating aliasing effects. Antialiasing filters are not a solution, since they will slow down the electronic system, thus decreasing the number of readable pixels. Therefore, TDM is a good option for sensors with small bandwidth, such as bolometers, where the pulse fall time is of the order of milliseconds. An other reason that makes TDM suitable for bolometer arrays read-out is that this method keeps on measuring all over the time. While in the case of microcalorimeters, whose signal is not continuous over time, most of the measuring time contents no information.

An other choice is FDM, developed at Berkeley [250], ISAS [251], and SRON-VTT [252, 253]. Since TES is a resistive component FDM is normally applied by using amplitude modulation, however, frequency modulation is also possible. In that case, each pixel is polarised with an AC voltage bias into a LC circuit, usually with a sinusoidal signal of frequency

$$f_i = \frac{1}{2\pi\sqrt{L_i C_i}} \tag{13.1}$$

and the changes in the TES resistance caused by a photon absorption modulate the amplitude of the carrier signal. Each of the pixels read-out by the same SQUID are AC biased at a different frequency, therefore, they are separate in the frequency space, and can be carried by the same cable without loosing information. The absence of a switch makes this multiplexing method faster than TDM, and increases the available bandwidth. In order to avoid a continuous measurement, like in TDM, bias current cancellation (BCC) is used, in this way information gets into the amplification chain only when there is a signal in one or more of the pixels. The main technical limitations for FDM development are the difficulties of obtaining compact LC filters with high Q, the carrier slew rate that can originate cable crosstalk due to higher harmon-

ics or the availability of Squids with a high enough dynamic range, crucial to guarantee low noise and a high linear response.

13.1.2 Other multiplexing methods.

Besides these widely used multiplexing methods other techniques are currently under development. TDM and FDM operate at low frequencies, where usual experimental techniques as low-power twisted-pair wiring and low-noise amplifiers can be used. Microwave TES multiplexers can use compact microwave filters and present larger total bandwidths than traditional FDM and TDM; that would allow to multiplex more signals in each wire [254, 255]. Disadvantages are the difficulty of room-temperature electronics and the lack of maturity of the technique. Hybrid designs combining a low-frequency TDM with a second-stage FDM in a microwave resonant circuit [256] or two stages of FDM [257] are also under development, as well as code division multiplexing, where a *"code"* band is define by switching the polarity with which each detector is coupled to the output channel in an orthogonal Walsh patter [258].

In order to use a frequency domain based system to multiplex and read a TES array, is essential to demonstrate that the observed good performance of a single pixel under constant voltage bias is maintained even when the TES works as a modulator. This chapter is devoted to resume the experimental effort set on at SRON –Netherlands Institute for Space Research–, to demonstrate this equivalent behaviour [259]. In this chapter, a full comparison of the performance of a high resolution X-ray TES microcalorimeter under DC bias and AC bias at a frequency of 370 kHz is presented. In Section 13.2 the measurement system and the characteristics of the detector are described. In Section 13.3 the characteristics of AC data acquisition and the differences with DC measurements are explained. A full characterisation of the TES behaviour under AC bias is performed, and, since the studied sensor has already been characterised under DC bias [152, 260], the obtained results are compared with those in Sections 13.4 and 13.5. Finally a summary of the main results presented on this chapter is exposed in Section 13.6

13.2 Measurement system

The detector has been mounted in a Janis two-stage ADR cooler, precooled at 3.5 K by a mechanical Cryomech Pulse Tube(PT). This system make use of two built in pills: a gadolinium-gallium garnet (GGG) crystal operating at a temperature of $\sim$1 K, and a ferric ammonium alum (FAA) salt pill operating at $\sim$50mK. This base temperature can be hold for a three day period and can

be restored after a recycling period of three hours. Both pills are magnetised simultaneously using a 4 Tesla conductively cooled multi-filamentary Niobium-Titanium superconducting magnet, whose temperature is monitored by two thermometers. Ruthenium oxide thermometers control the temperature of the different stages.

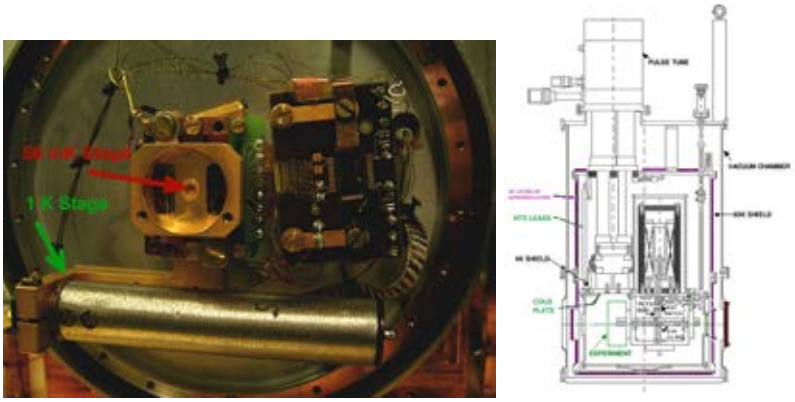

(a) (b)

Figure 13.1: (a) Picture of the characterisation set-up mounted in the ADR cold stage. (b) Cross section of the two-stage Adiabatic Demagnetisation Refrigerator precooled by a Pulse Tube.

Each pill has its own ultra low thermal conducting support structure, isolating it from the 4 K flange and the intermediate stage, and a high permeability magnetic shield surrounding the magnet and the two pills, to reduce the stray magnetic field in the vicinity of the cold stages The detector cold-head, the harness and the room temperature electronics are placed in a Faraday cage in order to reduce the electromagnetic interferences from the external environment. This Faraday cage is completed in the cold stage with a double shield attached to the 3.5 K stage. This double shield consists of a cryoperm shield an a copper load-tin plated superconducting shield. A picture of the experimental set-up, together with a cross section of the two-stage Adiabatic Demagnetisation Refrigerator are shown in Fig.13.1. The current through the TES was measured by a PTB SQUID, operated in flux locked loop (FLL). The inductance of the SQUID input coil is $L_s \sim 70$ nH. The SQUID array is directly read out by a low noise commercial PTB-Magnicon electronics in the DC bias case, and by a FrontEndElectronics(FEE) developed at SRON in the AC bias case. The L and C elements required for the AC bias experimental case are discrete components: L is a 700nH coil made of a Nb wire wounded around a Teflon cylinder and C is an NP0 capacitor with nominal value C=220nF.

The sensor is a single-pixel of a 5x5 array and consists of a Ti/Au bilayer with a Cu absorber at the centre of the TES. The sensor is deposited on a Si_xN_y

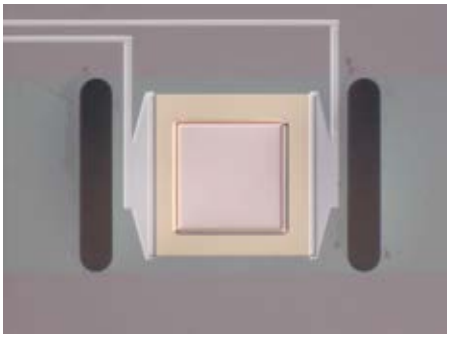

(a)

TES area	146μmx150μm
Ti thickness	25 nm
Au thickness	50nm
Cu absorber area	100μmx100μm
Cu thickness	1000nm
T_C	100mK
R_N	143mΩ
G at T_C	0.36nW/K
C	0.3pJ/K
P at T_{bath}	6.5pW

(b)

Figure 13.2: (a) Picture of the sensor. *Credit: SRON/Utrecht.* (b) TES microcalorimeter main parameters.

membrane, which provides a weak thermal link to the ADR bath temperature [244]. The transition temperature of the TES is T_C∼100mK, and the normal state resistance is $R_N = 143m\Omega$. A top-view picture of the sensor and its main parameters are displayed in Fig.13.2.

13.3 AC bias measurement analysis

A schematic description of the TES characterisation system under AC polarisation can be seen in Fig.13.3. The only difference between this measurement system and the one used for DC bias is the presence of an LC filter that defines the bias circuit resonance frequency. In this system the TES is not voltage biased with a constant DC level through a shunt resistance; instead, an alternating bias current at the resonance frequency of the circuit is used. When a photon reaches the detector it heats up the TES, thus inducing a change in the resistance of the device. This change modulates the AC current flowing through the TES, therefore, the signal at the input of the amplification chain can be described as: $A(t)\cdot B(t)\sin(\omega_0 t)$, where $A(t)$ is the TES response and $B(t)sin(\omega_0)$ is the carrier wave.

13.3.1 Recovery of sensor response information.

There are two different ways to regain the sensor behaviour information. First, one can try to fit the output signal, taking advantage of the fact that the signal frequency is a known value, however, this method is extremely complicated since the system response is not linear. In this chapter, the method we use is the following: the output signal is multiplied by itself, then, if one considers

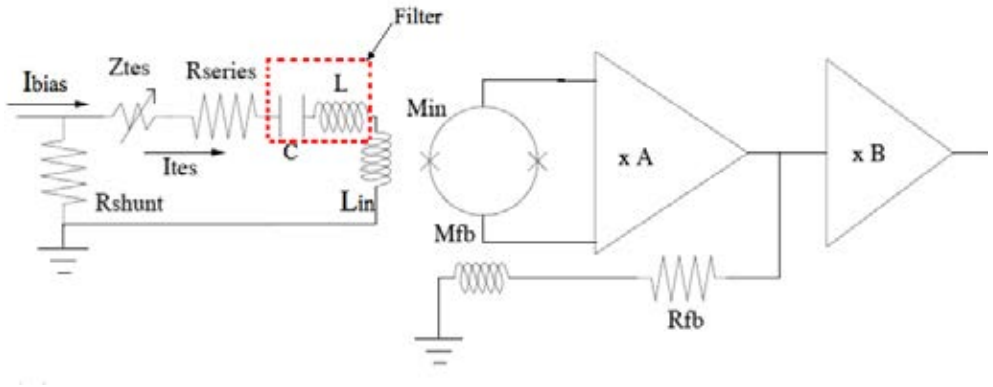

Figure 13.3: Diagram of TES measurement circuit under AC bias.

the carrier wave amplitude to be equal to one, the final product is:

$$\frac{A(t)^2}{2} \cdot (1 - \cos(2\omega_0 t)) \tag{13.2}$$

Then, this signal is filtered at a frequency lower than $2\omega_0$ and the square root value is taken. This value, $A(t)/\sqrt{2}$, is the RMS value of I_{TES}, that is, the DC equivalent value. This means that, if one assumes that ω_0 is high enough to consider the TES thermally decoupled from the carrier wave, the sensor behaves as if it was DC biased with a constant amplitude level equal to $A(t)/\sqrt{2}$. Therefore, one can use the same analysis equations developed for TES operated under DC bias in the AC bias case, that is, after demodulating the output signal, data analysis under AC bias is equivalent to DC bias data analysis.

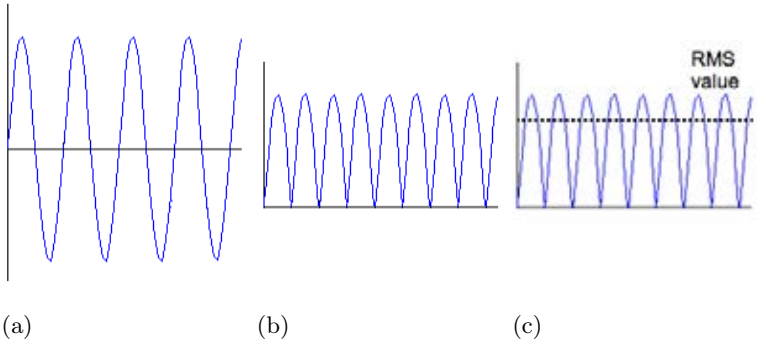

Figure 13.4: Different steps of AC signal analysis: (a) Carrier wave. (b) $\frac{A(t)^2}{2} \cdot (1 - \cos(2\omega_0 t))$. (c) I_{RMS}

13.3.2 Feedback loop gain estimation.

In order to linearise the output of the SQUID a feedback loop is used to cancel out the signal at the input of this amplifier, as exemplified by Fig.13.5a. Therefore, the output of the system can be expressed as:

$$V = A \cdot V_{ext} \tag{13.3}$$

in open loop, whereas in close loop the proper expression would be:

$$V = A \cdot V_{in} = A \cdot (V_{ext} - \beta V) \tag{13.4}$$

Thus, the signal at the input of the SQUID would be:

$$V_{ext} = V_{in} \cdot (1 - \beta A) \tag{13.5}$$

where βA is the SQUID feedback loop gain, $\mathscr{L}$. In a DC bias circuit this loop gain is infinite and, as a result, the total gain of the amplification chain is equal to one($\mathscr{L}/(1-\mathscr{L})=1$). This can be easily seen when one considers a more complex sketch of the amplification chain(see Fig. 13.5b).

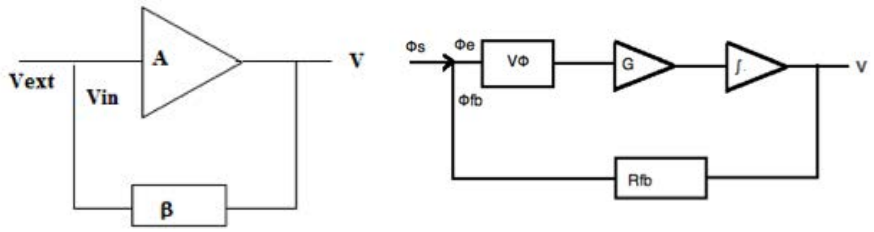

(a) (b)

Figure 13.5: Schematic drawing of the amplification circuit

In this case V_Φ is the SQUID gain, G in an amplifier of constant gain, $\int$ is an integrator with just one pole, $\beta = M_{fb}/R_{fb}$ and $\Phi_e = \Phi_s - \Phi_{fb} \approx 0$. Taking into account all this information, the feedback loop gain can be expressed as:

$$\mathscr{L} = \frac{M_{fb}}{R_{fb}} V_\Phi G \frac{f_1}{if} \tag{13.6}$$

That means that for frequencies different than zero it is no longer possible to consider $\mathscr{L}$ as infinite, moreover, the gain of the amplification chain depends on the feedback resistance of the SQUID. Thus, when measuring the response of

the sensor to the variations of the carrier wave- I-V measurements- a correction factor associated with each R_{fb} must be taken into account. The influence of this correction factor is shown in Fig. 13.6, where I-V curves measured with different R_{fb} with and without correction factor are displayed.

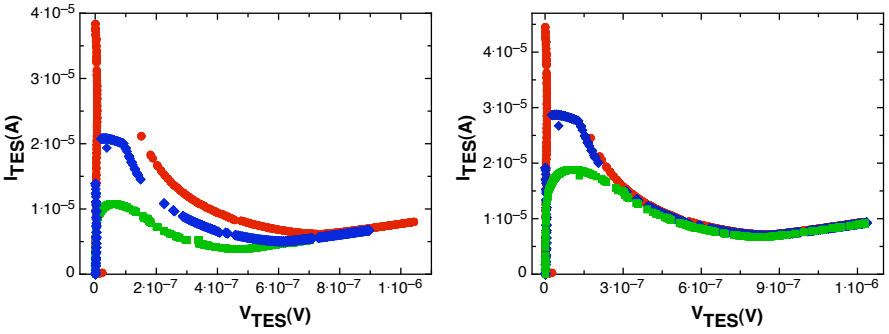

(a) (b)

Figure 13.6: (a) I-V measurement at T_{bath}=73 mK for different R_{fb} values. Full circles represent an I-V measurement with $R_{fb} = 1.9k\Omega$, full diamonds with $R_{fb} = 4.2k\Omega$ and full squares with $R_{fb} = 8.2k\Omega$. (b) I-V measurement at T_{bath}=73 mK for different R_{fb} values corrected to take into account the change of $\mathscr{L}$. Full circles represent an I-V measurement with $R_{fb} = 1.9k\Omega$, full diamonds with $R_{fb} = 4.2k\Omega$ and full squares with $R_{fb} = 8.2k\Omega$

This correction factor can be estimated by using Eq. 13.7:

$$\frac{V_{open\ loop}}{V_{close\ loop}} = 1 + \mathscr{L} \tag{13.7}$$

The main difficulty that one has to face in order to determine the loop gain at the circuit resonance frequency is that this frequency is not the same when working in open loop or in close loop. The coupling through the mutual inductance M_{fb} between the feedback loop and the TES bias circuit originates this difference, modifying the system when working in close loop and changing slightly the resonance frequency.

To avoid this problem, the circuit response of the system was measured in open loop and in close loop in a wide range of frequencies. An example of these measurements for R_{fb}=1.9 kΩ is shown in Fig.13.7a. In order to obtain the $\mathscr{L}$ value, the quotient of both measurements is taken. Since this quotient diverges at the resonance frequency, so as to estimate the loop gain value at resonance, the quotient is fitted to Eq. 13.8 for frequencies above and below the resonance one.

$$y = \frac{a}{1 + \frac{x}{f_0}^2} \tag{13.8}$$

This fitting and the quotient result are ploted in Fig.13.7b. Using the estimated loop gain values at the circuit resonance frequency, obtained from this analysis, the I-V measurement data are corrected as displayed in Fig.13.6b. For feedback resistance values of R_{fb}=4.2 kΩ and 8.2 kΩ, I-V curves presented in Fig. 13.6 saturate at high values of I_{TES}. When $\mathscr{L}$ is not high enough, the signal at the SQUID input is not fully cancel out, thus the signal that the SQUID has to amplify is bigger and, at some point, when I_{TES} is too large the SQUID response becomes saturated.

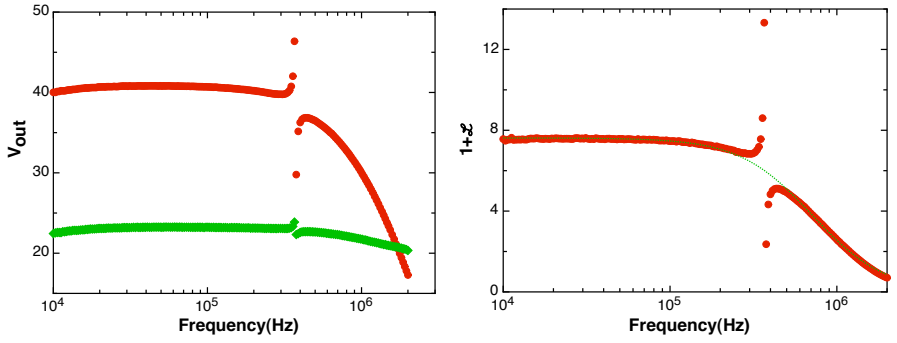

(a) (b)

Figure 13.7: (a) Full circles represent the SQUID output voltage when operated in open loop, full diamonds represent the SQUID output voltage when operated in close loop. (b) Full circles represent the quotient between SQUID output voltage when operated in open loop and in close loop. Dash line represents the fitting of these data to Eq.13.8.

13.3.3 Extra negative resistance in the TES bias circuit

In the TES characterisation circuit there are couplings between the different parts of the system - the bias circuit, the amplification chain and the feedback loop- through various mutual inductances, as can be seen in Fig.13.8.

These couplings can be expressed as:

- Coupling between the bias circuit and the feedback loop: M_{if}=$\alpha_{if}(L_{in}L_{fb})^{1/2}$
- Coupling between the SQUID and the feedback loop: M_{fb}=$\alpha_{fb}(L_{fb}L_{SQUID})^{1/2}$
- Coupling between the bias circuit and the SQUID: M_{in}=$\alpha_{in}(L_{in}L_{SQUID})^{1/2}$

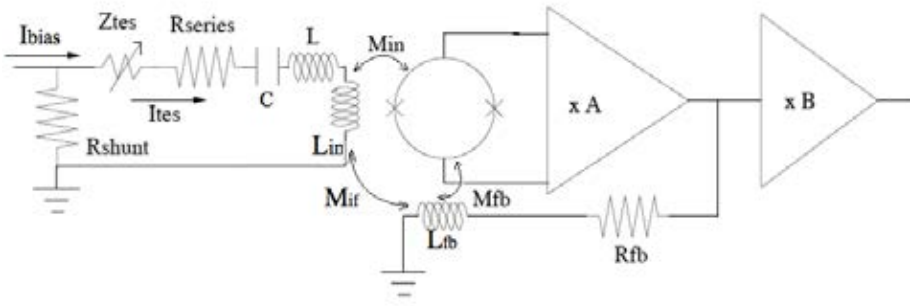

Figure 13.8: Mutual inductances in TES AC bias circuit.

Thus, the voltage at L_{in} inductance terminals is described by Eq.13.9.

$$V_{in} = \Big[i\omega(L_{in} + L_{SQUID}) + R_T + \frac{1}{i\omega C} \Big] I_{in} + i\omega M_{in} J + i\omega M_{if} I_{fb} \qquad (13.9)$$

In Eq.13.9 J is the current running through the SQUID and R_T is the total resistance of the circuit. Since in the PTB chip [261] the feedback inductance, L_{fb}, is deposited over the SQUID, the coupling between this L_{fb} and the bias inductance, L_{in}, is similar to the coupling between the SQUID and L_{in} and it cannot be neglected. The response of the feedback loop can be expressed as:

$$M_{fb} I_{fb} = \Big(- \frac{\mathscr{L}}{1 + \mathscr{L}} \Big) \frac{M_{in} I_{in}}{V_\phi^r} \qquad (13.10)$$

where V_ϕ^r is the reduced flux to voltage transfer function of the SQUID, i.e. the measure output of the SQUID. When neglecting the current running through the SQUID, one gets:

$$Z_{in} = \frac{V_{in}}{I_{in}} = \underbrace{i\omega \left[L_{in} \left(1 - \frac{\mathscr{L}}{1 + \mathscr{L}} \frac{1}{V_\phi^r} \frac{\alpha_{if} \alpha_{in}}{\alpha_{fb}} \right) + L_{SQUID} \right]}_{(1)} + \frac{1}{i\omega C} + R_T \qquad (13.11)$$

At ω=0, $\mathscr{L}/(1+\mathscr{L})$ is a constant and real value, as it was shown in Eq.13.6, therefore (1) is a purely imaginary number, and the only real part in Z_{in} is R_T. Thus, under DC bias there is no influence of the feedback loop in the effective resistance of the circuit. However, at high frequency Z_{in} is equal to:

$$Z_{in} = R_{eff} + i\omega L_{eff} \tag{13.12}$$

where:

$$R_{eff} = R_T + \underbrace{i\omega Im\left(\frac{\mathscr{L}}{1+\mathscr{L}}\right)\frac{1}{V_\phi^r}\frac{M_{if}M_{in}}{M_{fb}}}_{(2)} \tag{13.13}$$

$$L_{eff} = L_{in} + L_{SQUID} - Re\left(\frac{\mathscr{L}}{1+\mathscr{L}}\right)\frac{1}{V_\phi^r}\frac{M_{if}M_{in}}{M_{fb}} \tag{13.14}$$

Therefore, at high frequency (2), that is always a real value, generates a negative contribution to the circuit effective resistance, whose absolute value increases as R_{fb} increases.

13.3.4 TES loading curve.

Until this point, it has been considered that the TES is decoupled from the AC bias signal. Since the signal fall time of this sensor is $\sim 100\mu s$ [262] and the working resonance frequency is $\sim 400kHz$, the TES has a response much slower than the bias signal and, therefore, from a thermal point of view it is correct to assume this decoupling. However, for the electrons, the current running through the system is not equivalent to I_{RMS} because they can follow the current changes between I_{max} and -I_{max}. In the current regions where the TES is either in normal or superconducting state, the sensor behaves as a resistor and, as a result, the sensor response is equivalent under AC or DC bias voltage, but this is no longer true in the transition state. In order to determine if considering the TES under AC bias as polarised by a DC level equal to I_{RMS} is correct, the system loading curve is analysed. The transition to the superconducting region is studied in order to determine if this transition is caused by thermal effects, as in a DC bias sensor, or by the fact that the real maximum value of the current that electrons *"see"* is higher than the RMS value considered so far.

To obtain the loading equation of the system one has to consider the Thevenin equivalent of the circuit presented in Fig.13.9

where:

$$R_{Load} = R_S + R_{series} \tag{13.15}$$

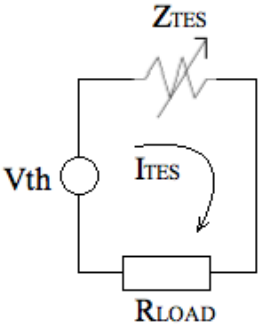

Figure 13.9: Thevenin equivalent of TES circuit.

$$V_{th} = I_{bias} \cdot R_S \tag{13.16}$$

Since:

$$V_{TES} = V_{th} - I_{TES} \cdot R_{Load} \tag{13.17}$$

the loading curve of the system can be written as:

$$I_{TES} = \frac{I_{bias} \cdot R_S}{R_{Load}} - \frac{V_{TES}}{R_{Load}} \tag{13.18}$$

In an ideal system (R_{Load}=0) a TES could be bias in the transition for an arbitrary small value of V_{TES}, whereas in a real case the TES can only be bias in the transition while the corresponding loading curve crosses the ideal system I-V curve. The reason why, is that, when I_{bias} is reduced a point is reached where the current supply by the source is not enough to keep the TES *"hot"* –i.e., in the transition–, and the sensor *"jumps"* into the superconducting state. If the TES under AC bias is working electrically as if it was biased by a DC current equivalent to the RMS value of the AC signal, for the last stable bias point in the transition region the loading curve should be tangent to the I-V curve in that point. On the contrary, if the electrons on the TES were seeing a higher I_{bias} than the RMS value assume in the I-V curve, the loading curve and the corresponding bias point in the I-V curve wouldn't match.

As can be seen in Fig.13.10, the loading curve of the last stable bias point in the transition is tangent to the I-V curve in this point. Therefore, considering that a TES under AC bias behaves as if it was DC biased with a voltage

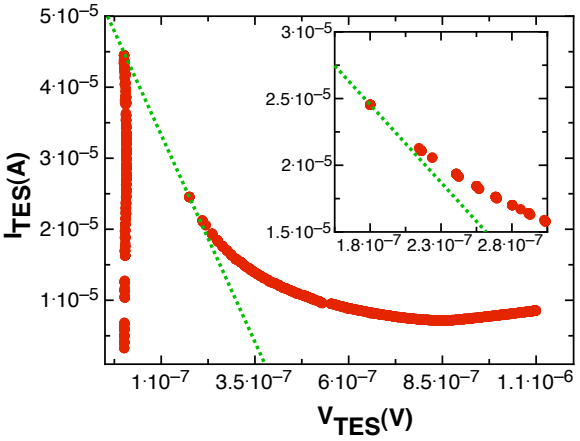

Figure 13.10: Example of an I-V measurement at T_{bath}=73 mK with R_{fb} = 1.9$k\Omega$ and the loading curve corresponding to the last stable bias point in the transition. Inset shows a zoom of the region at which both curves cross

equivalent to the RMS value of the alternating signal is a correct assumption from both electrical and thermal point of view.

13.4 I-V measurements

13.4.1 Measurement conditions optimisation.

To establish the optimum measurement conditions for I-V determination, a set of I-V curves with different R_{fb} and magnetic fields are obtained. Considering the transition temperature of the TES (T_c ∼100 mK) and the cooling power of the ADR these measurements where taken at T_{bath}=73 mK, where the temperature stability of the refrigerator is long enough to fully characterise the sensor. As can be seen in Fig.13.6, for R_{fb} = 4.2 kΩ and 8.2 kΩ I-V curves saturate for high values of I_{TES}. In these cases, as explained in Section 13.6, $\mathscr{L}$ is too small and it is not possible to cancel out the signal at the SQUID input, therefore, for high values of the input current, the SQUID response becomes saturated. Moreover, for R_{fb} = 8.2 kΩ, the amplifier gain is not constant, it depends on the carrier wave amplitude; so, the superconducting branch is no longer a straight line of infinite slope, instead it becomes bent to the left. Because of all these problems caused by the system readout electronics, the complete characterisation of the system was performed using R_{fb} = 1.9 kΩ.

In Fig.13.11, the dependence of I-V measurements with an external applied magnetic field is shown. For this propose a small coil made of Nb/Ti wire coated with Cu/Ni is mounted into a gold plated oxygen free copper plate

and placed behind the TES holder. In Fig. 13.12, the TES response as a function of the applied magnetic field at a constant value of V_{TES} is plotted. In both figures is observed that, for the same TES voltage, the maximum TES current response is found for an applied magnetic field of 88 mOe; this value was also obtained for previous DC measurements on the same detector and measurement set-up. This optimum value is assumed to be the one that cancels out the remanent magnetic fields present in the system because of wiring, among others. With these data the optimum measurement conditions are established to be T_{bath}=73 mK, R_{fb} = 1.9 kΩ and H = 88 mOe.

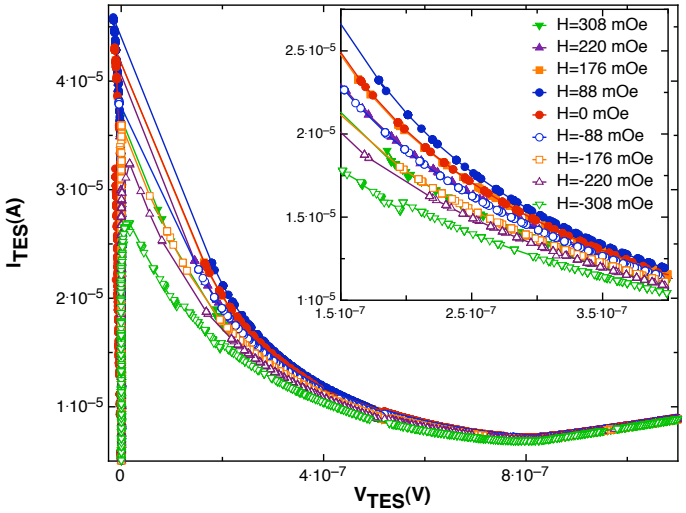

Figure 13.11: I-V measurements with $R_{fb} = 1.9k\Omega$

The importance of working at resonance is analysed in Fig. 13.13. I-V curves raw data, measured for carrier wave frequencies slightly different from the resonance one, show that the slope of the superconducting branch of the curve depends on the frequency. being its difference with the slope of the I-V curve raw data at resonance bigger, the larger the deviation from resonance. When the carrier wave is not at resonance, not all the signal goes through the LC filters, consequently the real gain of the system is smaller than considered when calibrating the curves, affecting the superconducting and the transition region. In the normal part no effect is observed since, due to the high resistance of the sensor in the normal state, the current does not enter the bias circuit but runs directly into L_{in} without loses. Thus, to ensure that all the signal goes through the circuit, and that the estimated correction factors for I-V curves calibration are the proper ones, measurements need to be taken at resonance frequency.

To be sure that the system and the measurement conditions are stable an

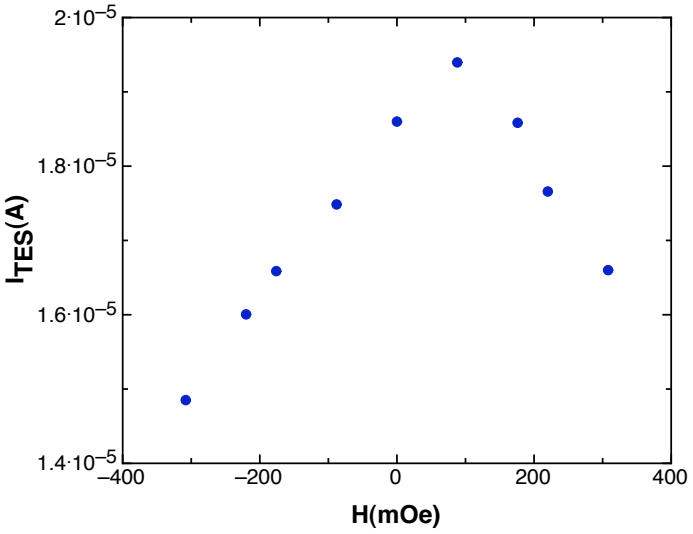

Figure 13.12: TES response to different magnetic fields at a constant V_{TES} value, $V_{TES} = 2.24 \cdot 10^{-5}$.

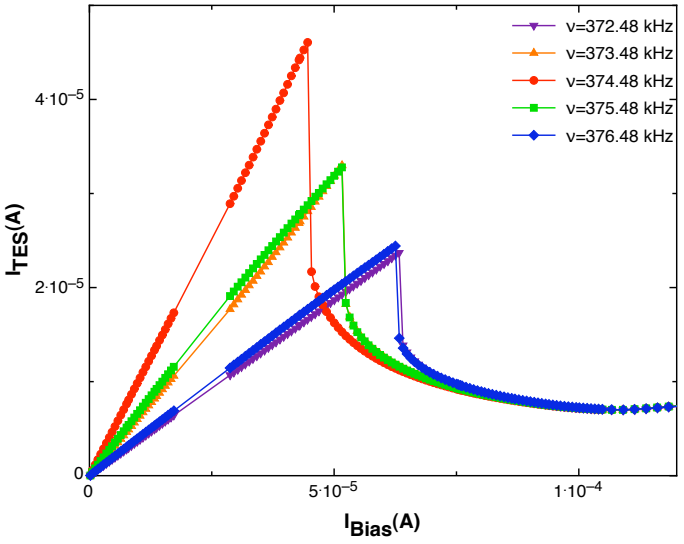

Figure 13.13: I-V measurements with $R_{fb} = 1.9k\Omega$ and H=88 mG at different frequencies of the carrier wave

I-V measurement with $R_{fb} = 1.9k\Omega$ and H=88 mOe at resonance is performed on different days. These results are displayed in Fig. 13.14, and show that measurements under AC bias voltage are reproducible and the system is stable.

In Fig. 13.15 two current-to-voltage(I-V) and power-to-voltage (P-V) measurements in the same TES and in the same conditions under AC and DC bias voltage are compared. Although the TES behaviour under AC and DC is

almost equivalent, a small deviation that remains unexplained is observed low in the transition region.

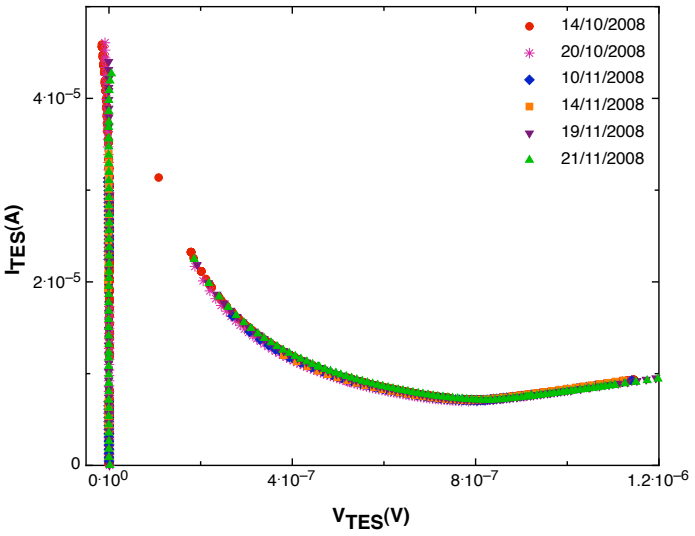

Figure 13.14: I-V measurements with $R_{fb} = 1.9k\Omega$ and H=88 mG at resonance taken during different days.

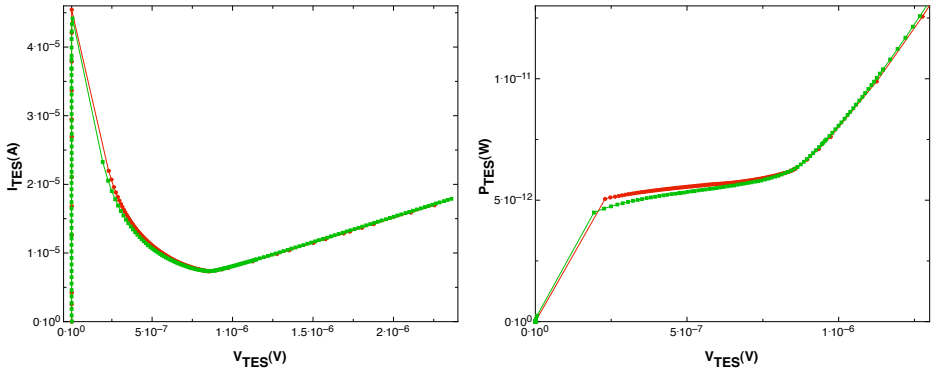

(a) (b)

Figure 13.15: (a) Comparison between AC –full squares– and DC –full circles– bias I-V curves measured in the same TES and in the same conditions. (b) Comparison between AC –full squares– and DC –full circles– bias power plateau measured in the same TES and in the same conditions.

Some suggested explanations are that, since the I-V measurement under DC bias was taken a few months before than the AC bias ones, the thermal coupling between the cooler and the TES has changed or that the ruthenium oxide thermometer has been degraded. As can be seen in Fig.13.17a a change as small as 3 mK could explain this difference. An other possibility is that the

higher harmonics of the bias signal were adding extra power to the sensor. This option is discarded because the intensity of the second harmonic is just 1/30 part of the sinusoidal signal intensity and, therefore the power contribution would be negligible, just 1/900 of the bias signal. It was also considered that in the AC bias case the remanent magnetic fields generated by the current running in the system are not properly cancel, since a DC current is being use for this propose, as observed in 13.11 a small remanent magnetic field could explain the observed small differences between AC and DC I-V curves.

However, this difference has been observed and studied in other systems [263] suggesting a common origin and, therefore, the first two previous explanations can be rejected. In this article, van der Kuur et al. stated that this effect might be due to the non-linear behaviour of the TES resistance when the detector is AC biased. Since the resistance is a function of the sinusoidal bias current, the time dependent part of the resistance would originate current higher harmonics. This effect depends on the dynamics of the superconductor in the transition and it is probably geometry dependent, thus being difficult to quantify and model. An other possible explanation could be a change in the circuit resonance frequency due to the effect of the TES impedance, since this effect is larger low in the transition.

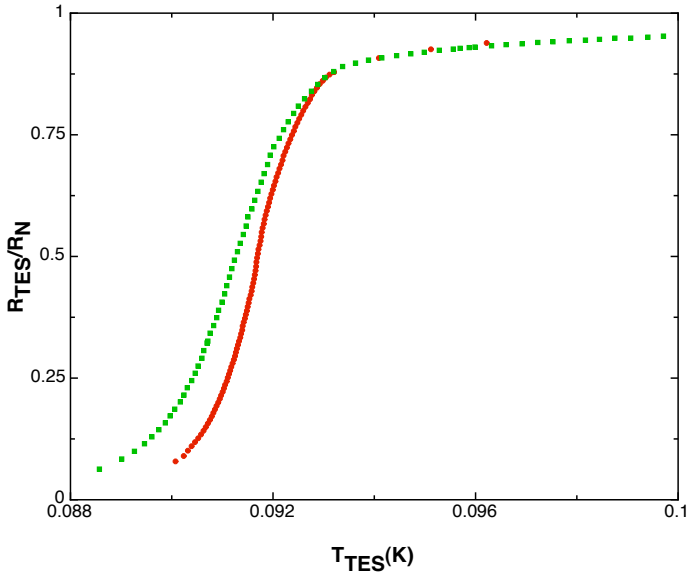

Figure 13.16: Comparison between normalised resistance under AC –□– and DC –●– bias as a function of temperature in the same TES detector and in the same conditions.

In order to check the change in the TES resistance as a function of the bias type, the normalised resistance versus temperature curve derived from the I-V

characteristics is shown in Fig.13.16 . The transition is clearly broadened in the AC bias case, and, for the same bias temperature in the lowest part of the transition the effective TES resistance under AC bias is about a factor of 2 higher. This difference could be explained by the reduction of $\alpha = \mathrm{d}logR/\mathrm{d}logT$ and $\beta = \mathrm{d}logR/\mathrm{d}logI$ when operating under AC bias instead of DC bias –see Section 13.5–, since the R(T) curve obtained from IV measurements is affected by these two parameters.

13.4.2 I-V measurements for different bath temperatures: estimation of the thermal conductivity of the sensor.

In order to complete the current-to-voltage characterisation of the sensor, I-V curves at different bath temperatures are measured. In Fig. 13.18 these curves are shown together with the power-to-voltage representations. From these data, one can determine some characteristic parameters of the system, such as n, K and the thermal conductivity of the sensor. Since the power flow to the heat bath can be assumed to follow Eq. 13.19:

$$P = K \cdot (T^n - T_{bath}^n) \tag{13.19}$$

n and K parameters can be obtained from a set of I-V curves at different temperatures. This is possible because, in the transition, providing that it is sharp enough, $T = T_C$ can be assumed in the whole current range and, thus, $P_{bath} = I_{TES} \cdot V_{TES} \approx constant$ in the transition region. The knowledge of the sensor parameters K and n, governed by the geometry and properties of the sensor the first one and by the dominant thermal conductivity process the latter, allow to estimate the thermal conductivity to the heat sink:

$$G = \frac{dP}{dT_C} = K \cdot nT_C^{n-1} \tag{13.20}$$

These expressions are only valid for the power dissipated through the membrane. The total power can be expressed as:

$$P_{total} = P_{membrana} + \Delta P_{ETF} \tag{13.21}$$

Where ΔP_{ETF} is the power due to the electro-thermal feedback of the TES. The electrical and thermal circuits of the TES are interconnected, in such a way that a thermal signal is translated into a change in the TES resistance. In the same way, a current signal is transformed in a thermal signal as a consequence of the Joule power dissipation. Since in a TES α is positive ($\alpha = \mathrm{d}logR/\mathrm{d}logT$) the TES resistance increases when the temperature

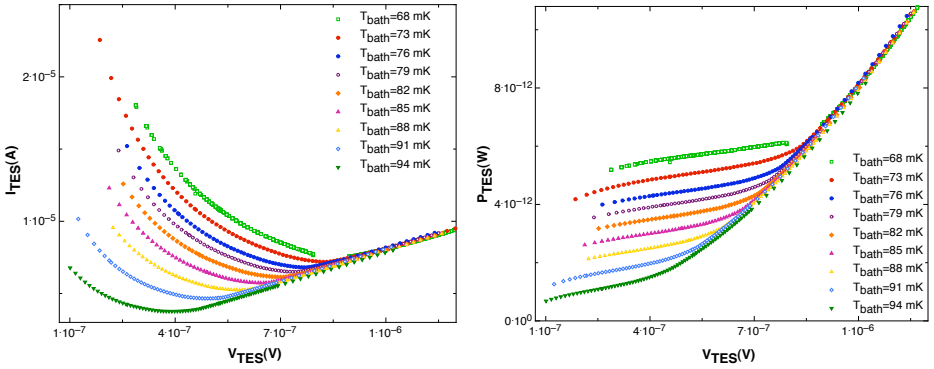

(a) (b)

Figure 13.17: (a) I-V curves determined at the optimum measurement conditions for different bath temperatures. (b) P-V curves determined at the optimum measurement conditions for different bath temperatures.

increases; therefore, when, as in this case, the TES is voltage biased, the dissipated Joule power is $P_J = V^2/R$ and the electro-thermal feedback of the TES is negative. This feedback stabilises the system since, when the sensor temperature increases, the TES resistance increases and, therefore the dissipated part in the total power decreases. This dissipated part is expressed as:

$$\Delta P_{ETF} \propto \frac{R_S - R_T}{R_S + R_T} \alpha \tag{13.22}$$

and this term is only equal to zero at the beginning of the transition, where $\alpha = 0$ and in the last stable point in the transition, where $R_S = R_T$. Consequently, n and K parameters are estimated by using points in the beginning of the transition in Eq. 13.19. Seeing that these parameters are not fully independent, so as to ensure that the best possible fit is obtained, one of the two parameters is fixed and the other is changed constantly into a wide range of values. After repeating this procedure by changing the other parameter the best fit is searched and showed in Fig.13.18b. The same procedure is applied to I-V curves measured in the same system under DC bias and, as it can be seen in Fig.13.18a similar parameters values, within the error limits, are obtain showing than the heat propagation mechanism under AC and DC bias are equivalent.

In order to study how independent is the determination of n and K parameter from thermometer calibration and critical temperature estimation the fitting procedure is repeated by changing slightly the critical temperature and both the critical temperature and the bath temperature.

In the first case, this new fitting shows that n and K determination is

extremely sensitive to changes in the critical temperature, therefore T_C must be properly measured in order to establish the thermal conductivity of the sensor.

T_C=T_C-3 mK	→	n=4.1, K=1.14·10^{-7}, G=0.348 nW/K
T_C=T_C-2 mK	→	n=3.67, K=4.2·10^{-8}, G=0.321nW/K
T_C=T_C+2 mK	→	n=2.8, K=5.49·10^{-9}, G=0.257nW/K

On the other hand, changes in the system thermometer calibration is not so critical since it would affect simultaneously the determination of T_C and T_{bath} and the influence on n and K would be somehow compensated. Therefore n and K determination is quiet stable to changes in the thermometry readout.

T=$T_{measured}$-2 mK	→	n=3.1, K=1.16·10^{-8}, G=0.280nW/K
T=$T_{measured}$+3 mK	→	n=3.2, K=1.3·10^{-8}, G=0.286 nW/K
T=$T_{measured}$+4 mK	→	n=3.2, K=1.3·10^{-8}, G=0.292 nW/K

In all the cases, the observed change in G due to the different variations is not as marked as the change in n and K due to the interdependence of both parameters.

According to the results shown above, it is crucial that T_C and T_{bath} are measured with the same thermometer and under identical experimental conditions. Since R(T) curves, in this case, were measured in a different set-up, the T_C value obtained from them could not be used to estimate n and K parameters. Instead, T_C = 100 mK, as reported by Takei et al [152], was used. This value was obtained by sending a small oscillating current ($\sim$ kHz) via the input bias line through the SQUID while warming up slowly the TES. At T_C, the TES becomes normal and the current in the SQUID drops because all the current flows through the shunt. In this way, one can ensure that both T_C and T_{bath} are determined under the same experimental conditions and with the same thermometer. n and K parameters displayed in Fig. 13.18 are, therefore determined assuming T_C = 100 mK, giving as a result G_{DC} = 0.31 nK/W and G_{DC} = 0.28 nK/W, equivalent values within the error limits.

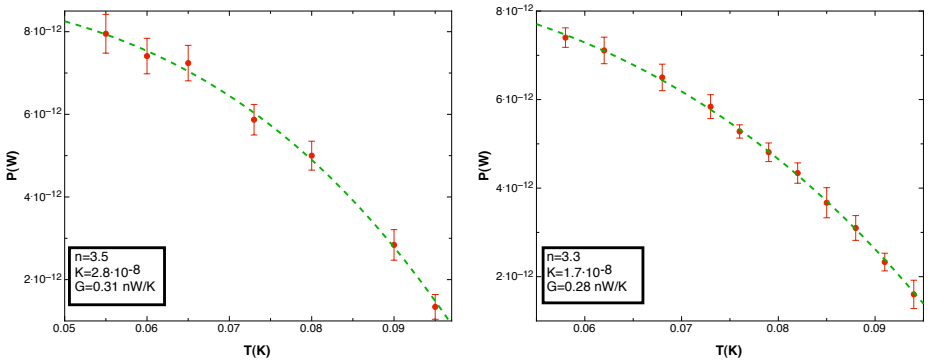

(a) (b)

Figure 13.18: (a) n and K parameters determination from DC bias I-V measurements. (b) n and K parameters determination from AC bias I-V measurements.

13.5 Complex impedance and noise measurements

13.5.1 Complex impedance under AC bias

The thermal and electrical response of a TES is characterised through several parameters that vary with bias voltage, such as resistance –R–, sensitivity on temperature –α– or heat capacity –C–. These parameters can be determined from measurements of the TES impedance $Z_{TES}(\omega)$ [264]. A squeme of the circuit used for complex impedance measurements under AC bias is displayed in Fig.13.19. The only difference between this circuit and the one used for I-V measurements is that, besides biasing the TES with a sinusoidal carrier wave, a white noise (V_{AC}) is introduced in the system in order to study its behaviour as a function of frequency.

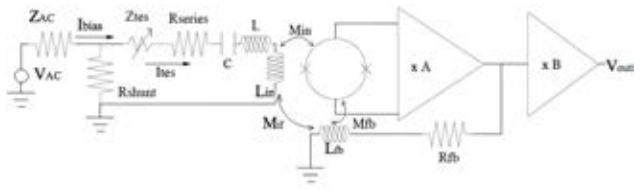

Figure 13.19: TES AC bias circuit for complex impedance measurements.

Impedance is calculated from the ratio of input and output signals in frequency domain, after the transfer function of the signal lines is corrected. Since modelling the transfer function is too complicated it is derived experimentally [152]. To do so, one has to start from the circuit Thevenin equivalent (Fig.13.20):

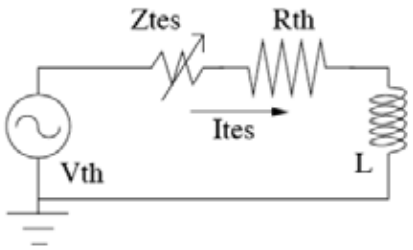

Figure 13.20: Squematic of the Thevenin equivalent of the TES bias circuit.

$$Z_{th} = R_S + R_{series} + i\omega L + \frac{1}{i\omega C} \tag{13.23}$$

$$Z_{TES} = \frac{V_{TES}}{I_{TES}} \tag{13.24}$$

$$V_{TES} = V_{th} - Z_{th} \cdot I_{TES} \tag{13.25}$$

Thus,

$$Z_{TES} = \frac{V_{th}}{I_{TES}} - Z_{th} \tag{13.26}$$

From the experimental point of view, taking into account the different elements in the amplification chain, the complex impedance of the TES can be written as:

$$Z_{TES} = \frac{V_{AC}}{V_{OUT}} \cdot \frac{R_S R_{fb}}{Z_{AC}} \cdot \frac{M_{in}}{M_{fb}} \cdot B \cdot Tr(\omega) - Z_{th}(\omega) \tag{13.27}$$

In the normal and the superconducting part the complex impedance is reduced to a resistance value equivalent to R_N in the first case and zero in the second case, and the transfer function is assumed to be independent of the bias point. Thus, if one takes the ratio of the experimental data in the normal part and the superconducting part, the transfer function contribution is cancel out, and the ratio can be fitted to Eq. 13.28

$$\frac{R_N + R_S + R_{series} + i\omega L + \frac{1}{i\omega C}}{R_S + R_{series} + i\omega L + \frac{1}{i\omega C}} = \frac{(V_{AC}/V_{OUT})_N}{(V_{AC}/V_{OUT})_S} \tag{13.28}$$

From this fitting one can determine L, and from Eq.13.27, in the normal superconducting state, estimate the transfer function of the system Tr(ω):

$$Z_{th} \cdot \frac{M_{fb}}{M_{in}} \cdot \frac{Z_{AC}}{R_S \cdot R_{fb}} \cdot \frac{V_{OUT}SC}{V_{AC}} = Tr(\omega) \tag{13.29}$$

Therefore, from Eqs.13.27 and 13.29 one gets that the complex impedance can be estimated from experimental data as Eq.13.30:

$$Z_{TES} = \left(\frac{V_{AC}/V_{OUT}}{(V_{AC}/V_{OUT})_{SC}} - 1\right) \cdot Z_{th} \tag{13.30}$$

and fitted to the theoretical expression 13.31:

$$Z_{TES} = \frac{R_0(1 + \alpha_i + L_0)(1 + i\omega\tau_{fall})}{(1 - L_0)(-1 + i\omega\tau_{fall})} \tag{13.31}$$

The parameters that characterise the system are, as a result, deduced from this fitting. The only difference between the data analysis under DC bias and AC bias is the presence of the LC filter in the Z_{th} expression and, so far, we have shown that there is no influence of the bias type on the TES behaviour, both from the thermal and electrical point of view. Consequently, the same analysis procedured and TES thermal modelling use for DC bias analysis [152] is applied to the AC bias case adding the LC filter to the Thevenin equivalent impedance expression (Eq. 13.23).

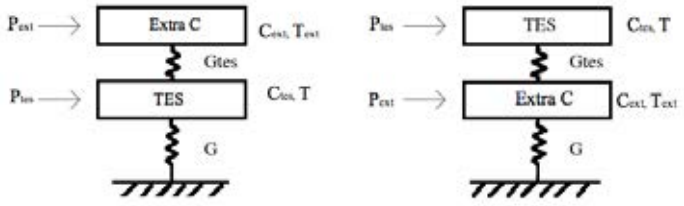

Figure 13.21: The two thermal-decoupling cases for TES.

Both in the DC bias [152] and the AC bias case, a simple thermal model including just one heat capacity, C, and one thermal conductivity, G, is not enough to reproduce the experimental complex impedance data for all the frequencies. This suggests the presence of an additional heat capacity that is decoupled from the TES [265]. In Fig.13.21 two more complex models of TES thermal circuit including two heat capacities and two thermal conductance are represented; both are equivalent when estimating complex impedance and noise. By using these models, where a part of the system is decoupled thermally

from the TES [266], the impedance is well fitted, as shown in Fig.13.22 for R/R_N=0.5. These measurements and the ones that will be presented later in this chapter are taken at the optimum conditions established in Section 13.4.1: T_{bath}=73 mK, R_{fb}=1.9 KΩ and H=88 mOe.

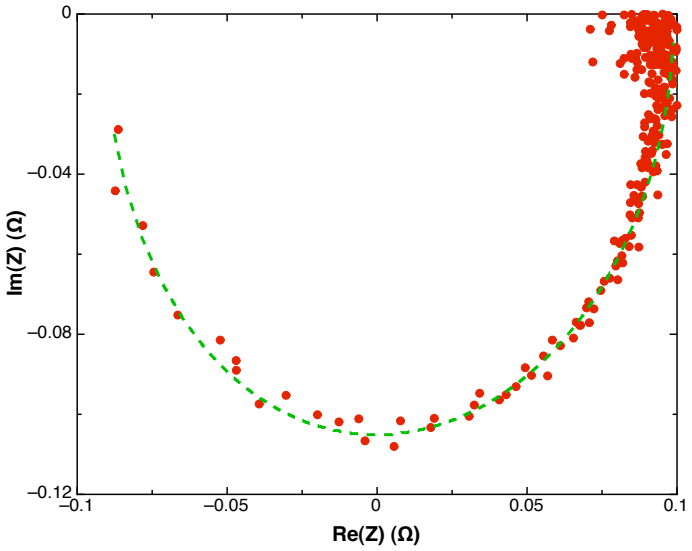

Figure 13.22: Impedance curve at R/R_N. Points show the measured data and the solid line is the model calculated with the thermal decoupling

From this fit, the parameters that characterise the sensor are estimated in every bias point. The comparison between these data and the ones obtained in the same sensor operated under DC bias is presented in Fig. 13.23. This plot shows that the dependence of the AC obtained parameters with R/R_N has the same shape as the one obtained under DC. The biggest differences are observed for α and β, where the DC bias case is higher and a peak in the middle of the transition is observed. The origin of this peak and its absence in the AC bias case is not clear jet. As stated in reference [259], features like this are often observed in SRON pixels, being reproducible, but magnetic field and pixel dependent. It has been suggested that these peaks might be caused by an inhomogeneous current distribution flowing in the TES. This effect could be reduced in the AC case due to the change in the current direction of the carrier wave associated to the AC signal.

In the AC case, a step at the first part of the transition is found for some parameters, as displayed in Fig. 13.23. Contrary to the peak observed in the DC bias case, the shape of this feature seems to indicate that it is probably not a real effect, but the result of a calibration problem at the beginning of the transition.

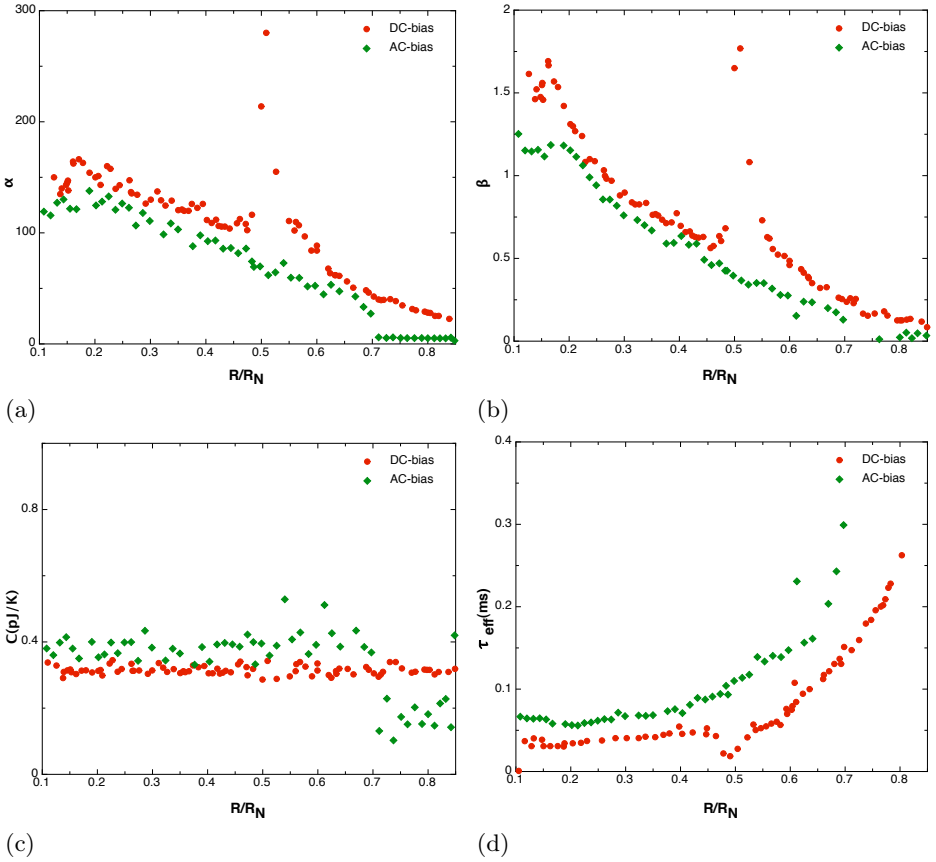

Figure 13.23: (a) α parameter as a function of the bias point for both AC and DC bias. (b) β parameter as a function of the bias point for both AC and DC bias. (c)Total heat capacity of the sensor as a function of the bias point for both AC and DC bias. (d) Detector effective time constant as a function of the bias point for both AC and DC bias.

13.5.2 Noise measurements under AC bias

Once the parameters that characterise the sensor are determined, they can be used to model the TES noise. In Fig.13.24 the different estimated noise sources are over-plotted to the measured noise under DC (a) and AC (b) bias at the same bias point R/R_N=0.29. It has to be remarked that no fitting process is used to determine the different noise contributions, but the theoretical expressions for these contributions explained in [131] together with the characteristic parameters of the sensor.

As can be seen in Fig.13.24b, the SQUID electronic noise in the AC case is too high ($\sim 10pW$) and it can hide other effects, making difficult to characterise the TES. This level increases as R_{fb} decreases, therefore, in order to

improve the SQUID noise level, the loop gain should be increased allowing to characterise the sensor by using a higher R_{fb}. An example of a noise measurement of this TES under AC bias with a higher loop gain is shown in reference [259].

SQUID electronic noise is the main external source of noise, that is, a source not related to the sensor and, therefore it can be reduced without changing any device parameter. There are other noise sources, intrinsic to the device that cannot be eliminated, but the system can be optimised to reduce them as much as possible. The most important ones are equilibrium TES Johnson noise and phonon noise between the different parts of the device and heat bath.

Although approximating the TES as a set of several heat capacitances and considering previous noise sources for the different parts [266] provides better results than a simple thermal model, it is still not enough to account for the TES observed noise. Other intrinsic noise sources are needed to explain the "excess noise" [267, 268], that once was considered to be extrinsic, and therefore susceptible of being eliminated. One of these sources is the internal thermal fluctuation noise (TFN) between TES-Absorber and dangling heat capacity [152, 269]. This simple model describes properly the noise generated by thermal fluctuations between the different regions of the TES bilayer, regions with slightly different temperature and power dissipation. Both in the AC and the DC case, the measured noise is well explained by these sources for frequencies below 1KHz, while an extra noise that cannot be modelled with any of these sources is observed for frequencies in the range of the Johnson noise. According to [164], this extra noise can be expressed as M-times the Johnson noise, finding, in our case that, a M factor of $\sim$1.2, that allows us to model the experimentally measured noise both under DC and AC bias. The origin of this extra factor is an uncompleted characterisation of the Johnson noise, that has been estimated from an equilibrium theory, due to the complexity of the non-equilibrium one [213]. This M factor, can then be defined as the ration between an intrinsic noise term and the high frequency limit of non-equilibrium Johnson noise $\sqrt{4k_BTR(1+2\beta)}$, being $\beta = (\mathrm{d}logR)/(\mathrm{d}logI)$ [270]. An other known source of "excess noise" is the flux flow noise, a voltage noise associated with the vortex motion perpendicular to current flow. However this noise is negligible at most TES working regimes [213] and, therefore, has not been considered here.

It is also interesting to notice that the main noise contribution in the region of interest is the one caused by thermal fluctuation noise between the TES and the dangling heat capacity, thus, if one wants to reduce the sensor noise it is clear that thermal coupling between the different parts of the system has to be improved.

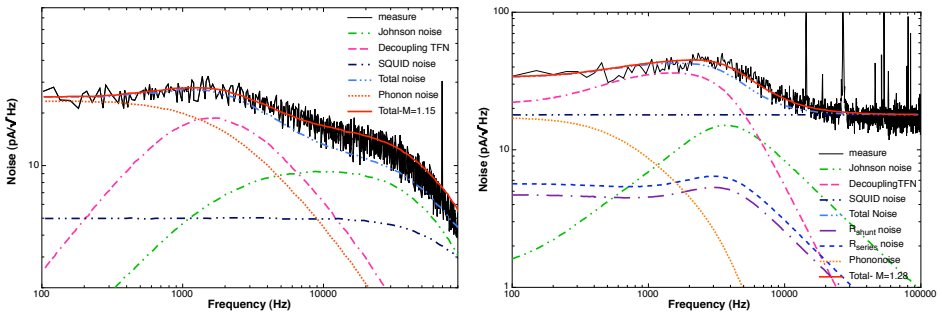

(a) (b)

Figure 13.24: (a) Noise spectra at bias point R/R_N=0.29 for TES under DC bias. (b) Noise spectra at bias point R/R_N=0.29 for TES under AC bias.

13.6 Conclusions.

In this chapter a full comparison of a single pixel TES microcalorimeter performance under DC and AC bias is achieved. Before carrying out this comparison the equivalence of the TES behaviour under AC and DC bias is established from the electrical and thermal point of view through a load curve plot. A complete study of the influence of different elements, such as R_{fb}, applied magnetic field, carrier frequency and bath temperature is performed in order to determine the optimum measurement conditions. The analysis of the thermal response of the TES shows that the same values of n and K parameters, and therefore of G, are obtained both in the DC and the AC data case. Moreover, the influence of the accuracy in the different thermal measurements is study showing the importance of a well determined critical temperature.

After correcting the different calibration factors studied in this chapter current-to-voltage characteristics, complex impedance and noise were measured under AC bias at the optimum measurement conditions (H=88mG, R_{fb}=1.9kΩ, T_bath=73mK, f_0=374kHz) and compared to measurements performed under DC bias. This comparison shows that the behaviour of the TES is very similar in both cases, being equivalent at bias points in the beginning of the superconducting transition, while it starts to differ as the resistance of the device decreases. As stated in [263] this effect might be due to the non-linear behaviour of the TES resistance when the detector is AC biased, or to a change in resonant frequency low in the transition. However, it is necessary to point out that the calibration of IV curves and complex impedance data taken under DC bias are very sensitive to offsets around zero current. Therefore, in order to ensure a proper comparison between AC and DC bias, one has to guarantee the proper cancelation of all the possible offsets.

Chapter 14

AC-DC bias characterisation of a TES bolometer

14.1 Introduction

On the previous chapter we focus on the complete characterisation of a TES microcalorimeter under AC bias and compare the obtained results to previous measurements under DC bias. In this chapter a similar comparison is described for a TES bolometer. In this case, measurements were taken within a few weeks, thus allowing to discard ageing effects or calibration problems as the cause of possible differences between AC and DC polarisation.

TES are thermal radiation detectors, including, as above mentioned, an absorbing element to convert radiation into heat, attached to a heat sink through a thermal conductance, and they can be used as bolometers or as microcalorimeters. The difference is the ratio of the mean time between the arrival of the energy carriers and the response time of the instrument. In the calorimetric case, the average time between arrival of the individual quanta should be bigger than the characteristic time constant of the system, since the goal is to be able to detect individual photons. While in the bolometric case the TES time constant should be bigger than the time between photon arrival, since the purpose of a bolometer is the measurement of a flux of particles or radiation, rather than determining the energy of a single quanta [271].

A device designed as a bolometer can be used as a calorimeter and vice versa. The observation of the detector cannot determine whether a detector is a bolometer or a calorimeter, only the type of radiation that one aim to detect and the characteristic time ratio define the type of sensor we are dealing with. Thus no difference in its characterisation can be found except for the figure of

merit. In both cases $R(T)$, current to voltage response and complex impedance measurements are required to understand the device behaviour. However, the quantity of the detector considered figure of merit will be different. In the calorimetric case the key parameter is the energy resolution, while in the bolometric case the usual one is the noise equivalent power, NEP, the power in a 1 HZ bandwidth required to achieve a response equal to the noise of the system [272].

The studied TES bolometers were developed and fabricated at SRON/Utrecht, in the framework of the SPICA mission [273]. These sensors are aimed to the SAFARI instrument [274], an imaging Fourier Transform Spectrometer (FTS) with three bands covering the wavelength ranges: 35-60 μm, 60-110 μm, and 110-210 μm. The loading in these bands is estimated to be dominated by emission from the Zodiacal light at a level of 0.3-1 fW [274]. This gives a photon noise equivalent power (NEP) at the detectors of 1-3$\cdot 10^{-18}$ W/$\sqrt{Hz}$, what is traduced in a NEP three times lower than this photon noise limit, 2 orders of magnitude higher than the detectors currently operating in ground based telescopes. This high sensitivity requirement imposes a great challenge on the detector technology.

This chapter is structured as follows: in Section 14.2 the sensors and the measurement system are described. In Section 14.3 I-V curves measurements under DC bias are described and analysed, while in Section 14.4 the obtained sensor noise is compared with the expected NEP. In Section 14.5.1 the proper calibration of I-V curves under AC bias is discussed, so as to be able to compare the obtained results with the measurements described in Section 14.3. This comparison is performed in Sections 14.5.2 and 14.6. In Section 14.7 complex impedance measurements under DC bias are studied. Finally, the main results are summarised in Section 14.8

14.2 Sensors and measurement system

The TES used in this work is a Ti/Au (16/60 nm) bilayer deposited on a 1μm thick Si_3N_4 membrane, part of a 5x5 array. Since these sensors are aimed to infrared radiation detection, a Ta absorber is deposited on the membrane close to the TES. In order to achieve the noise equivalent power (NEP) SPICA requirement –$3 \cdot 10^{-19}$ W$\sqrt{(Hz)}$– a low thermal conductance (G) is needed. Using similar TES suspended by four long Si_3N_4 straight legs of about 1.8 mm length, Khosropanah et al. achieved a G = 320 fW/K, which correspond to a NEP of $3.1 \cdot 10^{-19}$ W$\sqrt{(Hz)}$ [153]. Despite its good performance, its size make this design unsuitable for array fabrication as required for the SAFARI mission. Thus a new design, shown in Fig. 14.1, has been developed at SRON;

a structure based on concentric rings connected by four points to their neighbours. This structure allows SRON to maintain legs length, an thus, low G, while reducing the pixel area [275].

Due to its low G, superconducting transition in this type of sensors occur for current values as small as 3 μA and power plateaux of the order of femtowatts [154]. Thus, the determination of the sensor T_C from $R(T)$ measurements becomes extremely difficult, since the current applied for these measurements would bring the sensor easily to its normal state. For the TES studied in this chapter, the critical temperature was determined from noise measurements since, as can be observed in Fig. 14.5, noise profile changes abruptly from the flat spectra of the normal state to a bumped profile for sensors in the transition or superconducting state. In this way, the transition temperature of the TES is determined to be T_C=155 mK. The normal resistance, determined from IV measurements, is R_N=212 mΩ.

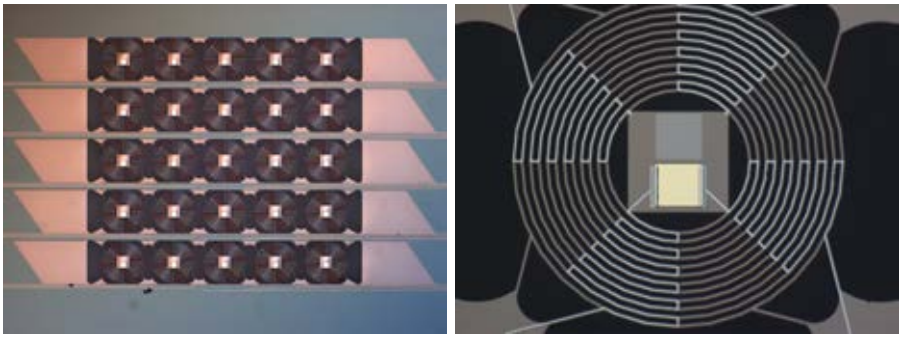

(a) (b)

Figure 14.1: (a) Picture of the TES bolometer array. (b) Picture of one of the pixels, showing a TES and an absorber on a suspended Si_3N_4 structure with a spider-web design. *Credit: SRON/Utrecht.*

All measurements were performed on a Kelvinox dilution fridge with a base temperature of 30 mK located at SRON/Utrecht. The mentioned low TES bias power ($\sim$ fW) makes this type of sensors greatly sensitive to electromagnetic pick-up. For that reason, the studied sensors are placed inside a Cu light-tight box sealed with indium to prevent any external EM radiation to reach the TES. The electrical wiring going into the box is covered with Stycast mixed with SiC grains to stop any possible incoming light [153]. With this system, a power leakage smaller than 1 fW has been detected [153]. Since this level is small compared to the observed power levels presented is Section 14.3, one can consider that the outcome of measured IV is dark and reliable. Moreover, the aluminium can that encloses the space beneath the mixing chamber is covered by a black *"coal-like"* painting to avoid radiation reflections on the superconducting shield walls.

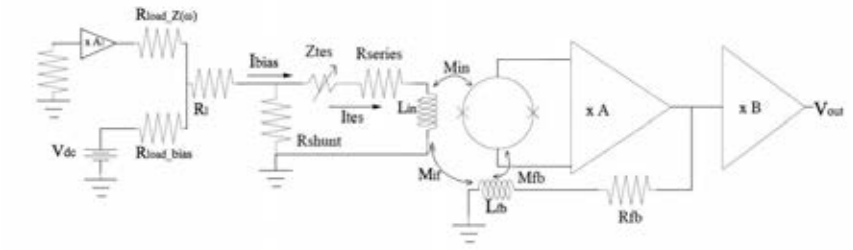

Figure 14.2: Schematic view of the TES measurement circuit under DC bias. For current-to-voltage and noise measurements no white noise source is connected to the circuit. For complex impedance measurements, white noise is introduce into the system by a 10 kΩ resistance connected to an amplifier.

14.3 IV measurements under DC bias

In fig. 14.2 a schematic drawing of the TES characterisation system for current-to-voltage (IV), noise and complex impedance (Z(ω)) measurements is shown. In the case of IV and noise, the wide band noise source is disconnected from the system. The sensor is voltage biased by means of a current source in parallel with a 5 mΩ shunt resistance, and its current response measured using a PTB SQUID operated in flux locked loop (FLL). The SQUID array is directly read out by a low noise commercial PTB-Magnicon electronics through a 4-CH 14-Bit 2 MS/s ADLink acquisition card.

All DC bias measurements analysed in this chapter were acquired using R_{fb}=1 kΩ. As already discussed, TES bolometers display low power plateau, being the current range at which the superconducting transition occurs extremely narrow. Therefore, R_{fb} value was chosen to provide the highest possible SQUID amplification, within the limits of highest resolution range of the acquisition card.

As it was explained in Section 13.4.1 the other parameter that one needs to fix to determine optimum measurements conditions is the value of the applied magnetic field that provides the maximum TES current response. This field will be the one that cancels out residual magnetic fields on the sensor. The effect of residual magnetic fields on the TES behaviour becomes evident in IV measurements when both the positive and negative sides of the curve are analysed. When magnetic fields are not properly eliminated, the symmetry of the curve is destroyed, since it becomes shifted towards one side. This is not the case for the analysed bolometer pixel, where no displacement in IV curves is found. This pixel, as shown in Fig. 14.1b, is design in a way that current wires arriving at the sensor are not parallels, as it was the case of the pixel studied in Chapter 13. Moreover, wiring in this bolometer follows the ring structure,

making them somehow *"twisted"*, what could lead to the cancellation of any magnetic field generated by the current flow into the wiring. Therefore, for the IV curves presented here, no external magnetic field is needed to ensure optimum measurements conditions.

After the measurement parameters are fixed, I-V curves at different bath temperatures are taken. In Fig. 14.3a, the SQUID output at different T_{bath} is presented as a function of the bias current; while in Fig. 14.3b the calibrated current-to voltage response of the analysed pixel is presented. As explained in Chapter 13, the power flow to the heat bath can be written as a power-low (see Eq. 13.19), where the characteristic parameters depend on the nature of the thermal weak link to the heat bath. Therefore, from the *DC* power level at the transition, measured at different temperatures, K and n parameters can be obtained.

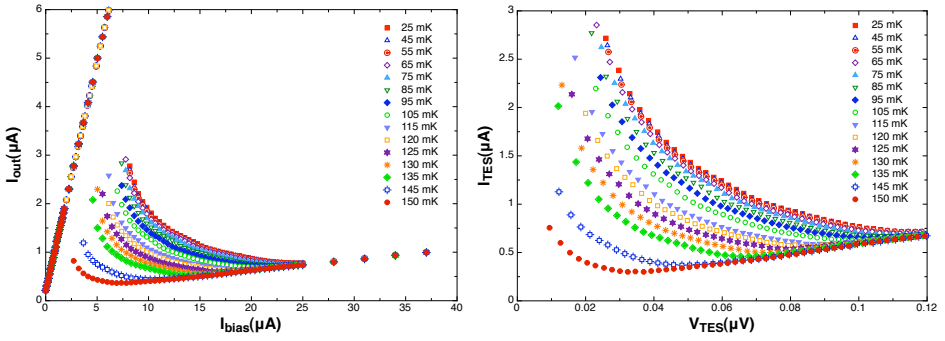

(a) (b)

Figure 14.3: (a) Signal output as a function of current bias, determined at the optimum measurement conditions for different bath temperatures. (b) I-V curves determined at the optimum measurement conditions for different bath temperatures.

As can be seen in Fig. 14.4a, the power plateau is almost constant in the transition. However, a small *"bump"* is observed at the end of the transition, being this *"bump"* shifted to lower values of R/R_N as T_{bath} increases. In the current case, superconducting transition occurs in a extremely narrow bias current range ($\sim \mu$A) and, moreover, output signals are smaller than 2μA, as shown in Fig. 14.3a. Therefore, the measurement system cannot provide enough resolution to properly discriminate the minimum in the I-V response of the sensor, that translates in distorted power plateaux. Since this minimum is shifted to lower bias current values as T_{bath} increases, the observed distortion is shifted in the same way.

The fitting of this power plateau measurements to Eq. 13.19 is depicted in Fig. 14.4b. The thermal conductance exponent, n, is material dependent, since it is governed by the nature of the dominant thermal conduction process. For

TES this process is usually the electron-phonon coupling, being typical values of n between 3 and 4 [131]. Since similar materials, except for the absorber, are used in the sensor studied in this chapter and in Chapter 13, it is not rare that similar values of n are found: n=3.3 in the latter case and n=3.39 in the present case. On the contrary, K depends not only on the material properties of the supporting membrane, but also on the geometry, thus being completely different in the mentioned cases: $K = 1.7 \cdot 10^{-8}$ for the analysed TES microcalorimeter and $4.2 \cdot 10^{-11}$ in the present bolometer.

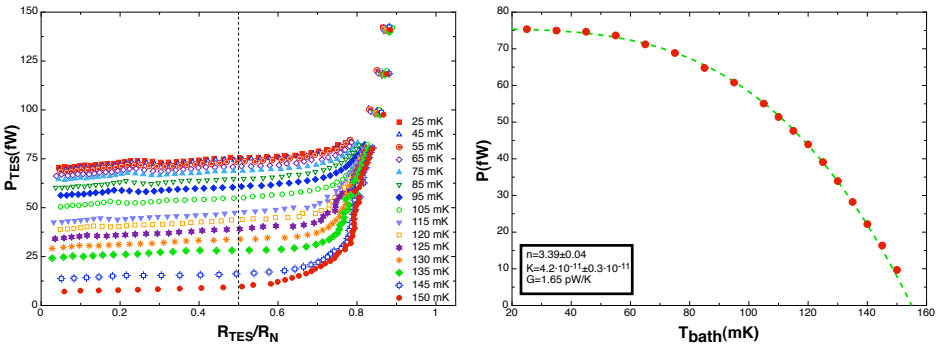

(a) (b)

Figure 14.4: (a) P-V curves determined at the optimum measurement conditions for different bath temperatures. (b) n and K parameters determination from DC bias I-V measurements.

14.4 Noise measurements under DC bias

As already mentioned in Chapter 13, these values allow us to estimate the thermal conductivity of the system through Eq. 13.20, being in the present case $G = 1.66$ pW/K. Using a finite element method simulation on the bolometer structure [154] and comparing the device with previous ones with different leg design [153, 276], heat conductance was estimated to be $G = 0.44$ pW/K. The difference between the measured G and the predicted one is due to the discrepancy between the expected T_C of 100 mK and the *"real"* one, 155 mK.

Since bolometers are used to detect continuous radiation levels, the frequently used figure of merit, equivalent to the energy resolution in the case of TES microcalorimeter, is the noise equivalent power, NEP. As it was shown in Fig. 13.24, at low frequencies the fundamental phonon noise is the dominant noise source. Since the fundamental phonon noise equivalent power in a TES can be written as [149]:

$$NEP = \sqrt{4\gamma k_B T_C^2 G} \tag{14.1}$$

where γ is a number between 0.5 and 1 that accounts for temperature gradients along the supporting legs and that is estimated to be 0.5 in our case [154], k_B is the Boltzmann's constant, T_C is the critical temperature of the TES and G is the thermal conductance. Thus, considering the critical temperature, T_C=155 mK, our measured G allows us to estimate NEP as $1.05 \cdot 10^{-18}$ W/$\sqrt{Hz}$.

Fig. 14.5a display the measured noise current spectra at different bias points in the transition at T_{bath}=25 mK. Data were taken with a frequency resolution of 2 Hz. From these data, NEP can be estimated by multiplying the measured noise current by the voltage of the TES in that point of the transition. Results are shown in Fig. 14.5b. The NEP values at low frequency, where they can be considered as equivalent to the phonon noise NEP, are $\sim 2 \cdot 10^{-18}$ W/$\sqrt{Hz}$, a factor of 2 higher than what we have estimated from the measured G. An other interesting feature, is a shoulder in the noise spectra that grows in amplitude and frequency as the bias current decreases. This hump was neither observed in the case analysed in Chapter 13 and nor in bolometers with different legs geometry [153]. Both problems might be associated with an excess noise coming from one of the sources exposed in Chapter 13 and that are often found in TES, with photon noise originated by external radiation reaching the sensor despite the taken precautions, or it can be due to thermal decoupling of some part of the device, what would lead to a second order behaviour in the TES.

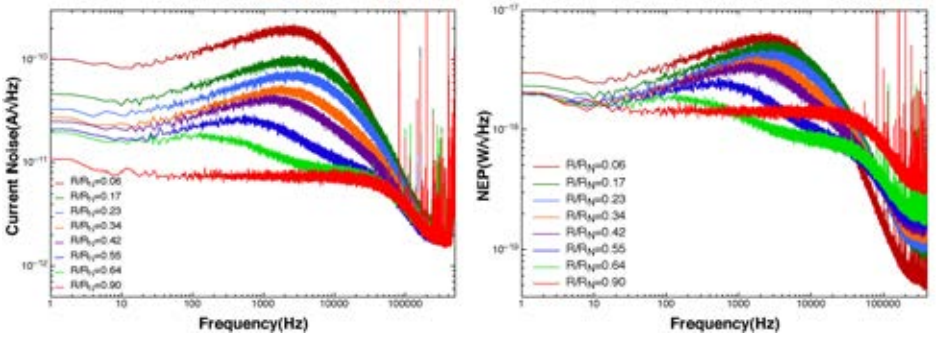

(a) (b)

Figure 14.5: (a) Noise current spectra measured at T_{bath}=25 mK at different points of the transition. R is the sensor resistance in each bias point and R_N is the normal resistance of the TES. (b) Noise equivalent power measured at T_{bath}=25 mK at different points of the transition.

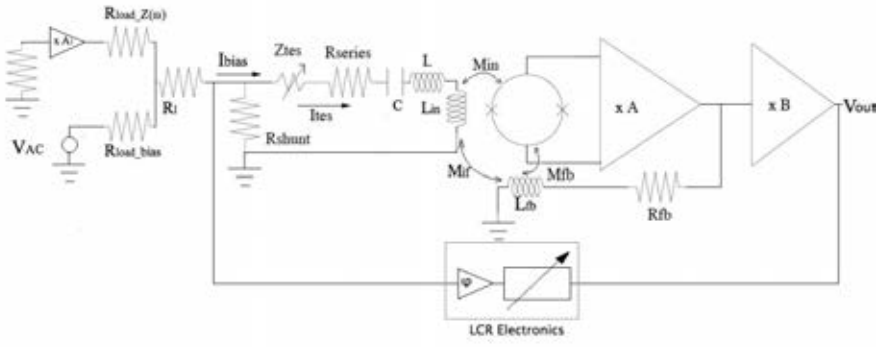

Figure 14.6: Schematic view of the TES measurement circuit under AC bias. For current-to-voltage and noise measurements no white noise source is connected to the circuit. For complex impedance measurements, white noise is introduce into the system by a 10 kΩ resistance connected to an amplifier.

14.5 IV measurements under AC bias

14.5.1 Calibration of IV measurements under AC bias

A similar current to voltage response and noise characterisation was performed on the same pixel under AC bias, being the data analysed as described in Chapter 13. A schematic picture of the TES characterisation system for current-to-voltage (IV), noise and complex impedance (Z(ω)) measurements is shown in Fig. 14.6. Again, in the case of IV and noise, the wide band noise source is disconnected from the system. The sensor is voltage biased with a sinusoidal carrier wave through the same R_S as in the DC bias case, 5 mΩ, as described in Chapter 13. The TES response is measured using a 8 turns NIST SQUID arrays[1] operated in flux locked loop (FLL), with an input inductance of 180 nH. The SQUID array is read out by a low noise commercial PTB-Magnicon electronics through a 2-Channel 14-Bit 65 MS/s Keithley acquisition card, since the one used for DC bias measurements was too slow for the AC system. The L and C elements required for AC bias experimental case are discrete components: L is a 400nH coil made of a Nb wire wounded around a Teflon cylinder and C is an commercial high-Q NP0 SMD capacitor with nominal value C=240nF. These factors provide a system resonant frequency of around 370 kHz.

As discussed in Chapter 13, the different parts of the TES characterisation circuit are coupled through various mutual inductances. Under AC bias the influence of the feedback loop in the effective resistance of the circuit cannot be neglected, since, at high frequencies it generates a negative contribution.

[1]Kindly provided by NIST

This contribution, as shown in Eq. 13.13, increases as R_{fb} and Q increases, leading to instability, for high enough values of Q and R_{fb}, when the SQUID is operated in FLL. High R_{fb} is required, as discuss in Section 14.3, to provide resolution to the small signal bolometer response. AC filters used in this case have less losses than the ones used in Chapter 13; moreover M_{in}/M_{fb} in this case is high, 8, while in the microcalorimeter case was only 3. Due to these 3 factors, it was impossible to close the SQUID feedback loop to operate the system.

Two possible solutions were studied. The function of the SQUID feedback loop is to linearise the output of the SQUID by cancelling out the signal at the input of the amplifier. In this way, the range of linear amplification is enlarged. However, the studied bolometer, when voltage biased, produces an output as small as a few μA (see Fig. 14.3a), therefore no feedback loop is needed to provide a linear behaviour of the SQUID amplifier in the bolometer bias range.

The other possible solution analysed in this chapter is the compensation of the negative effective resistance introduced by the feedback loop through a tuning feedback network as shown in Fig. 14.6. A fraction of the SQUID output signal is fed back to the bias current after transforming its amplitude and phase. This extra signal provides an extra resistance to the circuit, r_{fb} that can be either positive or negative depending on the phase shift, and that can be used to stabilise the whole system allowing to operate the SQUID in FLL. It is worth noting that, because this resistance is an effect of a feedback scheme, there is no thermal noise associated with it. A more detailed analysis of this system can be found in Ref. [277]

In Fig. 14.7a I-V curves measured at T_{bath}= 25 mK under AC bias using the two proposed solutions are shown together with an I-V measurement of he same pixel taken at the same temperature but under DC bias. Contrary to what we observed for the TES calorimeter case described in Chapter 13, AC bias and DC bias data seem to be very different from each other. Moreover, AC bias data measured in open loop or in FLL using the external feedback solution produce results that are not comparable.

The latter leads us to consider that calibration factors were not properly estimated, since the observed behaviour is similar to the one found in Fig. 13.6a. In that previous case, the error in the estimation of the SQUID output calibration factor was caused by the finite value of the loop gain under AC bias. This finite $\mathscr{L}$ was not enough to cancel out the signal at the input of the SQUID modifying the chain amplification factor. This cannot be the case for the TES bolometer under study in this chapter since the effect, although larger in the data measured in FLL is also observed in open loop, where $\mathscr{L}$ has no contribution at all. Moreover, bolometer signals are too small to cause

linearisation problems in the amplification chain.

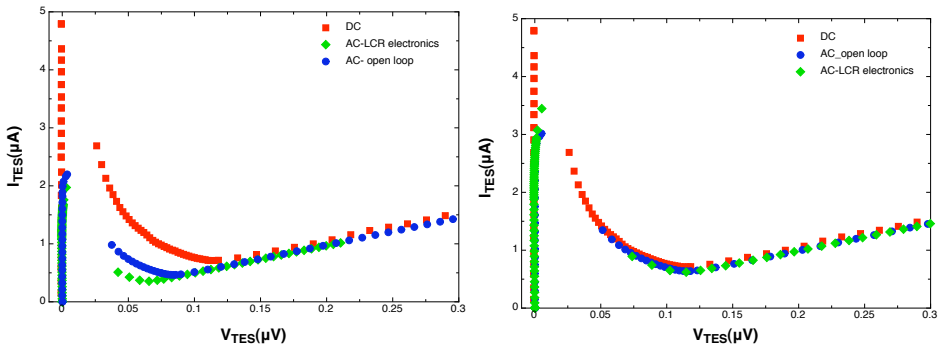

(a) (b)

Figure 14.7: (a) I-V measurements at T_{bath}= 25 mK under DC bias (▪), and AC bias in open loop (♦) and with the extra tuning feedback (●) (b) I-V measurements at T_{bath}= 25 mK under DC bias (▪), and AC bias in open loop (♦) and with the extra tuning feedback (●) corrected to account for the observed loading effects.

To calibrate data in Fig. 14.7a, two correction factors where used, one for the output signal of the SQUID, and one for the applied bias current. The first one was estimated from the known impedances in the system, while the second one was estimated by measuring the gain of the amplification chain at low frequency, where the effect of the feedback is negligible. However, as shown in Fig. 14.8a the gain of the amplification system is not constant in frequency, being also dependent on the presence of the external feedback loop for frequencies of the order of the resonant one, marked in the plot by a dash line. Therefore, the output of the characterisation system has to be modified by an extra calibration factor for the two studied configurations. To estimate this term a small signal is send through the amplification chain both at high (370 kHz) and low (9 kHz) frequency, being the change in the output signal used as an extra calibration factor (1.33 for the open loop case and 2.53 for the FLL case).

Moreover, an impedance mismatch between the different elements of the bias chain was found. These losses are expected to increase the input impedance above the nominal value of R_l, therefore modifying the required calibration factor of the applied bias current. Due to the extreme difficulty of achieving a reliable direct estimation of this calibration factor, an indirect route was followed in this case. The calibration factor was chosen to ensure that the R_S obtained from the calibrated data was similar to the nominal value and equal to the one found in the DC case. This last assumption comes from the fact that in the normal state the TES behaves as a resistor of $R = R_N$ and, therefore, no difference in the total resistance of the circuit should be found between DC

and AC bias.

In Fig. 14.7b the same data presented in Fig. 14.7a are displayed after being corrected as above explained. In this way data measured under AC bias in open loop and close loop are equivalent. The difference between these data and the ones taken under DC bias is now smaller, but still remains. When compared to the difference observed in the case of the TES microcalorimeter discussed before, it seems clear that, in the current case a problem in the estimation of the correction factors still remains. This is evidenced by the mismatch of the I-V curve normal part and the position of the beginning of the transition under both bias types, that is expected to be equal. Regarding the latter, when changing slightly the output signal calibration factor, this minimum is shifted, as plotted in Fig. 14.8b. In this way it is found that an overestimation of 10% of this calibration factor could explain the observed differences between the AC bias and the DC bias case, therefore, a more precise determination of the calibration parameters will be necessary to match the data of the two different bias systems.

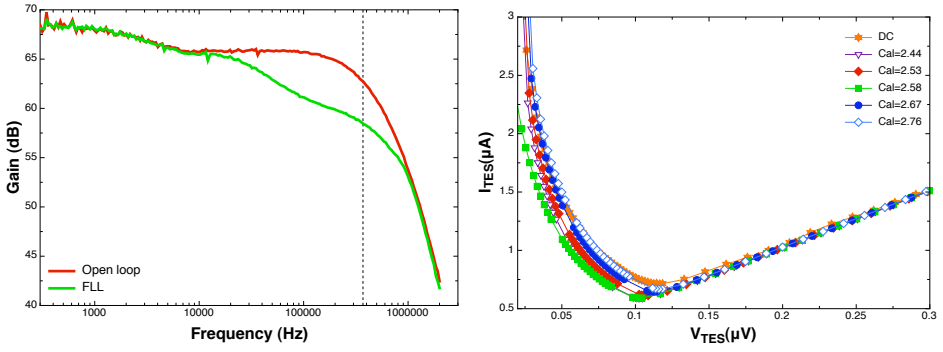

(a) (b)

Figure 14.8: (a) Gain of the amplification chain in open loop (–) and FLL (–). Dash line corresponds to the resonance frequency of the circuit, 370 kHz. (b) I-V curves at T_{bath}=25 mK corrected using different calibration factors. (♦) are data corrected by the measured calibration factor, while other symbols represent data corrected by slightly different calibration factors.

One may wonder why to use an external feedback loop to achieve the FLL operation, since not only it is a more complicated system, but also modifies the input impedance of the bias system and the output gain of the amplification chain. However, once the required calibration factors are properly estimated it shows a mayor advantage: one can increase the quality factor of the system, Q. This quality factor can be expressed as:

$$Q = \frac{1}{\omega C R_{Load}} \tag{14.2}$$

where $R_{Load} = R_{series} + R_S + r_{fb} + r_{LC}$. Increasing Q ensures that R_{Load} is reduced and, thus, that the sensor stays stable in the transition for lower values of I_{bias} (see Eq. 13.18). In Fig. 14.9a, I-V curves for different resonator quality factors tuned by the extra external feedback are plotted. It can be observed that, as expected, as Q increases, the TES can be operated lower in the transition without becoming unstable.

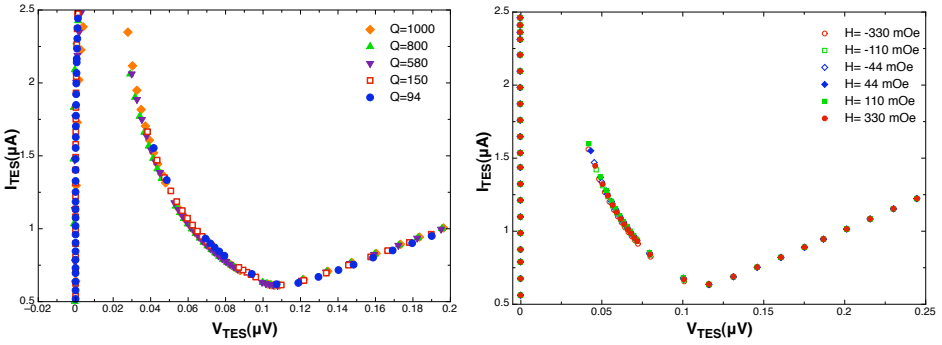

(a) (b)

Figure 14.9: (a) I-V measurements at T_{bath}=25 mK in FLL for different Q factors. (b) I-V measurements at T_{bath}=25 mK in open loop for different applied magnetic fields.

14.5.2 I-V curves analysis under AC bias

As already mentioned in Section 14.3, no evidence of residual magnetic field was observed for this bolometer under DC bias. In Fig. 14.9b some I-V curves measured under different applied magnetic fields are shown. In this case, the influence of external magnetic field is also negligible, therefore, no H is required to achieve the maximum current response.

After the resonance frequency of the system is found, I-V curves at different bath temperatures are taken. In Fig. 14.10a SQUID output at different T_{bath} is presented as a function of the bias current; while in Fig. 14.10b the calibrated current-to-voltage response of the analysed pixel is presented. As it was done in Chapter 13 and Section 14.3, the power levels at the transition are used to determine n and K parameters and the thermal conductivity.

As can be seen in Fig. 14.11a, the power plateau are extremely flat in the transition without any distortion. Under AC bias, only the positive part of the I-V curve can be measured, thus, no zero offset will be found. This makes the fitting process easier, once the calibration factors are properly estimated. The fitting of this power plateau measurements to Eq. 13.19 is depicted in Fig. 14.11b. The n and K values obtained under AC bias are quite different from

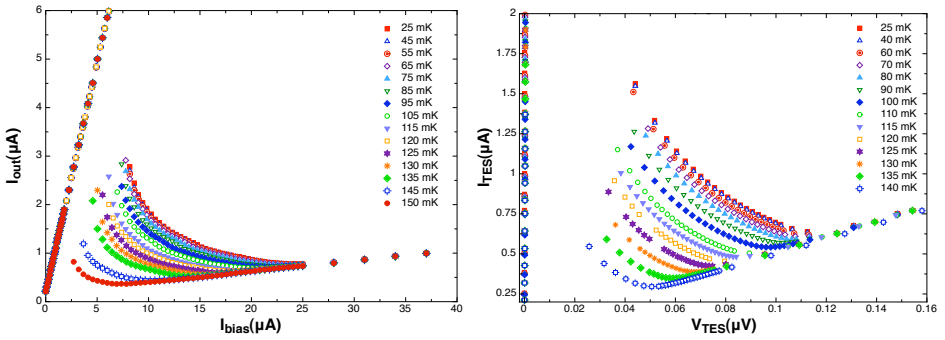

(a) (b)

Figure 14.10: (a) Signal output as a function of current bias, determined at the optimum measurement conditions for different bath temperatures under AC bias. (b) I-V curves determined at the optimum measurement conditions for different bath temperatures under AC bias.

the ones obtained under DC bias, being this divergence of a around 30% in the case of n and nearly 100 % for K. These values produce a G of 1.19 pW/K, again, a 30% different from the one obtained under DC bias. This difference is probably associated with the deficiencies mentioned on the estimation of the calibration factors in the AC case.

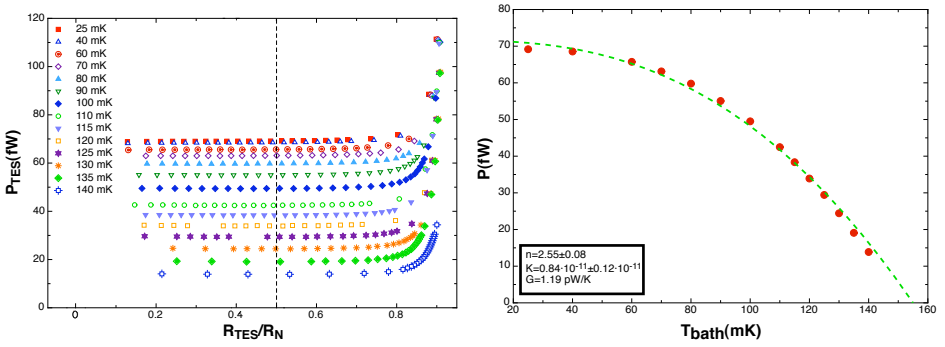

(a) (b)

Figure 14.11: (a) P-V curves determined at the optimum measurement conditions for different bath temperatures under AC bias. (b) n and K parameters determination from AC bias I-V measurements.

14.6 Noise measurements under AC bias

Since the calculated G under AC bias is quite different from the one obtained under DC bias, the estimated noise will also be different. Considering, as in the previous case that the critical temperature, T_C=155 mK, the substitution of

our measured G in Eq. 14.1 provides an estimated NEP of $0.9 \cdot 10^{-18}$ W/$\sqrt{Hz}$, only a 15% away from the one determined in Section 14.4.

Fig. 14.12a displays the measured NEP spectra at different bias points in the transition at T_{bath}=25 mK. Data were taken with a frequency resolution of 6 Hz. Although the measured current noise spectra is significantly higher in this case than in the DC bias case, this difference is reduced when considering NEP values. I-V curves under AC and DC are not completely equivalent, even after calibrating the first ones, therefore, the comparison of noise measurements in both cases is not straight forward, since measurements under AC bias and DC bias do not correspond to the same TES state. Since, as can be seen comparing Figs. 14.5a and 14.5b, NEP measurements are more stable throughout the transition than current noise, NEP data at the same resistance ratio R/R_N are compared. This comparison will give an idea of how the sensor behave; from the noise point of view under different bias systems. In Fig. 14.12b a comparison between the measured NEP spectra under AC and DC bias in the R/R_N =0.34 point in the transition is shown. The observed noise in AC is slightly above the noise obtained in the DC case, being the difference of only $\sim 0.5 \cdot 10^{-18}$ W/$\sqrt{Hz}$. The best NEP value is, as in the DC case around $2 \cdot 10^{-18}$ W/$\sqrt{Hz}$, a factor of 2 higher than what we have estimated from the measured G and Eq. 14.1 under AC. Regarding the observed shoulder in the DC bias noise spectra, a similar feature growing in amplitude and frequency as the bias current decreases is observed here. However its amplitude is smaller than the one observed in the DC bias case, and seems to have a maximum for points in the middle of the transition, being both its amplitude and frequency position reduced as the bias current is reduced. Again, the origin of this hump is not clear.

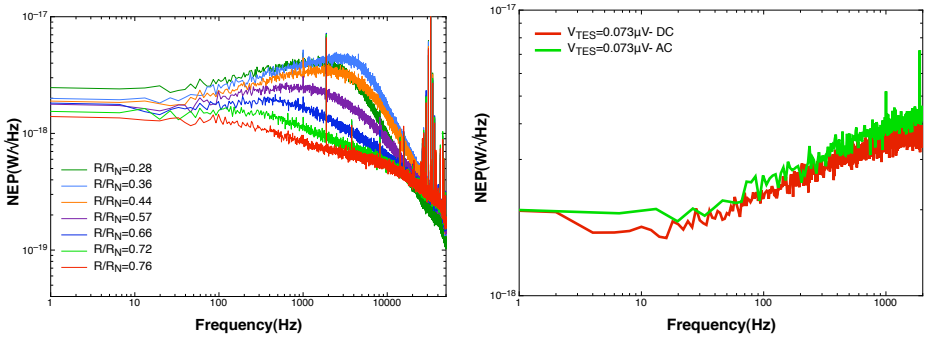

(a) (b)

Figure 14.12: (a) Noise equivalent power under AC bias measured at T_{bath}=25 mK at different points of the transition. (b) Comparison of the measured NEP under AC and DC bias at T_{bath}=25 mK in the R/R_N =0.34 bias point.

14.7 Complex impedance measurements under DC

As discussed in Chapter 13, the analysis of complex impedance measurements is required to determine all the parameters that characterise both the thermal and electrical response of the TES bolometer. Despite the small differences in the TES behaviour between DC and AC bias that have been found so far, mainly associated with I-V calibration problems in the AC case, in this chapter, only data in the DC bias case on this sensor are discussed due to the poor quality of the ones available under AC bias.

The configuration of the TES characterisation set up for complex impedance measurements is shown in Fig. 14.2. The only difference with the circuit for I-V measurements is that an amplifier connected to a 10 kΩ resistance, used as a white noise generator, is placed in parallel to the bias current source. This way, the behaviour of the TES as a function of frequency can be studied.

As already explained for the AC bias case in Chapter 13, the impedance is calculated comparing the input and output signals in frequency domain as stated in Eq. 13.30. Parameters are extracted by fitting these data to Eq. 13.31, that can also be rewrite as Eq. 14.3

$$\begin{aligned} Z_{TES} &= Z_\infty + (Z_\infty - Z_0)\frac{1}{-1 + i\omega\tau_{eff}} \\ Z_0 &= -R_0\frac{1 + \alpha_I + L_0}{L_0 - 1} \\ Z_\infty &= R_0(1 + \alpha_I) \end{aligned} \tag{14.3}$$

where Z_0 and Z_∞ are the impedances at ω=0 and ∞ respectively, and τ_{eff} is the effective time constant. Thus, complex impedance data are fitted just by choosing three parameters. As already mentioned, the only difference between the AC bias case above discussed and the DC bias case that we are analysing here is the expression of Z_{th}, that, in this case will not be Eq. 13.23 but Eq. 14.4:

$$Z_{th} = R_S + R_{series} + i\omega L_{in} \tag{14.4}$$

In Fig. 14.13a some complex impedance curves at different bias points in the transition at T_{bath}=25 mK are shown. It can be observed that for points in the low part of the transition impedance, curves are very close to a perfect semicircle, while for higher values of R/R_N, curves are slightly more distorted. This means that, for the latter, the simplest thermal TES model of an isolated element with heat capacity C connected to the bath with a

low heat conductance G, might not be enough. In Fig. 14.13b a complex impedance curve at R/R_N=0.37 is shown together with the fitting results to the simplest model described above (first order model) and the more complex model described in Chapter 13, where part of the system is decoupled thermally from the TES (second order model). It can be observed that the latter provides a better modelling of the complex impedance at low frequencies and in the upper part of the transition.

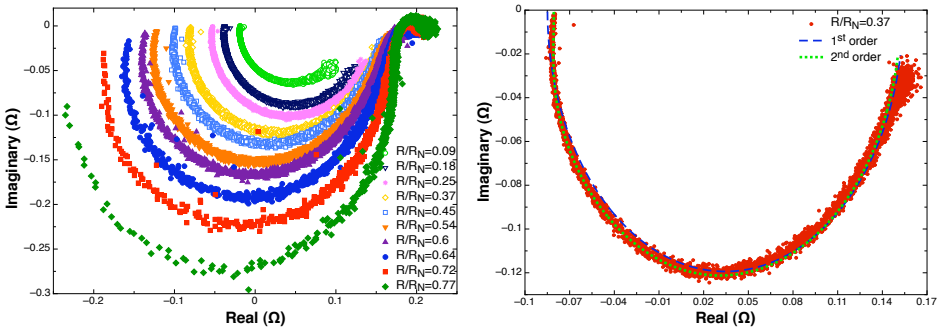

(a) (b)

Figure 14.13: (a) Measured TES bolometer complex impedance at various points in the transition. (b) Measured TES bolometer complex impedance at R/R_N=0.37(•), fitting result using a first order model (– –) and fitting result using a second order model (· · ·).

Some of the relevant parameters obtained from complex impedance data analysis in every bias point are depicted in Fig. 14.14. This plot shows that the dependence of the parameters with R/R_N obtained using a first order model and a second order model is similar. However, as expected from the results shown in Fig. 14.13b, the quality of the fitting in the first case is poorer than in the second case. The small second order behaviour observed in the device is expressed by a dangling capacity of the order of 1 fJ/K, too small to draw a firm conclusion about the proper model for this device, in which one will need to consider the distributed heat conductance through the legs and other extra heat capacities. The incomplete device description of the model is shown up by the impossibility of a complete reproduction of the measured noise, specially the shoulder feature that appears in Fig. 14.5b.

Since the accuracy of the second order model is not clear, and no significant differences in parameter results is observed between first and second order models. In Table 14.1 the outcome of the first order analysis is summarised. In this case, the bias point in the TES transition where R/R_N=0.37 is considered, since it is similar to the one considered for noise comparisons and as an example of complex impedance fitting.

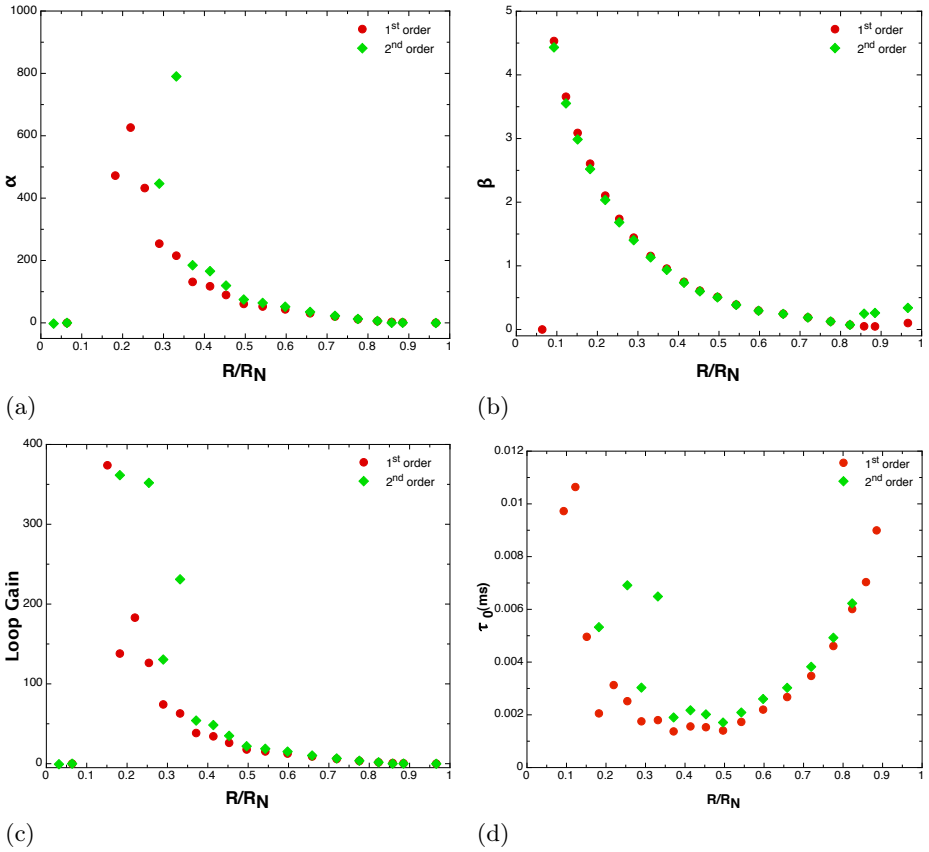

Figure 14.14: (a) α parameter as a function of the bias point for both first order model and second order model. (b) β parameter as a function of the bias point for both first order model and second order model. (c) Loop gain as a function of the bias point for both first order model and second order model. (d) Detector effective time constant as a function of the bias point for both first order model and second order model.

14.8 Conclusions

In this chapter a comparison of a TES bolometer behaviour under AC and DC bias is performed from measurements taken on the same pixel and the same measurement system within 2 months time period. This way one can rule out possible differences due to ageing effects on the sensor or changes in measurement conditions.

I-V measurements under DC bias allow us to determine n and K parameters and, thus, to estimate the sensor thermal conductivity and the expected phonon noise NEP, being this value twice lower than the measured noise at low frequency. Noise measurements also show a *hump* that grows in amplitude

Table 14.1: Parameters from impedance measurement analysis using a first order model

TES parameter	Value
G	1.7 pW/K
C	2.3 fJ/K
τ_0	1.37 ms
τ_{eff}	37 μs
L_0	38
R_0	79 mΩ
P_0	77 fW
α	131
β	0.96

and frequency as one moves down in the transition. The origin of this feature is not clear yet.

As discussed in Chapter 13, under AC bias the coupling between the feedback loop and the bias circuit induce an effective negative resistance into the circuit that could lead to instabilities in the system when the SQUID is operated in FLL mode. Due to the filters high-Q, the high R_{fb} required to achieve enough resolution in I-V curves and the high M_{in}/M_{fb} ratio in the SQUID it was not possible to close the feedback loop. Two solutions were adopted to solve this problem: to operate the SQUID in open loop and an external feedback loop that will compensate the effective negative resistance induced in the system. The latter has the advantage of allowing us to tune the quality factor of the measurement system to increase the number of stable bias points in the transition. However, in both cases a proper calibration of I-V curves was not possible due to impedance mismatches between the different elements of the measuring circuit. When comparing AC bias I-V measurements with DC bias ones a small discrepancy is found. This difference could be explain by a 10 % misestimation of the calibration factors.

I-V curves analysis as a function of T_{bath} provides different n and K parameter values from the ones obtained under DC bias. This leads to a different estimated G, however, the calculated phonon NEP is quite similar, being in both cases $\sim 1 \cdot 10^{-18}$ W/$\sqrt{Hz}$. When comparing AC bias NEP noise to the DC bias NEP, similar values are obtained, $\sim 2 \cdot 10^{-18}$ W/$\sqrt{Hz}$, being the best NEP under AC bias also a factor of two higher than the estimated phonon noise at low frequencies. It was also found that the *hump* dependence on frequency and amplitude changes from the AC to the DC bias case.

Under DC bias, complex impedance measurements were also analysed using

a first order model and the second order model described in Chapter 13. The first one is not enough to fit neither the low frequency part of the $Z(\omega)$ measurements nor the bias points in the beginning of the transition. The thermal decoupling model produces a better fitting result. However, the impossibility to reproduce noise features with the obtained parameters, leads to conclude that this model is incomplete. Yet, the low value obtained for the dangling heat capacity prevent to achieve a more complex model.

To complete the analysis presented in this chapter further work is required. First, a better estimation of the AC calibration factor would be required, along with a study of complex impedance measurements under AC bias. This is a critical point to perform a full comparison between AC and DC bias voltage, since, as already mentioned in Chapter 13, α and β parameters could show different values in both cases. Moreover, problems with offset estimations seem to be present in the DC bias mode, where no flat power plateaux could be achieved from I-V measurements. Thus, the AC-DC comparison performed so far has to be regarded as still incomplete.

Chapter 15

Part II Final Conclusions

The second topic of this thesis, the use of calorimetry as a detection tool, is divided in two main parts. In the first one we have focused on the development of TES based in Mo/Au bilayers by studying in detail the morphology and functional properties of both the individual layers involved and the final bilayer. The suitability of the obtained thermometers for radiation detection applications is discussed. The second part deals with the comparison of the TES behaviour under AC and DC bias, thus, under Frequency Domain Multiplexing or Time Domain Multiplexing. To do so, we used Ti/Au TES fabricated at SRON/Utrecht with proven excellent performance for radiation detection in two wavelength regimes –FIR and X-ray radiation–. In this chapter, we enumerate the main conclusions extracted from this second part of this thesis.

- Mo, Au and Cu optimum deposition conditions for TES applications are determined by means of their functional properties, stress and morphology through $R(T)$, XRD, AFM, TEM and SEM measurements.
  - Resistivity measurements on Mo thin films show that both residual resistance and critical temperature increase with deposition voltage bias, and relate to each other in a reproducible way. Results point to a change in the grain boundary scattering as the cause of the R_N dependency with the deposition voltage bias. An indirect effect of stress is, for instance, a possible reduction of grain size, therefore the increase of the stress with V_C determined by XRD can also be a cause for the enhancement of R_N. The same holds for the dependence of T_C with RRR, that could be explained by changes in the electronic density of states caused by compressive stress, or by an increase of electron-phonon coupling associated to stress or to progressively reduced grain size.
  - Resistivity measurements on Mo samples with different thickness and

with different applied magnetic fields have been used to study the existence of possible finite size effects in Mo thin layers, since those effects could affect the final sensor performance. In this case, lateral grain size is found to limit the electronic mean free path, giving rise to finite size effects for thickness values similar to the grain size. Moreover, grain size is found to affect Mo fundamental lengths(λ and ξ), what may cause transitions from type I to type II superconductor and from 3D to 2D behaviour in Mo films with thickness close to the usually employed in TES applications, what could significantly affect their performance.

- According to the results above discussed, optimum deposition conditions for Mo layers dedicated to TES applications, have been established. The chosen deposition parameters ensure a minimum compressive stress, a low R_N and a T_C as close as possible to the bulk one. The minimal layer thickness allowing to neglect possible size effects in Molybdenum films has been established.
- The optimum deposition method, morphology and functional properties of two different metals, Au and Cu, was explored. It was found that sputtered Au does not fulfil the low R_N requirement for stability to phase separation in proximity bilayers. Evaporated Au and sputtered Cu are the most viable possibilities for a Mo-based TES.

- Functional properties, quality of the interface and structure of the developed Mo/Au and Mo/Cu bilayers are tested with $R(T)$ measurements combined with RBS, XRD, SEM and TEM.

  - Despite the good quality of sputtered Cu, that eases the bilayer fabrication process, degradation on the final Mo/Cu bilayer caused by ageing effects, together with the difficulties of the lithographic route to process Mo/Cu bilayers into sensors, lead us to discard this possibility against Mo/Au bilayers.
  - The bad quality of sputtered Au when compared to Cu is overcome by substituting the deposition technique by e-beam evaporation, obtaining R_N values similar to the ones of Cu. The impossibility to deposit an evaporated Au layer in the same chamber as the sputtered Mo, led us to find an alternative fabrication route. Mo layer is covered by a thin protective sputtered Au layer before bringing the sample to the e-beam evaporator, this way Mo degradation is prevented. Experiments prove that the addition of a 15 nm sputtered gold layer ensures flat Mo/Au interfaces and sharp superconducting transitions.
  - The dependence of the critical temperature of a Mo/Au bilayer with Mo thickness for a fixed value of d_{Au} can be study in detail due to the excellent reproducibility of samples T_C. Equations developed by Martinins

et al. [146] from Usadel theory are used, and their application limit for $d_{Au} \geqslant \xi_M$ is discussed. Results show that the “trilayer" fabrication process provides good coupling between normal and superconducting layers. Moreover, they also generate a $T_C(d_{Mo})$ dependency that help us to unequivocally determine the d_{Mo} required to obtain the $T_C = 100$ mK working temperature for $d_{Au} \geqslant \xi_M$. Under this condition, R_N can be tuned without affecting T_C by changing the thickness of the normal metal layer.

- The stability of Mo/Au bilayers functional properties under temperature heating process at temperatures below the limit of interdifussion was studied. Samples heated at different temperatures and time periods show small changes in R_N and T_C, being these changes approximately constant when $T \geqslant 200\,^{\circ}\mathrm{C}$. The same holds for heating periods larger than 8 hours, when changes saturate reaching a constant value not modified by subsequent heating cycles. Our procedure provides a way to prevent future thermal degradation in TES.
- No change in T_C is observed neither when a lithography is applied to our bilayers in order to fabricate TES thermometers, nor when samples are deposited over membranes. This ensures that the excellent performance found in our Mo/Au bilayers is maintained when used for TES development. Mo/Au TES basic functional properties – T_C, R_N and α – are determine showing results comparable to the ones found in literature for similar sensors [160, 161]. The excellent reproducibility, the sharpness of the transitions and the low residual resistance make these thermometers ideal for radiation detection applications.

- The behaviour of a TES under AC bias is studied for a Ti/Au bolometer and a Ti/Au microcalorimeter so as to establish if FDM is a viable option for TES array readout. Results are compared with DC bias measurements on the same systems to determine if the observed good performance of a single pixel under constant voltage bias is maintained even when the TES works as a modulator.

  - A Ti/Au microcalorimeter for X-ray applications was completely characterised under AC bias and the results compared with the ones obtained for the same sensor under DC bias in the same ADR cooler. Results show that the behaviour of the TES is very similar in both cases, being equivalent at bias points in the beginning of the superconducting transition, while it starts to differ as the resistance of the device decreases.
  - A DC-AC comparison of a Ti/Au TES bolometer is performed from measurements acquired on the same pixel and in the same dilution

refrigerator. As in the microcalorimeter case similar results were found in both cases.

Final comment: Although Mo/Au TES have been studied for high-resolution radiation detection applications since the end of the nineties, no detailed analysis of the influence of the deposition conditions on the TES performance had previously been undertaken. The complete analysis presented in this thesis allows us to understand the difficulties found when facing the deposition of Mo layers with characteristics suited for TES applications and to solve irreproducibility problems in this type of sensors. The designed procedure optimises the production of TES with the chosen T_C, α and R_N. To check the viability of FDM systems has been crucial, as high-performance multiplexing schemes are essential for applications such as the International X-ray Observatory (IXO) and the Japanese infrared telescope SPICA. Results presented in this thesis are part of the collective effort of different groups inside the CSIC to develop Spanish technology for radiation detection, as a way to improve the quality of the Spanish contributions to the next generation of space missions and to reduce the huge gap between Spain and the leading countries in Europe developing cryogenic technologies for space.

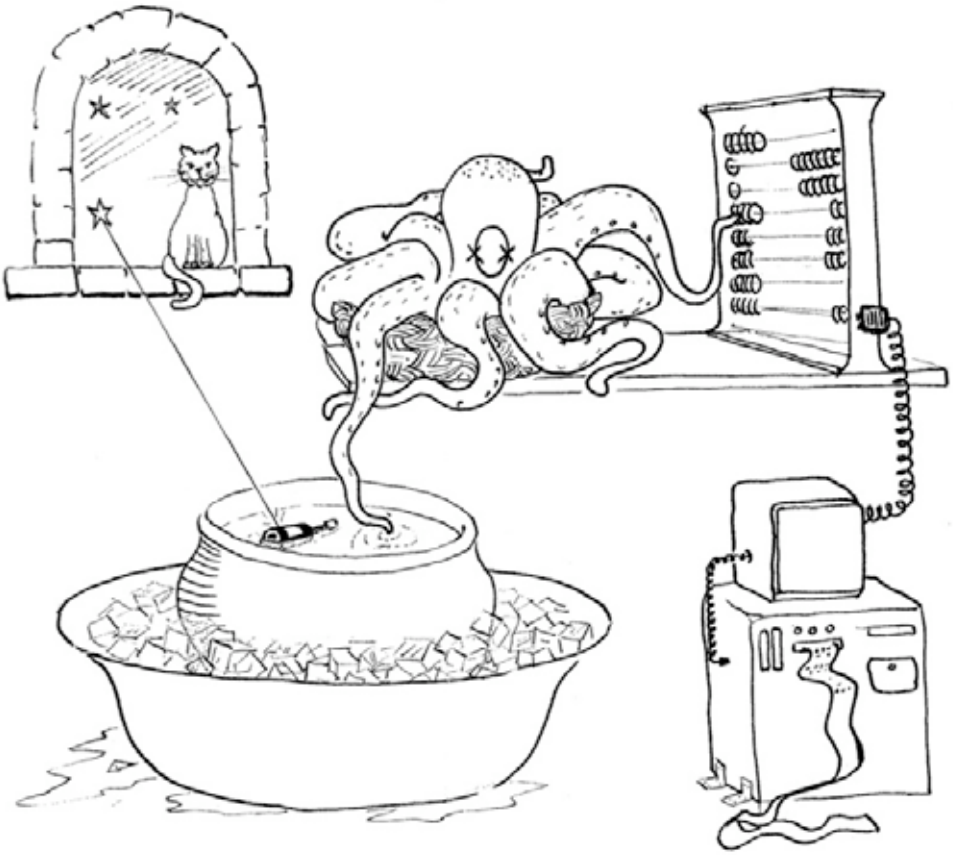

Bibliography

[1] E. Gmelin, Thermochimica Acta **29**, 1 (1979).

[2] A. Einstein, Annalen der Physik **22**, 180 (1907).

[3] C. Kittel, *Introduction to Solid State Physics* (John Wiley and Sons, Inc., New York, 1996), 7th ed.

[4] A. Miiller, *Specific Heat of Solids* (Hemisphere, New York, 1990), vol. 1-2 of *CINDAS Data Series on Material Properties*, pp. 1–90.

[5] R. Burriel, in *Introduction of Physical Techniques in Molecular Magnetism* (Servicio de Publicaciones, Universidad de Zaragoza, Zaragoza, Spain, 2000), pp. 377–403.

[6] H. Y. Hwang, S.-W. Cheong, P. G. Radaelli, M. Marezio, and B. Batlogg, Physical Review Letters **75**[5], 914 (1995).

[7] H.-C. Z. Loye, K. J. Leary, S. W. Keller, W. K. Ham, T. A. Faltens, J. N. Michaels, and A. M. Stacy, Science **238**[4833], 1558 (1987).

[8] S. Kondoh, M. Sera, Y. Ando, and M. Sato, Physica C: Superconductivity **157**[3], 469 (1989).

[9] K. Belov, A. Zvezdin, and A. Kadomtseva, *Soviet Scientific Reviews. Section A. Physics Reviews* (Harwood Academic Publishers, 1987), vol. 9, chap. Rare-earth orthoferrites, symmetry and non-Heisenberg exchange, pp. 117–222.

[10] F. Bartolomé, M. Kuz'min, R. Merino, and J. Bartolomé, IEEE Transactions on Magnetics **30**[2], 960 (1994).

[11] R. Hornreich and I. Yaeger, International Journal of Magnetism **4**, 71 (1973).

[12] R. M. Hornreich, Y. Komet, R. Nolan, B. M. Wanklyn, and I. Yaeger, Physical Review B **12**[11], 5094 (1975).

[13] J. L. García-Muñoz, J. Rodríguez-Carvajal, and P. Lacorre, Physical Review B **50**[2], 978 (1994).

[14] P. Pataud and J. Sivardière, Le Journal de Physique **31**, 803 (1970).

[15] I. Sosnowska and P. Fischer, Phase Transitions **8**, 319 (1987).

[16] J. Bartolomé, E. Palacios, M. Kuzmin, F. Bartolomé, I. Sosnowska, R. Przenioslo, R. Sonntag, and M. Lukina, Physical Review B **55**[17], 11432 (1997).

[17] F. Bartolomé, J. Bartolomé, and R. S. Eccleston, Journal of Applied Physics **87**[9], 7052 (2000).

[18] F. Bartolomé, J. Bartolomé, M. Castro, and J. Melero, Physical Review B **62**[2], 1058 (2000).

[19] F. Bartolomé, J. Herrero-Albillos, L. García, J. Bartolomé, N. Jaouen, and A. Rogalev, Journal of Applied Physics **97**[10, Part 2] (2005).

[20] A. Kadomtseva, A. Zvezdin, M. Lukina, V. Milov, A. Mukhin, and T. Ovchinnikova, Zhurnal Eksperimentalnoi I Teoreticheskoi Fizikiz **46**[6], 1216 (1977).

[21] V. Derkachenko, A. Zvezdin, A. Kadomtseva, N. Kovtun, M. Lukina, and A. Mukhin, Physica Status Solidi A-Applied Research **84**[1], 215 (1984).

[22] F. Bartolomé and J. Bartolomé, Solid State Sciences **7**, 700 (2005).

[23] A. Zvezdin, A. Kadomtseva, and A. Mukhin, Izvestiya Akademii Nauk SSSR Seriya Fizicheskaya **44**[7], 1348 (1980).

[24] S. Geller and E. Wood, Acta Crystaolgraphica **9**, 563 (1956).

[25] W. Marti, M. Medarde, S. Rosenkranz, P. Fischer, A. Furrer, and C. Klemenz, Physical Review B **52**[6], 4275 (1995).

[26] M. Marezio, J. Remeika, and P. Dernier, Acta Crystallograhica. Section B **26**, 2008 (1970).

[27] J. Rodríguez-Carvajal, Physica B **192**[1-2], 55 (1993).

[28] T. Roisnel and J. Rodríguez-Carvajal, in R. Delhez and E. Mittenmeijer, eds., *Proceedings of the Seventh European Powder Diffraction Conference (EPDIC 7)* (2000), pp. 118–123.

[29] L. Vasylechko, L. Akselrud, W. Morgenroth, U. Bismayer, A. Matkovskii, and D. Savytskii, Journal of Alloys and Compounds **297**, 46 (2000).

[30] P. Pataud and Sivardie.J, Le Journal de Physique **31**[11-1], 1017 (1970).

[31] F. Luis, M. Kuz'min, F. Bartolomé, V. Orera, J. Bartolomé, M. Artigas, and J. Rubín, Physical Review B **58**[2], 798 (1998).

[32] F. Bartolomé, M. Kuzmin, J. Bartolomé, J. Basco, J. García, and F. Sapina, Solid State Communications **91**[3], 177 (1994).

[33] I. Plaza, E. Palacios, J. Bartolomé, S. Rosenkranz, C. Ritter, and A. Furrer, Physica B: Condensed Matter **234**, 635 (1997).

[34] I. Plaza, E. Palacios, J. Bartolomé, S. Rosenkranz, C. Ritter, and A. Furrer, Physica B: Condensed Matter **234**, 632 (1997).

[35] I. Sosnowska and E. Steichele, AIP Conference Proceedings [89], 309 (1982).

[36] K. Belov, A. Kadomtseva, T. Ovchinnikova, V. Timofeeva, and V. Uskov, Soviet Physics- Solid State **13**[2], 518 (1971).

[37] R. Przenioslo, I. Sosnowska, P. Fischer, W. Marti, F. Bartolomé, J. Bartolomé, E. Palacios, and R. Sonntag, Journal of Magnetism and Magnetic Materials **160**, 370 (1996).

[38] F. Bartolomé and J. Bartolomé, Journal of Applied Physics **97**, 10A501 (2005).

[39] T. Okuda, K.-I. Kobayashi, Y. Tomioka, and Y. Tokura, Physical Review B **68**[14], 144407 (Oct 2003).

[40] R. Bachmann, J. F. J. DiSalvo, T. H. Geballe, R. L. Greene, R. E. Howard, C. N. King, H. C. Kirsch, K. N. Lee, R. E. Schwall, H.-U. Thomas, *et al.*, Review of Scientific Instruments **43**[2], 205 (1972).

[41] J. S. Hwang, K. J. Lin, and C. Tien, Review of Scientific Instruments **68**[1], 94 (1997).

[42] J. C. Lashley, M. F. Hundley, A. Migliori, J. L. Sarrao, P. G. Pagliuso, T. W. Darling, M. Jaime, J. C. Cooley, W. L. Hults, L. Morales, *et al.*, Cryogenics **43**[6], 369 (2003).

[43] N. Shamir, M. Melamud, H. Shaked, and S. Shtrikman, Physica B+C **90**[2], 217 (1977).

[44] J. Rubin, C. Piquer, G. Filoti, M. Parra-Borderías, F. Bartolomé, and J. Bartolomé, Journal of Magnetism and Magnetic Materials **316**[2], E684 (2007).

[45] J. A. Mydosh, *Spin Glasses. An Experimental Introduction.* (TAYLOR & FRANCIS, 4 John St. London WC1N 2ET, 1993), 1st ed.

[46] A. Mamchik and I.-W. Chen, Physical Review B **70**[10], 104409 (2004).

[47] K. Lefmann, *Neutron Scattering: Theory, Instrumentation and Simulation*, Lecture notes, Faculty of Science, University of Copenhagen (2007).

[48] M. A. Ricci, *Introduction to the Neutron Scattering Differential Cross-Section*, Lecture notes, School of Netron Scattering "Francesco Paolo Ricci" (2008).

[49] F. R. Elder, A. M. Gurewitsch, R. V. Langmuir, and H. C. Pollock, Physical Review **71**[11], 829 (1947).

[50] A. C. Thompson and D. Vaughan, eds., *X-Ray data Booklet* (Lawrence Berkeley National Laboratory, University of California, Berkeley, California 94720, 2001), 2nd ed.

[51] D. H. Tomboulian and P. L. Hartman, Phys. Rev. **102**[6], 1423 (1956).

[52] J. Stöhr and Y. Wu, *New Directions in Research with Third-Generation Soft X-Ray Synchrotron Radiation Sources* (NATO ASI Series, 1994), vol. 254 of *Series E: Applied Sciences*, pp. 221–250.

[53] S. Pizzini, in *Ecole Franco-Roumaine : Magnétisme des systèmes nanoscopiques et structures hybrides*, Brasov (2003).

[54] S. Bedanta and W. Kleemann1, Journal of Physics D: Applied Physics **42**, 013001 (2009).

[55] E. Dagotto, *Nanoscale Phase Separation and Colossal Magnetoresistance* (Springer-Verlag, Berlin, 2002).

[56] J. Herrero-Albillos, F. Bartolomé, and L. García, Physical Review B **76**, 094409 (2007).

[57] F. Bartolomé, J. Bartolomé, and J. Campo, Physica B **312-313**, 769 (2002).

[58] N. Marcano, J. C. G. Sal, J. I. Espeso, L. F. Barquín, and C. Paulsen, Physical Review B **76**[22], 224419 (2007).

[59] J. Iglesias, J. Espeso, N. Marcano, and J. G. Sal, Physical Review B **79**, 195128 (2009).

[60] T. Westerkamp, M. Deppe, R. KuÂ¨chler, M. Brando, C. Geibel, P. Gegenwart, A. Pikul, and F. Steglich, Physical Review Letters **102**, 206404 (2009).

[61] M. Brando, T. Westerkamp, M. Deppe, P. Gegenwart, C. Geibel, and F. Steglich, Journal of Physics:Conference Series **200**, 012016 (2010).

[62] J. Herrero-Albillos, L. García, and F. Bartolomé, Journal of Physics: Condensed Matter **21**, 216004 (2009).

[63] M. Salamon and P.Lin, Physical Review Letters **88**[19], 197203 (2002).

[64] M. Salamon and S. Chun, Physical Review B **68**, 014411 (2003).

[65] R. J. Elliott and B. R. Heap, Proceedings of the Royal Society of London. Series A, Mathematical and Physical Sciences **265**[1321], 264 (1962).

[66] D. Breed, K. Gilijamse, J. Sterkenburg, and A. Miedema, Journal of Applied Physics **41**[3], 1267 (1970).

[67] A. Sur, J. L. Lebowitz, J. Marro, M. H. Kalos, and S. Kirkpatrick, Journal of Statistical Physics **15**[5], 345 (1976).

[68] Y. Deng and H. W. J. Blöte, Physical Review E **72**[1], 016126 (2005).

[69] S. Sachdev, *Quantum Phase Transitions* (Cambridge University Press, 1999).

[70] T. Vojta and J. Schmalian, Physical Review Letters **95**[23], 237206 (2005).

[71] J. Alonso, L. Fernández, F. Guinea, V. Laliena, and V. Martín-Mayor, Physical Review B **66**[10] (2002).

[72] J. De Teresa, P. Algarabel, C. Ritter, J. Blasco, M. Ibarra, L. Morellón, J. Espeso, and J. Gómez-Sal, Physical Review Letters **94**[20] (2005).

[73] W. C. Koehler, E. O. Wollan, and M. K. Wilkinson, Physical Review **118**[1], 58 (1960).

[74] C. A. M. Mulder, A. J. van Duyneveldt, and J. A. Mydosh, Physical Review B **23**[3], 1384 (1981).

[75] R. N. Bhowmik and R. Ranganathan, Journal of Magnetism and Magnetic Materials **248**[1], 101 (2002).

[76] S. Shtrikman and E. P. Wohlfarth, Physics Letters A **85**[8-9], 467 (1981).

[77] J. L. Tholence, Solid State Communications **35**[2], 113 (1980).

[78] K. Binder and A. P. Young, Review of Modern Physics **58**[4], 801 (1986).

[79] J.-L. Tholence, Physica B+C **126**[1-3], 157 (1984).

[80] J. L. Dormann, L. Bessais, and D. Fiorani, Journal of Physics C: Solid State Physics **21**[10], 2015 (1988).

[81] W. Slawinski, R. Przeniosko, I. Sosnowska, and E. Suard, Journal of Physics: Condensed Matter pp. 4605–4614 (2005).

[82] I. Sosnowska, E. Steichelea, and A. Hewat, Physica B+C **136**[1-3], 394 (1986), neutron Scattering, Proceedings of the International Conference on Neutron Scattering.

[83] T. Yamaguchi, Journal of Physics and Chemistry of Solids **35**, 479 (1974).

[84] R. Przenioslo, I. Sosnowska, and P. Fischer, Journal of Magnetism and Magnetic Materials **140-144**, 2153 (1995).

[85] T. Vojta, Journal of Physics A: Mathematical and General **39**[22], R143 (2006).

[86] L. J. de Jongh, in M. Ausloos and R. J. Elliott, eds., *Proceedings of the European Physical Society Summer School on Magnetic Phase Transitions, Ettore Majorana Centre, Erice, Italy* (Springer, New York, 1983), vol. 48 of *Series in Solid State Sciences*, p. 172.

[87] A. V. Mahajan, D. C. Johnston, D. R. Torgeson, and F. Borsa, Physical Review B **46**[17], 10966 (1992).

[88] Y. Ren, T. T. M. Palstra, D. I. Khomskii, A. A. Nugroho, A. A. Menovsky, and G. A. Sawatzky, Physical Review B **62**[10], 6577 (2000).

[89] K. Yoshii, Journal of Solid State Chemistry **159**[1], 204 (2001).

[90] K. Yoshii, A. Nakamura, Y. Ishii, and Y. Morii, Journal of Solid State Chemistry **162**[1], 84 (2001).

[91] V. Khomchenko, I. Troyanchuk, R. Szymczak, and H. Szymczak, Journal of Materials Science **43**, 5662 (2008).

[92] J. Hemberger, S. Lobina, H.-A. Krug von Nidda, N. Tristan, V. Y. Ivanov, A. A. Mukhin, A. M. Balbashov, and A. Loidl, Physical Review B **70**[2], 024414 (2004).

[93] I. O. Troyanchuk, V. A. Khomchenko, G. M. Chobot, A. I. Kurbakov, A. N. Vasil'ev, V. V. Eremenko, V. A. Sirenko, M. Y. Shvedun, H. Szymczak, and R. Szymczak, Journal of Physics: Condensed Matter **15**[50], 8865 (2003).

[94] N. Menyuk, K. Dwight, and D. G. Wickham, Phys. Rev. Lett. **4**[3], 119 (1960).

[95] S.-i. Ohkoshi, Y. Abe, A. Fujishima, and K. Hashimoto, Physical Review Letters **82**[6], 1285 (1999).

[96] S. Pizzini, L. García, A. Fontaine, J. Rueff, J. Vogel, R. Galèra, J. Goedkoop, N. Brookes, G. Krill, and J. Kappler, Journal of Electron Spectroscopy and Related Phenomena **86**[1-3], 165 (1997).

[97] Y. Chukalkin and V. Shirts, Physica Status Solidi A-Applied Research **173**, 459 (1999).

[98] Y. Ren, A. A. Nugroho, A. A. Menovsky, J. Strempfer, U. Rütt, F. Iga, T. Takabatake, and C. W. Kimball, Physical Review B **67**[1], 014107 (2003).

[99] P. Debye, *Polar molecules* (The Chemical Catalog Co., New York, 1929).

[100] C. Gorter and R. de L. Kronig, Physica **3**[9], 1009 (1936).

[101] H. Casimir and F. du Pré, Physica **5**[6], 507 (1938).

[102] D. W. Davidson and R. H. Cole, The Journal of Chemical Physics **18**[10], 1417 (1950).

[103] K. Matsuhira, Y. Hinatsu, and T. Sakakibara, Journal of Physics: Condensed Matter **13**[31], L737 (2001).

[104] J. Herrero-Albillos, L. García, and F. Bartolomé, Journal of Physics: Condensed Matter **21**[21], 216004 (2009).

[105] P. Fannin, B. Scaife, and S. Charles, Journal of Magnetism and Magnetic Materials **72**[1], 95 (1988).

[106] K. S. Cole and R. H. Cole, The Journal of Chemical Physics **9**[4], 341 (1941).

[107] O. Petracic, S. Sahaoo, C. Binek, W. Kleemann, J. Sousa, S. Cardoso, and P. Freitas, Phase Transitions **76**[4-5, Part B], 367 (2003).

[108] C. Dekker, A. Arts, H. de Wijn, and A. D, Physical Review B **40**, 11243 (1989).

[109] M. Hagiwara, Journal of Magnetism and Magnetic Materials **177-181**, 89 (1998).

[110] J. Chaboy, L. M. García, F. Bartolomé, H. Maruyama, A. Marcelli, and L. Bozukov, Physical Review B **57**[21], 13386 (1998).

[111] M. Parra-Borderías, F. Bartolomé, J. A. R. Velamazán, and J. Bartolomé, Journal of Physics: Condensed Matter **23**[4], 046003 (2011).

[112] A. T. Lee, P. L. Richards, S. W. Nam, B. Cabrera, and K. D. Irwin, Applied Physics Letters **69**[12], 1801 (1996).

[113] M. J. Myers, W. Holzapfel, A. T. Lee, R. O'Brient, P. L. Richards, H. T. Tran, P. Ade, G. Engargiola, A. Smith, and H. Spieler, Applied Physics Letters **86**, 114103 (2005).

[114] M. D. Audley, W. S. Holland, W. D. Duncan, D. Atkinson, M. Cliffe, M. Ellis, X. Gao, D. C. Gostick, T. Hodson, D. Kelly, *et al.*, Nuclear Instruments and Methods in Physics Research Section A **520**[1-3], 479 (2004).

[115] M. Cunningham, J. N. Ullom, T. Miyazaki, S. Labov, J. Clarke, T. M. Lanting, A. T. Lee, P. L. Richards, and J. Yoon, Applied Physics Letters **81**[1], 159 (2002).

[116] W. B. Doriese, J. N. Ullom, J. A. Beall, W. D. Duncan, L. Ferreira, G. C. Hilton, R. D. Horansky, K. D. Irwin, J. A. B. Mates, C. D. Reintserna, *et al.*, Applied Physics Letters **90**, 193508 (2007).

[117] D. Chow, M. Lindeman, M. Cunningham, M. Frank, T. B. Jr., and S. Labov, Journal of Low Temperature Physics **444** (2000).

[118] S. R. Bandler, R. P. Brekosky, A. D. Brown, J. A. Chervenak, E. Figueroa-Feliciano, F. M. Finkbeiner, N. Iyomoto, R. L. Kelley, C. A. Kilbourne, F. S. Porter, *et al.*, Journal of Low Temperature Physics **151**[1-2], 400 (2008).

[119] B. Cabrera, Journal of Low Temperature Physics **151**, 82 (2008).

[120] K. Mitsuda, R. Kelley, and T. X. Team, in H. Inoue and H. Kunieda, eds., *New Century of X-ray Astronomy, ASP Conference Proceedings* (San Francisco: Astronomical Society of the Pacific, 2001), vol. 251.

[121] D. M. Glowacka, D. J. Goldie, S. Withington, M. Crane, V. Tsaneva, M. D. Audley, and A. Bunting, Journal of Low Temperature Physics **151**[1-2], 249 (2008).

[122] P. Mauskopf, D. Morozov, D. Glowacka, D. Goldie, S. Withington, M. Bruijn, P. DeKorte, H. Hoevers, M. Ridder, J. V. D. Kuur, *et al.* (SPIE, 2008), vol. 7020, p. 70200N.

[123] W. M. B. Tiest, *Energy resolving power of transition Edge X-rau Microcalorimeters*, Phd thesis, SRON National Institute for Space Research, Utrecht, Sorbonelaan 2, Utrecht 3584 CA, The Netherlands (2004).

[124] R. Abusaidi, D. S. Akerib, P. D. Barnes, D. A. Bauer, A. Bolozdynya, P. L. Brink, R. Bunker, B. Cabrera, D. O. Caldwell, J. P. Castle, *et al.*, Physical Review Letters **84**[25], 5699 (2000).

[125] B. Cabrera, L. M. Krauss, and F. Wilczek, Physical Review Letters **55**[1], 25 (1985).

[126] D. Bassi, A. Boschetti, M. Scotoni, and Z. Zen, Applied Physics B: Lasers and Optics **26**, 99 (1981).

[127] G. C. Hilton, J. M. Martinis, D. A. Wollman, K. D. Irwin, L. Dulcie, D. Gerber, P. Gillevet, and D. Twerenbold, Nature **391**, 672 (1998).

[128] V. Andrianov, K. Beckert, A. Bleile, C. Chatterjee, A. Echler, P. Egelhof, A. Gumberidze, S. Ilieva, O. Kiselev, C. Kilbourne, *et al.*, in B. Cabrera, A. J. Miller, and B. Young, eds., *Proceedings of the 13th International Workshop on Low Temperature Detectors (LTD-13), AIP Conference Proceedings* (2009), vol. 1185, pp. 42–47.

[129] K. D. Irwin, Scientific American **295**, 86 (2006).

[130] H. Onnes, Communications from the Laboratory of Physics at the University of Leiden **12**, 120b (1911).

[131] K. D. Irwin and G. C. Hilton, *Cryogenic Particle Detection* (Springer-Verlag, 2005), vol. 99 of *Topics in Applied Physics*, chap. Transition-Edge Sensors, pp. 63–149, ISBN 3-540-20113-0.

[132] D. Andrews, W. Brucksch, W. Ziegler, and E. Blanchard, Review of Scientific Instruments **13**, 281 (1942).

[133] D. Andrews, R. Fowler, and M. Williams, Physical Review **1**, 154 (1949).

[134] J. Bardeen, L. N. Cooper, and J. R. Schrieffer, Physical Review **106**, 162 (1957).

[135] L. N. Cooper, Physical Review **104**[4], 1189 (1956).

[136] V. Ginzburg and L. Landau, Zhurnal Eksperimentalnoi i Teoreticheskoi Fiziki **20**, 1064 (1950).

[137] H. Meissner, Physical Review **117**[3], 672 (1960).

[138] N. Werthamer, Physical Review **132**[6], 2440 (1963).

[139] P. Hilsch, Zeitschrift für Physik A Hadrons and Nuclei **167**, 511 (1962).

[140] P. D. Gennes and E. Guyon, Physics Letters **3**[4], 168 (1963).

[141] J. J. Hauser, H. C. Theuerer, and N. R. Werthamer, Physical Review **136**[3A], A637 (1964).

[142] U. Nagel, A. Nowak, H.-J. Gebauer, P. Colling, S. Cooper, D. Dummer, P. Ferger, M. Frank, J. Igalson, A. Nucciotti, *et al.*, Journal of Applied Physics **76**[7], 4262 (1994).

[143] W. L. McMillan, Physical Review **167**[2], 331 (1968).

[144] M. Khusainov, JETP Letters **53**[11], 579 (1991).

[145] A. Golubov, in I. Bozovic, ed., *Superconducting Superlattices and Multilayers* (SPIE, Bellingham, WA, 1994), vol. 2157, p. 353.

[146] J. M. Martinis, G. C. Hilton, K. D. Irwin, and D. A. Wollman, Nuclear Instruments and Methods in Physics Research A **444**, 23 (2000).

[147] A. Kozorezov, A. Golubov, D. Martin, P. Verhoeve, and J. Wigmore, in B. Cabrera, A. J. Miller, and B. Young, eds., *Proceedings of the 13th International Workshop on Low Temperature Detectors (LTD-13), AIP Conference Proceedings* (2009), vol. 1185, pp. 538–541.

[148] K. Irwin, Applied Physics Letters **66**[15], 1998 (1995).

[149] J. C. Mather, Applied Optics **21**[6], 1125 (1982).

[150] S. H. Moseley, J. C. Mather, and D. McCammon, Journal of Applied Physics **56**[5], 1257 (1984).

[151] M. Frank, D. Dummer, S. Cooper, J. Igalson, F. Pröbsta, and W. Seidel, Nuclear Instruments and Methods in Physics Research Section A **345**[2], 367 (1994).

[152] Y. Takei, L. Gottardi, H. F. C. Hoevers, P. A. J. de Korte, J. van der Kuur, M. L. Ridder, and M. P. Bruijn, Journal of Low Temperature Physics **151**, 161 (2008).

[153] P. Khosropanah, B. Dirks, J. van der Kuur, M. Ridder, M. Bruijn, M. Popescu, H. Hoevers, J. R. Gao, D. Morozov, and P. Mauskopf, in B. Cabrera, A. J. Miller, and B. Young, eds., *Proceedings of the 13th*

International Workshop on Low Temperature Detectors (LTD-13), AIP Conference Proceedings (2009), vol. 1185, pp. 42–47.

[154] P. Khosropanah, B. Dirks, M. Parra-Borderías, M. Ridder, J. van der Kuur, L. Gottardi, M. Bruijn, M. Popescu, J. R. Gao, and H. Hoevers, IEEE Transactions on Applied Superconductivity (to be published) **21**, 236 (2011).

[155] R. Gross and A. Marx, *Applied Superconductivity: Josephson Effect and Superconducting Electronics*, Walther-Meissner-Institut (2005).

[156] J. Hohne, M. Altmann, G. Angloher, P. Hettl, J. J. amd T. Nussle, S. Pfnur, J. Schnagl, M. Sarsa, S. Wanninger, and F. Feilitzsch, X-Ray Spectrometry **28**[5], 396 (1999).

[157] K. Irwin, G. Hilton, D. Wollman, and J. Martinis, Applied Physics Letters **69**[13], 1945 (1996).

[158] F. M. Finkbeiner, T. C. Chen, S. Aslam, E. Figueroa-Feliciano, R. L. Kelley, M. Li, D. Mott, C. Stahle, and C. Stahle, IEEE Transactions on Applied Superconductivity **9**[2], 2940 (1999).

[159] B. Dirks, M. Popescu, M. Bruijn, L. Gottardi, H. Hoevers, P. de Korte, J. van der Kuur, M. Ridder, and Y. Takei, Nuclear Instruments and Methods in Physics Research Section A **610**[1], 83 (2009).

[160] G. Hilton, J. Martinis, K. Irwin, N. Bergren, D. Wollman, M. Huber, S. Deiker, and S. Nam, IEEE Transactions on Applied Superconductivity **11**[1], 739 (2001).

[161] J. A. Chervenak, F. M. Finkbeiner, T. Stevenson, D. Talley, R. P. Brekosky, S. R. Bandler, E. Figueroa-Feliciano, M. A. Lindeman, R. L. Kelley, T. Saab, *et al.*, Nuclear Instruments and Methods in Physics Research A **520**, 460 (2004).

[162] T. B. Massalski, ed., *Binary Alloy Phase Diagrams*, vol. 1 (ASM International, 1990), 2nd ed.

[163] A. Luukanen, H. Sipilä, K. Kinnunen, A. Nuottajärvi, and J. Pekola, Physica B: Condensed Matter **284-288**[Part 2], 2133 (2000).

[164] J. N. Ullom, J. A. Beall, W. B. Doriese, W. D. Duncan, L. Ferreira, G. C. Hilton, K. D. Irwin, C. D. Reintsema, and L. R. Vale, Applied Physics Letters **87**[19], 194103 (2005).

[165] J. A. Chervenak, F. M. Finkbeiner, S. R. Bandler, R. Brekosky, A. D. Brown, N. Iyomoto, R. L. Kelley, C. A. Kilbourne, F. Porter, J. Sadleir, *et al.*, Journal of Low Temperature Physics **151**, 255 (2008).

[166] E. Monticone, M. Rajteri, C. Portesi, C. Gandini, S. Bodoardo, and G. Picotto, Physica C- Superconductivity and its applications **372**[Part 1], 440 (2002).

[167] N. Tralshawala, R. Brekosky, M. Li, E. Figueroa-Feliciano, F. Finkbeiner, M. Lindeman, C. Stahle, and C. Stahle, IEEE Transactions on Applied Superconductivity **11**[1], 755 (2001).

[168] L. Fàbrega, I. Fernández-Martínez, M. Parra-Borderías, O. Gil, A. Camón, R. González-Arrabal, J. Sesé, J. Santiso, J.-L. Costa-Krämer, and F. Briones, IEEE Transactions on Applied Superconductivity **19**[6], 3779 (2009).

[169] Y. G. Shen, Materials Science and Engineering A **359**[1-2], 158 (2003).

[170] D. Adams, M. Vill, J. Tao, J. Bilello, and S. Yalisove, Journal of Applied Physics **74**[2], 1015 (1993).

[171] M. Vill, D. Adams, S. Yalisove, and J. Bilello, Acta Metallurgica et Materialia **43**[2], 427 (1995).

[172] C. Montcalm, B. Sullivan, H. Pepin, J. Dobrowolski, and M. Sutton, Applied Optics **33**[10], 2057 (1994).

[173] J. H. Scofield, A. Duda, D. Albin, B. L. Ballard, and P. K. Predecki, Thin Solid Films **260**[1], 26 (1995).

[174] J. Olsen, E. Kirk, P. Lerch, M. Huber, k. Arzner, W. Hajdas, A. Zehnder, and H. Ott, Nuclear Instruments and Methods in Physics Research A **520**, 296 (2004).

[175] K. Irwin, G. C. Hilton, J. M. Martinis, S. Deiker, N. Bergren, S. Nam, D. Rudman, and D. Wollman, Nuclear Instruments and Methods in Physics Research A **444**, 184 (2000).

[176] T. Chen, A. Bier, B. Campano, D. Cottingham, F. M. Finkbeiner, C. O'Dell, E. Sharp, R. Silverberg, and G. Wilson, Nuclear Instruments and Methods in Physics Research A **520**, 446 (2004).

[177] C. Stahle, F. M. Finkbeiner, K. Boyce, T. Chen, E. Figueroa-Feliciano, J. Gygax, R. L. Kelley, M. Li, B. Mattson, D. Mott, *et al.*, Nuclear Instruments and Methods in Physics Research A **444**, 224 (2000).

[178] N. Tralshawala, S. Aslam, R. P. Brekosky, T. Chen, E. Figueroa-Feliciano, F. M. Finkbeiner, M. Li, D. Mott, C. Stahle, and C. Stahle, Nuclear Instruments and Methods in Physics Research A **444**, 188 (2000).

[179] H. Oikawa, J. Vac. Sci. Technol. **15**[3], 1117 (1978).

[180] T. Vink, M. Somers, J. Daams, and A. Dirks, Journal of Applied Physics **70**[8], 4301 (1991).

[181] L. Fàbrega, I. Fernández-Martínez, O. Gil, M. Parra-Borderías, A. Camón, J.-L. Costa-Krämer, R. González-Arrabal, J. Sesé, F. Briones, J. Santiso, *et al.*, IEEE Transactions on Applied Superconductivity **19**[3, Part 1], 460 (2009).

[182] A. Blachman, Metallurgical Transactions **2**[699-709] (1971).

[183] D. Hoffman and C. Kukla, Journal of Vacuum Science and Technology A **3**, 2600 (1985).

[184] A. Bensaoula, J. Wolfe, A. Ignatiev, F.-O. Fong, and T.-S. Leung, Journal of Vacuum Science and Technology **A2**, 389 (1984).

[185] B. Cullity and S. Stock, *Elements of X-ray diffraction* (Prentice Hall, 2001).

[186] R. A. Holmwood and R. Glang, Journal of The Electrochemical Society **112**[8], 827 (1965).

[187] R. González-Arrabal, A. Camón, M. Parra-Borderías, L. Fàbrega, J. Anguita, J. Sesé, and F. Briones, Journal of Low Temperature Physics **151**[1-2], 239 (2008).

[188] E. Fawcett and D. Griffiths, Journal of Physics and Chemistry of Solids **23**[11], 1631 (1962).

[189] A. F. Mayadas, M. Shatzkes, and J. F. Janak, Applied Physics Letters **14**[11], 345 (1969).

[190] H. Oikawa and Y. Nakajima, Journal of Vacuum Science and Technology **14**, 1153 (1977).

[191] D. Seraphim, D. Novick, and J. Budnick, Acta Metallurgica **9**[5], 446 (1961).

[192] P. M. Hall, Journal of Applied Physics **36**[8], 2471 (1965).

[193] V. M. Kuz'menko and T. P. Chernyaeva, Low Temperature Physics **31**[2], 111 (2005).

[194] J. J. Cuomo, J. M. E. Harper, C. R. Guarnieri, D. S. Yee, L. J. Attanasio, J. Angilello, C. T. Wu, and R. H. Hammond, Journal of Vacuum Science and Technology **20**[3], 349 (1982).

[195] J. Rairden and C. Neugebauer, Proceedings of the IEEE **52**[10], 1234 (1964).

[196] A. Karkin, V. Pilyugin, V. Voronin, R. Kuznetsov, B. Goshchitskiy, and G. Taluts, Fizika Metallov i Metallovedenie **66**[1], 112 (1988).

[197] J. W. Garland, K. H. Bennemann, and F. M. Mueller, Physical Review Letters **21**[18], 1315 (1968).

[198] E. H. Sondheimer, Advances in Physics **1**[1], 42 (1952).

[199] T. Coutts, *Electrical conduction in thin metal films* (Elsevier Scientific Pub. Co., Amsterdam, 1974).

[200] T. Geballe, B. Matthias, E. Corenzwit, and J. G.W. Hull, Physical Review Letters **8**[8], 313 (1962).

[201] P. H. Schmidt, R. N. Castellano, H. Barz, A. S. Cooper, and E. G. Spencer, Journal of Applied Physics **44**[4], 1833 (1973).

[202] G. Linker and O. Meyer, Solid State Communications **20**[7], 695 (1976).

[203] R. G. Mallon and J. H.E. Rorschach, Physical Review **158**[2], 418 (1967).

[204] R. A. Hein, J. W. Gibson, M. R. Pablo, and R. D. Blaugher, Physical Review **129**[1], 136 (1963).

[205] D. C. Rorer, D. G. Onn, and H. Meyer, Physical Review **138**[6A], A1661 (1965).

[206] A. Waleh and N. H. Zebouni, Physical Review B **4**[9], 2977 (1971).

[207] R. French, Physica Status Solidi **21**, K35 (1967).

[208] B. Jin and J. Ketterson, Advances in Physics **38**[3], 189 (1989).

[209] J. J. Hauser and H. C. Theuerer, Physical Review **134**[1A], A198 (1964).

[210] B. Abeles, R. W. Cohen, and W. R. Stowell, Physical Review Letters **18**[21], 902 (1967).

[211] J. M. Kosterlitz and D. J. Thouless, Journal of Physics C: Solid State Physics **6**[7], 1181 (1973).

[212] P. Minnhagen, Reviews of Modern Physics **59**[4], 1001 (1987).

[213] M. Galeazzi, submitted to IEEE Transactions on Applied Superconductivity, pre-published by ESNF conforming to IEEE Policy on Electronic Dissemination, Section 8.1.9 (2010).

[214] A. F. Mayadas and M. Shatzkes, Physical Review B **1**[4], 1382 (1970).

[215] S. Maekawa and H. Fukuyama, Journal of the Physical Society of Japan **51**[5], 1380 (1982).

[216] J. Simonin, Physical Review B **33**[11], 7830 (1986).

[217] M. S. M. Minhaj, S. Meepagala, J. T. Chen, and L. E. Wenger, Physical Review B **49**[21], 15235 (1994).

[218] J. M. Graybeal and M. R. Beasley, Physical Review B **29**[7], 4167 (1984).

[219] M. Strongin, R. S. Thompson, O. F. Kammerer, and J. E. Crow, Phys. Rev. B **1**[3], 1078 (1970).

[220] E. Shapoval, Soviet Physics. JETP-USSR **24**[2], 443 (1967).

[221] L. N. Cooper, Physical Review Letters **6**[12], 689 (Jun 1961).

[222] R. Boucher, T. May, T. Wagner, V. Zakosarenko, S. Anders, and H. G. Mayer, Superconductor Science and Technology **19**, 138 (2006).

[223] D'Yakov and A. Svets, Soviet Physics. JETP **22** (1966).

[224] M. Tinkham, *Introduction to Superconductivity* (Dover Publications, INC., Nwe York, U.S.A., 2004), 2nd ed.

[225] K. D. Irwin, G. C. Hilton, D. A. Wollman, and J. M. Martinis, Journal of Applied Physics **83**[8], 3978 (1998).

[226] R. A. Matula, Journal of Physical and Chemical Reference Data **8**[4], 1147 (1979).

[227] P. A. B. Toombs and P. Bennett, Journal of Applied Physics **39**[6], 2948 (1968).

[228] C. A. Kilbourne, S. R. Bandler, A. D. Brown, J. A. Chervenak, E. Figueroa-Feliciano, F. Finkbeiner, N. Iyomoto, R. L. Kelley, F. S. Porter, and S. J. Smith, Journal of Low Temperature Physics **151**, 223 (2008).

[229] K. L. Chopra, L. C. Bobb, and M. H. Francombe, Journal of Applied Physics **34**[6], 1699 (1963).

[230] J. R. Sambles, K. C. Elsom, and D. J. Jarvis, Philosophical Transactions of the Royal Society of London. Series A, Mathematical and Physical Sciences **304**[1486], 365 (1982).

[231] E. V. Barnat, D. Nagakura, P.-I. Wang, and T.-M. Lu, Journal of Applied Physics **91**[3], 1667 (2002).

[232] B. Cabrera, R. M. Clarke, P. Colling, A. Miller, S. Nam, and R. Romani, Applied Physics Letters **73**[6], 735 (1998).

[233] H.-G. Kadereit, Thin Solid Films **1**, 109 (1967).

[234] A. Christou and H. Day, Journal of Applied Physics **44**[12], 5259 (1973).

[235] L. Fàbrega, A. Camón, I. Fernández-Martínez, J. Sesé, M. Parra-Borderías, G. O., R. González-Arrabal, J. Costa-Krämer, and F. Briones, Supercond. Sci. Technol. **24**, 075014 (2011).

[236] A. Tesauro, A. Aurigemma, C. Cirillo, S. L. Prischepa, M. Salvato, and C. Attanasio, Superconductor Science and Technology **18**[1], 1 (2005).

[237] K. D. Usadel, Physical Review Letters **25**[8], 507 (1970).

[238] V. N. Kushnir, S. L. Prischepa, C. Cirillo, and C. Attanasio, Journal of Applied Physics **106**[11], 113917 (2009).

[239] O. Bourgeois, A. Frydman, and R. C. Dynes, Physical Review B **68**[9], 092509 (2003).

[240] Z. Ali, O. Drury, M. Cunningham, J. Chesser, J. Barbee, T.W., and S. Friedrich, IEEE Transactions on Applied Superconductivity **15**[2], 526 (2005).

[241] T. C. Chen, F. M. Finkbeiner, A. Bier, and B. DiCamillo, Superconductor Science and Technology **12**[11], 840 (1999).

[242] A. E. Ennos, British Journal of Applied Physics **8**[3], 113 (1957).

[243] D. Lide, *Handbook of Chemistry and Physics* (CRC Press, New York, 1996), 75th ed.

[244] M. P. Bruijn, M. L. Ridder, L. Gottardi, H. F. C. Hoevers, P. A. J. de Korte, and J. van der Kuur, Journal of Low Temperature Physics **151**[1-2], 500 (2008).

[245] M. Kiviranta, J. van de Kuur, H. Seppä, and P. A. J. de Korte, in J. Wolf, J. Farhoomand, and C. McCreight, eds., *Proceedings of the Far-IR, sub-mm and mm Detector Technology Workshop* (2002).

[246] J. A. Chervenak, K. D. Irwin, E. N. Grossman, J. M. Martinis, C. D. Reintsema, and M. E. Huber, Applied Physics Letters **74**[26], 4043 (1999).

[247] C. D. Reintsema, J. Beyer, S. W. Nam, S. Deiker, G. C. Hilton, K. D. Irwin, J. M. Martinis, J. N. Ullom, and L. R. Vale, Review of Scientific Instruments **74**[10], 4500 (2003).

[248] P. A. J. de Korte, J. Beyer, S. Deiker, G. C. Hilton, K. D. Irwin, M. J. MacIntosh, S. W. Nam, C. D. Reintsema, and L. R. Vale, Review of Scientific Instruments **74**[8], 3807 (August 2003).

[249] W. Doriese, J. Beall, W. Duncan, L. Ferreira, G. Hilton, K. Irwin, C. Reintsema, J. Ullom, L. Vale, and Y. Xu, Nuclear Instruments and Methods in Physics Research A **559**[2], 808 (2006).

[250] T. M. Lanting, H.-M. Cho, J. Clarke, W. L. Holzapfel, A. T. Lee, M. Lueker, and P. L. Richards, Applied Physics Letters **86**, 112511 (2005).

[251] N. Iyomoto, T. Ichitsubo, K. Mitsuda, N. Yamasaki, R. Fujimoto, T. Oshima, K. Futamoto, Y. Takei, T. Fujimori, K. Yoshida, *et al.*, Nuclear Instruments and Methods in Physics Research Section A **520**[1-3], 566 (2004).

[252] M. Kiviranta, H. Seppä, J. van der Kuur, and P. A. J. de Korte, in F. S. Porter, D. McCammon, M. Galeazzi, and C. Stahle, eds., *Proceedings of the 9th International Workshop on Low Temperature Detectors (LTD-9), AIP Conference Proceedings* (2002), vol. 605, pp. 295–300.

[253] J. van de Kuur, P. A. J. de Korte, P. de Groene, N. Baars, M. Lubbers, and M. Kiviranta, Nuclear Instruments and Methods in Physics Research A **520**, 551 (2004).

[254] K. D. Irwin and K. W. Lehnert, Applied Physics Letters **85**[11], 2107 (2004).

[255] J. A. B. Mates, G. C. Hilton, K. D. Irwin, L. R. Vale, and K. W. Lehnert, Applied Physics Letters **92**[2], 023514, 023514 (3 pages) (2008).

[256] K. D. Irwin, J. A. Beall, W. B. Doriese, W. D. Duncan, G. C. Hilton, J. A. B. Mates, C. D. Reintsema, D. Schmidt, J. N. Ullom, L. R. Vale, *et al.*, Nuclear Instruments and Methods in Physics Research A **559**, 802 (2006).

[257] I. Hahn, P. Day, B. Bumble, and H. G. LeDuc, Journal of Low Temperature Physics **151**[3-4], 934 (2008).

[258] K. Irwin, in B. Cabrera, A. J. Miller, and B. Young, eds., *Proceedings of the 13th International Workshop on Low Temperature Detectors (LTD-13), AIP Conference Proceedings* (2009), pp. 229–236.

[259] L. Gottardi, J. van der Kuur, P. A. J. de Korte, R. D. Hartog, B. Dirks, M. Popescu, H. Hoevers, M. P. Bruijn, M. Parra-Borderías, and Y. Takei, in B. Cabrera, A. J. Miller, and B. Young, eds., *Proceedings of the 13th International Workshop on Low Temperature Detectors (LTD-13), AIP Conference Proceedings* (2009), vol. 1185, pp. 538–541.

[260] L. Gottardi, Y. Takei, J. van der Kuur, P. A. J. de Korte, H. F. C. Hoevers, D. Boersma, M. Bruijn, W. Mels, M. Ridder, D. Takken, *et al.*, Journal of Low Temperature Physics **151**, 106 (2008).

[261] D. Drung, C. Assmann, J. Beyer, A. Kirste, M. Peters, F. Ruede, and T. Schurig, IEEE Transactions on Applied Superconductivity **17**[2, Part 1], 699 (2007).

[262] P. A. J. de Korte and et. al, Journal of Low Temperature Physics **151**, 733 (2008).

[263] J. van de Kuur, P. A. J. de Korte, H. F. C. Hoevers, M. Kiviranta, and H. Seppä, Applied Physics Letters **81**[23], 4467 (2002).

[264] M. A. Lindeman, S. Brandler, R. P. Brekosky, J. A. Chervenak, E. Figueroa-Feliciano, F. Finkbeiner, M. K. Li, and C. A. Kilbourne, Review of Scientific Instruments **75**[5], 1283 (2004).

[265] B. L. Zink, J. N. Ullom, J. A. Beall, K. D. Irwin, W. B. Doriese, W. D. Duncan, L. Ferreira, G. C. Hilton, R. D. Horansky, C. D. Reintsema, *et al.*, Applied Physics Letters **89**, 124101 (2006).

[266] M. Galeazzi and D. McCammon, Journal of Applied Physics **93**[8], 4856 (2003).

[267] M. A. Lindeman, R. P. Brekosky, E. Figueroa-Feliciano, F. M. Finkbeiner, M. Li, C. K. Stahle, C. M. Stahle, and N. Tralshawala, AIP Conference Proceedings **605**[1], 203 (2002).

[268] W. M. B. Tiest, H. F. C. Hoevers, W. A. Mels, M. L. Ridder, M. P. Bruijn, P. A. J. de Korte, and M. E. Huber, AIP Conference Proceedings **605**[1], 199 (2002).

[269] H. F. C. Hoevers, M. P. Bruijn, B. Dirks, L. Gottardi, P. A. J. de Korte, J. van de Kuur, A. Popescu, M. L. Ridder, Y. Takei, and D. Takken, Journal of Low Temperature Physics **151**, 94 (2008).

[270] K. Irwin, Nuclear Instruments and Methods in Physics Research Section A **559**[2], 718 (2006).

[271] H. Kraus, Superconductor Science and Technology **9**[10], 827 (1996).

[272] P. L. Richards, Journal of Applied Physics **76**[1], 1 (1994).

[273] H. Kaneda, T. Nakagawa, T. Onaka, T. Matsumoto, H. Murakami, K. Enya, H. Kataza, H. Matsuhara, and Y. Y. Yui, in J. C. Mather, ed., *Optical, Infrared, and Millimeter Space Telescopes*, Proceedings of the SPIE (2004), vol. 5487, pp. 991–1000.

[274] B. Swinyard, in *Space Telescopes and Instrumentation I: Optical, Infrared, and millimeter*, Proceedings of the SPIE (2006), vol. 6265(1), p. 62650L.

[275] P. Khosropanah, B. Dirks, M. Parra-Borderías, M. Ridder, R. Hijmering, J. van der Kuur, L. Gottardi, M. Bruijn, M. Popescu, J. R. Gao, *et al.* (SPIE, 2010), vol. 7741, p. 77410L.

[276] D. Morozov, P. Mauskopf, P. A. R. Ade, M. Bruijn, P. A. J. de Korte, H. F. C. Hoevers, M. Ridder, P. Khosropanah, B. Dirks, and J.R.Gao, in B. Cabrera, A. J. Miller, and B. Young, eds., *Proceedings of the 13th International Workshop on Low Temperature Detectors (LTD-13), AIP Conference Proceedings* (2009), vol. 1185, p. 48.

[277] L. Gottardi, J. van de Kuur, S.Bandler, M.Bruijn, P. Korte, J.R.Gao, R. Hartog, R.A.Hijmering, H.Hoevers, P.Koshropanah, *et al.*, IEEE Transactions on Applied Superconductivity **21**, 272 (2011).

Publications

- **Glassy behaviour of the Nd sublattice induced by Fe doping in $NdFe_xGa_{(1-x)}O_3$**

  F. Bartolomé, **M. Parra-Borderías**, J. Blasco, J. Bartolomé.

  Journal of Magnetism and Magnetic Materials **316**, E659-E662 (2007)

- **Mössbauer spectral study of $NdFe_xGa_{(1-x)}O_3$ perovskites**

  J. Rubín, C. Piquer, G. Filoti, **M. Parra-Borderías**, F. Bartolomé, J. Bartolomé.

  Journal of Magnetism and Magnetic Materials **316**, E684-E687 (2007)

- **Mo/Au bilayers deposited at Room Temperature for Transition Edge Sensors applications**

  R. González-Arrabal, A. Camón, **M. Parra-Borderías**, L. Fàbrega, J.V. Anguita, J. Sesé y F. Briones.

  Journal of Low Temperature Physics **151**, 239-244 (2008)

- **EURECA - A European-Japanese microcalorimeter array**

  P. de Korte, J. Anquita, F. Bakker, X. Barcons, P. Bastia, J. Beyer, D. Boersma, F. Briones, M. Bruijn, J. Bussons, A. Camón, F. Carrera, M. Ceballos, L. Colasanti, D. Drung, L. Fàbrega, L. Ferrari, F. Gatti, R. González-Arrabal, L. Gottardi, W. Hajdas, P. Helistö, J.W. den Herder, H. Hoevers, Y. Ishisaki, M. Kiviranta, J. van der Kuur, C. Macculi, A. Mchedlishvili, K. Mitsuda, B. Monna, R. Mossel, T. Ohashi, **M. Parra**, L. Piro, J. Sesé, Y. Takei, G. Torrioli, H. van Weers, N. Yamasaki.

  Journal of Low Temperature Physics **151**, 733-739 (2008)

- **EURECA - A European-Japanese micro-calorimeter array - art. no. 701122**

  P. de Korte, J. Anguita, X. Barcons, P. Bastia, J. Beyer, F. Briones, M. Bruijn, J. Bussons, A. Camón, F. Carrera, M. Ceballos, L. Colasanti, B. Dirks, D. Drung, L. Fàbrega, F. Gatti, R. González-Arrabal, L. Gottardi, W. Haidas, P. Helisto, J. den Herder, H. Hoevers, C. Macculi, A. Mchedlishvili, K. Mitsuda, S. Paltani, **M. Parra-Borderías**, L. Piro, R. Rohlfs, J. Sesé, Y. Takei, G. Torrioli, N. Yamasaki.

  Space Telescopes and Intrumentation 2008: ultravioleta to gamma ray, pts 1 and 2 **7011**, 1122 (2008)

- **Detailed discrimination of the order of magnetic transitions and magnetocaloric effect in pure and pseudobinary Co Laves phases.**

  M. Parra-Borderías, F. Bartolomé, J. Herrero-Albillos and L. M. García.

  Journal of Alloys and Compounds **481**, 45-56 (2009)

- **Mo-based proximity bilayers for TES: microstructure and properties.**

  L.Fábrega, I.Fernández-Martínez, O.Gil, **M. Parra-Borderías**, A.Camón, J.L.Costa-Krämer, R.González-Arrabal, J.Sesé, F.Briones, J.Santiso and F.Peiró.

  IEEE Transactions in Applied Superconductivity **19**, 460-464 (2009)

- **Effects of stress and morphology on the resistivity and critical temperature of room temperature sputtered Mo thin films.**

  L.Fábrega, I.Fernández-Martínez, **M. Parra-Borderías**, O.Gil, A.Camón, R.González-Arrabal, J.Sesé, J.Santiso, J..L.Costa-Krämer and F.Briones.

  IEEE Transactions in Applied Superconductivity **19**, 3779-3785 (2009)

- **Performance of an X-ray single pixel TES microcalorimeter under DC and AC biasing.**

  L.Gottardi, J.van der Kuur, P.A.J. de Korte, R. Den Hartog, B. Dirks, M. Popescu, H.F.C.Hoevers, M.Bruijn, **M. Parra-Borderías** and Y.Takei.

AIP Conference Proceedings, 13th International Workshop on Low Temperature Detectors **1185**, 538-541 (2009)

- **A new criterion to distinguish the order of magnetic transitions by means of magnetic measurements.**

  C.M. Bonilla, F. Bartolomé, L.M. García, **M. Parra-Borderías**, J. Herrero-Albillos and V. Franco.

  Journal of Applied Physics **107**, 09E131 (2010)

- **Universal behavior for magnetic entropy change in magnetocaloric materials: An analysis on the nature of phase transitions**

  C.M. Bonilla, J. Herrero-Albillos, F. Bartolomé, L.M. García, **M. Parra-Borderías** and V. Franco.

  Physical Review B **81**, 224424 (2010)

- **Evolution of Fe magnetic order in $NdFe_xGa_{(1-x)}O_3$.**

  M. Parra-Borderías, F. Bartolomé, J.A. Rodríguez-Velamazán and J. Bartolomé.

  Journal of Physics: Condensed Matter **23**, 046003 (2011)

- **Size and dimensionality effects in superconducting Mo thin films**

  L. Fábrega, A. Camón, I. Fernández-Martínez, J. Sesé, **M. Parra-Borderías**, O. Gil, R. González-Arrabal, J.L. Costa-Krämer and F. Briones.

  Superconductor Science and Technology **24**, 075014 (2011)

- **AC read-out circuits for single pixel characterization of TES microcalorimeters and bolometers.**

  L.Gottardi, J. van de Kuur, S.Bandler, M.Bruijn, P.de Korte, J.R.Gao, R.den Hartog, R.A.Hijmering, H.Hoevers, P.Koshropanah, C.Kilbourne, M.A.Lindemann, **M.Parra-Borderías** and M.Ridder.

  IEEE Transactions in Applied Superconductivity **21**, 272 (2011)

- **Transition Edge Sensors (TES) using a Low-G Spider-web-like SiN Supporting Structure.**

  P. Khosropanah, B.P.F. Dirks, **M. Parra-Borderías**, M. Ridder, R. Hijmering, J. van der Kuur, L. Gottardi, M. Bruijn, M. Popescu, J. R. Gao, H. Hoevers.

  IEEE Transactions in Applied Superconductivity **21**, 236 (2011)

- **Low Noise Transition Edge Sensor (TES) for SAFARI instrument on SPICA.**

  P. Khosropanah, M. Ridder, B.P.F. Dirks, J. van der Kuur, M. Bruijn, P.A.J. de Korte, J. R. Gao, H. Hoevers, **M. Parra-Borderías**, D. Morozov, P.D. Mauskopf, D. Audley, D.J. Goldie and S. Withington.

  Millimeter, Submillimeter, and Far-Infrared Detectors and Instrumentation for Astronomy V. Proceedings of the SPIE **7741**, 7410L (2011)

- **Small-Signal Behavior of a TES Under AC Bias.**

  J.van der Kuur, L.Gottardi, **M. Parra-Borderías**, B. Dirks, P.A.J. de Korte, M. Lindeman, P. Khorospanah, R. Den Hartog, H.F.C.Hoevers.

  IEEE Transactions in Applied Superconductivity **21**, 281 (2011)

- **Proximity effect and interface transparency in Mo/Au bilayers for TES applications.**

  María Parra-Borderías, Lourdes Fàbrega, Iván Fernández-Martínez, Agustín Camón, Oscar Gil, Raquel González-Arrabal, Javier Sesé, José Costa-Kramer and Fernando Briones.

  in progress

- **Development and characterisation of Mo/Au thermometers for TES applications.**

  María Parra-Borderías, Iván Fernández-Martínez, Lourdes Fàbrega, Agustín Camón, Oscar Gil, Raquel González-Arrabal, Javier Sesé, José Costa-Kramer and Fernando Briones.

  in progress

- **Thermal stability of Mo/Au bilayers for TES applications.**

  María Parra-Borderías, Iván Fernández-Martínez, Lourdes Fàbrega,

Agustín Camón, Oscar Gil, Raquel González-Arrabal, Javier Sesé, José Costa-Kramer and Fernando Briones.

in progress

- **Inhibition of Nd magnetic ordering induced by Fe doping in $NdFe_xGa_{(1-x)}O_3$.**

  M. Parra-Borderías, F. Bartolomé, J.A. Rodríguez-Velamazán and J. Bartolomé.

  in progress

- **Disorder induced Negative Magnetization in $NdFe_xGa_{(1-x)}O_3$ series.**

  M. Parra-Borderías, F. Bartolomé, Fabrice Wilhelm, J. Bartolomé, Laura Badía-Romanos and Andrei Rogalev.

  in progress

Acknowledgements

Durante estos cuatro largos años, mucha gente ha contribuido de forma significativa a la realización de este trabajo, tanto que me hubiera sido imposible llegar a este punto sin ellos. Por eso, me gustaría terminar esta tesis expresando mi gratitud.

En primer lugar, a mis directores de tesis Fernando Bartolomé y Agustín Camón, por darme la oportunidad de embarcarme en esta aventura, que me ha llevado a descubrir personas y lugares increíbles, a ponerme a prueba y a conocerme un poco más. Gracias por vuestra paciencia y apoyo. Porque nadie sabe lo que nos ha costado llevar a cabo dos temas que, inicialmente, parecían tan distantes y ahora, parecen casi uno; gracias por hacer que fuera posible sin que haya tenido que desdoblarme. También por ser conscientes de mis límites y empujarme a superarlos. Y sobre todo, muchas gracias por todo lo que me habéis enseñado.

Al pequeño-gran grupo de Eureca en España: Lourdes Fábrega, Raquel Gónzalez-Arrabal, Iván Fernández-Martínez, Javier Sesé, Oscar Gil, José Costa-Kramer y Fernando Briones, con los que he compartido el camino hacia el primer TES español y sin cuyo trabajo y generosidad esta tesis no hubiera sido posible. A Iván, por estar siempre dispuesto a preparar hasta la última muestra que te pidiéramos. A Oscar, por esas estupendas imágenes de TEM, SEM o lo que hiciera falta. A Javier y Raquel por su entusiasmo y apoyo. Y en especial, muchas gracias Lourdes, por tener siempre tiempo para responder mis dudas, por tu disponibilidad y empeño en hacernos avanzar a todos.

Al personal de ORBIMAT e IMANA. A Juan Bartolomé por resolver mis dudas sobre las perovskitas de Neodimio y por sus múltiples sugerencias y comentarios que han contribuido a mejorar cualitativamente el contenido de este trabajo. A Maria José Pastor por todas las muestras preparadas. A Marisa Bonilla por enfrentarte siempre a todos los follones burocráticos que he dejado en tus manos con una sonrisa. A Enrique Burzurí, Marco Evangelisti y Fernando Luis por sus medidas en el refrigerador de dilución. Enrique, gracias por realizarlas restando tiempo de tu propia tesis, aún cuando nada tenían que

ver con ella. A Julia Herrero por toda la ayuda recibida desde el principio, cuando más perdida estaba, por el LaTex, el SQUID, los artículos y tu tesis, que me ha sacado de más de un apuro al escribir la mía.

Al personal del Departamento de Física de Materia Condensada y del Instituto de Ciencia de Materiales de Aragón. A Marta Castrillo y Fernando Gómez, por tener siempre a punto el Helio y el Nitrógeno necesarios. A Leticia Tocado por estar disponible cuando la necesitábamos en las transferencias y por las referencias de calorimetría. A Ana Arauzo, Ainhoa Urtizberea y Enrique Guerrero por su ayuda en cada medida en el SQUID y el PPMS. A Miguel Ángel Gil por todas las piezas fabricadas a pesar de mis pésimos planos. A Pedro Tellez por los cableados, las reparaciones y el Labview y también al resto del personal del Servicio de Instrumentación Científica de la Universidad de Zaragoza. A Concha Sánchez por su rapidez con las medidas de Rayos-X. A Javier Blasco por estar siempre dispuesto a resolver mis dudas, desde la fabricación de mis perovskitas hasta el uso de FullProf. A Javier Campo, Jose Alberto Rodríguez Velamazán y al resto del personal del ICMA en el ILL por su apoyo en los experimentos en D20, D2B y D1B, y al personal de esas líneas. En especial, gracias Jose Alberto por pelearte hasta el final con el monocromador de D20 y conseguir que nuestras medidas salieran adelante. A Fabrice Wilhelm y al resto de personal de ID12 en el ESRF. A María Abadías, Aurora Espinosa y Concha Arasanz por su ayuda con los trámites burocráticos y, por supuesto, a los becarios del departamento.

To Jan van der Kuur, Bob Dirks, Pourya Khorospanah, Marcel Ridder, Marcel Bruijn, Roland den Hartog, Piet de Korte, Mark Lindeman, Henk Hoevers and all the staff of the Netherlands Institute for Space Research for accepting me as a visiting PhD student and receiving me with open arms during my two research stays. I am specially thankful to Manuela Popescu for helping me to familiarise with all the characterisation equipment and for caring about me not feeling alone, and to Luciano Gottardi for offering me the opportunity to work with all of you, for your patience and for being always willing to help. Thanks to you, my knowledge of the TES operation and my PhD work reached a qualitative leap. It was a pleasure to work with all of you.

A mis compañeros de café, despacho, casa...Sol, Sara, Pepa, Raquel, Enrique, Vera y Clara, por las dudas compartidas, las cenas y las cervezas, o lo que hiciera falta. A Marcelo, Katrin, Rosa y Tabaré por hacer que la fría Holanda se pareciera mucho a casa, en especial a Luis, vecino, por las tortillas, las películas, y por llevarme a tantos sitios y presentarme a tanta gente. A las del Azúa, Elena, Alex, Laura, Talía, Violeta y María Vic, gracias, por seguir estando ahí. Alex, mil gracias por escucharme aunque lo que te cuente te suene a chino (y por esa estupenda portada!) y Ele, por que sabes lo que es esto y,

aunque no te suena a chino, me escuchas también. Gracias a las dos por las risas y los ánimos, por aguantar en los peores momentos, por ayudarme a relativizar y por, a pesar de Madrid, Huesca, Astudillo, trabajos y locuras varias seguir esforzándoos por no quedarnos sin nuestros raticos. A Leticia, Juan, Chava, Graham, Ana Ramo, Esti y Mor, por los cafés, las tapas y las salidas de los últimos años. A Marcos, Jesús, Marian, Toño, Carlos y demás oscenses, por haber convertido Huesca en mi segunda casa. En especial a Jana y Chala, por los viajes de los lunes por la mañana y las excursiones de los domingos, que me devolvían las fuerzas para enfrentarme a la semana. A Pilar, Antonio y Sofía, por abrirme las puertas de vuestra casa y hacerme sentir como en la mía.

A mis abuelos Antonia y Antonio y a mi yaya Juana, por su preocupación constante en mis idas y venidas por Europa. A mis primos Juan y Ana, por las comidas, cenas y vermuts varios, que con vosotros siempre parecen mejores, a mis tíos Inma y Javier por estar siempre pendientes de mi. Al resto de mis primos y tíos de la enorme familia Borderías y de mi familia en Villalba, gracias por vuestros ánimos a pesar de la distancia. A mis padres, gracias a vosotros soy lo que soy, gracias por darme la libertad de equivocarme. A mi hermano, por estar siempre a mi lado y por alegrarme el día a día. Y, sobre todo, a Andrés, porque a tu lado siento que puedo con todo, por darme la calma que me falta, por no juzgarme y darme siempre tu apoyo y por estar siempre dispuesto a arrancarme una sonrisa.

ISBN 978-84-15274-87-2

Prensas Universitarias
Universidad Zaragoza